TESIS DE LA UNIVERSIDAD DE ZARAGOZA

2021

176

Anastasios Tzotzis

Implementation of CAD-based and 3D non-linear finite element methodologies on modelling of machining processes

Director/es

Kyratsis, Panagiotis

García Hernández, César

ISSN 2254-7606

Prensas de la Universidad Universidad Zaragoza

ISSN 2254-7606

Universidad Zaragoza
1542

Tesis Doctoral

IMPLEMENTATION OF CAD-BASED AND 3D NON-LINEAR FINITE ELEMENT METHODOLOGIES ON MODELLING OF MACHINING PROCESSES

Autor

Anastasios Tzotzis

Director/es

Kyratsis, Panagiotis
García Hernández, César

UNIVERSIDAD DE ZARAGOZA
Escuela de Doctorado

2021

Universidad Zaragoza
1542

Tesis Doctoral

Implementation of CAD-based and 3D non-linear finite element methodologies on modelling of machining processes

Autor

Anastasios Tzotzis

Directores

Dr. César García-Hernández

Dr. Panagiotis Kyratsis

Universidad de Zaragoza

Departamento de Ingeniería de Diseño y Fabricación

2020

Universidad Zaragoza
1542

Doctoral Thesis

Implementation of CAD-based and 3D non-linear finite element methodologies on modelling of machining processes

Author

Anastasios Tzotzis

Directors

Dr. César García-Hernández

Dr. Panagiotis Kyratsis

For obtaining the title of Doctor

by University of Zaragoza

Zaragoza, November 2020

University of Zaragoza

Department of Design and Manufacturing Engineering

CONTENTS

PUBLICATIONS INCLUDED IN THE PRESENT DOCTORAL THESIS

1. PUBLICATIONS INCLUDED IN THE PRESENT DOCTORAL THESIS

The present work of Doctoral Thesis is titled "**Implementation of CAD-based and 3D non-linear finite element methodologies on modelling of machining processes**". It is presented as a thesis by compendium of publications according to Articles 12, 13 and 14 of RD 99/2011 of January 28 (BOE of February 10), which regulates the official teachings of doctorate and Title IV, Chapter III of the Agreement of 25/06/2020, of the Governing Council of the University of Zaragoza, by which the Regulation of Doctoral Thesis is approved (BOUZ 13/07/2020). The relevant text is integrated in: https://escueladoctorado.unizar.es/es/normativa-general

This Doctoral Thesis is composed by the following publications:

- Tzotzis A., García-Hernández C., Huertas-Talón J.L. and Kyratsis P., (2020), CAD-based automated design of FEA-ready cutting tools, *Journal of Manufacturing and Materials Processing*, 4(4), pp. 1-14, https://doi.org/10.3390/jmmp4040104

- Tzotzis A., García-Hernández C., Huertas-Talón J.L. and Kyratsis P., (2020), FEM based mathematical modelling of thrust force during drilling of Al7075-T6, *Mechanics & Industry*, 21(4), pp. 1-14, https://doi.org/10.1051/meca/2020046

- Tzotzis A., García-Hernández C., Huertas-Talón J.L. and Kyratsis P., (2020), 3D FE Modelling of Machining Forces during AISI 4140 Hard Turning, *Strojniški vestnik - Journal of Mechanical Engineering*, 66(7-8), pp. 467-478, https://doi.org/10.5545/sv-jme.2020.6784

- Tzotzis A., García-Hernández C., Huertas-Talón J.L. and Kyratsis P., (2020), Influence of the Nose Radius on the Machining Forces Induced during AISI-4140 Hard Turning: A CAD-Based and 3D FEM Approach, *Micromachines*, 11(9), pp. 1-16, https://doi.org/10.3390/mi11090798

ACKNOWLEDGMENTS

2. ACKNOWLEDGEMENTS

The present Doctoral Thesis is the result of my four-year research in the Department of Design and Manufacturing Engineering, University of Zaragoza, in the field of FEM-based and CAD-assisted machining. The completion of this work fulfilled one of my lifetime dreams and for that I would like to express my sincere gratitude to all those who contributed to the success of its completion.

First of all I would like to thank my directors, Dr. César García-Hernández and Dr. Panagiotis Kyratsis for placing their trust in me with the assignment of the dissertation, for their efficient and continuous guidance and finally for their constructive supervision of my research. I dare to say that this feat would not be possible without their support. Moreover, they contributed to the shaping of my future and showed me the way to the fascinating universe of research. I also feel the need to warmly thank Dr. José-Luis Huertas-Talón, whose vast experience in the field and his valuable comments on each of my research steps helped me to efficiently improve the quality of my thesis.

Finally, I would like to thank my family and all those close to me for their full support and the confidence they showed me all these years. Special thanks go to my wife Argyro, for believing in me and encouraging me to carry on. It has been a privilege to be part of the University of Zaragoza during the preparation of my Doctoral Thesis.

Zaragoza, November 2020

Anastasios Tzotzis

NOMENCLATURE

3. NOMENCLATURE

Symbol	Description	Unit
T_0	Bulk temperature of the workpiece material	K
h_{cond}	Conduction heat transfer coefficient	N/(s×mm× °C)
h_{conv}	Convection heat transfer coefficient	N/(s×mm× °C)
V_c	Cutting speed	m/min
ρ	Density	kg/m^3
ap	Depth of cut	mm
D	Drill diameter	mm
$\bar{\sigma}$	Effective stress	MPa
f	Feed	mm/rev
F_a	Feed force	N
τ_f	Frictional stress at the tool – chip interface	MPa
c	Heat capacity	J/kgK
λ	Inclination angle	
A	Initial yield stress	MPa
IC	Inscribed circle diameter (for turning insert)	mm
k_r	Lead angle	
ε_f	Limit fracture strain	
D_c	Material constant in the fracture criterion	
σ_{max}	Maximum tensile principal stress	MPa
T_m	Melting temperature	K
σ_n	Normal stress	MPa
re	Nose radius	mm
ε	Plastic strain	
$\dot{\varepsilon}$	Plastic strain rate	s^{-1}
μ	Poisson's ratio	
F_r	Radial force	N
$\dot{\varepsilon}_0$	Reference plastic strain rate	s^{-1}
T	Reference temperature	K
γ	Rake angle	
F_{main}	Resultant force	N
m	Shear friction coefficient	
μ	Sliding friction coefficient	
N	Spindle speed	min^{-1}
k_τ	Sticking friction coefficient	
n	Strain hardening exponent	
B	Strain hardening modulus	MPa
C	Strain rate dependence coefficient	

Symbol	Description	Unit
F_t	Tangential force	N
α	Thermal expansion	μm/mK
λ	Thermal conductivity	W/mK
m	Thermal softening coefficient for JC model	
S	Thickness (for turning insert)	mm
F_z	Thrust force	N
σ_y	Uniaxial yield stress	MPa
E	Young's modulus	MPa

LIST OF FIGURES

4. LIST OF FIGURES

LIST OF TABLES

5. LIST OF TABLES

INTRODUCTION

6. INTRODUCTION

6.1. Thesis Framework

Since ancient times humankind searched for ways of processing materials. Nowadays, many metallic products are produced by metal removal process. Therefore, metal cutting is probably the most common manufacturing process. Operations such as drilling, turning and milling fall in this category and are essential for every manufacturing industry including automotive, aerospace, shipbuilding, consumer products and medical equipment.

As technology advances, manufacturing industries search for ways of taking advantage the intuitive tools that modern technology has to offer, mainly for increasing productivity as well as decreasing production costs. The reason for the continuous race for improvement are the ever-increasing needs of the world, combined with the high level of competition between companies. In addition, the need for high-end products lead to a demand for increased precision production techniques.

The Computer Aided Design (CAD) resources combined with the Finite Element Method (FEM) are powerful tools that greatly contribute towards the achievement of the aforementioned goals. With the implementation of such tools it is possible to:

- visualize the manufacturing process of a product,
- predict failures and
- estimate production costs, without the need for a physical test setup.

Moreover, these techniques and methodologies enable the fast and cost-effective optimization of the fabrication processes.

Even though the employment of FEM during investigations into the manufacturing processes is relatively new [1], the advent of more sophisticated Finite Element Analysis (FEA) software such as DEFORM™, ABAQUS™, AdvantEdge™ and ANSYS™ in the last decades, conduced to the increased interest for FEM-assisted researches. Until recently, the two-dimensional (2D) modelling was the primary tool for machining investigations [2-4] because it provides a good approximation of the under study process within reasonable amount of time. Additionally, the lack of powerful computer systems in the previous decades prevented the development of three-dimensional (3D) modelling. Despite the fact that the 2D FEM is used successfully to date by many researchers [5-7] for specific purposes, it bears several restrictions that limits its range of application. For example, 2D FEM cannot be used to fully model a drilling, turning or milling operation, as it is not possible to capture the full cutting tool geometry and therefore the complete material chip formation cannot be visualized nor the resultant cutting forces can be estimated. In contrast, the

3D modelling provides researchers with extended information on the under study subject. In the past two decades, an effort was made to harness the increasing computer resources so that 3D finite element (FE) modelling can be feasible. Beginning with the modelling of drilling process in three dimensions [8], several researchers developed an interest in 3D machining. Especially for drilling, the key points of research include the chip morphology and evolution [9,10], the produced thrust forces and torque, as well as the occurring stresses [11-15] and finally the built-up heat and wear [16,17]. Similarly, the main investigation aspects in turning are the chip formation, flow and breakage [18,19], the generated machining force components as well as the induced residual stresses [20-24] and lastly the developed tool wear and heat transfer [25-27]. Finally, numerous studies exist in the literature that deal with critical milling topics such as the chip formation, the stress and temperature distribution plus the developed cutting forces [28-33].

Summarizing, the employment of 3D FEM enables the investigation for more complicated machining operations compared to 2D, in addition to the greater extent of research that it offers. Hence, researchers can study the effect of several machining conditions such as cutting speed, feed, depth of cut and tool geometry on the generated cutting forces, the induced stresses, the built-up heat and tool wear as well as the formed chip morphology with minimal effort and under a cost-effective way. In general, the most important benefits that derive from the use of 3D FEM in machining are the following:

- It is possible to visualize the complete machining process.
- A great number of machining aspects can be thoroughly investigated.
- There is no need for a physical experimental setup.
- Costs related to safety procedures can be eliminated.
- Both production costs and times can be minimized.
- It is possible to predict manufacturing failures and errors.
- And finally several cutting results may be accurately predicted.

The previously mentioned advantages depend on the accuracy and efficiency of the developed FE model. In order to successfully establish an accurate and efficient FE model, especially a three-dimensional one, it is imperative to import a cutting tool model of high fidelity to the setup. Modern CAD systems allow for the robust design of the cutting tool's geometry by exploiting their programming resources and powerful design functions. With these in mind, present Doctoral Thesis examines the possibility of combining CAD-based techniques (i.e. parametric design plus CAD-based programming) and 3D-FEM approach to model commonly used machining processes at increased level of accuracy, in addition to investigating the effect of critical machining parameters on the generated cutting forces and the formed chip

morphology. Furthermore, it deals with the establishment of mathematical models for prediction purposes of the cutting forces, based on recognized statistical methodologies. Figure 1 visually explains the four key points of this thesis, as already mentioned above.

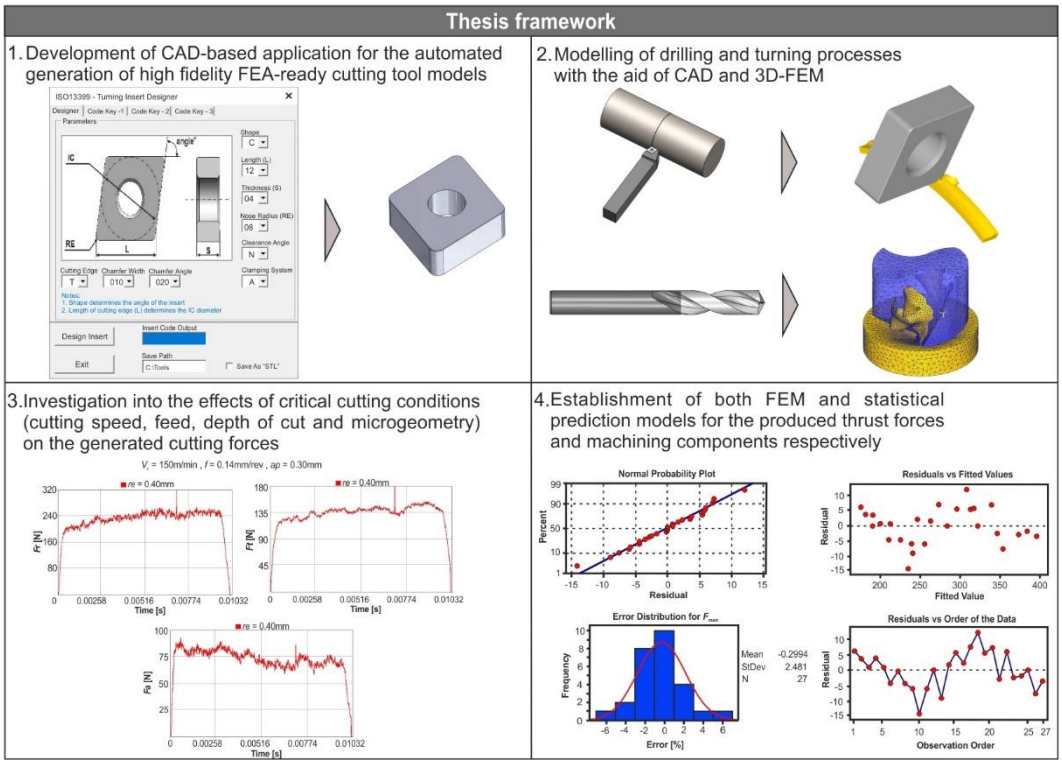

Figure 1. The four key points of the thesis framework

6.2. Motivation

Material removal is one of the most important shaping processes in the industry. Moreover, a wide variety of products spanning from a simple hand tool to an aircraft part can be produced via machining. These significant facts along with the constant need for evolution in engineering became the foundation for the present thesis.

The primary objective during research and development in the FEM-based machining area, focus on:

- increasing the accuracy of the developed FE models,
- reducing the preparation time and
- minimizing the required experimental work.

In order to achieve the high standards and to ensure the reliability of the cutting processes, new methods of theoretical analysis must be determined. Additionally, new simulation models are required to cover the continuous development of cutting tools. In the light of these considerations, an extensive literature survey was carried

out as a first step towards the deeper understanding of previous works in the field. Next, the processing of the findings revealed certain topics that required further investigation or improvement. Such topics include:

- The accuracy improvement during FE modelling.
- The investigation for the effect of critical machining conditions on several parameters such as the developed cutting forces, the chip morphology, as well as the stress and the temperature distribution.
- And the establishment of efficient and user-friendly prediction models.

Upon finalizing the literature survey, the research was divided into four stages (see Figure 1). The first stage is associated with the enhancement of the accuracy in FE modelling. The second one deals with the FE modelling of drilling and turning operations in three dimensions, assisted with CAD-based techniques. The third stage is related to the machining investigation into industrial materials under critical cutting conditions. Finally, the last one presents the development of prediction models with the aid of statistical methodologies.

1) Most researchers use in their studies either cutting tool models provided by manufacturers or design them by themselves. However, in the first case it is possible that the yielded simulation results may be of low accuracy, due to the fact that the models downloaded from a manufacturer's site are usually simplified and often miss critical geometric characteristics. In the latter, the researcher may be forced to spend hours for repetitive design tasks that could be frustrating, especially when design errors occur. To avoid confusions and to focus on more creative tasks, an application for the automated design of cutting tools was designed and developed with the aid of Application Programming Interface (API) of SolidWorks™ CAD system. In this stage, the programming resources of SolidWorks™ were employed, combined with the parametric design strategy so that the conception of the application could be achieved.
2) With the finalization of the application, a number of 3D FE models were prepared and the equivalent cutting tools were generated for testing purposes. The simulation tests completed successfully and the acquired results revealed an increased correlation with the corresponding experimental results. Later, similar FE models for drilling and turning were set, according to findings and recommendations from already published works, by using modern FEA software, namely DEFORM™-3D. The material properties, the damage evolution, the friction approximation, as well as the thermal flow, were all set with respect to experimental work carried out during this research, in addition to the findings that were published by experts in the field. Furthermore, an effort to simplify the machining problems was made, by employing several

well-established strategies such as the CAD-assisted configuration of the tool-workpiece interface and the mesh refinement localization.

3) The third stage of the thesis is directly linked to the previous one. The acquired simulation results were processed with the aid of computing environments such as Excel™ and MATLAB®, so that the results can be converted into usable data sets. Later, the processed data were visualized and compared directly to equivalent findings that are available in the literature. This comparison showed that the developed FE models were in agreement with the ones found in already published studies. Furthermore, a number of experimental tests were carried out to further validate the accuracy of the developed FE models. In order to accurately perform the experimental work, a CNC machining center was utilized along with the measuring equipment (i.e. dynamometer). At the same time, an investigation regarding the effects of cutting speed, feed, depth of cut and tool geometry on the developed cutting forces was conducted. Specifically, the thrust forces generated during drilling were studied, as well as the machining components (radial, tangential and feed forces) induced during turning. In addition, both the chip evolution and morphology were studied with respect to the applied operation, material, tool and cutting conditions.
4) Finally, the verified simulated results were used for the development of mathematical models that can predict the generated cutting forces within specific limits. The models that were represented by polynomial functions, can generate results of high accuracy instantly and without the need of any specialized software. The modelling was performed by utilizing the broadly used Response Surface Methodology (RSM), which in addition enhanced the visualization of the investigation concluded during stage three. To further strengthen the validity of the statistical models, the Analysis of Variance (ANOVA) was employed. Results from the analysis revealed that the developed models are robust and can be safely used for prediction purposes.

6.3. Presentation and justification of publication thematic parts

The publications presented in this Doctoral Thesis work are framed within the CAD-based programming and the implementation of 3D FEM for the modelling of machining processes, as well as the investigation for machining conditions. As mentioned in the previous section, the publications are the following:

- **CAD-based automated design of FEA-ready cutting tools**
- **FEM based mathematical modelling of thrust force during drilling of Al7075-T6**
- **3D FE modelling of machining forces during AISI 4140 hard turning**

- **Influence of the nose radius on the machining forces induced during AISI-4140 hard turning: A CAD-based and 3D FEM approach**

The accuracy of the yielded results is the key factor when it comes to 3D FE modelling. In order to achieve satisfying results, it is imperative that the FE model is properly set and the cutting tool model is designed to the last detail. Unfortunately, tool manufacturers usually do not provide models of high quality, rather they offer simplified versions so that they can reduce costs and maintain their databases at reasonable sizes. It is also possible that they do not include critical geometric characteristics to the CAD models, so that they can protect their intellectual property. In the light of this situation, researchers must design the necessary cutting tools on their own, which can prove a really tiresome and time-consuming procedure, especially when a large number of different models is required. The publication entitled "**CAD-based automated design of FEA-ready cutting tools**" presents an application for the automated generation of cutting tool models that can be directly imported to most commercially available FEA software. The application was developed by exploiting the programming resources of the API of SolidWorks™ and can cover a wide variety of cutting tools used in the turning processes. Additionally, it can be extended to generate more sets of tools by editing a fraction of the code. Moreover, the design procedure follows the proposed algorithm that is based on the parametric design technique.

Drilling is one the most broadly used machining operations during the manufacturing process of a product, thus numerous studies related to drilling exist in the literature. However, the number of studies that involves FE modelling is still limited. More importantly, a lack in 3D FE models was revealed once the relevant literature survey was performed. The published paper with title "**FEM based mathematical modelling of thrust force during drilling of Al7075-T6**" presents a 3D FE model for drilling of Al7075-T6, under a range of conditions that are recommended by most tool manufacturers. In addition, the selected aluminium alloy demonstrates excellent mechanical properties and is often used in the aerospace industry. Except the presentation of the FE model, the paper investigates the effects of the applied conditions and tool diameter on the generated thrust forces, as well as the produced chip formation with the aid of DEFORM™-3D and several computing tools and methodologies. In fact, the effects were graphically presented by using the RSM and additionally, a prediction model for the thrust forces was developed, which was verified with ANOVA. Finally, the paper describes the experimental work that was conducted to validate the numerical model.

Similarly to drilling, a great number of studies related to turning is available worldwide. Since turning is one of the most used machining processes, along with

drilling and milling, it is logical to draw the interest of many researchers. Even though orthogonal cutting has been studied widely by using 2D FE modelling, the level of engagement with the 3D FE modelling in general remains low. The publication entitled "**3D FE modelling of machining forces during AISI 4140 hard turning**" proposes a schematic in three dimensions for hard turning of AISI-4140 steel. The chosen material is another commonly used metal in the manufacturing industry. Moreover, the selected cutting conditions meet the manufacturer's standards and recommendations. At the same time, this publication presents a statistical model for prediction purposes of the generated machining forces by using similar methodologies to the previously mentioned publication "FEM based mathematical modelling of thrust force during drilling of Al7075-T6". Furthermore, a study on the performance of the cutting tool is included, according to the selected cutting speed, feed and depth of cut.

Further investigation into the behavior of AISI-4140 steel during turning was conducted in the paper "**Influence of the nose radius on the machining forces induced during AISI-4140 hard turning: A CAD-based and 3D FEM approach**" to provide a better understanding of the induced turning force components, the chip morphology and formation. During this research, emphasis was given on the microgeometry of the tool models. For this reason, the CAD-based application presented in the paper "CAD-based automated design of FEA-ready cutting tools" was utilized. In addition, a CAD-assisted method was selected for the process layout setup. The paper contains findings regarding the influence of the cutting conditions on the induced turning forces, as well as the performance of the cutting tools in terms of their microgeometry. Moreover, both a numerical and a statistical model of high accuracy are proposed.

6.3.1. Presentation of the publication "CAD-based automated design of FEA-ready cutting tools"

One of the most important considerations during FE model setup is the representation of the cutting tool in three dimensions, so that the full geometry of the tool can be analyzed. In the case of turning, the tool's micro-geometry plays a major role on the generated numerical results. It is possible to utilize the Application Programming Interface (API) and the parametric modelling to support the integration of Computer-Aided Design (CAD), Computer-Aided Manufacturing (CAM) and Computer-Aided Engineering (CAE) [34-50].

The present paper describes a CAD-based application that can be used to generate CAD models of standardized turning inserts. The application was developed with the aid of the SolidWorks™ API and the Visual Basic for Applications (VBA)

programming language. The tools that are designed by the described application are solid, consistent models including the full geometry and can be easily imported to commercially-available FEA software [51-52]. Finally, a set of 3D simulations were carried out by utilizing DEFORM™-3D, to verify the functionality of the generated models.

The principal geometric parameters embedded in the presented application can be found in the ISO-13399 catalogues. Even though modern cutting tools are standardized, some details such as the combinations of chamfer width and chamfer angle can be different from manufacturer to manufacturer. Figure 2a illustrates a common turning insert used during machining of industry-standard materials such as hardened steel, cast iron and aluminium alloys: the 80° rhombic CNGA120408T01020. The symbol *IC* represents the inscribed diameter, *RE* is the corner radius, *S* denotes the thickness and finally *L* is the theoretical cutting edge length.

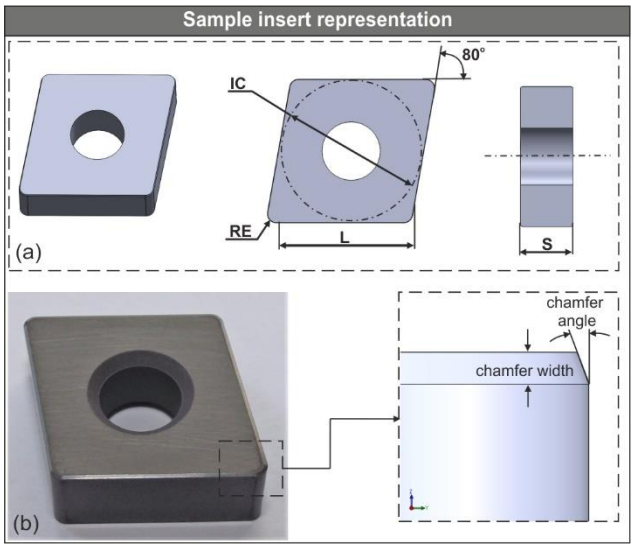

Figure 2. Basic geometric parameters of the CNGA120408T01020 insert (a) and its micro-geometry (b).

Figure 2b depicts the cutting edge micro-geometry, which affects several aspects of the tool such as the life-cycle, the generated machining forces and temperatures [53-57]. One of the most common tool materials is the Cubic Boron Nitride [58].

The provided toolbox of the SolidWorks™ API was used to design the user interface [59]. The idea was to design a simple, yet visually-enhanced interface with easy parameter selection. Figure 3 illustrates the main tab of the application's user interface. Nine combo-boxes were used to facilitate the properties selection procedure. Each combo-box contains a variety of options according to its function. For example, the combo-box entitled "Shape" defines the shape of the insert. This combo-box, along

with the one entitled "Length (L)" determine the shape, the corner angle and the size of the insert which are the most basic characteristics.

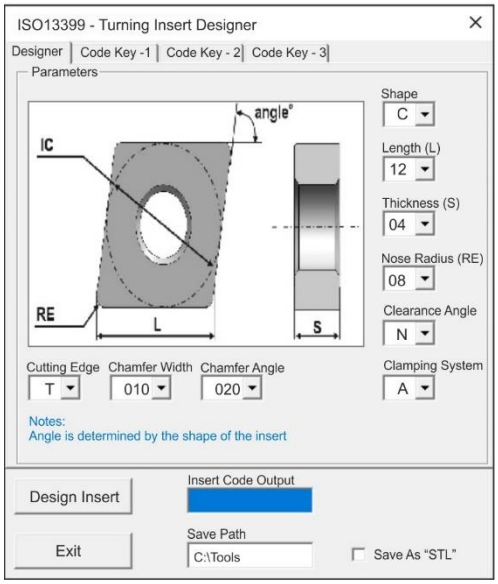

Figure 3. The application's interface.

The coding of the application was performed with VBA which derives from Microsoft™ Visual-Basic™ 6. In addition, a feature-based parametric methodology was implemented during the 3D modelling procedures, as such the workflow (Figure 4) of the application's code was based on similar principals. By observing Figure 5, the steps that are required to be performed in order to realize the design process are the following:

- Declaration of the necessary variables. These variables correspond to each of the geometric characteristics and dimensions such as the shape, the inscribed circle, the corner angle and the corner radius.
- Linking of the defined variables to the input and output controls (i.e. combo-boxes) of the interface.
- Creation of a new Part document with "NewDocument" method.
- Insert shape selection, according to the inputs, with the aid of the "Select…Case" statement.
- Selection of the plane with respect to the FEA standard coordinate system and activation of a new sketch ("InsertSketch" method).
- Realization of the design process according to the selected design scheme, which includes the sketch of the inscribed circle ("CreateCircleByRadius" method) and the contour lines ("CreateLine" method). Finally, the code for the design process is responsible for the application of both the dimensions ("AddDimension2" method) and the geometric relations ("SketchAddConstraints" method) that fully define the contour.

- Extrusion of the base solid model based on the selected thickness and the clearance angle. This action is carried out with the "FeatureExtrusion2" method.
- Definition of the micro-geometry, which includes the corner radii ("FeatureFillet3" method) and the cutting edge ("InsertFeatureChamfer" and "FeatureFillet3" methods). The automatic selection of the corresponding topology (i.e. edges), was achieved with the aid of a "For" loop traversing all available topology objects of the CAD model such as faces and edges. The recognized topology objects are given new IDs and are then stored to an array so that they can be accessible.
- Creation of the center hole according to the selected clamping system.
- Export of the generated model to FEA-ready file formats (i.e. "STL"), as well as to "SLDPRT" native format for editing purposes.

The produced models were finally checked for errors such as gaps, holes, non-manifolds and intersecting geometry to ensure their robustness [60,61].

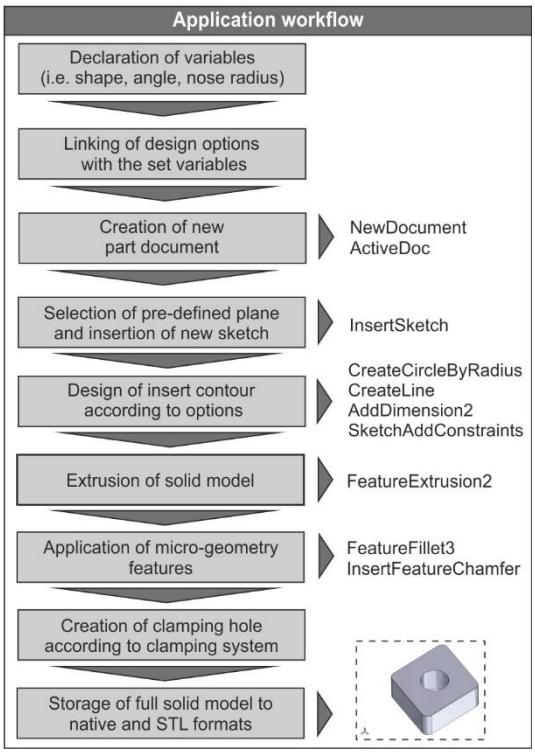

Figure 4. The application's workflow.

The goal of this workflow is to create a simple model tree [62]. This is achieved by creating a base feature and then adding the rest of the design features, rather than creating a cubic solid and then trying to remove material. In addition, the relationship between the designed objects is defined in such a way, so that in the case a design change occurs, the objects will automatically follow this change. Figure 5a illustrates

the application of the aforementioned modelling technique in order to design a standardized type of insert of the CNGA family. The steps followed include:

- The selection of the sketch plane with respect to the FEA coordinate system.
- The sketching of a construction circle with diameter equal to the IC variable value (see Figure 2a).
- The insertion of an appropriate number of line sketches (four in this case) that form the selected shape of the tool and the application of the equivalent number of tangent geometric relations.
- The forming of the corner angle according to the corresponding variable value (80° for the diamond-shaped inserts). Because the formed contour is always a tangential quadrilateral, except for the cases of square and triangle, the varying edge length is determined by Equation 1.

$$x = \frac{2r}{\sin\alpha}, \tag{1}$$

Where: x is the length of the edge, r denotes the inradius and α is the corner angle.

- The creation of the solid model based on the selected thickness and cutting edge. In the case of the example, thickness is equal to 4.76mm and cutting edge equal to zero.
- The design of the cutting edge, which is formed according to the selected cutting edge type, chamfer width and chamfer edge (see Figure 2b).
- Finally, the creation of the center hole that is used for the clamping of the insert to the tool-holder.

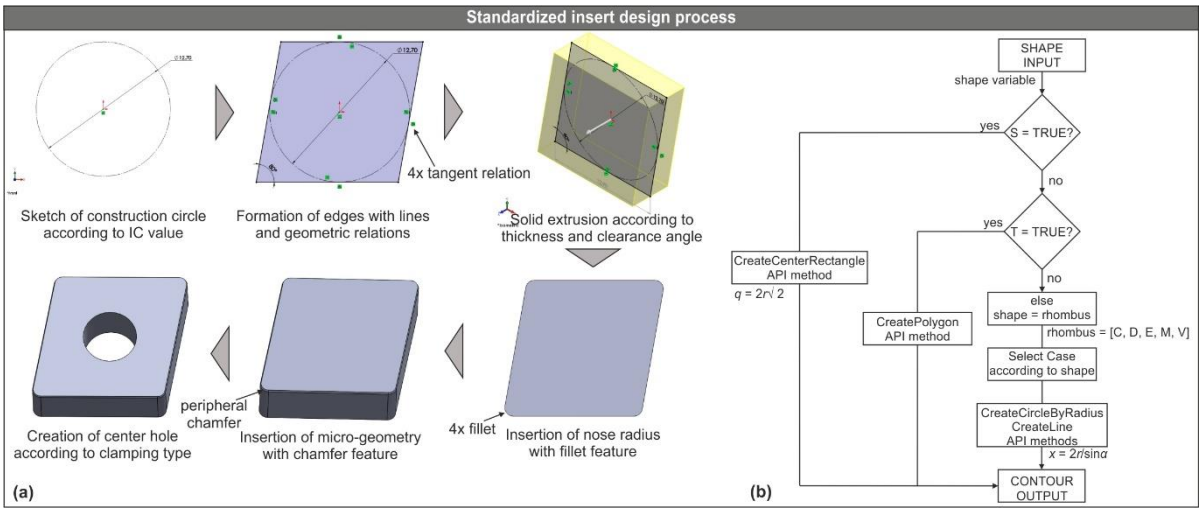

Figure 5. The design workflow for the CNGA-family inserts (a) and the design algorithm (b).

Figure 5b presents a simple algorithm that performs a check on the shape so that the proper values can be applied accordingly. In the case of a square-shaped insert, the algorithm skips the tangential quadrilateral shape and uses a center rectangle

sketch instead, whereas in the case of a triangular insert it uses a polygon sketch with three edges. For the first case, the diagonal q must be determined, while for the latter the inradius.

In order to validate the functionality of the generated models, a FE model was prepared and nine 3D turning simulations were run. An effort was made to create a test setup according to widely-used parameters and settings. The selected cutting tool, material and cutting conditions, have already been successfully studied [63-65] and thus, were chosen for this study. Figure 6a presents the test setup. A sample insert model was generated, saved in STL file format and then imported to DEFORM™-3D ver. 12 for the preparation of the FE model as follows:

- The tool is modelled as rigid and meshed with approximately 50000 tetrahedral elements.
- The workpiece is modelled as plastic and its mesh varied according to the value of feed. The size of the minimum element was fixed to 25% of the feed for all tests [66].
- The selected workpiece material is AISI-4140 steel.
- The tool used is the CNGA120408 (corner radius of 0.8mm).
- The cutting conditions applied are the produced combinations of the three levels of cutting speed V_c (80m/min, 115m/min and 150m/min) and feed f (0.08mm/rev, 0.11mm/rev and 0.14mm/rev) at depth of cut ap = 0.30mm.
- The lead angle k_r is 75° and both the rake γ and inclination λ angles are negative with a value of −6°.
- The heat transfer coefficient via convection (h_{conv}) was set to 0.02 N/(s×mm×°C) for dry cutting and via conduction (h_{cond}) was set to 45 N/(s×mm×°C).

The simulation tests yielded relatively accurate results both for the cutting forces and the chip formation since the level of convergence for all simulation tests was adequate, considering that most of the FE model parameters such as the material properties, the flow stress constants and the friction coefficients were kept to their default values as provided by the software. The yielded results were compared to experimental values that are available in the literature, for the same cutting conditions, to prove the validity of the generated CAD models.

The following graphs (Figure 6b-e) were plotted to visualize all three machining force components and the resultant force, in addition to comparing the mean values of the produced cutting force components graphically. Figure 6b depicts the results for the radial force, Figure 6c for the tangential force, Figure 6d for the feed force and finally Figure 6e for the calculated resultant force. By observing these graphs, it is concluded that the generated CAD model contributed to the convergence of the

results, despite the fact that a few discrepancies occurred (mostly in the tangential and the feed force).

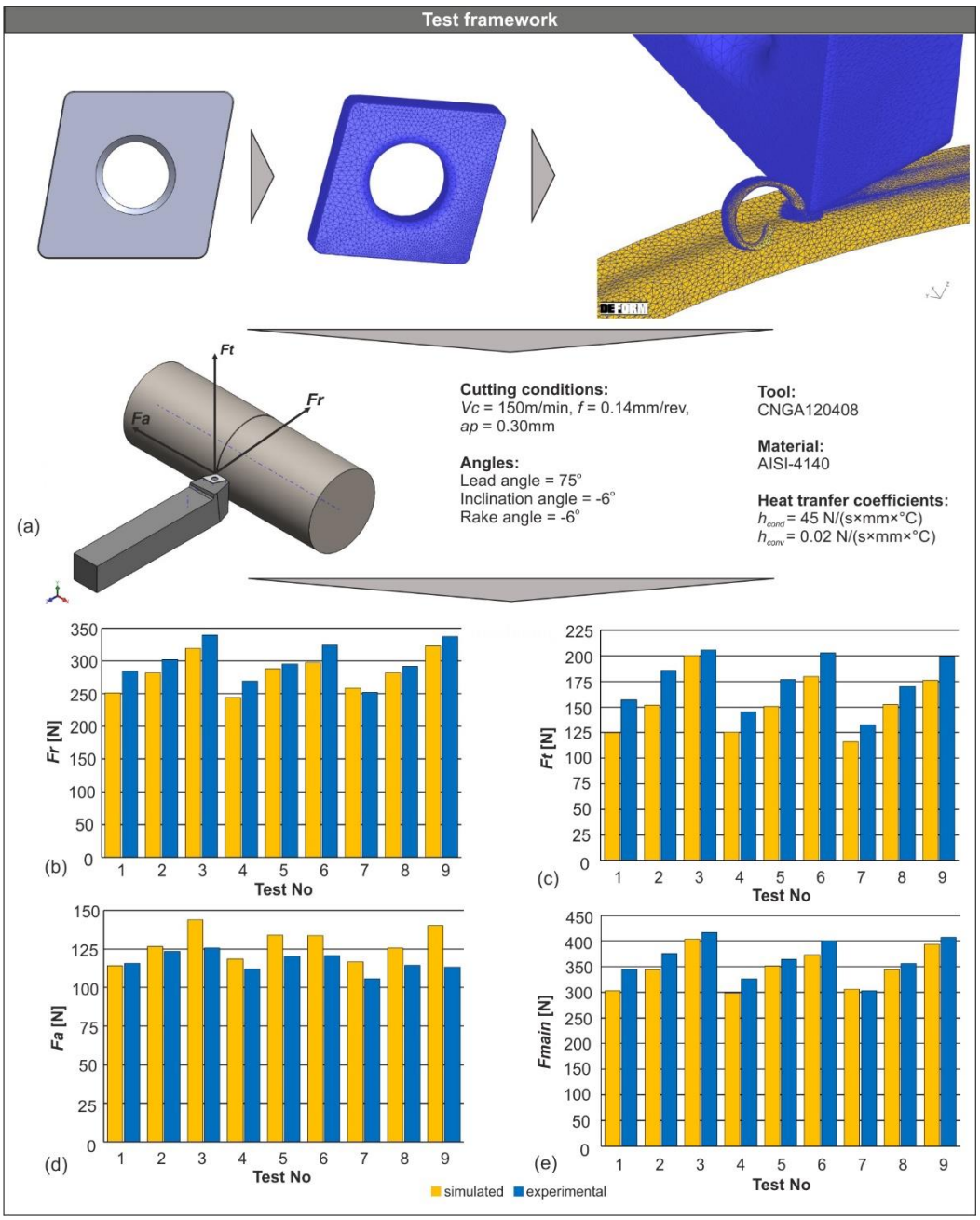

Figure 6. The test framework including: (a) the FE model setup and the results comparison for (b) the radial force, (c) the tangential force, (d) the feed force and (e) the resultant machining force.

The high level of agreement in the case of the resultant force is due to the fact that the radial force component is the main contributor to the calculated resultant machining force, which at the same time proves the validity of the FE model.

6.3.2. Presentation of the publication "FEM based mathematical modelling of thrust force during drilling of Al7075-T6"

The present research contributes towards both an experimental and a 3D numerical study on drilling of Al7075-T6, with solid carbide drills. The aim of this study is to develop a mathematical model, with the employment of Response Surface Methodology (RSM) and 3D Finite Element Method (FEM) [67-76], for predicting the generated thrust forces induced during Al7075-T6 drilling under commonly-used conditions. This way, most of the experimental work can be skipped and the preparation costs can be reduced.

During the experimental stage of this research, three solid carbide (10% cobalt) drills of the same grade (Kennametal KC7325 - B041A series) were used with 8mm (B041A08000CPG), 10mm (B041A10000CPG) and 12mm (B041A12000CPG) diameter respectively. These drills have double coating; a multilayer of TiN/TiAlN with 3.5 micron thickness and an outer layer of TiN with 15 micron thickness. Figure 7a illustrates the CAD model of the Ø10 drill compared to the physical model.

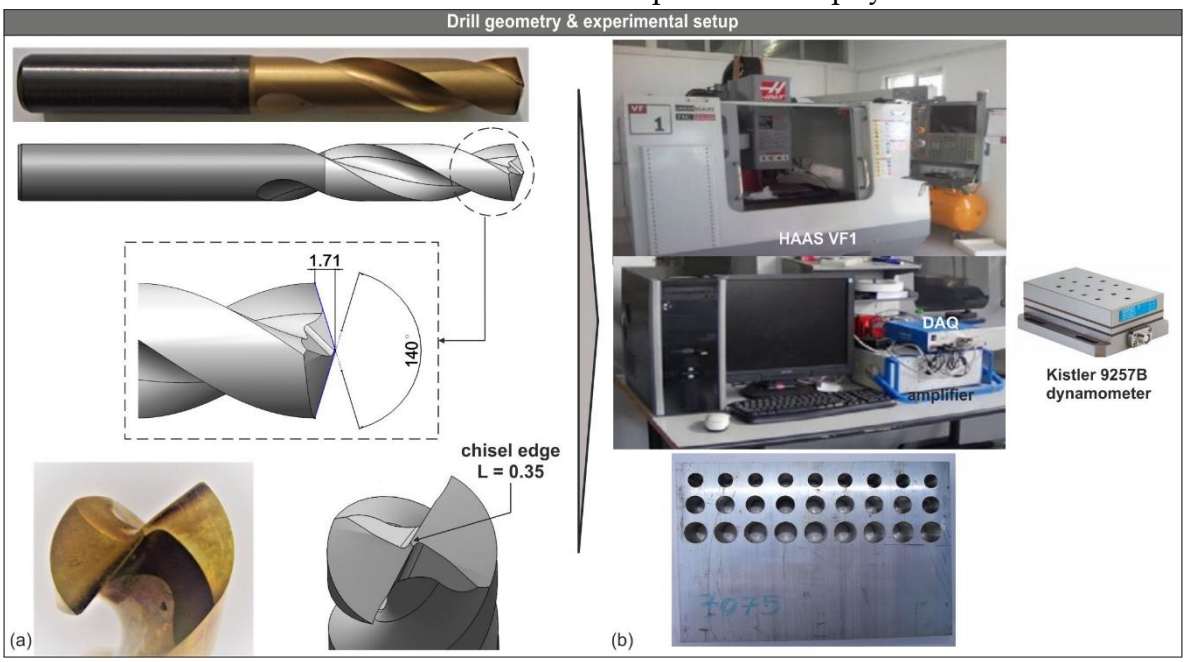

Figure 7. Geometry of the B041A10000CPG drill (a) and the experimental setup (b).

A rectangular piece of Al7075-T6 with dimensions 150mm x 130mm x 15mm served as the workpiece for the experiments that were carried out at three different levels of cutting speed V_c (50m/min, 100m/min, 150m/min) and feed f (0.15mm/rev, 0.2mm/rev, 0.25mm/rev) according to the manufacturer's recommended limits. The selected alloy is an industry-standard material that draws the attention of many researchers [77-80]. Thus, the combination of the cutting conditions combined with the three drill diameters, led to a setup of 27 experiments (each tool was used to drill nine holes). The drilling processes were performed with the aid of a HAAS VF1 CNC

machining center and a BT40 cone. Additionally, a Kistler type 9257B 3-component dynamometer was used for measuring the developed thrust forces. The processing and storing of the measured values was achieved by using a standard measuring system (Kistler type 5697A1 with 16-bit resolution), a three-channel charge amplifier (10kHz sampling rate) and DynoWare type 2825A software. Similar setup is used in most cases where multiple machining parameters are involved [81-83].

A steady flow of semi-synthetic oil-based coolant (KOOLrite 2270) was channeled to the tool during the drilling process. Table 1 contains the most important thermo-mechanical properties of the workpiece material.

Table 1. Basic mechanical and thermal properties of Al7075-T6 [84,85].

Mechanical properties					
Young's Modulus E	**Density ϱ**	**Poisson's ratio μ**	**Hardness [HV]**	**Yield Strength**	**Tensile Strength**
71.7 GPa	2810 kg/m^3	0.33	175	503 MPa	572 MPa
Thermal properties					
Heat capacity c		**Thermal expansion α**		**Thermal conductivity λ**	
0.960 J/g°C		22 μm/m°C		41.7 W/mK	

The 3D cutting simulations were performed with DEFORM™-3D ver. 11.3. Most of the simulations were stopped when the thrust force entered steady state to shorten the simulation times. The steady state occurred at a different point for each simulation, according to the specified time step, which was calculated based on the drill diameter and cutting speed used in each simulation, as shown in Equation 2.

$$V_c = \frac{\pi DN}{1000} \tag{2}$$

Where: V_c is the cutting speed in m/min, D is the tool diameter in mm and N is the spindle speed in min^{-1}.

For instance, the 10mm tool at 100m/min cutting speed rotates with 3183min^{-1} or 53.05s^{-1}, hence the tool completes one full rotation in 0.0189s. With this in mind, the time step can be determined by dividing the previously calculated time value with the number of steps of the tool per revolution (360 steps). Hence, the time step for this example is 5.24×10^{-5}s. According to DEFORM™, the number of steps during drilling simulation should be close to 360 so that the tool can rotate about one degree per step [86]. This way, the simulations complete within reasonable amount of time.

The specifications of the 3D Finite Element (FE) model that was prepared for the drilling simulations are the following:

- The workpiece was modelled to be circular and thin [87], with a thickness of about the radius of the drill. In addition, a center spot with regard to the drill point angle was designed on the workpiece (Figure 8a) for simplification purposes.
- Three similar workpieces were designed, but of different size (one for each drill). They were modelled as deformable with a varying mesh. The minimum element size of the mesh was set to 50% of the feed [86].
- A finer mesh (10:1 size ratio) was localized at the center of the workpiece in order to optimize the number of elements at the contact interface. Figure 8b depicts the tool-workpiece setup for the Ø10mm drill.
- The side of the workpiece was fixed (Figure 8c) in such a way so that the velocity of all nodes is equal to zero.
- Only the tips of the drills were used instead of the whole model for simplification purposes. In addition, they were modelled as rigid with a mesh of about 20,000 to 30,000 tetrahedral elements. A finer mesh (4:1 size ratio) was used at the tip (Figure 8d), which is in contact with the workpiece and together constitute the analysis domain.
- The drill was allowed to rotate around Z axis and move along Z axis accordingly.
- A convection coefficient (h_{conv}) for heat transfer via the oil based coolant was set, with value equal to 2 N/(s×mm×°C) [86], whereas for heat transfer through conduction in the tool-workpiece interface, the equivalent coefficient (h_{cond}) with the default value of 45 N/(s×mm×°C) was used.

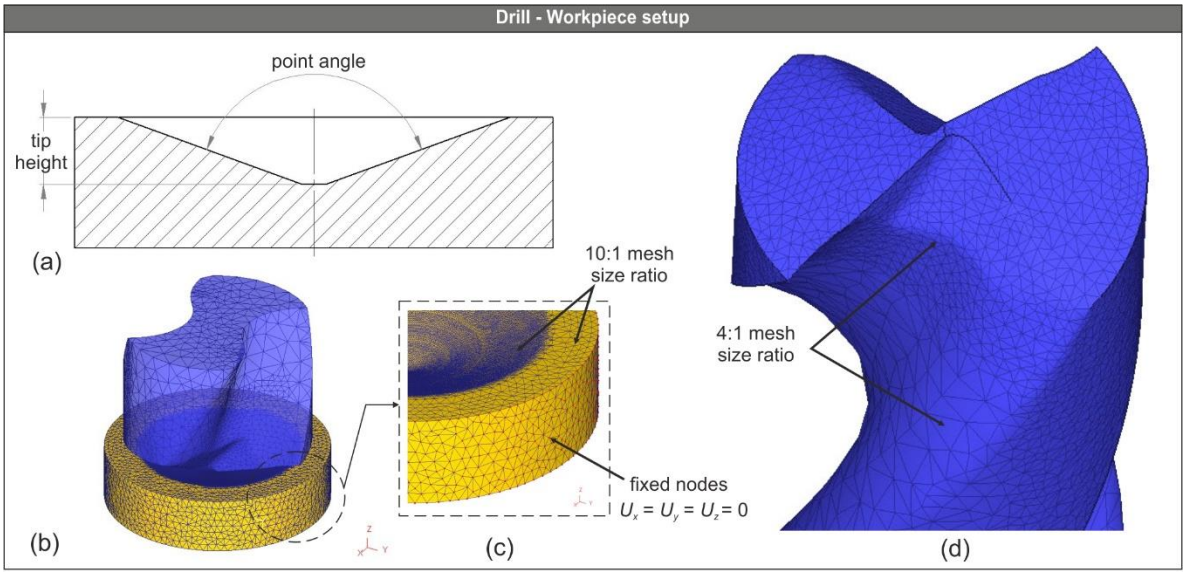

Figure 8. Workpiece section (a), tool-workpiece setup (b), workpiece nodes (c) and drill model mesh (d).

The flow stress of the workpiece material was modelled with the generalized Johnson-Cook equation. This model is widely used for stress analysis in deformations involving high strain, strain rate and temperature, and can be described by Equation 3.

$$\sigma = \left(A + B\varepsilon^{n}\right)\left(1 + C\ln\frac{\dot{\varepsilon}}{\dot{\varepsilon}_0}\right)\left[1 - \left(\frac{T - T_0}{T_m - T_0}\right)^{m}\right] \quad (3)$$

Where: A is the initial yield stress, B is the strain hardening modulus, C is the strain rate dependence coefficient, ε denotes the plastic strain, n denotes the strain hardening exponent, m denotes the thermal softening coefficient, $\dot{\varepsilon}$ represents the plastic strain rate, $\dot{\varepsilon_0}$ represents the reference plastic strain rate, T is the reference temperature, T_0 is the bulk temperature and finally T_m is the melting temperature of the workpiece material. The material constants for Al7075-T6 alloy are included in Table 2. In the present study, a reference strain rate of 1/s was used.

Table 2. Johnson-Cook constitutive model constants for Al7075-T6 [88].

A [MPa]	B [MPa]	C	n	m	T_0 [°C]	T_m [°C]
546	678	0.024	0.71	1.56	20	635

The material separation was modelled with the normalized Cockcroft and Latham model which is defined as a function of the maximum principal stress σ' normalized with the effective stress $\bar{\sigma}$ [89].

Finally, the interaction between tool-chip interface, was defined via a hybrid model [15]. To approximate the frictional stresses around the tool tip, where a more sticking behavior occurs, the shear friction model was used which can be determined by Equation 4. This relationship is based on the assumption that the frictional stress is proportional to the shear strength of the weaker of the two materials that are in contact [90].

$$\tau_f = k_\tau \frac{\sigma_y}{\sqrt{3}} \quad (4)$$

Where: τ_f is the frictional stress, k_τ is a constant and σ_y is the uniaxial yield stress for the material.

Additionally, the Coulomb's friction model was used to approximate the generated friction at the sliding zone, which is determined by Equation 5.

$$\tau_f = \mu\sigma_n \quad (5)$$

Where: τ_f is the frictional stress, μ is the friction coefficient and σ_n is the normal stress along the tool-chip interface.

The presented model uses a constant shear friction coefficient m = 0.7 and a constant Coulomb friction coefficient μ = 0.6.

The sample thrust force diagram of Figure 9a, indicates that the produced thrust force increases rapidly, as soon as chisel's edge starts to press the surface of the workpiece. Thrust force quickly reaches a steady state and just before 0.0171s stops to increase any further, maintaining a steady state until the end of the simulation. The thrust forces of the sample simulation fluctuated between 370 and 605N, resulting in a mean value of about 500N. Any excessive values of force are due to the remeshing process on the workpiece's mesh. In order to minimize this effect, the default exponential smoothing (first order) of DEFORM™-3D was applied.

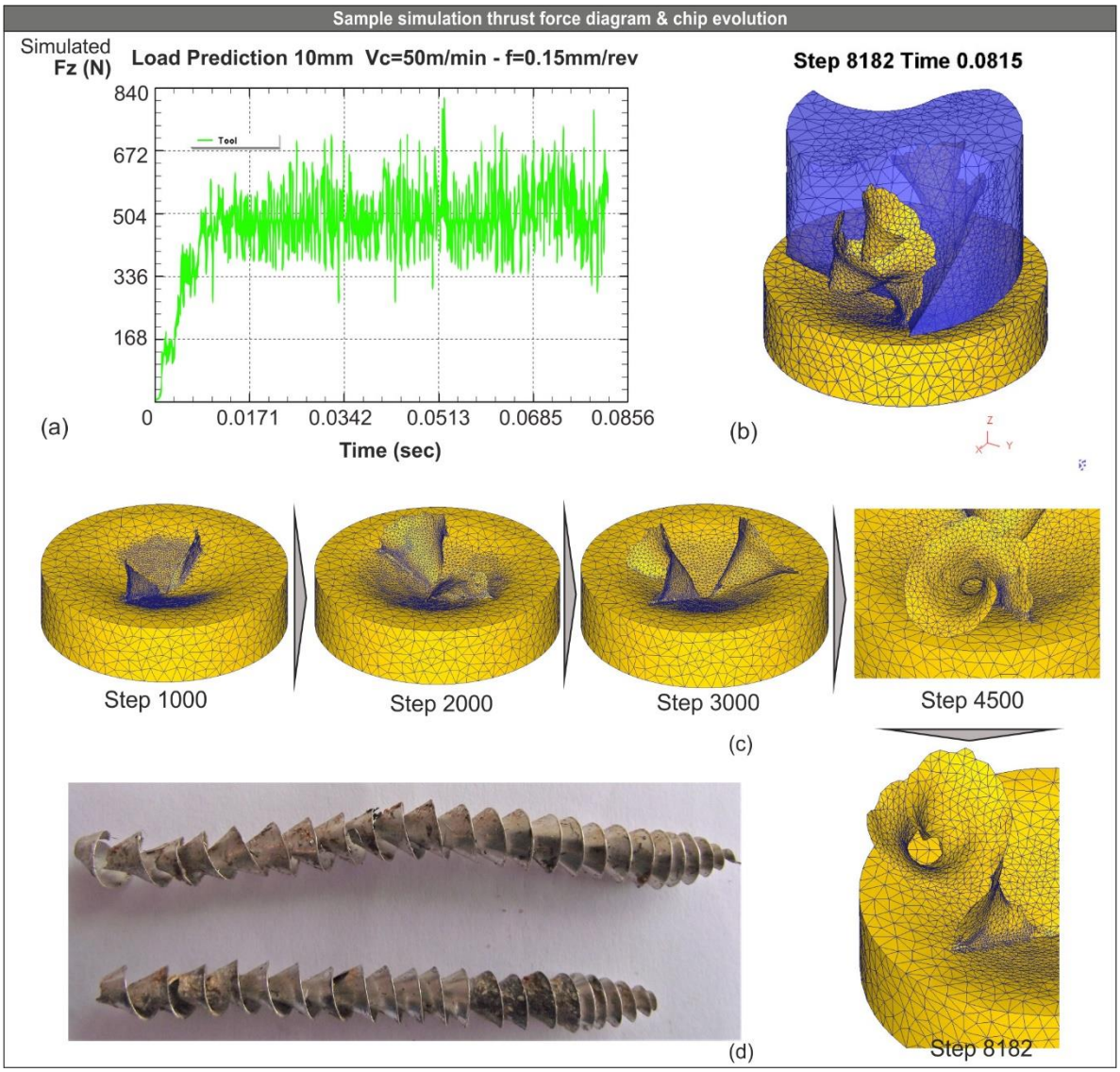

Figure 9. The thrust force diagram for the 10mm tool (a), the tool-chip interface (b), the evolution of the formed chips (c) and the physical chips for the same conditions (d).

Figure 9b illustrates the produced chip after 8182 steps or 0.0815s. It is concluded that both the experimental and the simulated process generates chips of the same conical shape regardless of the cutting conditions. However, the size of the chip (diameter of the conical shape chip) strongly depends on the tool diameter, which is reasonable considering the fact that a larger flute can remove more material from the workpiece. Lastly, Figure 9c depicts the evolution of the generated simulated chip during drilling of Al7075-T6 with a 10mm, two flute twist drill, at 50m/min cutting speed and 0.15mm/rev feed rate, whereas Figure 9d illustrates the equivalent physical chip for the same cutting conditions.

Figures 10a, 10c and 10e illustrate the variation of the experimental thrust forces with feed for each drill diameter, at the three levels of cutting speed. Similarly, Figures 10b, 10d and 10f depict the variation of the simulated values.

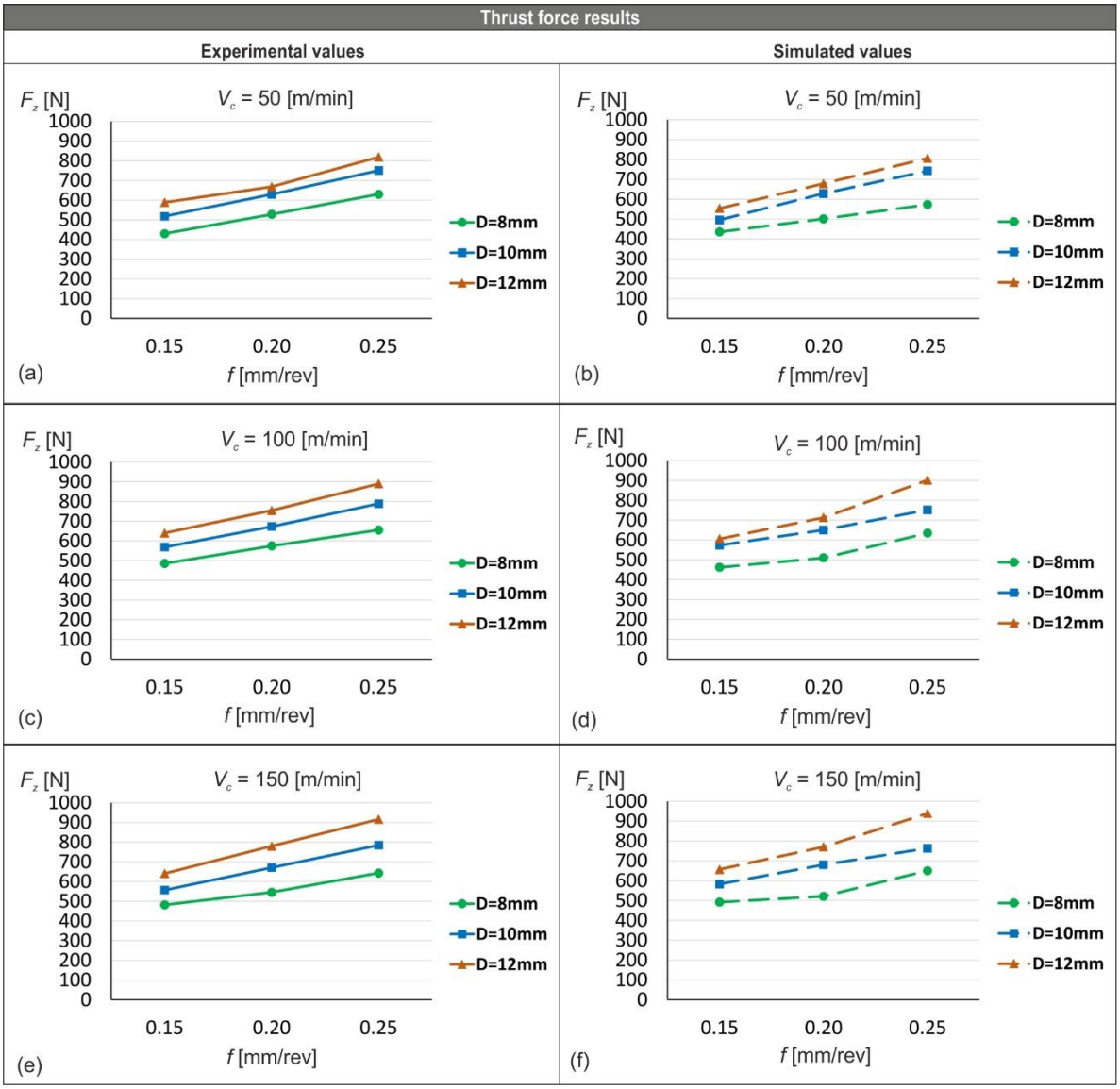

Figure 10. Variation of the experimental (a), (c), (e) and the numerical (b), (d), (f) values of thrust force with feed for varying tool diameter.

By observing these graphs it is concluded that both feed and cutting speed, especially feed, contribute to the produced thrust forces, regardless of the tool diameter. Specifically, a small but steady increase in thrust forces can be observed as cutting speed increases for each feed value and tool diameter. Similarly, a noticeable and constant increase in thrust forces is noted as feed increases for each cutting speed. Furthermore, as cutting speed increases, it is clear that the simulated thrust forces increase for each value of feed in a similar manner.

The increased correlation between the experimental and the numerical results allowed for the development of a mathematical model for thrust force. The RSM was employed to generate the prediction model. Numerous machining-related studies [14,81,91-93] that are available in the literature, prove that RSM is a well-established tool providing excellent results and neat presentation. Since all 27 drilling experiments and simulations were performed, the statistical model was developed with a full factorial design in mind, based on the numerical results. Table 3 presents the design of experiments and the produced output.

Table 3. Design of experiments for drilling simulations

Std Order	D [mm]	V_c [m/min]	f [mm/rev]	$F_{z\,sim}$ [N]
1	8	50	0.15	435.6
2	8	50	0.20	501.4
3	8	50	0.25	573.5
4	8	100	0.15	462.5
5	8	100	0.20	510.3
6	8	100	0.25	634.9
7	8	150	0.15	491.5
8	8	150	0.20	520.8
9	8	150	0.25	649.8
10	10	50	0.15	495.9
11	10	50	0.20	628.8
12	10	50	0.25	742.9
13	10	100	0.15	573.5
14	10	100	0.20	650.4
15	10	100	0.25	751.6
16	10	150	0.15	582.4
17	10	150	0.20	679.9
18	10	150	0.25	763.0
19	12	50	0.15	553.8
20	12	50	0.20	612.9
21	12	50	0.25	806.7
22	12	100	0.15	605.8
23	12	100	0.20	713.2
24	12	100	0.25	901.3
25	12	150	0.15	656.5
26	12	150	0.20	770.0
27	12	150	0.25	938.7

Based on the number of factors (drill diameter, cutting speed and feed) that are involved in the numerical study, the fitted regression model that occurred is a second order polynomial with linear, quadratic and interactive terms. Equation 6 represents the second order polynomial for this study.

$$Y = a_0 + \sum_{i=1}^{n} b_i X_i + \sum_{i,j}^{n} b_{ij} X_i X_j + \sum_{i=1}^{n} b_{ii} X_i^2 \quad (6)$$

Where: Y is the response of the model (F_z), a_0 denotes the fixed term, X_i are the input variables (V_c, f and D), and b_i, b_{ij}, b_{ii} refer to the vectors that contain the regression coefficients (linear, quadratic, and cross-product, respectively).

Using the previously-mentioned polynomial and the data that are presented in Figure 10 and Table 3, the complete mathematical model based on the verified simulated results, is represented by Equation 7.

$$F_z = 238 + 79.5D - 0.21V_c - 4797f - 5.52D^2 - 0.00451V_c^2 + 9883f^2 + 0.2DV_c + 301.6Df - 0.56V_c f \quad (7)$$

Where: F_z is the thrust force in N, D is the drill diameter in mm, V_c is the cutting speed in m/min and f is the feed in mm/rev.

In order to validate the developed model, Analysis of Variance (ANOVA) has been performed by using a confidence level of 95% for all intervals. The adjusted R-squared for this model found to be as high as 97.25% proving the validity of the fit. Moreover, the validity of the model is further enhanced by the contribution of the next factors to the model: f with a p-value of 0.007, D^2 with $p = 0.022$, f^2 with $p = 0.012$, $D \times V_c$ with $p = 0.005$ and $D \times f$ with $p = 0.000$. Table 4 contains the sum of squares and degrees of freedom of the analysis, in addition to the p-values of the factors. Last but not least, the fact that the p-value of the analysis was found to be 0.000, the correlation is considered to be very high, eliminating the probability of getting an extreme result.

Table 4. ANOVA results for thrust force model.

Source	Degree of Freedom	Sum of Squares	Mean Square	f-value	p-value
Regression	9	427676	47519.5	103.01	0.000
Residual Error	17	7842	461.3		
Total	26	435518			
R-sq (adj) = 97.25%					
Term	**PE Coefficient**	**SE Coefficient**	**t-value**		**p-value**
Constant	238	295	0.81		0.432
D	79.5	46.1	1.73		0.102
V_c	− 0.21	1.06	− 0.19		0.848
f	− 4797	1557	− 3.08		0.007
D^2	− 5.52	2.19	− 2.52		0.022
V_c^2	− 0.00451	0.00351	− 1.29		0.215
f^2	9883	3507	2.82		0.012
$D \times V_c$	0.20	0.062	3.23		0.005
$D \times f$	301.6	62.0	4.86		0.000
$V_c \times f$	− 0.56	2.48	− 0.22		0.825

The graphs presented in Figure 11 were plotted in order to check the accuracy of the model. By observing Figure 11a it is concluded that the errors follow a normal distribution pattern. Similarly, the residuals versus the fitted values graph (Figure 11b) shows that the residuals are evenly scattered on both sides of the reference line of the graph, indicating that the variance is constant. In addition, the histogram (Figure 11c) depicts a normality in distribution between the error percentages. The residuals versus order graph (Figure 11d) indicates that there are no obvious systematic effects in the data due to time. Moreover, Figure 11e highlights the significance of the tool diameter D, cutting speed V_c and feed rate f.

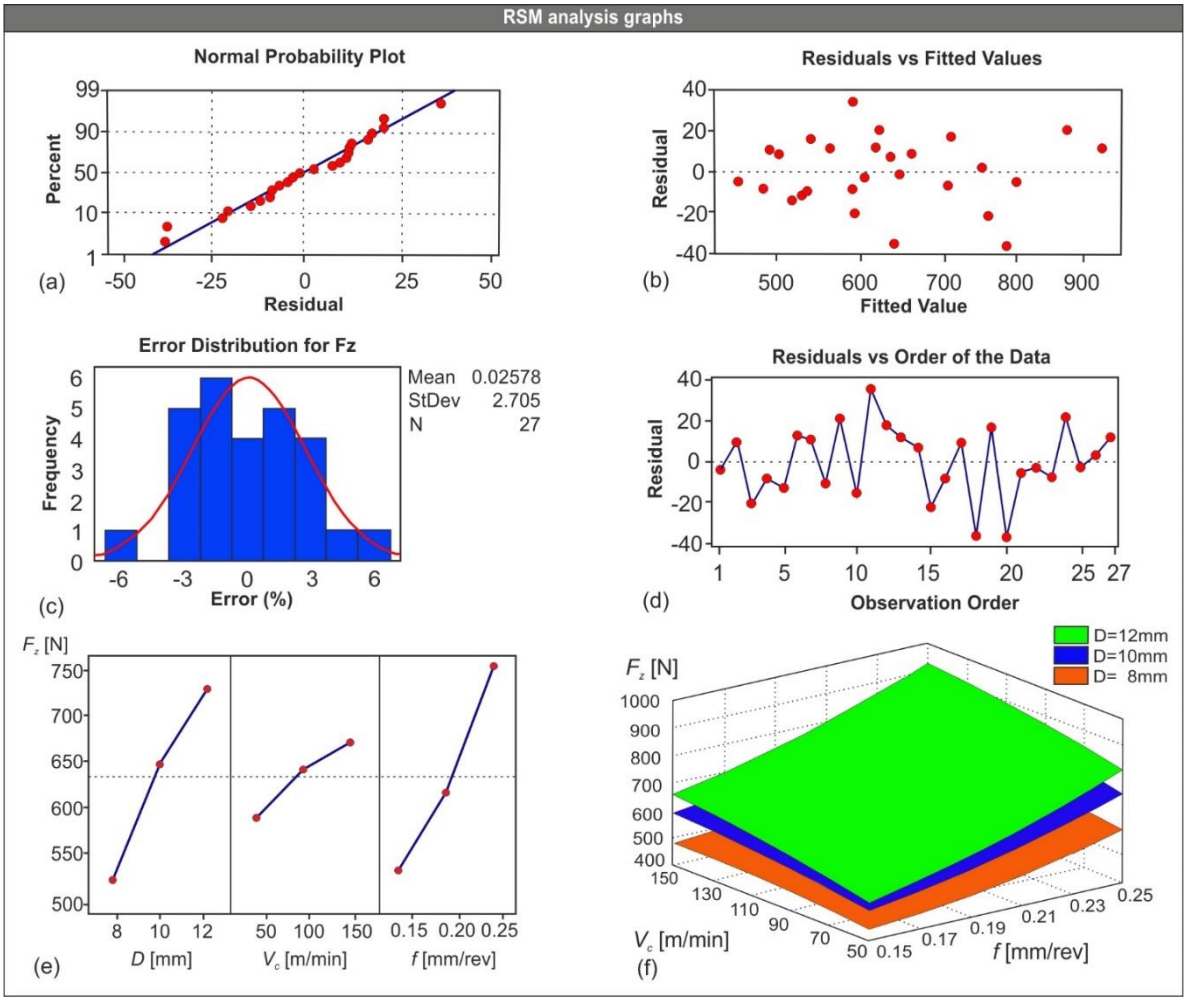

Figure 11. Probability plot (a), residuals versus fitted values (b), error histogram (c), residuals versus order (d), main effects plot (e) and 3D plots of the thrust force for each drill (f).

Finally, the 3D response surface plots (Figure 11f), graphically explain the combined effect of the tool diameter and cutting conditions on thrust force. The illustrated 3D surfaces are generated for each drill diameter based on the polynomial solutions (see Table 3 for inputs). According to Figures 11e and 11f it is observed that:

- The larger the diameters used, the higher the values of the produced thrust forces are.

- Similarly, feed affects the produced thrust force significantly; as feed increases so does the thrust force.
- In contrast, any increase in cutting speed has limited effect on thrust force; the increase is marginal.

6.3.3. Presentation of the publication "3D FE modelling of machining forces during AISI 4140 hard turning"

Hardened steel is one of the most sought-after materials in manufacturing industry. Therefore, investigations into hard turning and similar machining processes [63,65,94-96] is a topic that draws the attention of many researchers. Even though numerous experimental studies exist in the literature related to hard turning of steel, the implementation of Finite Element Method (FEM) during such investigations is still limited [97-104]. In the present study, hard turning of AISI-4140 was investigated with respect to three levels of cutting speed, feed and depth of cut. The finding of this research were used to establish a 3D Finite Element (FE) model, as well as a prediction model for the machining forces based on statistical methods.

The numerical values were compared to experimental results that are available in the literature. The setup of the turning experiments comprise of a universal lathe type SN 40C and the tool-holder with designation number PCBNR2525M12. The chemical composition of the workpiece material (AISI-4140) in wt%, is as follows: C 0.43, Mn 0.79, Si 0.24, S 0.024, Cu 0.025, Al 0.029, Ti 0.004, Nb 0.001, Ni 0.022, Cr 1.10, Mo 0.19, Va 0.005, Sn 0.002, and Fe in balance. In addition, the chemical composition of the used ceramic tool (CNGA120408) is 70% Al_2O_3 and 30% TiC.

An equivalent CAD-based setup was prepared with the aid of SolidWorks™ 2018. The most important settings of the model are the following:

- The workpiece was modelled as cylindrical bar with a diameter of 72mm.
- The selected material for the workpiece is AISI-4140 steel, whereas for the insert is an uncoated ceramic.
- The angles that are inherited from the tool-holder and the tool geometry are: lead angle $k_r = 75°$, rake angle $\gamma = -6°$ and inclination angle $\lambda = -6°$.

The cutting conditions applied in the present study were chosen with respect to the manufacturer's suggestions and include three levels of cutting speed (80m/min, 115m/min, 150m/min), feed (0.08mm/rev, 0.11mm/rev, 0.14mm/rev) and depth of cut (0.10mm, 0.20mm, 0.30mm). This means that the total number of simulation runs that were carried out is twenty seven. The applied cutting conditions and their levels are included in Table 5.

Table 5. Process conditions of the turning FE model.

Level	V_c [m/min]	f [mm/rev]	ap [mm]
I	80	0.08	0.10
II	115	0.11	0.20
III	150	0.14	0.30

Figure 12a depicts a schematic of the tool-workpiece setup; F_t stands for the tangential force, F_r is the radial force and finally F_a is the developed feed force. According to this setup, the FE model is derived as shown in Figure 12b. The insert belongs to the CNGA-ceramic family that comprises of 80° rhombic inserts used for machining hardened steel. The critical dimensions of the tool are depicted in Figure 12c.

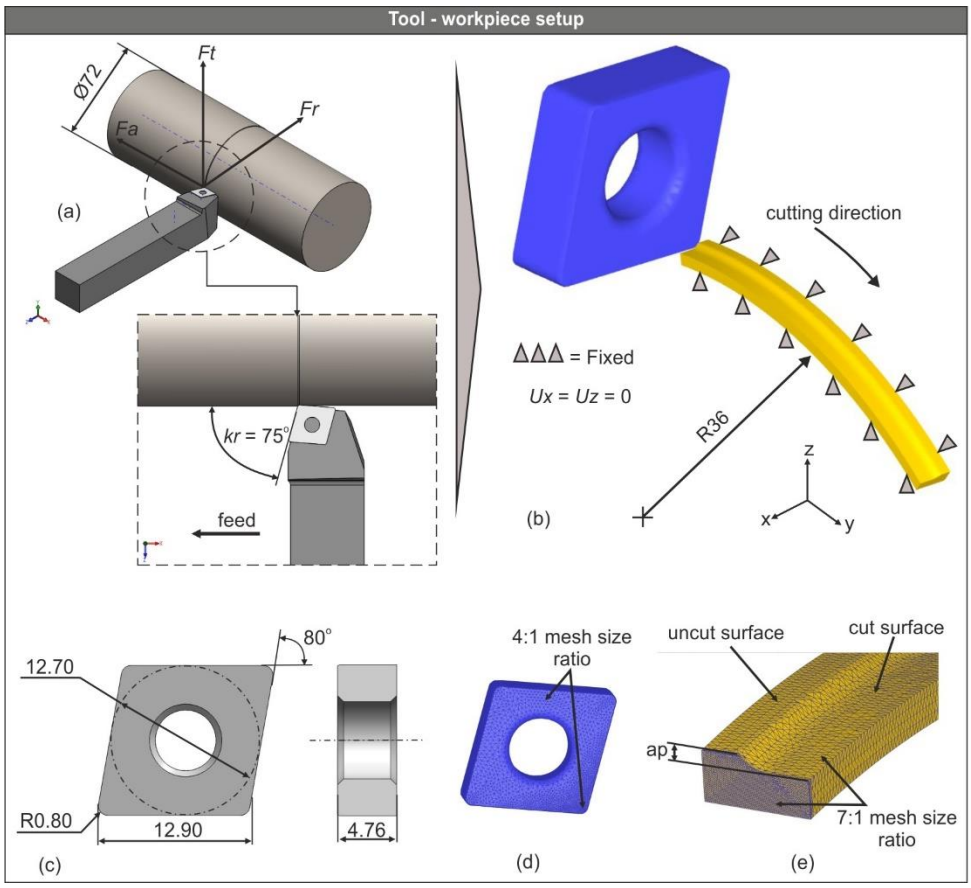

Figure 12. The CAD-based setup (a), the FE model setup (b), the tool's dimensions (c), the meshed insert (d) and the analysis domain (e).

The 3D FE model for the turning process simulation was set according to the following instructions:

- For simplification purposes, the workpiece was designed as a circular arc with a diameter of 72mm and an angle of 45° (Figure 12b) instead of a full cylinder. In addition, the workpiece was generated with an already cut surface with respect to the depth of cut, the corner radius of the tool and the diameter of the steel bar. (Figure 12e).

- The cutting tool was designed according to the ISO-13399 norm. Moreover it was modelled as rigid and meshed with approximately 50,000 tetrahedral elements.
- A local refinement with a size ratio of 4:1 was applied close to the cutting tip of the tool, as shown in Figure 12d, because this area is in contact with the uncut surface of the workpiece.
- The workpiece was modelled to be deformable with a mesh size that varied between roughly 90,000 and 140,000 elements depending on the value of feed; the size of the minimum element was fixed to 25% of the feed value [86].
- A more dense mesh (size ratio of 7:1) was applied to the section of the workpiece where contact with the tool is in effect.
- The workpiece was fixed in such a way so that the velocity of the nodes in both X and Z axis was equal to zero (Figure 12b). Contrarily, the tool was allowed to follow the path as dictated by the cutting direction (Figure 12b).
- The convection coefficient (h_{conv}) for heat transfer in dry cutting conditions was set to 0.02 N/(s×mm×°C), whereas the conduction coefficient (h_{cond}) for heat transfer between the tool-workpiece interface, was set to 45 N/(s×mm×°C).

The well-established Johnson-Cook plasticity model was used to approximate the machining process where large deformations and high temperatures occur. The relationship between the constitutive parameters is described by Equation 3.

The most important thermo-mechanical properties of AISI-4140 steel and ceramic tool material are shown in Table 6. The elastic modulus, the thermal expansion, the thermal conductivity and the heat capacity of the workpiece material are all temperature dependent, hence their values were expressed as a function of temperature *f*(Temp). Additionally, the Johnson-Cook model constants are presented in Table 7. For the simulation tests that are presented in this research, a reference strain rate of 1/s was employed.

Table 6. Thermo-mechanical properties for tool [21] – workpiece [86].

Mechanical properties				
Material	**Young's Modulus E [GPa]**	**Density ϱ [kg/m³]**	**Poisson's ratio μ**	**Hardness [HRC]**
AISI4140	212 @ 20°C 192 @300°C 164 @600°C	7850	0.30	60
Ceramic	415	3500	0.22	–
Thermal properties				
Material	**Heat capacity c [J/kgK]**	**Thermal expansion α [μm/mK]**		**Thermal conductivity λ [W/mK]**
AISI4140	362 @ 20°C 446 @300°C 610 @600°C	11.9 @ 20°C 13.6 @300°C 14.9 @600°C		41.7 @ 20°C 41.4 @300°C 34.1 @600°C
Ceramic	334	8.4		7.5

Table 7. Johnson-Cook constitutive model constants for AISI-4140 [86].

A [MPa]	B [MPa]	C	n	m	T_0 [°C]	T_m [°C]
106	1167	0.0352	0.1424	0.763	20	1547

The normalized Cockcroft-Latham damage model was employed to approximate the phenomenon of material separation that takes place during machining. The model can be expressed with Equation 8 [105]. In this expression, the maximum principal stress is normalized by the effective stress.

$$D_c = \int_0^{\varepsilon_f} \frac{\sigma_{\max}}{\bar{\sigma}} d\varepsilon_{pl} \tag{8}$$

Where: D_c denotes the material constant in the fracture criterion, σ_{max} is the maximum tensile principal stress, $\bar{\sigma}$ is the effective stress, ε_f is the limit fracture strain and ε_{pl} is the plastic strain.

Finally, the friction situation at the tool-workpiece interface was modelled with the aid of Coulomb's law. Even though more advanced models are available in the literature, the Coulomb's friction model provides a good approximation of the friction forces that develop in the sliding zone, which is the zone of interest during machining processes. Equation 5 can be used to estimate the shear frictional stresses. The shear friction coefficient used in the present investigation was taken equal to 0.577 [106].

Figure 13 contains four graphs that were plotted for comparing the numerical results of both the machining force components and the resultant force to the equivalent experimental ones. Specifically, Figure 13a illustrates the mean values of the radial force for both simulation runs and experiments. Similarly, the tangential force is presented in Figure 13b, the feed force in Figure 13c and finally the resultant of the three components in Figure 13d. The overall agreement between the simulated and the experimental values is good with relative error between −5.3% and 12.7% for the F_r, −9.4% and 11.6% for the F_t, −14.8% and 13% for the F_a. Furthermore, the simulated resultant cutting force is in accordance with the calculated experimental one with relative error of about −9.1% to 9.4%.

By observing Figure 13 it can be concluded that the dominant of the three components is the radial force which eventually effects the most the resultant cutting force, in contrast to the effect of the feed force, which is marginal.

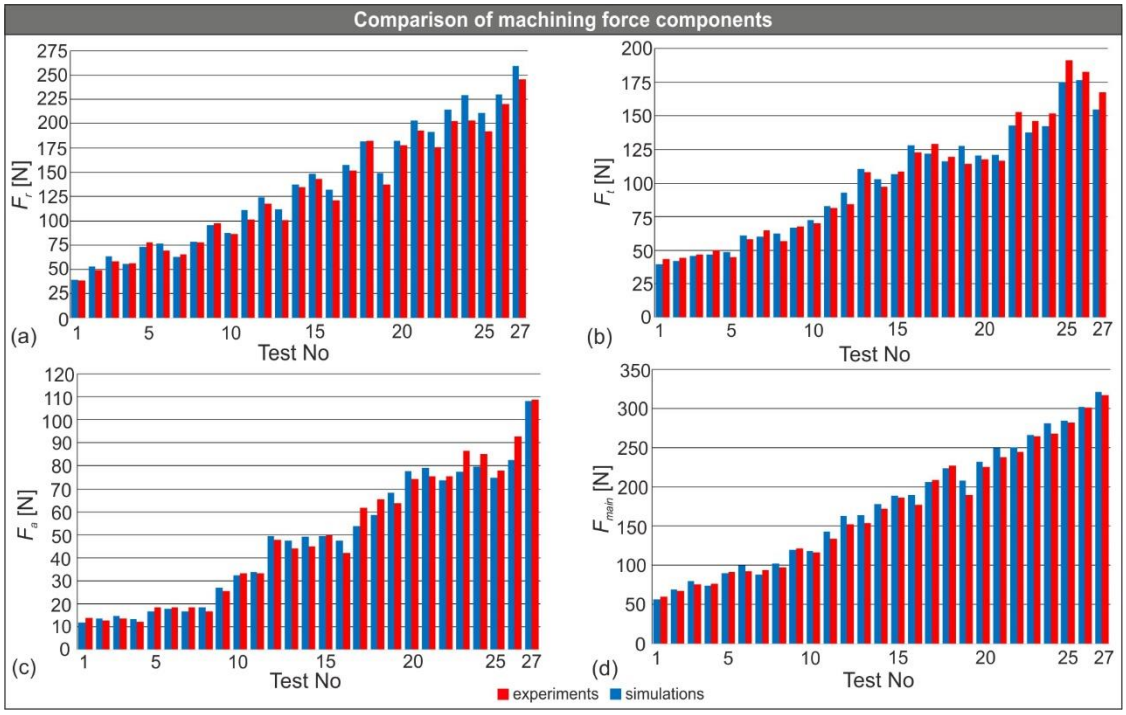

Figure 13. Comparison between simulated and experimental turning forces; (a) radial, (b) tangential, (c) feed and (d) resultant.

The high level of agreement allowed for the development of a statistical model so that future experiments for different depths of cut and similar machining conditions can be minimized. The Response Surface Methodology (RSM) was employed to develop the proposed model for prediction purposes [107-109] of the resultant cutting force during AISI-4140 hard turning. RSM is a proven tool that is often used to optimize process conditions or determine the interaction between multiple factors. This methodology was successfully utilized by many researchers in their studies [26,110-113], hence it was selected for the present study. A full factorial design with three factors was realized according to the involved machining parameters and the number of the simulation tests. The regression model defining the relationship between the factors and the output can be described with a second order polynomial (Equation 6) that includes linear, quadratic and interactive terms.

Equation 9 presents the complete statistical model for the resultant turning force based on Equation 6 and the data derived from the verified FE model.

$$F_{main} = -112.2 + 0.566V + 820f + 422.1ap - 0.00074V^2 - 1860f^2 + 125ap^2 - 0.67Vf + 0.708Vap + 3124fap \quad (9)$$

Where: F_{main} is the resultant machining force in N, V is the cutting speed in m/min, f denotes the feed in mm/rev and ap represents the depth of cut in mm.

Table 8 contains the estimation of the resultant turning force for all 27 combinations of machining conditions according to the experimental findings [64], the simulations and the prediction model. The comparison of these results revealed an increased correlation.

Table 8. Main machining force comparison between experimental, simulated and statistical values.

Cutting parameters				F_{main} [N]		
Std Order	**V_c [m/min]**	**f [mm/rev]**	**ap [mm]**	**Experimental**	**Numerical**	**Predicted**
1	80	0.08	0.10	59.9	56.9	51.9
2	115	0.08	0.10	67.5	69.0	73.6
3	150	0.08	0.10	76.0	79.5	92.0
4	80	0.11	0.10	76.3	73.9	67.2
5	115	0.11	0.10	91.5	89.7	88.3
6	150	0.11	0.10	92.4	99.6	106.0
7	80	0.14	0.10	94.2	88.4	80.8
8	115	0.14	0.10	97.5	102.2	101.1
9	150	0.14	0.10	121.3	119.5	118.1
10	80	0.08	0.20	116.1	118.2	128.5
11	115	0.08	0.20	134.3	142.8	159.6
12	150	0.08	0.20	152.2	163.1	187.4
13	80	0.11	0.20	154.2	164.1	146.3
14	115	0.11	0.20	172.2	178.4	176.8
15	150	0.11	0.20	186.5	189.2	203.8
16	80	0.14	0.20	177.3	189.7	162.4
17	115	0.14	0.20	208.6	206.1	192.1
18	150	0.14	0.20	227.3	223.4	218.5
19	80	0.08	0.30	189.8	207.7	207.6
20	115	0.08	0.30	225.7	232.1	248.1
21	150	0.08	0.30	238.0	249.6	285.3
22	80	0.11	0.30	244.6	250.2	227.9
23	115	0.11	0.30	264.1	266.2	267.7
24	150	0.11	0.30	267.7	281.2	304.2
25	80	0.14	0.30	282.3	284.5	246.4
26	115	0.14	0.30	300.9	301.5	285.5
27	150	0.14	0.30	316.9	320.7	321.3

By reviewing the results of Table 8 and the graphs included in Figure 13, the following points are highlighted:

- The radial force is the dominant of the three components.
- Higher values of feed rate have strong impact on all forces and especially on the tangential force. As feed increases so does the machining force.
- The depth of cut greatly affects all machining forces. This is due to the fact that the tool-workpiece contact length increases as the tool cuts deeper in the

material. For instance, F_{main} increases by approximately 43.6% (from 223.4N to 320.7N) for the same conditions (V_c = 150m/min, f = 0.14mm/rev) and an increase in ap from 0.20mm to 0.30mm.

- Finally, any increase in the cutting speed seems to lower the values of the turning force components. For example, at ap = 0.30mm, f = 0.14mm/rev and V_c = 150m/min, 115m/min and 80m/min the resultant force is estimated approximately 320.7N, 301.5N and 284.5N respectively.

An Analysis of Variance (ANOVA) was performed to analyze the validity of the model's fit due to the number of independent variables taken into account. A standard confidence level of 95% was used for all intervals, revealing a successful fit with an adjusted R-squared of 99.72%. Furthermore, the terms that contribute the most to the model based on the used significance level are: the ap and the $f \times ap$ with a p-value equal to 0.000, as well as the constant with p = 0.005. Last but not least, $V \times ap$ and f have impact on the model with p-values a bit higher that 0.050; 0.060 and 0.089 respectively. The sum of squares and the degrees of freedom for the ANOVA are included in Table 9. Lastly, the probability that the model will yield unusual results is eliminated due to the fact that the p-value was estimated 0.000.

Table 9. ANOVA results for the main turning force.

Source	Degree of Freedom	Sum of Squares	Mean Square	f-value	p-value
Regression	9	165668	18407.6	1012.4	0.000
Residual Error	17	309	18.2		
Total	26	165977			
R-sq (adj) = 99.72%					
Term	**PE Coefficient**	**SE Coefficient**	**t-value**		**p-value**
Constant	−112.8	35.1	−3.19		0.005
V	0.566	0.359	1.58		0.134
f	820	455	1.80		0.089
ap	422.1	92.9	4.55		0.000
V^2	−0.00074	0.00142	−0.52		0.609
f^2	−1860	1934	−0.96		0.350
ap^2	125	174	0.72		0.482
$V \times f$	−0.67	1.17	−0.57		0.574
$V \times ap$	0.708	0.352	2.01		0.060
$f \times ap$	3124	410	7.61		0.000

Following the validation of goodness of fit, a residual analysis was carried out to check the accuracy of the model. Figure 14 includes four graphs that prove the high level of accuracy that the model demonstrated. Particularly, the normal probability plot (Figure 14a) reveals zero serious departures from the straight line. Moreover, the

residuals versus the fitted values (Figure 14b) indicates a constant variance of the residuals; the residuals are almost evenly scattered on both sides of the reference line. The normality in distribution of the error percentages can be displayed in the error histogram (Figure 14c). Finally, the residuals versus the order graph (Figure 14d) indicates that no systematic faults are present. In addition, it is pointed out that the residuals are independent from one another.

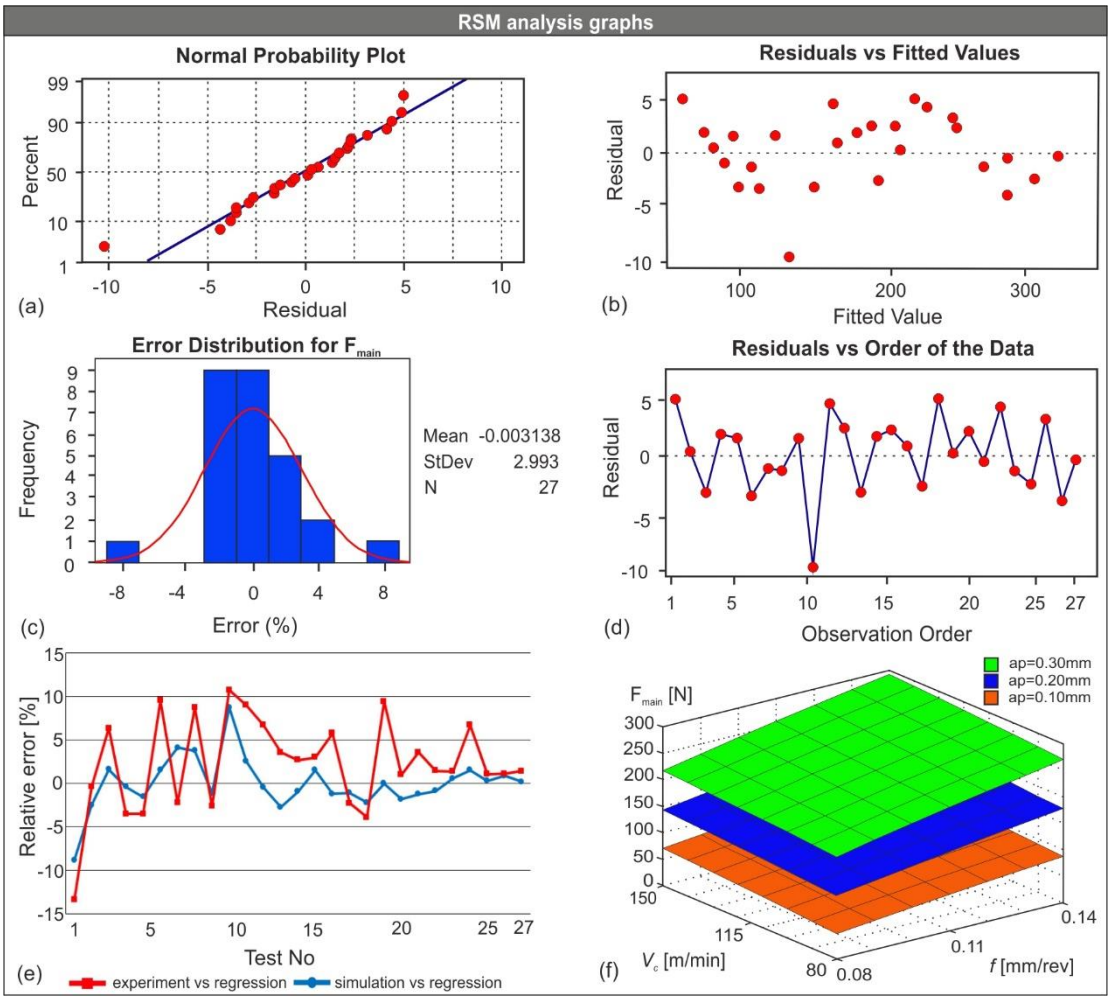

Figure 14. Probability plot (a), residuals versus fitted values (b), error histogram (c), residuals versus order (d), relative error chart (e) and 3D plots of the turning force for each *ap* (f).

Figure 14e illustrates the relative error percentage between the values of resultant turning force derived from the prediction model and the experiments, as well as between the prediction model and the simulations. The plot indicates that both lines follow a similar pattern, with the exception of tests number 6 and 19.

Moreover, the maximum error was calculated −13.4% and −8.8% for the prediction model versus experiments and the prediction model versus simulations respectively (test number 1 for both cases). On the other hand, the lowest value of error (−0.4%) was found in test 2 for the prediction model versus experiments and close to zero in test 19 for the prediction model versus simulations. Last but not least, the Mean

Absolute Percent Error (MAPE) was estimated 2% for the prediction model versus simulations and 4.6% for the prediction model versus experiments.

Lastly, Figure 14f illustrates the plotted 3D surfaces for each depth of cut based on the polynomial solutions. The depth of cut, the cutting speed and the feed are the input parameters with values within the investigated range, hence 0.10mm, 0.20mm and 0.30mm for depth of cut, 80 to 150 m/min for cutting speed (step of 10m/min) and 0.08 to 0.14 mm/rev for feed (step of 0.01mm/rev).

6.3.4. Presentation of the publication "Influence of the Nose Radius on the Machining Forces Induced during AISI-4140 Hard Turning: A CAD-Based and 3D FEM Approach"

Turning of hardened steel is an indispensable process in modern manufacturing industries. Moreover, AISI-4140 is preferred for the production of many standardized mechanical components such as gears, shafts, and bearings [114]. Therefore, a number of studies exist in the literature that investigate the machining of hardened steel [63,107,115-117]. The methods that are usually employed in this kind of research involve experimental work, statistical, and numerical analyses. However, the use of the Finite Element Method (FEM) in numerical studies is limited mostly to 2D modelling.

Present investigation deals with the effects of the cutting tool's micro-geometry (nose radius, chamfer width and angle) on the generated machining force components [118-122] during AISI-4140 hard turning. Particularly, the performance of three ceramic inserts that belong to the CNGA family was examined according to three levels of cutting parameters (cutting speed, feed rate, and nose radius) at a specific depth of cut. A number of numerical simulations were performed with the aid of DEFORM™-3D software, so that a Finite Element (FE) model could be established. Moreover, the acquired numerical results were compared to experimental ones that are available in the literature. Finally, the validation of the FE model led to the development of a statistical model based on the Response Surface Methodology (RSM).

Since the fidelity of the tool model is one of the most critical aspects when preparing a FE model, the designer application that is presented in section 8.3.1 was employed to generate the necessary tool models. Similar application exists for the design of drill models [123]. Even though most tool manufacturers provide CAD models of their products, these models are often too simplified and miss critical geometric characteristics (i.e. type of cutting edge) that affect strongly the yielded simulated results. For this, the models generated by the aforementioned application were preferred over the ones that are available in the internet. In addition, the application accelerated the design process and can be implemented in future projects.

The models generated by the application are consistent, fully defined solids, with the full geometry of the equivalent physical model that can be used in Finite Element Analysis (FEA).

A CAD-based, simplified analysis domain of the turning process was prepared with the aid of SolidWorks™ 2018 with respect to all conditions and geometric characteristics that may affect the process. The specifications of the setup are the following:

- The ISO designation number of the used tool-holder is PCBNR2525M12 and the equivalent codes for the three inserts are CNGA120404, CNGA120408, and CNGA120412, respectively.
- The workpiece model was designed as a round bar with diameter equal to 72 mm.
- The applied material for the workpiece is AISI-4140 steel, whereas for the insert is ceramic.
- The cutting angles that are inherited from the tool-holder and the turning insert geometry are: lead angle k_r = 75°, rake angle γ = −6° and inclination angle λ = −6°.

Figure 15a illustrates the CAD-based turning process setup along with the feed direction and the generated machining forces; F_t is the tangential force, F_r is the radial force, and F_a denotes the feed force. As Figure 15b indicates, only the insert model was used instead of the whole tool assembly for simplification purposes. Additionally, the round bar model was converted to a circular arc with respect to the cutting path, the depth of cut, the tool's geometry and the workpiece's diameter (Figure 15b). Figure 15c illustrates the physical model of the CNGA120408T01020 (*re* = 0.80) uncoated ceramic insert, in addition to the critical geometric characteristics of the CNGA1204xx tool group. The CNGA-ceramic family are negative, 80° rhombic inserts used for machining hardened steel and in some cases cast iron also.

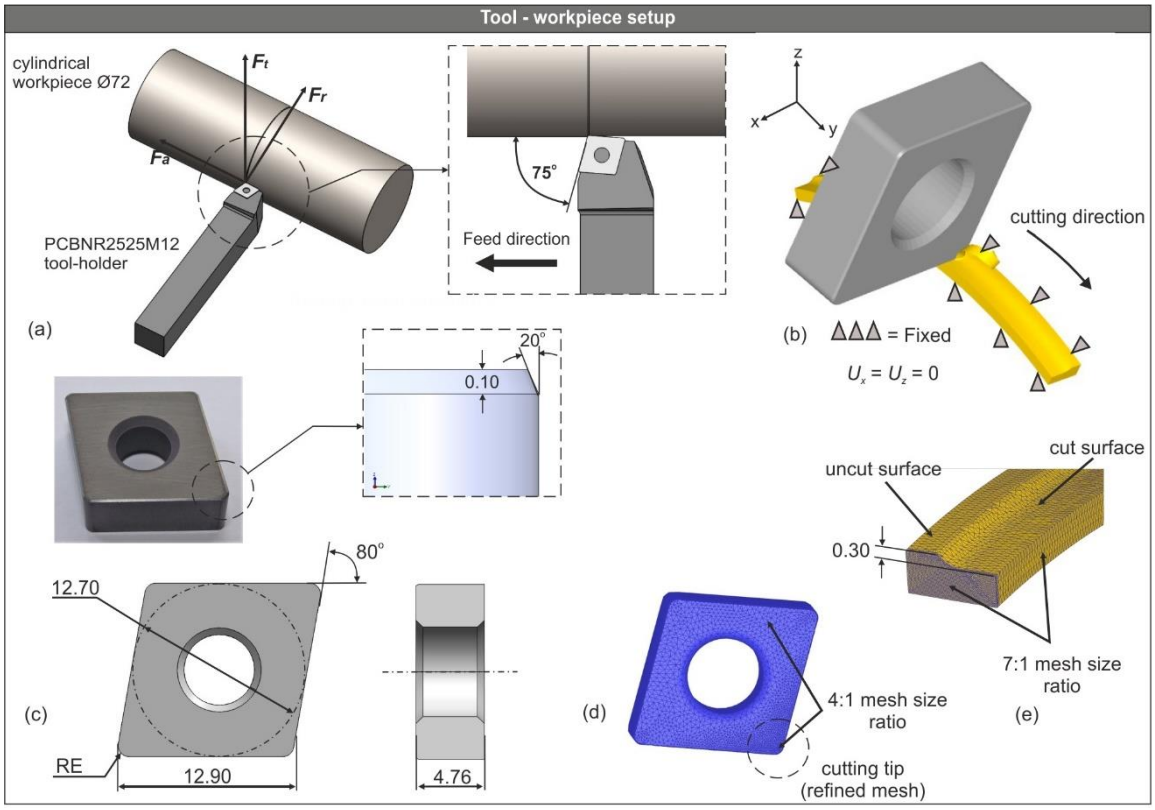

Figure 15. The CAD-based setup (a), the FE model setup (b), the tool's geometry (c), the meshed insert (d) and the analysis domain (e).

The establishment of the three-dimensional FE model was achieved with DEFORM™-3D. The pre-processing settings of the model including the material definition, the meshing and the boundary conditions are as follows:

- The tool models were designed according to the ISO-13399 norms, whereas the workpiece was designed with respect to the depth of cut, the nose radius and the diameter of the steel bar.
- The insert was modeled as rigid and meshed with the maximum allowed number of tetrahedral elements, which was approximately 50,000 for this case.
- The tool's mesh was locally refined with a size ratio of 4:1 (Figure 15d) near the tip that is always in contact with the uncut surface of the workpiece.
- The workpiece was modeled as deformable (plastic) with a mesh that varied between 100,000 and 150,000 elements. The variation occurred due to the size of the minimum element, which was fixed to 25% of the feed value [66].
- A finer mesh with a 7:1 ratio (Figure 15e) was applied to the workpiece near the contact area.
- In addition, the workpiece was designed partially cut based on the depth of cut (Figure 15e).
- The workpiece was fixed according to Figure 15b, so that the velocity of the nodes in both the X and Z axes was equal to zero. In contrast, the tool model was allowed to follow the trajectory as dictated by the arrow shown in Figure 15b.
- The value for the heat transfer coefficient via convection (h_{conv}) was set to 0.02 N/(s×mm×°C) for dry cutting and via conduction (h_{cond}) to 45 N/(s×mm×°C).

In the present study, twenty-seven simulation runs were carried out by combining three levels of cutting conditions at specific depth of cut; cutting speed (80 m/min, 115 m/min, 150 m/min), feed rate (0.08 mm/rev, 0.11 mm/rev, 0.14 mm/rev), and nose radius (0.40 mm, 0.80 mm, 1.20 mm). Table 10 includes these parameters and their levels.

Table 10. Process conditions of the turning FE model.

Level	V_c [m/min]	f [mm/rev]	re [mm]
I	80	0.08	0.40
II	115	0.11	0.80
III	150	0.14	1.20

The mechanical behavior of the workpiece material was approximated with the aid of the Johnson-Cook model, well-known for its simple form and flexibility [124]. The analytical expression described by the Johnson-Cook formula (see Equation 3) constitutes the strain hardening properties of the material, the strain rate sensitivity,

and the thermal softening properties accordingly. The next constants (Table 11) were used to adapt the model for the present study.

Table 11. The Johnson-Cook model constants for AISI-4140 steel [86].

A [MPa]	B [MPa]	C	n	m	T_0 [°C]	T_m [°C]
106	1167	0.0352	0.1424	0.763	20	1547

In addition to the material flow stress constants, Table 12 contains both the mechanical and the thermal properties that were used in the present numerical study; the elastic modulus, the thermal expansion, the thermal conductivity and the heat capacity of AISI-4140 were expressed as a function of temperature *f*(Temp) since these properties depend on temperature. In addition, a reference strain rate of 1/s was used.

Table 12. Thermo-mechanical properties for the ceramic insert [21] and steel workpiece [86].

Mechanical Properties	**AISI-4140**	**Ceramic**
Young's Modulus E [GPa]	212 @ 20 °C 192 @ 300 °C 164 @ 600 °C	415
Density ϱ [kg/m³]	7850	3500
Poisson's ratio μ	0.30	0.22
Hardness [HRC]	60	–
Thermal Properties	**AISI-4140**	**Ceramic**
Heat capacity c [J/kgK]	362 @ 20 °C 446 @ 300 °C 610 @ 600 °C	334
Thermal expansion α [μm/mK]	11.9 @ 20 °C 13.6 @ 300 °C 14.9 @ 600 °C	8.4
Thermal conductivity λ [W/mK]	41.7 @ 20 °C 41.4 @ 300 °C 34.1 @ 600 °C	7.5

In order to approximate the material separation process under the action of stress, the normalized Cockcroft-Latham damage model [89] was employed. Equation 8 represents the modified criterion developed by Cockcroft and Latham, in which the maximum principal stress is normalized by the effective stress. This criterion is widely accepted and was implemented in early FE studies [125-127].

Coulomb's law was utilized to model the friction that develops between the tool and the workpiece interface. The contact area can be divided into sticking and sliding zones [128] meaning that Equation 5 [90] can be used to estimate the developed frictional stresses. Previous studies [129,130] suggest a value of friction coefficient between 0.5 and 0.6 when studying the machining of AISI-4140 steel at cutting conditions similar to the ones utilized in this research. Hence, the shear friction coefficient for this numerical model was set to 0.577 [106].

Figure 16 depicts sample force versus time diagrams based on the 3D numerical simulations. All diagrams are divided into two phases; the entry phase where force increases quickly as soon as the tool touches the uncut surface of the material and the following steady state phase where force maintains a steady mean value. Finally, when the tool completes its translation on the workpiece and material removal halts, the force rapidly decreases until it reaches zero.

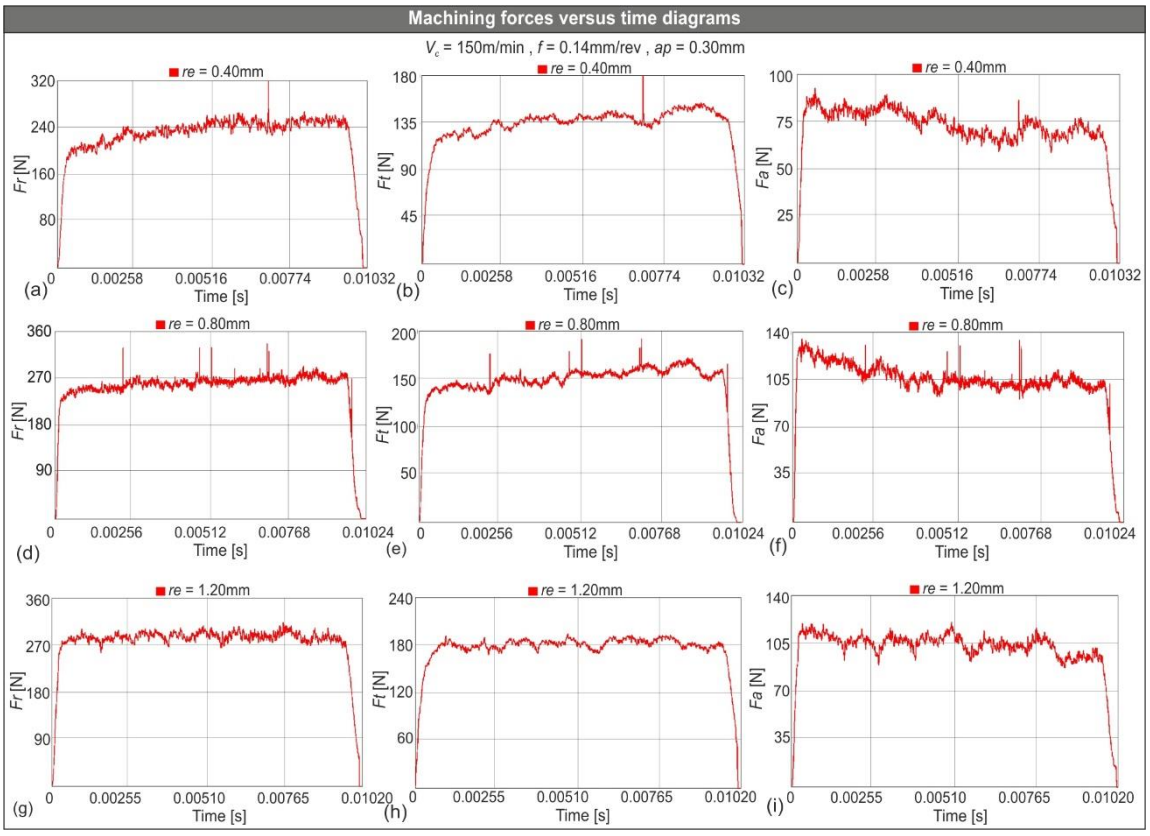

Figure 16. Sample machining forces versus time diagrams for 0.40 mm nose radius (a-c), 0.80 mm (d-f), and 1.20 mm (g-i).

Specifically, Figures 16a-c illustrate the aforementioned diagrams for the radial force (F_r), the tangential force (F_t), and the feed force (F_a) that were generated during AISI-4140 hard turning with the CNGA120404 (re = 0.40 mm) tool. Similarly, Figure 16d-f corresponds to the CNGA120408 (re = 0.80 mm) tool and Figure 16g-i to the CNGA120412 (re = 1.20 mm). Next cutting conditions apply for all the previously mentioned cases: V_c = 150 m/min, f = 0.14 mm/rev, and ap = 0.30 mm.

As set of simulation runs was carried out for calibration purposes. According to Table 13, the level of agreement between the experimental and the numerical results for the estimated resultant force is high. Furthermore, based on the experimental analysis [64] of the machining components for the next indicative parameters: V_c = 115 m/min, f = 0.11 mm/rev, and ap = 0.30 mm, the equivalent simulated results that were derived from the present study indicate a strong correlation. That is, F_r = 202.3 N, F_t = 146.0 N, and F_a = 86.6 N for the experiments and F_r = 214.4 N, F_t = 137.5 N, and F_a = 77.4 N for the simulations, leading to a calculated relative error of 6.0%, −5.8%, and −10.6%, respectively.

Table 13. Main machining force comparison between the experimental and numerical values.

	Cutting Parameters				F_{main} [N]		
Std Order	**V_c [m/min]**	**f [mm/rev]**	**ap [mm]**	**re [mm]**	**Experimental**	**Numerical**	**Relative Error [%]**
1	80	0.08	0.30	0.80	189.8	207.7	9.4
2	80	0.11	0.30	0.80	244.6	250.2	2.3
3	80	0.14	0.30	0.80	282.3	264.5	−6.3
4	115	0.08	0.30	0.80	225.7	232.1	2.8
5	115	0.11	0.30	0.80	264.1	266.2	0.8
6	115	0.14	0.30	0.80	300.9	281.5	−6.4
7	150	0.08	0.30	0.80	238.0	249.6	4.9
8	150	0.11	0.30	0.80	267.7	281.2	5.1
9	150	0.14	0.30	0.80	316.9	320.7	1.2

Two extra sets of 3D simulation runs were prepared, each consisting of nine tests that were carried out under the same conditions and in the same order as the calibration set, but with different cutting tools. The yielded results were used to plot the graphs that are presented in Figure 17.

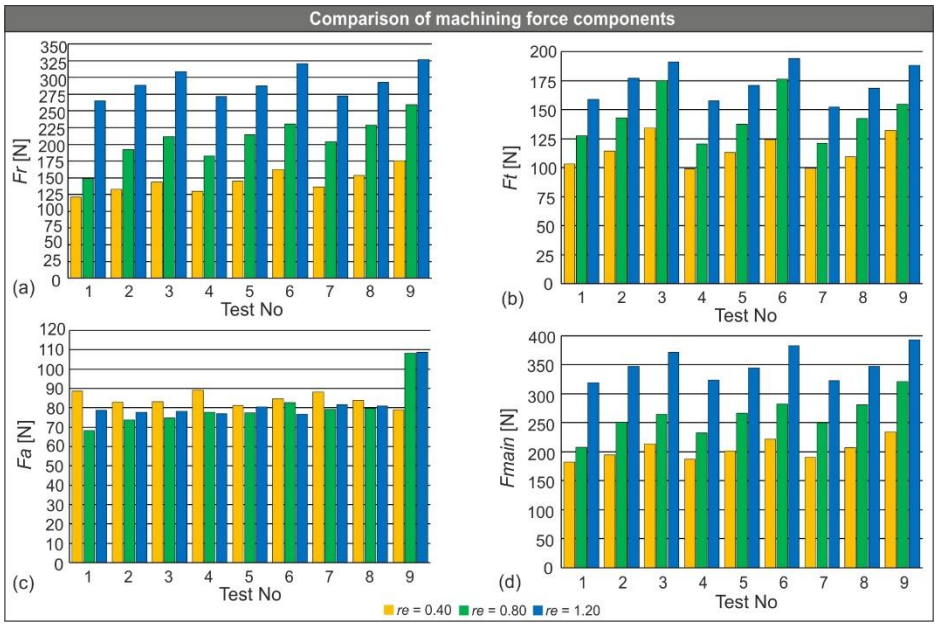

Figure 17. Comparison of the radial force (a), the tangential force (b), the feed force (c), and the resultant machining force (d) based on the different nose radii.

Figure 17 compares graphically the machining force components; the radial force (Figure 17a), the tangential force (Figure 17b), the feed force (Figure 17c), and the resultant of the three components (Figure 17d). The conditions that were applied in the present research, were successfully implemented in experimental studies for hard turning of steel that are available in the literature [96,107,108,131,132].

By reviewing the results that are available in Table 13 and Figure 17 the following conclusions can be deduced:

- The radial force is the component that contributes to the calculated resultant machining force the most. In test number 9 for instance, this contribution is about 56.6%, 65.3%, and 69.2% for each value of nose radius (0.40 mm, 0.80 mm and 1.20 mm accordingly). Similar trend is observed in the rest of the tests.
- Feed rate seems to affect all forces but the feed force. Particularly, any increase in feed lowers the generated turning forces (except for the feed force) by a small but not negligible amount.
- In contrast, the nose radius has a notable effect on the cutting forces. For example, the main machining force increases by 28% on average when the nose radius of the tool is changed from 0.40 mm to 0.80 mm. Additionally, the change from the 0.80 mm nose radius to the 1.20 mm one increases F_{main} even further (about 35% on average).
- Finally, it appears that any change in cutting speed has a limited effect on the generated forces. In particular, when lower cutting speeds are applied, a slight decrease in the developed forces is noted.

The RSM was utilized to establish a predictive model so that the number of simulation tests or the amount of experimental work can be minimized. The RSM is a popular statistical tool that formulates a defined relation between the dependent variables and the independent variables of a system. It was embraced by many researchers for prediction and optimization purposes during machining-related studies [81,107,112,113,115,132] due to the fact that it is versatile and can generate robust models. The full factorial design with the factors and the output for the total of twenty-seven experiments is available in Table 14.

The generated regression model is a second order polynomial that can be described by Equation 6. With this in mind, the complete statistical model for the resultant machining force based on the given formula and the data of the verified FE model (see Table 14) can be represented by Equation 10.

$$F_{main} = 158.1 - 0.109V - 822f + 48.8re + 0.00046V^2 + 4504f^2 + 56.6re^2 \\ +3.03Vf - 0.093Vre + 498fre \quad (10)$$

In Equation 10, F_{main} is the resultant machining force in N, V denotes the cutting speed in m/min, f is the feed rate in mm/rev and re represents the insert's nose radius in mm.

Table 14. Main machining force comparison between the simulated and statistical value.

	Cutting Parameters			F_{main} [N]	
Std Order	**V_c [m/min]**	**f [mm/rev]**	**re [mm]**	**FE Model**	**Regression Model**
1	80	0.08	0.40	182.3	176.3
2	80	0.11	0.40	194.1	190.6
3	80	0.14	0.40	213.6	212.9
4	115	0.08	0.40	186.5	182.8
5	115	0.11	0.40	201.0	200.3
6	115	0.14	0.40	221.3	225.8
7	150	0.08	0.40	190.2	190.5
8	150	0.11	0.40	206.5	211.1
9	150	0.14	0.40	233.7	239.8
10	80	0.08	0.80	207.7	236.0
11	80	0.11	0.80	250.2	256.2
12	80	0.14	0.80	284.5	284.5
13	115	0.08	0.80	232.1	241.2
14	115	0.11	0.80	266.2	264.6
15	115	0.14	0.80	301.5	296.1
16	150	0.08	0.80	249.6	247.5
17	150	0.11	0.80	281.2	274.1
18	150	0.14	0.80	320.7	308.8
19	80	0.08	1.20	319.1	313.7
20	80	0.11	1.20	346.9	339.9
21	80	0.14	1.20	371.3	374.3
22	115	0.08	1.20	323.3	317.6
23	115	0.11	1.20	344.4	347.0
24	115	0.14	1.20	382.6	384.5
25	150	0.08	1.20	322.4	322.7
26	150	0.11	1.20	347.4	355.2
27	150	0.14	1.20	392.3	395.9

To validate the established model, the Analysis of Variance (ANOVA) was employed with a standard significance level equal to 0.05. The analysis yielded a successful fit of the model with an adjusted R-squared of 98.80% proving that the power of the test is sufficient. The obtained results are presented in Table 15. The

constant, the re^2 term and the $f \times re$ term appear to contribute the most to the model, indicating a strong influence of the corner radius to the produced forces. Last but not least, the p-value of the regression model suggests that the probability of acquiring extreme results is subtle.

Table 15. ANOVA results for the resultant machining force.

Source	Degree of Freedom	Sum of Squares	Mean Square	f-value	p-value
Regression	9	113,045	12,560.6	238.87	0.000
Residual Error	17	894	52.6		
Total	26	113,939			
R-sq (adj) = 98.80%					
Term	**PE Coefficient**	**SE Coefficient**	**t-value**	**p-value**	
Constant	158.1	59.8	2.64	0.017	
V	−0.109	0.611	−0.18	0.861	
f	−822	774	−1.06	0.303	
re	48.8	39.5	1.24	0.233	
V^2	0.00046	0.00242	0.19	0.853	
f^2	4504	3289	1.37	0.189	
re^2	56.6	18.5	3.06	0.007	
$V \times f$	3.03	1.99	1.52	0.147	
$V \times re$	−0.093	0.150	−0.62	0.540	
$f \times re$	498	174	2.86	0.011	

Figure 18 contains the graphical results of the ANOVA; Figure 18a illustrates the normal probability plot, which highlights any departures of the data points from the fit line. It is clear that no serious departures exist in this case. Figure 18b depicts the residuals versus the fitted values plot, which indicates that the data points are almost evenly scattered on both sides of the line. Figure 18c shows the error percentage histogram along with the fit line that proves the error uniformity in the model. Furthermore, the overall normality can be checked by Figure 18d, which includes the residuals versus the order of the data. It is concluded that no systematic faults are present in the model, since data points do not form any systematic pattern. Finally, the 3D response surface plots (Figure 18e) were prepared in order to visualize the results of the developed regression model according to the acquired data. In addition, Figure 18e illustrates the performance of the used tools based on the polynomial solutions of Equation 10.

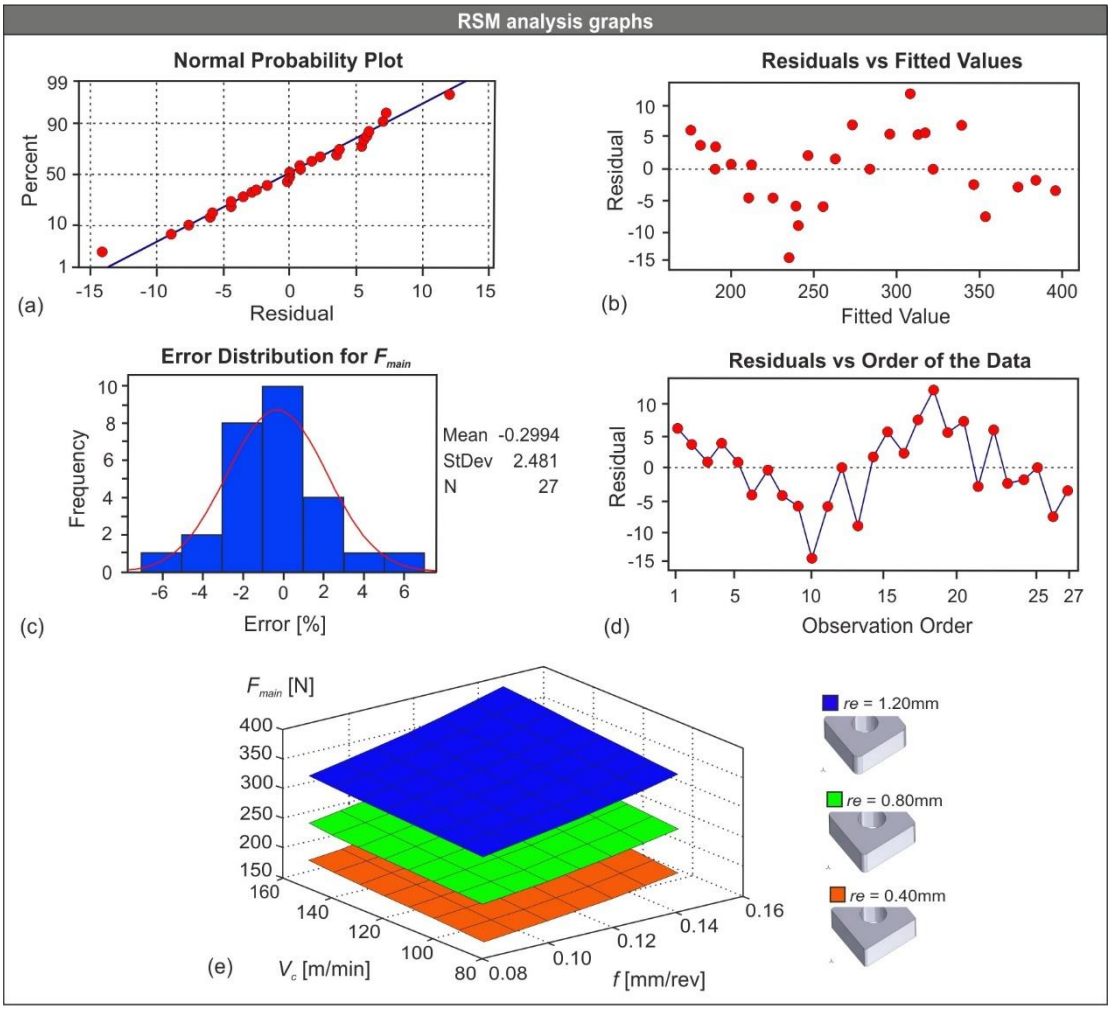

Figure 18. Probability plot (a), residuals versus fitted values (b), error histogram (c) residuals versus order (d) and 3D plots of the F_{main} for each nose radius €.

PUBLISHED WORK

7. PUBLISHED WORK

The below published content has been included in the Appendix of the full version of the Doctoral Thesis with respect to the copyright.

List of published articles:

- Tzotzis A., García-Hernández C., Huertas-Talón J.L. and Kyratsis P., (2020), CAD-based automated design of FEA-ready cutting tools, *Journal of Manufacturing and Materials Processing*, 4(4), pp. 1-14, https://doi.org/10.3390/jmmp4040104

- Tzotzis A., García-Hernández C., Huertas-Talón J.L. and Kyratsis P., (2020), FEM based mathematical modelling of thrust force during drilling of Al7075-T6, *Mechanics & Industry*, 21(4), pp. 1-14, https://doi.org/10.1051/meca/2020046

- Tzotzis A., García-Hernández C., Huertas-Talón J.L. and Kyratsis P., (2020), 3D FE Modelling of Machining Forces during AISI 4140 Hard Turning, *Strojniški vestnik - Journal of Mechanical Engineering*, 66(7-8), pp. 467-478, https://doi.org/10.5545/sv-jme.2020.6784

- Tzotzis A., García-Hernández C., Huertas-Talón J.L. and Kyratsis P., (2020), Influence of the Nose Radius on the Machining Forces Induced during AISI-4140 Hard Turning: A CAD-Based and 3D FEM Approach, *Micromachines*, 11(9), pp. 1-16, https://doi.org/10.3390/mi11090798

FINAL REPORT

8. FINAL REPORT

8.1. Objectives

Through this Doctoral Thesis, as part of the FEM-based and CAD-assisted machining, several well-established methods and techniques were evaluated, so that the development of similar methodologies and algorithms can be feasible. With the employment of this material, the present Doctoral Thesis aims to promote FEM in manufacturing research, update the current knowledge and investigate new possibilities that can be adopted by the industry.

In general, the following tasks were completed in order to achieve the set objectives:

- A review of the state-of-the-art has been carried out in each of the mentioned areas of research, to obtain an overview of the current state of technology. This way it was possible to determine the methodologies that required further investigation and the material that required new approaches.
- After the investigation into the methodologies related to manufacturing, the study focused on the development of a computer tool that supports the preparation of FE models. Moreover, an algorithm for the design process of cutting tools has been developed. A computer application that is responsible for the automated design of FEA-ready cutting tool models. The automated preparation of high quality models, ensures the validity of the simulated results.
- With the acquired knowledge on FEM-based model preparation, alternative modelling approaches for machining operations have been conceived. Typical cutting tool models were replaced with the models generated from the developed computer application. In addition, the tool-workpiece interface was defined by utilizing CAD software instead of using the default layout of the FEA software.
- Moreover, a study related to the influence of cutting conditions on the developed machining forces and chip formation was carried out, by utilizing both experimental and numerical work. This study focused on the promotion of the FEA in manufacturing research, as well as on the delivery of updated understanding about various crucial aspects of machining operations.
- Finally, a number of statistically-based models for prediction of the machining forces were established by employing acknowledged mathematical methods, formulated with results derived from numerical studies. This way, novel formulae can be adopted by industry.

8.2. Contribution

This section presents a summary of the contribution that derives from the publications that are part of the compendium presented in this Doctoral Thesis. Moreover, it is pointed out that the initial objectives of this research, were achieved through the published work. With respect to the objectives and to the publications, the following completed tasks can be considered that contribute towards the research field of FEM-based and CAD-assisted machining:

- The development of an application for the automated design of FEA-ready cutting tool models providing the next features and benefits:
  - ✓ The generated models are of high fidelity since they include the full geometry of the counterpart physical tools (in contrast to most downloaded models), improving this way the yielded simulated results.
  - ✓ It is possible to produce numerous models within short amount of time. Thus, researchers can better allocate their time and focus on the essence of their study.
  - ✓ The application was realized by means of CAD-based programming, which allows for the effortless extension of the code in case more types of tools are required.
  - ✓ In addition, the selected design methodology produces parametric models that can be manually edited by the user at any time.
  - ✓ The generated models can be imported to virtually every commercially available FEA system.
  - ✓ Moreover, the models cover a wide variety of needs related to turning testing, since they are designed according to the ISO-13399 standard, which is accepted by most manufacturers across the globe.
- The establishment of the three proposed 3D FE models, one for drilling and two for turning processes that are fully described along with their critical parameters.
  - ✓ Drilling and turning are considered two of the most applied processes in industry that are constantly developing. Thus, the proposed models can become updated additions to this area.
  - ✓ Furthermore, the models are developed in three dimensions. This fact adds further value to their usability, since the number of 3D FE models that is available in the literature is relatively low at present.
  - ✓ The models cover a range of cutting conditions that, at the time, is mostly studied via experimental work.
  - ✓ It is possible to edit the models effortlessly, so that different criteria can be met.

- ✓ Finally, future experimental testing can be omitted, as long as minor calibration is performed each time any of the critical parameters is changed.

- The study of key cutting conditions and their influence on the generated machining forces induced during hard turning of AISI-4140, as well as on the produced thrust forces during Al7075-T6 drilling. The findings of the studies provide the following practical knowledge:
  - ✓ Updated information on the effects of cutting speed, feed and tool diameter on the thrust forces that are generated during Al7075-T6 drilling, with respect to limits specified by both tool manufacturers and international bibliography.
  - ✓ An introduction to the chip formation mechanisms of Al7075-T6 during drilling processes.
  - ✓ In addition, updated information on the impact of commonly applied parameters such as cutting speed, feed, depth of cut and tool nose radius on the developed turning forces (tangential, radial and feed) in the course of AISI-4140 hard turning, as well as some insight on the formed chip morphology and evolution.
- Finally, the development of the three proposed statistically-based prediction models that can be applied in industry, one for drilling and two for turning. The advantages that derive from the employment of these models are as follows:
  - ✓ Instant and accurate estimation, under certain limits of cutting conditions, of the thrust forces for drilling, as well as of the machining force components for turning, without the need for a specialized piece of software.
  - ✓ The range of the applied cutting conditions can be easily extended as long as the equivalent verification experiments are conducted.
  - ✓ It is possible to embed the models in an open environment such as an application or a web-page.

8.3. Methodologies

The published papers that are presented in this thesis, were prepared by utilizing a number of methodologies that are described below.

8.3.1. Literature survey

An extensive literature survey was carried out, covering the advancements in several areas related to machining in the past twenty years. Specifically, the advancements in FEM was investigated, as well as the strategies and techniques that

are widely accepted and used to date. Moreover, the most contemporary experimental methods that are implemented in machining research were reviewed, in addition to the statistical methodologies and tools. Finally, communication was established with acclaimed cutting tool manufacturers such as Kennametal, Marena and Sandvik Coronmant, in order to maintain a steady flow of news related to cutting tool technologies. Of course, attention was given to the publications that deal with the first steps in FEM and its evolution.

8.3.2. Realization of tools, methodologies and mathematical models

The completion of the literature survey revealed the tools and methodologies that were required to carry out the presented research.

- The application presented in the publication "CAD-based automated design of FEA-ready cutting tools" was developed by means of CAD-based programming. A user interface was designed via the integrated programming interface of SolidWorks™, to facilitate the operation of the application. In addition, the code was written in the VBA event-driven programming language and was divided into multiple modules for easier access during editing. Furthermore, the design technique that was applied, is according to the parametric design principals so that the generated models can be editable. Lastly, an algorithm was conceived to simplify the design process of the various types of cutting tool models.
- In "FEM based mathematical modelling of thrust force during drilling of Al7075-T6" both an experimental and a numerical framework were set. The numerical model was set in three dimensions with the aid of FEA software, namely DEFORM™-3D. Moreover, the most recognized formulae were applied for the development of the FE model, such as the Johnson-Cook constitutive equation and the Cockcroft-Latham criterion. The contact relationship of the tool-workpiece interface was defined according to well-established theories that are available in the bibliography. Finally, the RSM and ANOVA were employed for the set of prediction mathematical models. Similar methodologies and tools were also used in "3D FE modelling of machining forces during AISI 4140 hard turning".
- A 3D numerical model was established in "Influence of the nose radius on the machining forces induced during AISI-4140 hard turning: A CAD-based and 3D FEM approach" by using both FEM and CAD-assisted layouts. Similarly to the other FEM related publications of the thesis, the RSM and ANOVA were used to establish mathematical models for the prediction of the generated turning forces.

8.3.3. Implementation and evaluation of methodologies

The efficiency of the generated cutting tool models was verified by carrying out simulation tests in which the tool models were integrated. In the case of the "FEM based mathematical modelling of thrust force during drilling of Al7075-T6" paper, a series of drilling tests were performed to validate the numerical model and then a statistically-based model was established for prediction purposes of the developed thrust forces. Finally, the turning simulation tests in both "3D FE modelling of machining forces during AISI 4140 hard turning" and "Influence of the nose radius on the machining forces induced during AISI-4140 hard turning: A CAD-based and 3D FEM approach" were analyzed via an assembly system in SolidWorks™ and then compared to experimental results for verification. Moreover, a prediction model for the generated turning force components was expressed with mathematical formulae. It is noted that all the statistical models were further validated by employing ANOVA and performing extra sets of simulations.

8.4. Conclusions

The paper with title "CAD-based automated design of FEA-ready cutting tools" presents the development of a designer application with the implementation of the SolidWorks™ API under VBA coding. The purpose of the developed application is to automatically generate CAD models of cutting tools that can be used with FEA software. Upon finalizing the application, a number of simulation tests have been successfully performed to verify the functionality of the generated models.

In general, the CAD-based programming can be used to automate almost all typical design tasks, hence enhancing the design process of products and systems. Moreover, by implementing the programming tools of modern CAD systems, it is possible to develop simple applets, macros and complete applications.

As the complexity of the under study product or system increases so does the value of the developed tools, further increasing the productivity of the engineers. The presented application can become the basis for developing downstream applications by integrating FEA-based capabilities related to estimation of cutting forces and tool wear, which in general can lead to cutting conditions optimization. Finally, it is safe to state the next conclusions with respect to the acquired results:

- The generated cutting tool was successfully imported to DEFORM™-3D and meshed with the maximum available number of elements.

- All the performed simulations were successfully completed within reasonable amount of time.
- The performance of the under study cutting tool model was high, since the yielded results for the machining forces were in par with the experimental ones.
- Finally, the simulated resultant of the machining forces was in high agreement with the experimental one exceeding 90% in most cases.

The paper entitled "FEM based mathematical modelling of thrust force during drilling of Al7075-T6" presents the development of a prediction model for the generated thrust forces during drilling of Al7075-T6, with the aid of RSM and the implementation of 3D FEA. A complete series of 27 3D simulations was carried out under different cutting conditions (speed and feed rate) in addition to the three different tool diameters that were used. The simulated results were validated via experiments and the correlation between the simulated and the experimental results exceeded 95% in most cases. After thoroughly analyzing the model for its accuracy (5.9%) and goodness of fit, it is concluded that the developed model can safely predict the thrust forces under certain limits that are discussed in this research. Moreover, the morphology of the produced chips during drilling of Al7075-T6 was introduced. Finally, through this analysis the following conclusions are drawn:

- Increase in tool diameter and feed rate leads to significant boost of thrust force. Specifically, an increase of close to 20% in thrust force is observed when changing to the 10mm drill from the 8mm one or when increasing the feed to 0.20mm/rev from 0.15mm/rev. The equivalent shift from 10mm to 12mm or from 0.20mm/rev to 0.25mm/rev amplifies F_z by more than 40% for both cases.
- On the other hand, any increase in cutting speed increases thrust force at a small but not negligible amount; a step-up from 50m/min to 100m/min was estimated to rise F_z approximately by 8.5%, whereas from 100m/min to 150m/min by 4%.
- The factors that affect the most the statistical model are: f, D^2, f^2, $D \times V_c$ and $D \times f$ since their p-values is lower than the significance level.
- The produced chips tend to maintain a conical shape, regardless of the cutting conditions, whereas the diameter of the curling of chip increases as larger tool diameter was selected.

In the work "3D FE modelling of machining forces during AISI 4140 hard turning", the development of a 3D FE model, as well as a prediction model for the main machining force induced during hard turning of AISI-4140 were presented. A series of 27 3D simulations were conducted under different conditions of cutting speed and

feed in addition to the three different depths of cut. The obtained numerical results were validated via experimental values that are available in the literature and it was observed that are in high agreement that surpasses 90% in most of the runs. The accuracy (8.8%) and goodness of fit of the statistical model, dictate that both the developed models (FE and statistical) can securely predict the resultant machining forces when applied within the scope of this study. Concluding, the following remarks are pointed out:

- Higher values of depth of cut and feed rate significantly increase machining forces, especially depth of cut is the factor that effects F_{main} the most. Specifically, according to the simulated values of F_{main}, an average increase of about 104% in the resultant cutting force is observed when depth of cut changes from 0.10mm to 0.20mm. The equivalent shift from 0.20mm to 0.30mm amplifies F_{main} by approximately 50%.
- Similarly, when feed changes from 0.08mm/rev to 0.11mm/rev and from 0.11mm/rev to 0.14mm/rev, the resultant cutting force gains an increase of about 24% and 16% respectively.
- On the contrary, the generated forces decrease as cutting speed increases, however the changes induced by cutting speed are trivial compared to the ones caused by the depth of cut and feed. The average percentage of decrease observed in F_{main}, is estimated approximately 10% when cutting speed shifts from 150m/min to 115m/min. Additionally, as the value of V_c lowers from 115m/min to 80m/min, the F_{main} decreases about 13% on average.
- The factors that have great impact on the statistical model based on the significance level are: ap, $f \times ap$, constant, $V \times ap$ and f.

In the publication "Influence of the nose radius on the machining forces induced during AISI-4140 hard turning: A CAD-based and 3D FEM approach" a 3D FE model for the hard turning of AISI-4140 as well as a prediction model for the resultant machining force, based on statistical methods, are presented. A set of experimental results that are available in the literature was used to verify the FE model and consequently a complete design of experiments was prepared according to three levels of cutting speed, feed rate and tool nose radius. Further validation of the statistical model was made to ensure that the model can safely predict the resultant cutting force within the range of conditions found in the present study. Additionally, the influence of the nose radius on the produced cutting forces was investigated and graphically presented. Finally, the next conclusions can be drawn:

- F_r is the governing force during hard turning of AISI-4140, which in most cases represents the two-thirds of the produced resultant machining force.

- When feed rate changes from 0.08mm/rev to 0.11mm/rev F_{main} gains an average increase of about 10.4%. Similarly, a shift from 0.11mm/rev to 0.14mm/rev increases F_{main} by approximately 11.7%, regardless of the nose radius value.
- The nose radius of the cutting edge affects the generated cutting forces substantially. It is highlighted that a higher value of nose radius leads to higher values of cutting forces and, depending on the applied cutting conditions, the increase percentage exceeds 30% in most cases.
- Finally, changing the cutting speed does not seem to influence the main cutting force notably.

8.5. Future work

It is anticipated to enrich the current work with additional features and research items. These additions will probably enhance the value of the presented work and strengthen the foundations for the realization of similar studies. Next tasks are expected to be carried out in due time:

- First of all, the functions of the designer application will be extended, so that it can generate more types of cutting tools. Furthermore, it is expected to embed the formulae of the established prediction models in the graphical user interface to facilitate the calculation process.
- Next, it is desired to conduct an extensive experimental investigation into the milling operations under recommended cutting conditions, so that useful data can be extracted about this widely used process. In addition, a counterpart FE model in three dimensions will be established along with an appropriate literature survey.
- To further update the knowledge about milling of standardized industrial metals with respect to modern cutting tools, it is expected to carry out a thorough investigation into the influence of critical parameters on the generated cutting forces, the chip formation, the surface roughness and other interesting results, by utilizing cutting-edge equipment such as CNC machining center, dynamometer, profilometer and data acquisition devices.
- Finally, it is possible to develop prediction models, with the gathered data, for the milling processes under certain conditions. In addition, the already developed models could be modified to provide results under a wider range of conditions.

BIBLIOGRAPHY

9. BIBLIOGRAPHY

1. Klamecki, B. Incipient Chip Formation in Metal Cutting - A Three Dimensional Element Analysis (PhD Thesis), Urbana-Champaign: University of Illinois, **1973**.

2. Arrazola, P.J.; Villar, A.; Ugarte, D.; Marya, S. Serrated chip prediction in finite element modeling of the chip formation process. *Mach. Sci. Technol.* **2007**, *11*, 367–390

3. Klocke, F.; Raedt, H.-W.; Hoppe, S. 2D-FEM Simulation of the orthogonal high speed cutting process. *Mach. Sci. Technol.* **2001**, *5*, 323–340, https://doi.org/10.1081/MST-100108618

4. Calamaz, M.; Coupard, D.; Girot, F. A new material model for 2D numerical simulation of serrated chip formation when machining titanium alloy Ti-6Al-4V. *Int. J. Mach. Tools Manuf.* **2008**, *48*, 275–288, https://doi.org/10.1016/j.ijmachtools.2007.10.014

5. Yameogo, D.; Haddag, B.; Makich, H.; Nouari, M. Prediction of the Cutting Forces and Chip Morphology When Machining the Ti6Al4V Alloy Using a Microstructural Coupled Model. *Procedia CIRP* **2017**, *58*, 335–340, https://doi.org/10.1016/j.procir.2017.03.233

6. Yaich, M.; Ayed, Y.; Bouaziz, Z.; Germain, G. Numerical analysis of constitutive coefficients effects on FE simulation of the 2D orthogonal cutting process: application to the Ti6Al4V. *Int. J. Adv. Manuf. Technol.* **2017**, *93*, 283–303, https://doi.org/10.1007/s00170-016-8934-4

7. Ducobu, F.; Rivière-Lorphèvre, E.; Filippi, E. Numerical contribution to the comprehension of saw-toothed Ti6Al4V chip formation in orthogonal cutting. *Int. J. Mech. Sci.* **2014**, *81*, 77–87, https://doi.org/10.1016/j.ijmecsci.2014.02.017

8. Guo, Y.B.; Dornfeld, D.A. Finite element modeling of burr formation process in drilling 304 stainless steel. *J. Manuf. Sci. Eng. Trans. ASME* **2000**, *122*, 612–619, https://doi.org/10.1115/1.1285885

9. Zhu, Z.; Guo, K.; Sun, J.; Li, J.; Liu, Y.; Chen, L.; Zheng, Y. Evolution of 3D chip morphology and phase transformation in dry drilling Ti6Al4V alloys. *J. Manuf. Process.* **2018**, *34*, 531–539, https://doi.org/10.1016/j.jmapro.2018.07.001

10. Nan, X.; Xie, L.; Zhao, W. On the application of 3D finite element modeling for small-diameter hole drilling of AISI 1045 steel . *Int. J. Adv. Manuf. Technol.* **2016**, *84*, 1927–1939, https://doi.org/10.1007/s00170-015-7782-y

11. Dou, T.; Fu, H.; Li, Z.; Ji, X.; Bi, S.S. Prediction model, simulation, and experimental validation on thrust force and torque in drilling SiCp/Al6063. *Int. J. Adv. Manuf. Technol.* **2019**, *103*, 165–175, https://doi.org/10.1007/s00170-019-03366-1

12. Xiang, J.; Xie, L.; Gao, F.; Zhang, Y.; Yi, J.; Wang, T.; Pang, S.; Wang, X. On Multi-Objective Based Constitutive Modelling Methodology and Numerical Validation in Small-Hole Drilling of Al6063/SiCp Composites. *Materials* **2018**, *11*, 1–22, https://doi.org/10.3390/ma11010097

13. Nan, X.; Xie, L.; Zhao, W. On the application of 3D finite element modeling for small-diameter hole drilling of AISI 1045 steel. *Int. J. Adv. Manuf. Technol.* **2016**, *84*, 1927–1939, https://doi.org/10.1007/s00170-015-7782-y

14. Kyratsis, P.; Garcia-Hernandez, C.; Vakondios, D.; Antoniadis, A. Thrust Force and Torque Mathematical Models in Drilling of Al7075 Using the Response Surface Methodology. In *Design of Experiments in Production Engineering*; Springer International Publishing: Cham, **2016**; pp. 151–164 ISBN 978-3-319-23838-8

15. Ucun, İ. 3D finite element modelling of drilling process of Al7075-T6 alloy and experimental validation. *J. Mech. Sci. Technol.* **2016**, *30*, 1843–1850, https://doi.org/10.1007/s12206-016-0341-0

16. Majeed, A.; Iqbal, A.; Lv, J. Enhancement of tool life in drilling of hardened AISI 4340 steel using 3D FEM modeling. *Int. J. Adv. Manuf. Technol.* **2018**, *95*, 1875–1889, https://doi.org/10.1007/s00170-017-1235-8

17. Lotfi, M.; Amini, S.; Al-Awady, I.Y. 3D numerical analysis of drilling process: heat, wear, and built-up edge. *Adv. Manuf.* **2018**, *6*, 204–214, https://doi.org/10.1007/s40436-018-0223-z

18. Buchkremer, S.; Klocke, F.; Veselovac, D. 3D FEM simulation of chip breakage in metal cutting. *Int. J. Adv. Manuf. Technol.* **2016**, *82*, 645–661, https://doi.org/10.1007/s00170-015-7383-9

19. Hu, H.J.; Huang, W.J. Effects of turning speed on high-speed turning by ultrafine-grained ceramic tool based on 3D finite element method and experiments. *Int. J. Adv. Manuf. Technol.* **2013**, *67*, 907–915, https://doi.org/10.1007/s00170-012-4535-z

20. Guo, Y.B.; Liu, C.R. 3D FEA modeling of hard turning. *J. Manuf. Sci. Eng. Trans. ASME* **2002**, *124*, 189–199, https://doi.org/10.1115/1.1430678

21. Hu, H.J.; Huang, W.J. Tool life models of nano ceramic tool for turning hard steel based on FEM simulation and experiments. *Ceram. Int.* **2014**, *40*, 8987–8996, https://doi.org/10.1016/j.ceramint.2014.01.095

22. Özel, T.; Karpat, Y.; Srivastava, A. Hard turning with variable micro-geometry PcBN tools. *CIRP Ann. - Manuf. Technol.* **2008**, *57*, 73–76, https://doi.org/10.1016/j.cirp.2008.03.063

23. Rami, A.; Kallel, A.; Sghaier, S.; Youssef, S.; Hamdi, H. Residual stresses computation induced by turning of AISI 4140 steel using 3D simulation based on a mixed approach. *Int. J. Adv. Manuf. Technol.* **2017**, *91*, 3833–3850, https://doi.org/10.1007/s00170-017-0047-1

24. Valiorgue, F.; Rech, J.; Hamdi, H.; Gilles, P.; Bergheau, J.M. 3D modeling of residual stresses induced in finish turning of an AISI304L stainless steel. *Int. J. Mach. Tools Manuf.* **2012**, *53*, 77–90, https://doi.org/10.1016/j.ijmachtools.2011.09.011

25. Attanasio, A.; Ceretti, E.; Rizzuti, S.; Umbrello, D.; Micari, F. 3D finite element analysis of tool wear in machining. *CIRP Ann. - Manuf. Technol.* **2008**, *57*, 61–64, https://doi.org/10.1016/j.cirp.2008.03.123

26. Malakizadi, A.; Gruber, H.; Sadik, I.; Nyborg, L. An FEM-based approach for tool wear estimation in machining. *Wear* **2016**, *368–369*, 10–24, https://doi.org/10.1016/j.wear.2016.08.007

27. Haddag, B.; Nouari, M. Tool wear and heat transfer analyses in dry machining based on multi-steps numerical modelling and experimental validation. *Wear* **2013**, 302, 1158–1170, https://doi.org/10.1016/j.wear.2013.01.028

28. Pittalà, G.M.; Monno, M. 3D finite element modeling of face milling of continuous chip material. *Int. J. Adv. Manuf. Technol.* **2010**, *47*, 543–555, https://doi.org/10.1007/s00170-009-2235-0

29. Davoudinejad, A.; Tosello, G.; Parenti, P.; Annoni, M. 3D finite element simulation of micro end-milling by considering the effect of tool run-out. *Micromachines* **2017**, *8*, 1–20, https://doi.org/10.3390/mi8060187

30. Soo, S.L.; Dewes, R.C.; Aspinwall, D.K. 3D FE modelling of high-speed ball nose end milling. *Int. J. Adv. Manuf. Technol.* **2010**, *50*, 871–882, https://doi.org/10.1007/s00170-010-2581-y

31. Mamedov, A.; Lazoglu, I. Thermal analysis of micro milling titanium alloy Ti-6Al-4V. *J. Mater. Process. Technol.* **2016**, *229*, 659–667, https://doi.org/10.1016/j.jmatprotec.2015.10.019

32. Maurel-Pantel, A.; Fontaine, M.; Thibaud, S.; Gelin, J.C. 3D FEM simulations of shoulder milling operations on a 304L stainless steel. *Simul. Model. Pract. Theory* **2012**, *22*, 13–27, https://doi.org/10.1016/j.simpat.2011.10.009

33. Wu, H.B.; Zhang, S.J. 3D FEM simulation of milling process for titanium alloy Ti6Al4V. *Int. J. Adv. Manuf. Technol.* **2014**, *71*, 1319–1326, https://doi.org/10.1007/s00170-013-5546-0

34. Wu, Y.; Zhou, Y.; Zhou, Z.; Tang, J.; Ouyang, H. An advanced CAD/CAE integration method for the generative design of face gears. *Adv. Eng. Softw.* **2018**, *126*, 90–99, https://doi.org/10.1016/j.advengsoft.2018.09.009

35. Wang, L.; Chen, Z.C. A new CAD/CAM/CAE integration approach to predicting tool deflection of end mills. *Int. J. Adv. Manuf. Technol.* **2014**, *72*, 1677–1686, https://doi.org/10.1007/s00170-014-5760-4

36. Bartłomiej, S. Method of spiral bevel gear tooth contact analysis performed in CAD environment. *Aircr. Eng. Aerosp. Technol.* **2013**, *85*, 467–474, https://doi.org/10.1108/AEAT-11-2012-0207

37. Garcia-Hernandez, C.; Marín, R.; Talón, J.; Efkolidis, N.; Kyratsis, P. WEDM manufacturing method for noncircular gears using CAD/CAM software. *Strojniški Vestn. - J. Mech. Eng.* **2016**, *62*, 137–144, https://doi.org/10.5545/sv-jme.2015.2994

38. Tzivelekis, C.A.; Yiotis, L.S.; Fountas, N.A.; Krimpenis, A.A. Parametrically automated 3D design and manufacturing for spiral-type free-form models in an interactive CAD/CAM environment. *Int. J. Interact. Des. Manuf.* **2015**, *11*, 223–232, https://doi.org/10.1007/s12008-015-0261-8

39. Oancea, G.; Haba, S.-A. Software Tool Used in CAPP/CAM Systems for Rotational Parts. *Sci. Bull. Ser. C Fascicle Mech. Tribol. Mach. Manuf. Technol.* **2016**, *30*

40. Dimitriou, V.; Vidakis, N.; Antoniadis, A. Advanced computer aided design simulation of gear hobbing by means of three-dimensional kinematics modeling. *J. Manuf. Sci. Eng. Trans. ASME* **2007**, *129*, 911–918, https://doi.org/10.1115/1.2738947

41. Kyratsis, P.; Bilalis, N.; Antoniadis, A. CAD-based simulations and design of experiments for determining thrust force in drilling operations. *Comput. Des.* **2011**, *43*, 1879–1890, https://doi.org/10.1016/j.cad.2011.06.002

42. Harik, R.F.; Derigent, W.J.E.; Ris, G. Computer aided process planning in aircraft manufacturing. *Comput. Aided. Des. Appl.* **2008**, *5*, 953–962, https://doi.org/10.3722/cadaps.2008.953-962

43. Deb, S.; Parra-Castillo, J.R.; Ghosh, K. An Integrated and Intelligent Computer-Aided Process Planning Methodology for Machined Rotationally Symmetrical Parts. *Int. J. Adv. Manuf. Syst.* **2011**, *13*, 1–26

44. Kyratsis, P.; Tzotzis, A.; Tzetzis, D.; Sapidis, N. Pneumatic cylinder design using cad-based programming. *Acad. J. Manuf. Eng.* **2018**, *16*, 107–113

45. Ong, S.K.; Nec, A.Y.C. Automating set-up planning in machining operations. *J. Mater. Process. Technol.* **1997**, *63*, 151–156, https://doi.org/10.1016/S0924-0136(96)02616-7

46. Kyratsis, P.; Tapoglou, N.; Bilalis, N.; Antoniadis, A. Thrust force prediction of twist drill tools using a 3D CAD system application programming interface. *Int. J. Mach. Mach. Mater.* **2011**, *10*, 18–33, https://doi.org/10.1504/IJMMM.2011.040852

47. Tzotzis, A.; Garcia-Hernandez, C.; Huertas-Talon, J.-L.; Tzetzis, D.; Kyratsis, P. Engineering applications using CAD based application programming interface. *MATEC Web Conf.* **2017**; 94, pp. 1–7, https://doi.org/10.1051/matecconf/20179401011

48. Sapidis, N.; Chatziparasidis, I. Framework to automate mechanical-system design using multiple product-models and assembly feature technology. *Int. J. Prod. Lifecycle Manag.* **2017**, *10*, 124–150, https://doi.org/10.1504/IJPLM.2017.085957

49. Roberto, V.; Osorio-Gómez, G. Assembly planning with automated retrieval of assembly sequences from CAD model information. *Assem. Autom.* **2012**, *32*, 347–360, https://doi.org/10.1108/01445151211262410

50. Du, B.; Wang, X.; Feng, Y.; Yu, D.; Xu, G. Intelligent Assembly Technology Based on Standard Parts Feature of CATIA. *Mod. Appl. Sci.* **2014**, *8*, 49–55, https://doi.org/10.5539/mas.v8n2p49

51. Vijayaraghavan, A.; Dornfeld, D.A. Automated Drill Modeling for Drilling Process Simulation. *J. Comput. Inf. Sci. Eng.* **2007**, *7*, 276–282, https://doi.org/10.1115/1.2768091

52. Li, A.; Zhao, J.; Pei, Z.; Zhu, N. Simulation-based solid carbide end mill design and geometry optimization. *Int. J. Adv. Manuf. Technol.* **2014**, *71*, 1889–1900, https://doi.org/10.1007/s00170-014-5638-5

53. Denkena, B.; Lucas, A.; Bassett, E. Effects of the cutting edge microgeometry on tool wear and its thermo-mechanical load. *CIRP Ann.* **2011**, *60*, 73–76, https://doi.org/10.1016/j.cirp.2011.03.098

54. Meyer, R.; Köhler, J.; Denkena, B. Influence of the tool corner radius on the tool wear and process forces during hard turning. *Int. J. Adv. Manuf. Technol.* **2012**, *58*, 933–940, https://doi.org/10.1007/s00170-011-3451-y

55. Tzotzis, A.; Garcia-Hernandez, C.; Huertas-Talón, J.L.; Kyratsis, P. Influence of the Nose Radius on the Machining Forces Induced during AISI-4140 Hard Turning : A CAD-Based and 3D FEM Approach. *Micromachines* **2020**, *11*, 1–16, https://doi.org/10.3390/mi11090798

56. Karpat, Y.; Ozel, T. Process simulations for 3D turning using uniform and variable microgeometry PCBN tools. *Int. J. Mach. Mach. Mater.* **2008**, *4*, 26–38, https://doi.org/10.1504/IJMMM.2008.020908

57. Denkena, B.; Koehler, J.; Rehe, M. Influence of the honed cutting edge on tool wear and surface integrity in slot milling of 42CrMo4 steel. *Procedia CIRP* **2012**, *1*, 190–195, https://doi.org/10.1016/j.procir.2012.04.033

58. Vel, L.; Demazeau, G.; Etourneau, J. Cubic boron nitride: synthesis, physicochemical properties and applications. *Mater. Sci. Eng. B* **1991**, *10*, 149–164, https://doi.org/10.1016/0921-5107(91)90121-B

59. Kyratsis, P. Computational design and digital manufacturing. *Int. J. Mod. Manuf. Technol.* **2020**, *12*, 82–91

60. González-Lluch, C.; Company, P.; Contero, M.; Camba, J.D.; Plumed, R. A survey on 3D CAD model quality assurance and testing tools. *CAD Comput. Aided Des.* **2017**, *83*, 64–79, https://doi.org/10.1016/j.cad.2016.10.003

61. Tessier, S.; Wang, Y. Ontology-based feature mapping and verification between CAD systems. *Adv. Eng. Informatics* **2013**, *27*, 76–92, https://doi.org/10.1016/j.aei.2012.11.008

62. Dassault Systemes; SOLIDWORKS API Help. Available online: https://help.solidworks.com/2020/English/api/sldworksapiprogguide/Welcome.htm (accessed on 17 July 2020)

63. Davim, J.P.; Figueira, L. Machinability evaluation in hard turning of cold work tool steel (D2) with ceramic tools using statistical techniques. *Mater. Des.* **2007**, *28*, 1186–1191, https://doi.org/10.1016/j.matdes.2006.01.011

64. Aouici, H.; Elbah, M.; Yallese, M.A.; Fnides, B.; Meddour, I.; Benlahmidi, S. Performance comparison of wiper and conventional ceramic inserts in hard turning of AISI 4140 steel: analysis of machining forces and flank wear. *Int. J. Adv. Manuf. Technol.* **2016**, *87*, 2221–2244, https://doi.org/10.1007/s00170-016-8567-7

65. Gaitonde, V.N.; Karnik, S.R.; Figueira, L.; Davim, J.P. Performance comparison of conventional and wiper ceramic inserts in hard turning through artificial neural network modeling. *Int. J. Adv. Manuf. Technol.* **2011**, *52*, 101–114, https://doi.org/10.1007/s00170-010-2714-3

66. Tzotzis, A.; Garcia-Hernandez, C.; Huertas-Talón, J.L.; Kyratsis, P. 3D FE Modelling of Machining Forces during AISI 4140 Hard Turning. *Strojniški Vestn. - J. Mech. Eng.* **2020**, *66*, 467–478, https://doi.org/10.5545/sv-jme.2020.6784

67. Abouridouane, M.; Klocke, F.; Lung, D. Microstructure-based 3D finite element model for micro drilling carbon steels. *Procedia CIRP* **2013**, *8*, 94–99, https://doi.org/10.1016/j.procir.2013.06.071

68. Asad, M.; Mabrouki, T.; Ijaz, H.; Aurangzeb Khan, M.; Saleem, W. On the turning modeling and simulation: 2D and 3D FEM approaches. *Mech. Ind.* **2014**, *15*, 427–434, https://doi.org/10.1051/meca/2014045

69. Arrazola, P.J.; Matsumura, T.; Kortabarria, A.; Garay, A.; Soler, D. Finite element modelling of chip formation process applied to drilling of Ti64 alloy. Proceedings of the 6th International Conference on Leading Edge Manufacturing in 21st Century: LEM 21, **2011**; pp. 1-6, https://doi.org/10.1299/jsmelem.2011.6._3402-1_

70. Gao, X.; Li, H.; Liu, Q.; Zou, P.; Liu, F. Simulation of stainless steel drilling mechanism based on Deform-3D. *Adv. Mater. Res.* **2011**, *160–162*, 1685–1690, https://doi.org/10.4028/www.scientific.net/AMR.160-162.1685

71. Isbilir, O.; Ghassemieh, E. Finite element analysis of drilling of titanium alloy. *Procedia Eng.* **2011**, *10*, 1877–1882, https://doi.org/10.1016/j.proeng.2011.04.312

72. Miller, S.F.; Shih, A.J. Thermo-mechanical finite element modeling of the friction drilling process. *J. Manuf. Sci. Eng. Trans. ASME* **2007**, *129*, 531–538, https://doi.org/10.1115/1.2716719

73. Davim, J.P.; Maranhão, C. Study on plastic strain and plastic strain rate in machining of steel AISI 1020 using FEM analysis. *Mater. Des.* **2009**, *30*, 160–165

74. Belis, T.; Kyratsis, P.; Antoniadis, A. Stress Analysis on Twist Drill Tools Combining CAD based Methodology and Finite Element Analysis. In book Machining: Operations, Technology and Management. **2013**; pp. 31–42, ISBN 978-1-62618-778-8

75. Parida, A.K. Simulation and experimental investigation of drilling of Ti-6Al-4V alloy. *Int. J. Light. Mater. Manuf.* **2018**, *1*, 197–205, https://doi.org/10.1016/j.ijlmm.2018.07.001

76. Nagaraj, M.; Kumar, A.J.P.; Ezilarasan, C.; Betala, R. Finite element modeling in drilling of Nimonic C-263 alloy using deform-3D. *C. - Comput. Model. Eng. Sci.* **2019**, *118*, 679–692, https://doi.org/10.31614/cmes.2019.04924

77. Flachs, J.R.; Salahshoor, M.; Melkote, S.N. Mechanistic models of thrust force and torque in step-drilling of Al7075-T651. *Prod. Eng.* **2014**, *8*, 319–333, https://doi.org/10.1007/s11740-014-0531-5

78. Bahçe, E.; Özdemir, B. Investigation of the burr formation during the drilling of free-form surfaces in al 7075 alloy. *J. Mater. Res. Technol.* **2019**, *8*, 4198–4208, https://doi.org/10.1016/j.jmrt.2019.07.028

79. Kao, J.Y.; Hsu, C.Y.; Tsao, C.C. Experimental study of inverted drilling Al-7075 alloy. *Int. J. Adv. Manuf. Technol.* **2019**, *102*, 3519–3529, https://doi.org/10.1007/s00170-019-03416-8

80. Davim, J.P.; Maranhão, C.; Jackson, M.J.; Cabral, G.; Grácio, J. FEM analysis in high speed machining of aluminium alloy (Al7075-0) using polycrystalline diamond (PCD) and cemented carbide (K10) cutting tools. *Int. J. Adv. Manuf. Technol.* **2008**, *39*, 1093–1100, https://doi.org/10.1007/s00170-007-1299-y

81. Sahu, N.K.; Andhare, A.B. Prediction of residual stress using RSM during turning of Ti–6Al–4V with the 3D FEM assist and experiments. *SN Appl. Sci.* **2019**, *1*, 1–14, https://doi.org/10.1007/s42452-019-0809-5

82. Grigoriev, S.N.; Volosova, M.A.; Gurin, V.D.; Seleznyov, A.Y. Investigation of force parameters acting on a single cutting insert made of ceramics in face milling of hardened steel. *Mech. Ind.* **2015**, *702*, 1–7, https://doi.org/10.1051/meca/2015086

83. Aouici, H.; Elbah, M.; Benkhelladi, A.; Fnides, B.; Boulanouar, L. Comparison on various machinability aspects between mixed and reinforced ceramics when machining hardened steels. *Mech. Ind.* **2019**, *109*, 1-15, https://doi.org/10.1051/meca/2018052

84. Jafarzadeh, E.; Movahhedy, M.R.; Khodaygan, S. Prediction of machining chatter in milling based on dynamic FEM simulations of chip formation. *Adv. Manuf.* **2018**, *6*, 334–344, https://doi.org/10.1007/s40436-018-0228-7

85. MatWeb Material Property Data. Available online: https://www.matweb.com (Accessed on 29 September 2019)

86. DEFORM, version 11.3 (PC); Documentation; Scientific Forming Technologies Corporation: Columbus, OH, USA, **2016**

87. Gardner, J.D.; Dornfeld, D. Finite Element Modeling ofDrilling Using DEFORM; Consortium on Deburring and Edge Finishing. Berkeley University: Berkeley, CA, USA, **2006**

88. Brar, N.S.; Joshi, V.S.; Harris, B.W. Constitutive model constants for Al7075-T651 and Al7075-T6. *AIP Conf. Proc.* **2009**, *1195*, 945–948, https://doi.org/10.1063/1.3295300

89. Cockcroft, M.G.; Latham, D.J. Ductility and the Workability of Metals. *J. Institue Met.* **1968**, *96*, 33–39

90. Agmell, M. *Applied FEM of metal removal and forming*; First edit.; Studentlitteratur: Lund, **2018**; ISBN 978-91-44-12507-7

91. Frifita, Wassila; Ben Salem, Sahbi; Haddad, Abdelkrim; Yallese, Mohamed Athmane Optimization of machining parameters in turning of Inconel 718 Nickel-base super alloy. *Mech. Ind.* **2020**, *21*, 203, https://doi.org/10.1051/meca/2020001

92. Kosaraju, S.; Anne, V.G. Optimal machining conditions for turning Ti-6Al-4V using response surface methodology. *Adv. Manuf.* **2013**, *1*, 329–339, https://doi.org/10.1007/s40436-013-0047-9

93. Kyratsis, P.; Markopoulos, A.; Efkolidis, N.; Maliagkas, V.; Kakoulis, K. Prediction of Thrust Force and Cutting Torque in Drilling Based on the Response Surface Methodology. *Machines* **2018**, *6*, 1-12, https://doi.org/10.3390/machines6020024

94. Asiltürk, I.; Akkuş, H. Determining the effect of cutting parameters on surface roughness in hard turning using the Taguchi method. *Meas. J. Int. Meas. Confed.* **2011**, 44, 1697-1704, https://doi.org/10.1016/j.measurement.2011.07.003

95. Mia, M.; Dhar, N.R. Response surface and neural network based predictive models of cutting temperature in hard turning. *J. Adv. Res.* **2016**, 7, 1035-1044, https://doi.org/10.1016/j.jare.2016.05.004

96. Quiza, R.; Figueira, L.; Davim, J.P. Comparing statistical models and artificial neural networks on predicting the tool wear in hard machining D2 AISI steel. *Int. J. Adv. Manuf. Technol.* **2008**, *37*, 641–648, https://doi.org/10.1007/s00170-007-0999-7

97. Yen, Y.C.; Söhner, J.; Weule, H.; Schmidt, J.; Altan, T. Estimation of tool wear of carbide tool in orthogonal cutting using FEM simulation. *Mach. Sci. Technol.* **2002**, *6*, 467–486, https://doi.org/10.1081/MST-120016256

98. Wan, L.; Wang, D.; Gao, Y. Investigations on the effects of different tool edge geometries in the finite element simulation of machining. *Stroj. Vestnik/Journal Mech. Eng.* **2015**, *61*, 157–166, https://doi.org/10.5545/sv-jme.2014.2051

99. Yameogo, D.; Haddag, B.; Makich, H.; Nouari, M. Prediction of the Cutting Forces and Chip Morphology When Machining the Ti6Al4V Alloy Using a Microstructural Coupled Model. *Procedia CIRP* **2017**, 58, 335-340, https://doi.org/10.1016/j.procir.2017.03.233

100. Agmell, M.; Ahadi, A.; Ståhl, J.E. The link between plasticity parameters and process parameters in orthogonal cutting. *Procedia CIRP* **2013**, *8*, 224–229, https://doi.org/10.1016/j.procir.2013.06.093

101. Arisoy, Y.; Özel, T. Prediction of machining induced microstructure in Ti-6Al-4V alloy using 3-D FE-based simulations: Effects of tool micro-geometry, coating and cutting conditions. *J. Mater. Process. Technol.* **2015**, *220*, 1–26, https://doi.org/10.1016/j.jmatprotec.2014.11.002

102. Vijayaraghavan, V.; Garg, A.; Gao, L.; Vijayaraghavan, R.; Lu, G. A finite element based data analytics approach for modeling turning process of Inconel 718 alloys. *J. Clean. Prod.* **2016**, *137*, 1619–1627, https://doi.org/10.1016/j.jclepro.2016.04.010

103. Lian, Y.S.; Mu, C.L.; Liu, M.; Chen, H.F.; Yao, B. Three-dimensional numerical simulation of soft/hard composite-coated textured tools in dry turning of AISI 1045 steel. *Adv. Manuf.* **2019**, *7*, 133–141, https://doi.org/10.1007/s40436-019-00249-2

104. Magalhães, F.C.; Ventura, C.E.H.; Abrão, A.M.; Denkena, B. Experimental and numerical analysis of hard turning with multi-chamfered cutting edges. *J. Manuf. Process.* **2020**, *49*, 126–134, https://doi.org/10.1016/j.jmapro.2019.11.025

105. Mirghasemi, S.M.; Eivani, A.R.; Seyedein, S.H.; Jafarian, H.R. A comparison between routine vs. normalized Cockcroft-Latham fracture criteria for prediction of fracture during equal channel angular pressing. *Eng. Fract. Mech.* **2018**, *199*, 721–729, https://doi.org/10.1016/j.engfracmech.2018.07.016

106. Astakhov, V.P. *Tribology of metal cutting*; First edit.; Elsevier Ltd: Amsterdam, **2006**; ISBN 0080451497

107. Gaitonde, V.N.; Karnik, S.R.; Figueira, L.; Davim, J.P. Analysis of machinability during hard turning of cold work tool steel (type: AISI D2). *Mater. Manuf. Process.* **2009**, *24*, 1373–1382, https://doi.org/10.1080/10426910902997415

108. Aouici, H.; Bouchelaghem, H.; Yallese, M.A.; Elbah, M. Machinability investigation in hard turning of AISI D3 cold work steel with ceramic tool using response surface methodology. *Int. J. Adv. Manuf. Technol.* **2014**, *73*, 1775–1788, https://doi.org/10.1007/s00170-014-5950-0

109. Lalwani, D.I.; Mehta, N.K.; Jain, P.K. Experimental investigations of cutting parameters influence on cutting forces and surface roughness in finish hard turning of MDN250 steel. *J. Mater. Process. Technol.* **2008**, *206*, 167–179, https://doi.org/10.1016/j.jmatprotec.2007.12.018

110. Mia, M.; Dhar, N.R. Prediction of surface roughness in hard turning under high pressure coolant using Artificial Neural Network. *Meas. J. Int. Meas. Confed.* **2016**, https://doi.org/10.1016/j.measurement.2016.06.048

111. Kıvak, A.; Samtaş, T.; Çay, G. Modelling of Thrust Forces in Drilling of AISI 316 Stainless Steel Using Artificial Neural Network and Multiple Regression Analysis. *Strojniški Vestn. - J. Mech. Eng.* **2012**, *58*, 492–498, https://doi.org/10.5545/sv-jme.2011.297

112. Efkolidis, N.; Hernández, C.G.; Talón, J.L.H.; Kyratsis, P. Modelling and prediction of thrust force and torque in drilling operations of Al7075 using ANN and RSM methodologies. *Strojniški Vestn. - J. Mech. Eng.* **2018**, *64*, 351–361, https://doi.org/10.5545/sv-jme.2017.5188

113. Tzotzis, A.; García-Hernández, C.; Huertas-Talón, J.L.; Kyratsis, P. FEM based mathematical modelling of thrust force during drilling of Al7075-T6. *Mech. Ind.* **2020**, *21*, 1–14, https://doi.org/10.1051/meca/2020046

114. Sayuti, M.; Sarhan, A.A.D.; Salem, F. Novel uses of SiO2 nano-lubrication system in hard turning process of hardened steel AISI4140 for less tool wear, surface roughness and oil consumption. *J. Clean. Prod.* **2014**, *67*, 265–276, https://doi.org/10.1016/j.jclepro.2013.12.052

115. Meddour, I.; Yallese, M.A.; Bensouilah, H.; Khellaf, A.; Elbah, M. Prediction of surface roughness and cutting forces using RSM, ANN, and NSGA-II in finish turning of AISI 4140 hardened steel with mixed ceramic tool. *Int. J. Adv. Manuf. Technol.* **2018**, *97*, 1931–1949, https://doi.org/10.1007/s00170-018-2026-6

116. Meddour, I.; Yallese, M.A.; Khattabi, R.; Elbah, M.; Boulanouar, L. Investigation and modeling of cutting forces and surface roughness when hard turning of AISI 52100 steel with mixed ceramic tool: cutting conditions optimization. *Int. J. Adv. Manuf. Technol.* **2015**, *77*, 1387–1399, https://doi.org/10.1007/s00170-014-6559-z

117. Elkaseer, A.; Abdelaziz, A.; Saber, M.; Nassef, A. FEM-based study of precision hard turning of stainless steel 316L. *Materials* **2019**, *12*, 1–16, https://doi.org/10.3390/ma12162522

118. Saez-de-Buruaga, M.; Soler, D.; Aristimuño, P.X.; Esnaola, J.A.; Arrazola, P.J. Determining tool/chip temperatures from thermography measurements in metal cutting. *Appl. Therm. Eng.* **2018**, *145*, 305–314, https://doi.org/10.1016/j.applthermaleng.2018.09.051

119. Ye, G.G.; Chen, Y.; Xue, S.F.; Dai, L.H. Critical cutting speed for onset of serrated chip flow in high speed machining. *Int. J. Mach. Tools Manuf.* **2014**, *86*, 18–33, https://doi.org/10.1016/j.ijmachtools.2014.06.006

120. Shuang, F.; Chen, X.; Ma, W. Numerical analysis of chip formation mechanisms in orthogonal cutting of Ti6Al4V alloy based on a CEL model. *Int. J. Mater. Form.* **2018**, *11*, 185–198, https://doi.org/10.1007/s12289-017-1341-z

121. Arrazola, P.J.; Özel, T.; Umbrello, D.; Davies, M.; Jawahir, I.S. Recent advances in modelling of metal machining processes. *CIRP Ann. - Manuf. Technol.* **2013**, *62*, 695–718, https://doi.org/10.1016/j.cirp.2013.05.006

122. Lotfi, M.; Jahanbakhsh, M.; Farid, A.A. Wear estimation of ceramic and coated carbide tools in turning of Inconel 625: 3D FE analysis. *Tribol. Int.* **2016**, *99*, 107–116, https://doi.org/10.1016/j.triboint.2016.03.008

123. Vijayaraghavan, A. Automated Drill Design Software; Consortium on Deburring and Edge Finishing. Berkeley University: Berkeley, CA, USA, **2006**

124. Melkote, S.N.; Grzesik, W.; Outeiro, J.; Rech, J.; Schulze, V.; Attia, H.; Arrazola, P.J.; M'Saoubi, R.; Saldana, C. Advances in material and friction data for modelling of metal machining. *CIRP Ann. - Manuf. Technol.* **2017**, *66*, 731–754, https://doi.org/10.1016/j.cirp.2017.05.002

125. Kobayashi, S.; Lee, C. Deformation mechanics and workability in upsetting solid circular cylinders. Proc. North. Am. Metalwork. Res. Conf. **1973**, 1, 185–204

126. Oh, S.I.; Chen, C.C.; Kobayashi, S. Ductile fracture in axisymmetric extrusion and drawing—part 2: workability in extrusion and drawing. *J. Manuf. Sci. Eng.* **1979**, *101*, 36–44, https://doi.org/10.1115/1.3439471

127. Oyane, M.; Sato, T.; Okimoto, K.; Shima, S. Criteria for ductile fracture and their applications. *J. Mech. Work. Technol.* **1980**, *4*, 65–81, https://doi.org/10.1016/0378-3804(80)90006-6

128. Zorev, N.N. Inter-relationship between shear processes occurring along tool face and shear plane in metal cutting. *Int. Res. Prod. Eng.* **1963**, *49*, 143–152

129. Arrazola, P.J.; Meslin, F.; Marya, S. A technique for the identification of friction at tool/chip interface during machining. In Proceedings of the 6th CIRP International Workshop on Modeling of Machining Operations, Hamilton, ON, Canada, **2003**; pp. 1–6

130. Haglund, A.J.; Kishawy, H.A.; Rogers, R.J. An exploration of friction models for the chip – tool interface using an Arbitrary Lagrangian – Eulerian finite element model. *Wear* **2008**, *265*, 452–460, https://doi.org/10.1016/j.wear.2007.11.025

131. Aouici, H.; Yallese, M.A.; Chaoui, K.; Mabrouki, T.; Rigal, J.F. Analysis of surface roughness and cutting force components in hard turning with CBN tool: Prediction model and cutting conditions optimization. *Meas. J. Int. Meas. Confed.* **2012**, *45*, 344–353, https://doi.org/10.1016/j.measurement.2011.11.011

132. Chmielewski, T.; Swiercz, D.O.- Multi-Response Optimization of Electrical Discharge Machining Using the Desirability Function. *Micromachines* **2019**, *10*, 1–25, https://doi.org/10.3390/mi10010072

APPENDIX

10. APPENDIX

10.1. Impact factor of the journals and areas corresponding to the publications included in the Thesis

In this section, the impact factors of the journals included in this Doctoral Thesis and their corresponding areas of research are presented.

Paper title	CAD-based automated design of FEA-ready cutting tools
SCOPUS journal	Journal of Manufacturing and Materials Processing
Areas of research	Materials Processing Manufacturing

Paper title	FEM based mathematical modelling of thrust force during drilling of Al7075-T6
JCR journal	Mechanics & Industry
Impact factor / Quartile	0.874 / Q4
Areas of research	Mechanics Mechanical Engineering

Paper title	3D FE modelling of machining forces during AISI 4140 hard turning
JCR journal	Strojniški vestnik – Journal of Mechanical Engineering
Impact factor / Quartile	1.377 / Q3
Areas of research	Mechanical Engineering

Paper title	Influence of the nose radius on the machining forces induced during AISI-4140 hard turning: A CAD-based and 3D FEM approach
JCR journal	Micromachines
Impact factor / Quartile	2.523 / Q2
Areas of research	Instruments & Instrumentation Nanoscience & Nanotechnology

10.2. Thesis summary and general conclusions in Spanish

La eliminación de material es uno de los procesos de conformación más importantes de la industria. Además, mediante el mecanizado se pueden producir una amplia variedad de productos que van desde una herramienta simple hasta una pieza de avión. Estos hechos significativos junto con la constante evolución por la ingeniería se convirtieron en la base de la presente tesis.

El objetivo principal durante la investigación y el desarrollo en el área de mecanizado basado en FEM, se centra en:

- aumentar la precisión de los modelos FE desarrollados,
- reducir el tiempo de preparación y
- minimizar el trabajo experimental requerido.

Para lograr los estándares altos y garantizar la confiabilidad de los procesos de corte, se deben determinar nuevos métodos de análisis teórico. Además, se requieren nuevos modelos de simulación para cubrir el desarrollo continuo de herramientas de corte. A la luz de estas consideraciones, se llevó a cabo un estudio extenso de la literatura como primer paso hacia una comprensión más profunda de trabajos previos en el campo. A continuación, el procesamiento de los hallazgos reveló ciertos temas que requerían mayor investigación o mejora. Dichos temas incluyen:

- La mejora de la precisión durante el modelado de FE.
- La investigación del efecto de las condiciones críticas de mecanizado sobre varios parámetros como las fuerzas de corte desarrolladas, la morfología de la viruta, así como la tensión y la distribución de la temperatura.
- Y el establecimiento de modelos de predicciones eficientes y fáciles de usar.

Una vez finalizada la revisión bibliográfica, la investigación se dividió en cuatro etapas. La primera etapa está asociada con la mejora de la precisión en el modelado de FE. La segunda trata sobre el modelado FE de operaciones de taladrado y torneado en tres dimensiones, asistido con técnicas basadas en CAD. La tercera etapa está relacionada con la investigación del mecanizado de materiales industriales en condiciones críticas de corte. Finalmente, la última presenta el desarrollo de modelos de predicción con la ayuda de metodologías estadísticas.

1) La mayoría de los investigadores utilizan en sus estudios modelos de herramientas de corte proporcionados por los fabricantes o los diseñan ellos mismos. Sin embargo, en el primer caso, es posible que los resultados de la simulación producidos sean de baja precisión, debido al hecho de que los modelos descargados de la web de un fabricante suelen estar simplificados y, a menudo, pierden características geométricas

críticas. En este último caso, el investigador puede verse obligado a dedicar horas a tareas de diseño repetitivas que pueden resultar frustrantes, especialmente cuando se producen errores de diseño. Para evitar confusiones y centrarse en tareas más creativas, se diseñó y desarrolló una aplicación para el diseño automatizado de herramientas de corte con la ayuda de Application Programming Interface (API) del sistema CAD SolidWorks ™. En esta etapa se emplearon los recursos de programación de SolidWorks ™, combinados con la estrategia de diseño paramétrico para que se pudiera lograr la concepción de la aplicación.

2) Con la finalización de la aplicación, se prepararon varios modelos 3D FE y se generaron las herramientas de corte equivalentes con fines de prueba. Las pruebas de simulación se completaron con éxito y los resultados adquiridos revelaron una mayor correlación con los resultados experimentales correspondientes. Posteriormente, se establecieron modelos de FE similares para taladrado y torneado, de acuerdo con los hallazgos y recomendaciones de trabajos ya publicados, mediante el uso de un software FEA de última generación, llamado DEFORM ™ -3D. Las propiedades de los materiales, la evolución de los daños, la aproximación de la fricción, así como el flujo térmico, se establecieron con respecto al trabajo experimental realizado durante esta investigación, además de los hallazgos publicados por expertos en la materia. Además, se hizo un esfuerzo por simplificar los problemas de mecanizado, empleando varias estrategias bien establecidas, como la configuración asistida por CAD de la interfaz herramienta-pieza de trabajo y la localización del refinamiento de la malla.

3) La tercera etapa de la tesis está directamente vinculada a la anterior. Los resultados de la simulación adquiridos se procesaron con la ayuda de entornos informáticos como Excel ™ y MATLAB®, de modo que los resultados se pueden convertir en conjuntos de datos utilizables. Posteriormente, los datos procesados se visualizaron y compararon directamente con hallazgos equivalentes que están disponibles en la literatura. Esta comparación mostró que los modelos de FE desarrollados estaban de acuerdo con los encontrados en estudios ya publicados. Además, se llevaron a cabo una serie de pruebas experimentales para validar aún más la precisión de los modelos de FE desarrollados. Para realizar con precisión el trabajo experimental, se utilizó un centro de mecanizado CNC junto con el equipo de medición (un dinamómetro). Al mismo tiempo, se realizó una investigación sobre los efectos de la velocidad de corte, el avance, la profundidad de corte y la geometría de la herramienta sobre las fuerzas de corte desarrolladas. En concreto, se estudiaron las fuerzas de empuje generadas durante el taladrado, así como los componentes de mecanizado (fuerzas radiales, tangenciales y de avance) inducidas durante el torneado.

Además, se estudiaron tanto la evolución de la viruta como la morfología con respecto a la operación aplicada, el material, la herramienta y las condiciones de corte.

4) Finalmente, los resultados simulados verificados se utilizaron para el desarrollo de modelos matemáticos que pueden predecir las fuerzas de corte generadas dentro de límites específicos. Los modelos que fueron representados por funciones, pueden generar resultados de alta precisión al instante y sin la necesidad de ningún software especializado. El modelado se realizó utilizando la Metodología de Superficie de Respuesta (RSM) ampliamente utilizada, que además mejoró la visualización de la investigación concluida durante la tercera etapa. Para fortalecer aún más la validez de los modelos estadísticos, se utilizó el Análisis de Varianza (ANOVA). Los resultados del análisis revelaron que los modelos desarrollados son robustos y se pueden utilizar de forma segura con fines de predicción.

El documento titulado “CAD-based automated design of FEA-ready cutting tools” presenta el desarrollo de una aplicación de diseñador con la implementación de la API de SolidWorks ™ implementada con VBA. El propósito de la aplicación desarrollada es generar automáticamente modelos CAD de herramientas de corte que se pueden utilizar con el software FEA. Al finalizar la aplicación, se han realizado con éxito una serie de pruebas de simulación para verificar la funcionalidad de los modelos generados. El resultado de simulación de las fuerzas de mecanizado al obtenido de forma experimental, superando el 90% en la mayoría de los casos.

El documento titulado "FEM based mathematical modelling of thrust force during drilling of Al7075-T6" presenta el desarrollo de un modelo de predicción para las fuerzas generadas durante la perforación de Al7075-T6, con la ayuda de RSM y la implementación de 3D FEA. Se realizó una serie completa de 27 simulaciones 3D bajo diferentes condiciones de corte (velocidad y avance) además de los tres diámetros de herramienta diferentes que se utilizaron. Los resultados simulados se validaron mediante experimentos y la correlación entre los resultados simulados y experimentales superó el 95% en la mayoría de los casos. Después de analizar a fondo el modelo para determinar su precisión (5,9%) y fidelidad de ajuste, se concluye que el modelo desarrollado puede predecir con seguridad las fuerzas de empuje bajo ciertos límites que se discuten en esta investigación. Además, se introdujo la morfología de las virutas producidas durante la perforación de Al7075-T6.

En el trabajo “3D FE modelling of machining forces during AISI 4140 hard turning” se presentó el desarrollo de un modelo 3D FE, así como un modelo de predicción de la principal fuerza de mecanizado inducida durante torneado duro de AISI-4140. Se realizaron una serie de 27 simulaciones 3D bajo diferentes condiciones de velocidad de corte y avance, además de las tres diferentes profundidades de corte. Los resultados numéricos obtenidos fueron validados mediante valores experimentales

que se encuentran disponibles en la literatura y se observó que están en alta concordancia superando el 90% en la mayoría de las situaciones. La precisión (8.8%) y la bondad de ajuste del modelo estadístico, determinan que los modelos desarrollados (FE y estadístico) pueden predecir con fiabilidad las fuerzas de mecanizado resultantes cuando se aplican dentro del alcance de este estudio.

Finalmente, en la publicación "Influence of the nose radius on the machining forces induced during AISI-4140 hard turning: A CAD-based and 3D FEM approach" un modelo 3D FE para el torneado de AISI-4140 como un modelo de predicción de la fuerza de mecanizado resultante, basado en métodos estadísticos. Se utilizó un conjunto de resultados experimentales que están disponibles en la bibliografía para verificar el modelo FE y, en consecuencia, se preparó un diseño completo de experimentos de acuerdo con tres niveles de velocidad de corte, velocidad de avance y radio de la punta de la herramienta. Se realizó una validación adicional del modelo estadístico para garantizar que el modelo pueda predecir con seguridad la fuerza de corte resultante dentro del rango de condiciones encontradas en el presente estudio. Finalmente, se investigó y presentó gráficamente la influencia del radio de la punta en las fuerzas de corte producidas.

10.3. Full texts of the publications included in the Thesis

In this section, the original and full texts of the published scientific articles related to this Doctoral Thesis are presented. In order to protect the copyright, the part of this Thesis that contains non-open access articles cannot be openly published (specifically article with title “FEM based mathematical modelling of thrust force during drilling of Al7075-T6”).

Journal of
Manufacturing and Materials Processing

MDPI

Article

CAD-Based Automated Design of FEA-Ready Cutting Tools

Anastasios Tzotzis [1,*], César García-Hernández [1], José-Luis Huertas-Talón [1] and Panagiotis Kyratsis [2,*]

[1] Department of Design and Manufacturing Engineering, University of Zaragoza, 50018 Zaragoza, Spain; cesarg@unizar.es (C.G.-H.); jhuertas@unizar.es (J.-L.H.-T.)
[2] Department of Product and Systems Design Engineering, University of Western Macedonia, 50100 Kozani, Greece
* Correspondence: atzotzis@unizar.es (A.T.); pkyratsis@uowm.gr (P.K.)

Received: 12 October 2020; Accepted: 30 October 2020; Published: 1 November 2020

Abstract: The resources of modern Finite Element Analysis (FEA) software provide engineers with powerful mechanisms that can be used to investigate numerous machining processes with satisfying results. Nevertheless, the success of a simulation, especially in three dimensions, relies heavily on the accuracy of the cutting tool models that are implemented in the analyses. With this in mind, the present paper presents an application developed via Computer-Aided Design (CAD) programming that enables the automated design of accurate cutting tool models that can be used in 3D turning simulations. The presented application was developed with the aid of the programming resources of a commercially available CAD system. Moreover, the parametric design methodology was employed in order to design the tools according to the appropriate standards. Concluding, a sample tool model was tested by performing a number of machining simulations based on typical cutting parameters. The yielded results were then compared to experimental values of the generated machining force components for validation. The findings of the study prove the functionality of the tool models since a high level of agreement occurred between the acquired numerical results and the experimental ones.

Keywords: CAD-based programming; automated design; API; SolidWorks; FEA; cutting tool; turning insert

1. Introduction

Nowadays, investigations on machining processes can benefit from the implementation of two dimensional or three dimensional Finite Element (FE) modelling. Especially, 3D FE modelling is considered to be a valuable asset during complicated investigations since it provides accurate results and allows the user to fully represent a problem. However, in order to properly carry out 3D simulations and yield acceptable results, it is imperative to define the problem with as much detail as possible. One of the most important aspects during FE model setup is the representation of the cutting tool in three dimensions, so that the full geometry of the tool can be analyzed. In the case of turning, the tool's micro-geometry seems to have a great impact on the generated numerical results. With the advent of more advanced Computer-Aided Design (CAD) systems, it is possible to utilize the Application Programming Interface (API) and the parametric modelling to develop macros, applets or even software tools that can support numerous engineering processes such as the design and manufacturing of machine components, the inspection of manufacturing quality, as well as the integration of CAD, Computer-Aided Manufacturing (CAM) and Computer-Aided Engineering (CAE).

Wu et al. [1] presented an integration of CAD and CAE for the generative design of face gears. This method uses a comprehensive algorithm that calculates the points as an even distribution on the

tooth surface of a gear which can facilitate the stress analysis process during Finite Element Analysis (FEA). Wang et al. [2] studied the prediction of tool deflection of end-mills by integrating CAD, CAE and CAM systems. Using the developed CAD model, authors managed to measure the distributed cutting forces along the tool axis via FE modelling of the cutting process. Bartłomiej [3] described a tool for analyzing the tooth contact and transmission errors of spiral bevel gear sets with tooth flanks. The tool was developed via a CAD system and is used for the analysis of meshing of spiral bevel gears prior to FEA. A number of studies prove that the APIs can be useful to the manufacturing-related area of research also. García-Hernández et al. [4] proposed a method to manufacture elliptical and oval gears using Wire Electro-Discharge Machining (WEDM). Authors presented the mathematical models and simulations based on CAD and CAM systems. Similarly, Tzivelekis et al. [5] proposed a novel approach for automating both the design and manufacturing processes of impeller-type geometries. For this reason, authors developed an application based on API programming of commercially available CAD/CAM software. Oancea and Haba [6] presented a new software tool which allows the user to obtain the manufacturing sequences and cutting data of a manufacturing process and in addition can be used for the simulation setup of these processes. Moreover, the tool was developed with Visual Lisp and is particularly helpful for rotational parts. Dimitriou et al. [7] described an effective simulation of gear hobbing, based on virtual kinematics of CAD models. The algorithm was developed and embedded in a commercial CAD software by using the modern programming resources available. According to authors, the resulting 3D data allow the prediction of the cutting forces, tool stresses, and wear development that can be used for the optimization of the gear hobbing process. With similar strategies that were implemented with a modern CAD system, Kyratsis et al. [8] developed DRILL3D application which can estimate the thrust forces that develop on both the main edges and chisel edge of a drill simultaneously. Thus, any equivalent lab work may be skipped. In addition to the automated design, CAD-based automated planning of manufacturing processes is a possibility [9–13], as well as the automation and enhancement of the assembly processes of engineering parts by taking advantage of the programming resources that modern CAD systems have to offer. Typical examples in this area involve the automated assembly process of large mechanical systems based on characteristics and features, as well as the extraction of the assembly sequences via CAD models for assembly planning [14–17].

The benefits and the possibilities that derive from the use of the APIs of modern CAD systems are vast. Engineers can increase their productivity and focus on more critical aspects of a project instead of spending time on repetitive and frustrating tasks. One such task is the design of cutting tools that can be implemented in FEA projects, especially when multiple geometric parameters are involved. Vijayaraghavan and Dornfeld [18] developed algorithms and a graphical interface that were used to design a complete application based on CAD programming. The aforementioned application deals with the automated drill modelling that can be implemented in commercial FEA software. Similarly, Li et al. [19] proposed the optimization method of critical parameters of solid end mills, based on 3D FE simulations, providing a design system for end mills. In light of these considerations, the present paper describes a CAD-based application that can be used to generate CAD models of standardized turning inserts. The application was developed with the aid of the SolidWorks™ API and the Visual Basic for Applications (VBA) programming language. Furthermore, the proposed design methodology complies with the parametric-based structure of the used CAD environment. The tools that are designed by the described application are solid, consistent models including the full geometry and can be easily converted to FE-ready file formats. Finally, a set of 3D simulations was carried out by utilizing the FEA software DEFORM™-3D to verify the functionality of the generated models and investigate their performance.

2. Materials and Methods

2.1. Description of Turning Inserts

The principal geometric parameters of the modern turning inserts can be found in the product catalogues of most manufacturers. Furthermore, ISO 13399 provides a schema for cutting tools

description including turning inserts. Despite the fact that modern cutting tools are standardized, some details such as the combinations of chamfer width and chamfer angle that relate to the turning inserts still differ from manufacturer to manufacturer. This means that a great number of possible tool variations is available. Figure 1 illustrates three commonly-used turning inserts that are used during machining of industry-standard materials such as hardened steel, cast iron and aluminum alloys: the insert of square shape with designation number SNGA120412S01525 (Figure 1a), the 80° rhombic CNGA120408T01020 (Figure 1b) and the 55° rhombic DNGA150404S01020 (Figure 1c), respectively. The symbol IC represents the inscribed diameter, RE is the corner radius, S denotes the thickness, L is the theoretical cutting edge length and finally LE is the cutting edge effective length.

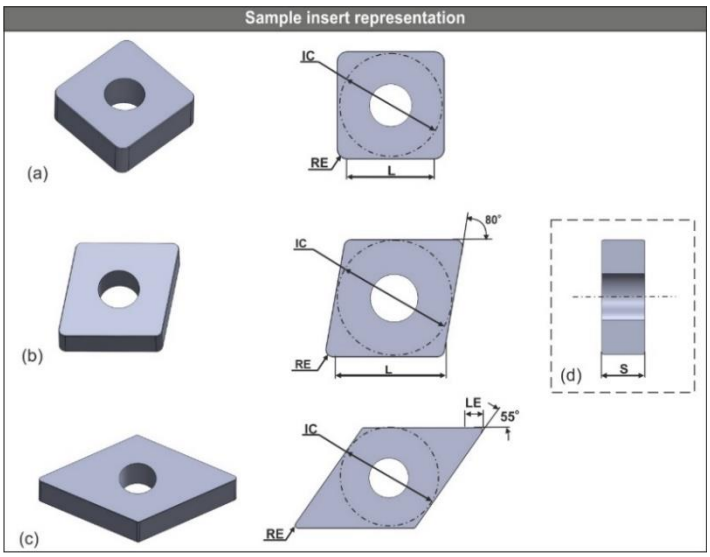

Figure 1. Basic geometric parameters of the SNGA120412S01525 (**a**), the CNGA120408T01020 (**b**) and the DNGA150404S01020 (**c**) inserts, along with their common sectioned view (**d**).

Nevertheless, these are not the only parameters that define the full geometry of a turning insert. Figure 2 depicts a standardized 80° rhombic insert with its micro-geometry which comprises the cutting edge type, the chamfer angle and the chamfer width. In addition to the corner radius, the aforementioned parameters are crucial because they greatly affect the cutting forces during machining [20–23]. Moreover, according to Denkena et al. [24] the cutting edge micro-geometry affects the tool life significantly due to changes in the characteristic tool wear behavior.

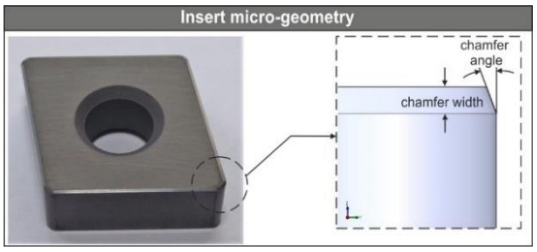

Figure 2. The micro-geometry of a typical 80° diamond-shaped insert.

Modern turning inserts are manufactured in such a way that they can withstand extreme forces and temperatures. To meet these criteria, most inserts are coated via Chemical Vapour Deposition (CVD) or Physical Vapour Deposition (PVD). Most common coatings are the Titanium Nitride (TiN), the Titanium Carbide (TiC) and the Aluminium Oxide (Al_2O_3). Moreover, the commonly used material for the manufacturing of inserts is the Cubic Boron Nitride (CBN) which is the hardest material in the world, second to diamond [25].

2.2. Design of the User Interface

The embedded toolbox of the SolidWorks™ API was used to design the user interface. The idea was to design a simple interface with easy parameter selection and visually conveyed information about the geometric aspects of the inserts. It is possible to generate a wide variety of tools since the user can change every available design parameter. In order to keep the code simple and to avoid developing multiple large modules, a few insert shapes and some special options were skipped from the present study. In addition, no input was provided for the tolerance class, which refers to the manufacturing tolerance of the tool's dimensions and does not affect the designed CAD model, since any dimension of the CAD model is represented exactly as it is designed. The third digit in the standardized coding of inserts denotes the tolerance class. For example, in the CNGA120408 tool, the "G" digit corresponds to a tolerance class of ±0.025 for both the nose height and the inscribed circle, and ± 0.13 for the thickness. Figure 3 illustrates the main tab of the application's user interface along with the code keys that correspond to the standardized design parameters such as shape, length, thickness, nose radius, clearance angle, micro-geometry and clamping system. Nine combo-boxes were used to facilitate the selection procedure. Each combo-box contains a variety of options according to its function. For example, the combo-box entitled "Shape" defines the shape of the insert and contains seven choices as dictated by the detail in Figure 3: five versions of the diamond-shaped with a corner angle of 80°, 55°, 75°, 86° and 35°, respectively; a triangular-shaped; and finally a square. This combo-box, along with the combo-box entitled "Length (L)" determine the shape, the corner angle and the size of the insert, which are the most basic geometric aspects. Specifically, the "Length (L)" combo-box contains ten choices that correspond to the inscribed circle diameter in mm. For the selection of the appropriate variables, the user may consult the tabs entitled "Code Key-1", "Code Key-2" and "Code Key-3" (see Figure 3) correspondingly to acquire the necessary explanations of the input parameters. On top of that, the main tab includes a schematic with the critical dimensions that further visualizes the parameter input process. Finally, a text-box was included so that the user can choose the folder where the generated models can be saved both in native format (SLDPRT) and in STL. With the command button entitled "Design Insert" the design process may begin and the desired model can be generated within seconds. Additionally, a non-editable text-box was included with the title "Insert Code Output", in order to display the designation number of the generated tool for reference purposes.

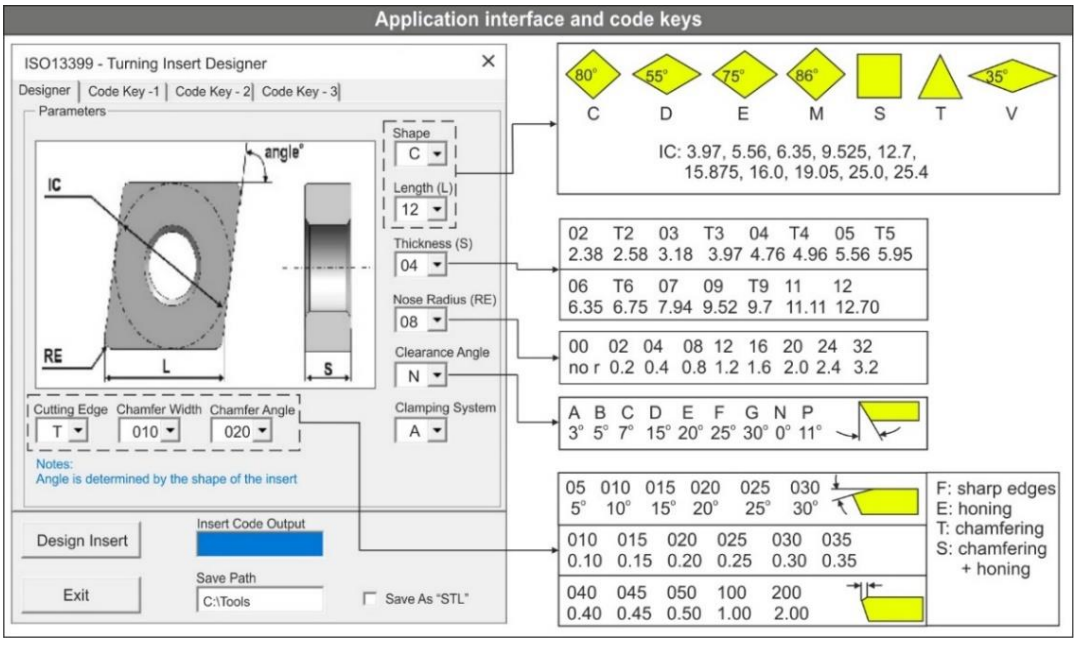

Figure 3. The application's interface and the corresponding code keys.

2.3. Modelling Procedure of Turning Cutting Tools

The development of the presented application was performed via the API of SolidWorks™. In addition, the programming language implemented is VBA which derives from Microsoft™ Visual-Basic™ 6. Due to the fact that SolidWorks™ uses a feature-based parametric methodology during 3D modelling, the workflow of the application's code follows similar principals. According to Figure 4, the declaration of the necessary variables is the first step that is performed when the "Design Insert" button is pressed. These variables correspond to each of the geometric aspects that were presented in Figure 3 such as the shape, the inscribed circle, the corner angle and the corner radius. Next, the declared variables are linked to the input and output controls (i.e., combo-boxes) of the interface to secure that the design process can initialize without errors. Additionally, all the input controls are populated with a pre-defined set of choices according to the standardized design framework. Even though it is relatively simple to alter the code in such a way that an option to generate customized inserts can also become available, it is not of great significance. However, the application allows the user to input custom values for the parameters that relate to the cutting edge, since some variations exist between different manufacturers. To do so, three simple text-boxes were included to enable insertion of custom values. Additionally, the text-boxes were locked so that only reasonable values could be inputted to prevent variable-based errors during the design process. For the employment of the shape according to the user selection, the "Select … Case" statement was used. This statement provides a more convenient way of condition checking, compared to the "If-Then-Else" statement, especially when a large number of conditions are available. With the declaration of the variables, a new part document is created and activated so that new sketches can be inserted. The used methods for the aforementioned actions are the "ActiveDoc" and "NewDocument", respectively. Subsequently, the front plane is selected, and a new sketch is activated. The selection of the sketch plane is always standard, based on the default coordinate system that most FEA software share. Then, the design process of the insert's contour is carried out according to the selected design scheme. The design process includes the sketch of the inscribed circle ("CreateCircleByRadius" method) and the sketch of the contour lines ("CreateLine" method), and finally the application of both the dimensions ("AddDimension2" method) and the geometric relations ("SketchAddConstraints" method) that fully define the contour. Later, the base solid model is produced according to the selected thickness and the clearance angle. For this action, the "FeatureExtrusion2" method is used. In order to acquire the complete solid model, micro-geometry is applied: the corner radii are created with the "FeatureFillet3" method, and the cutting edge is formed by using both the "InsertFeatureChamfer" and the "FeatureFillet3" methods depending on whether the selected edge type requires honing, chamfering or both. Because these methods require the automatic selection of the corresponding topology (i.e., edge), a "For" loop initiates that is responsible for traversing all available topology objects of the solid model that relate to the fillet and chamfer features. In particular, the code locates and recognizes all faces and edges of the solid model; next, it changes the default ID of each one of the objects to a pre-defined tag that comprises a prefix, such as "Edge" and a numerical suffix. This means that if a model contains fifteen edges they will be renamed "Edge" plus a number from one to fifteen. Lastly, all new IDs are stored to an array so that they can be accessed by the program at any time. The automated topology selection is an indispensable part of similar applications [26]. Last but not least, the center hole is created according to the selected clamping system. This feature does not play an important role during the FE analysis, rather it is used for more accurate representation of the cutting tool in a CAD-based layout of the turning process that includes a tool-holder. Upon finalizing the generated CAD model, the last step is the storage of the model to file formats that are used for FE analyses (i.e., "STL"), as well as to "SLDPRT" format that is the SolidWorks™ native format for part documents.

To ensure that no discrepancies will occur after the data translation, the highest possible level of resolution was set during the model conversion (angle tolerance of 0.5° and deviation tolerance of 0.0009968 mm), leading to finer tessellation as well as to greater accuracy. Moreover, to keep the file size at a reasonable level (less than 500 kB on average), the Binary model output was chosen.

Even though the generated STL models proved to be robust and consistent since they were flawlessly imported to the FEA software, their consistency was verified with a free-to-use mesh processing system, namely MeshLab. The models were checked for gaps, holes, non-manifolds, intersecting geometry and other faults. As expected, the models were found to be error-free. This result is enhanced by the fact that morphologic errors [27] are caused mainly due to structural heterogeneity [28], which would probably create errors during the translation of a model from one proprietary format to another, but not in this case.

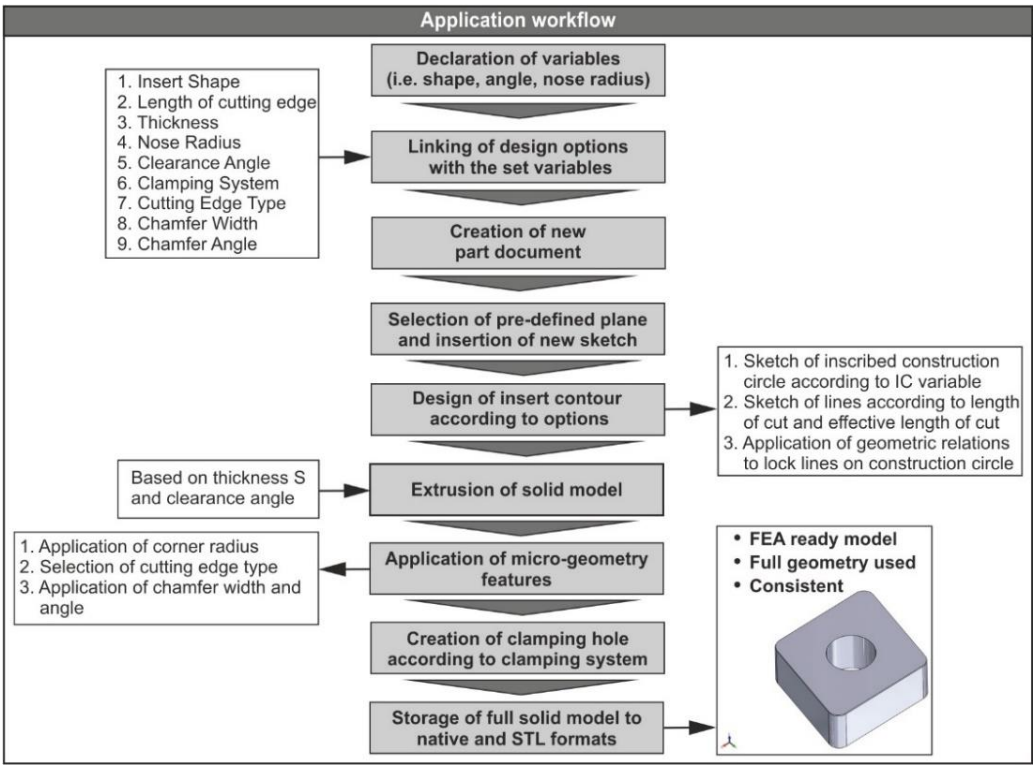

Figure 4. The application's workflow.

Tables 1 and 2 include the most basic API methods that were implemented during the development of the presented application, along with their functionality and return value. Most of these methods require a number of parameters to be set in order to function properly. The way of implementing each of the API methods can be found in the online help of SolidWorks™ API [29].

Table 1. API methods used for the contour creation.

Method	Functionality	Return Value
ActiveDoc	Connects to the currently active document	Model document
NewDocument	Creates a new document using the specified template	Newly created document
InsertSketch	Inserts a new sketch in the current part or assembly document	–
CreateCircleByRadius2	Creates a circle based on a center point and a specified radius	Newly created circle
CreateConstructionGeometry	Sets selected sketch segments to be construction geometry instead of sketch geometry	–
AddDimension2	Creates a display dimension at the specified location for selected entities	Newly created dimension
CreateLine	Creates a sketch line in the currently active 2D or 3D sketch	Sketch segment for the line
SketchAddConstraints	Adds the specified constraint to the selected entities	–
FeatureExtrusion3	Creates an extruded feature	IFeature

Table 2. API methods used for the topology selection.

Method	Functionality	Return Value
GetBodies2	Gets the bodies in the active part	Array of bodies
GetFaces	Gets all the faces on the body	Array of faces on the body
GetEdges	Get the edges bounding the selected face	Array of edges
SetEntityName	Sets the name of the entity	True/false
GetEntityByName	Gets an entity (face, edge, vertex) by name	Entity
Select4	Selects an entity and marks it	True/false
FeatureFillet3	Creates a fillet feature for selected edges and control point references	IFeature
InsertFeatureChamfer	Inserts a chamfer	Pointer to the IFeature object
FeatureCut4	Creates a cut extrude feature	Cut extrude feature
SaveAs	Saves the active document to the specified name in the specified format	True/false

The following examples describe the implementation of some API methods used in the presented application. The "CreateCircleByRadius" method that is used to design the inscribed circle, is syntaxed as follows: "value = instance.CreateCircleByRadius(XC, YC, ZC, Radius)". In addition, the appropriate variables are declared, in order for the method to function properly. The variables XC, YC and ZC represent the center of the circle, whereas Radius is the value of the circle's radius. Furthermore, the variable instance represents the ISketchManager interface that provides access to sketch-creation routines. Lastly, the variable value denotes the sketch segment. Similarly, the "CreateLine" method requires this syntax: "value = instance.CreateLine(X1, Y1, Z1, X2, Y2, Z2)". The variables are all the same except the X1, Y1, Z1, X2, Y2 and Z2 that represent the coordinates of the line start point and the coordinates of the line end point, respectively. To obtain the bodies of a part, the "GetBodies2" method is used in this manner: "value = instance.GetBodies2(BodyType, BVisibleOnly)". In this case, the variable instance represents the IPartDoc interface that provides access to functions that perform operations on parts in part documents. The variable BodyType defines the type of body, whereas the BVisibleOnly defines which bodies will be included depending on their visibility. Finally, the variable value is an object. The last example shows the syntax of the "GetEdges" method: "value = instance.GetEdges()", the variable value is an object and the variable instance denotes the IFace2 interface that allows access to the underlying edge, loop of edges and other data of a body.

Even though the modelling procedure of the turning inserts is rather simple compared to the one of drills, it is still critical that a manufacturing-oriented modelling strategy is followed so that the generated models are error-free. First of all, the design sequence applied, so that the model tree remains simple no matter the design parameters, plus, the geometric constraints are always locked. This way, the generated models are free of semantic errors [27]. The simple model tree is achieved by creating a base feature that resembles the contour of the tool and then adding the rest of the design features on top of the base, instead of creating a cubic solid and then trying to remove material. On the other hand, the minimum use of constraints, in addition to the application of the appropriate type of constraint, ensures that the sketch is fully-defined at all times. Hence, the relationship between the designed objects, which derives from the design intent, allows for an automated propagation of any design change to the objects. Figure 5 illustrates the aforementioned modelling technique applied to a standardized type of inserts (CNGA). Specifically, Figure 5a depicts the initial step of the design process. At first, the front plane of the part document is selected because it is important to define a coordinate system that will serve through the FE analysis [22]. Hence, the Z-axis must be parallel to the tangential force vector, the Y-axis must be parallel to the radial force vector and finally, the X-axis must be parallel to the feed force vector. Next, a sketch of a construction circle is inserted with diameter equal to the IC variable value. The IC variable represents the diameter of the inscribed circle of the insert (see Figure 1). This circle is determined by both the type of the insert (shape) and the length of cutting edge. However, not all cutting length values are available for all types of inserts during

standardized design process. For example, the cutting length of the diamond-shaped insert (type C) can be designed in six sizes: 6.35, 9.525, 12.7, 15.875, 19.05 and 25.0 mm, respectively.

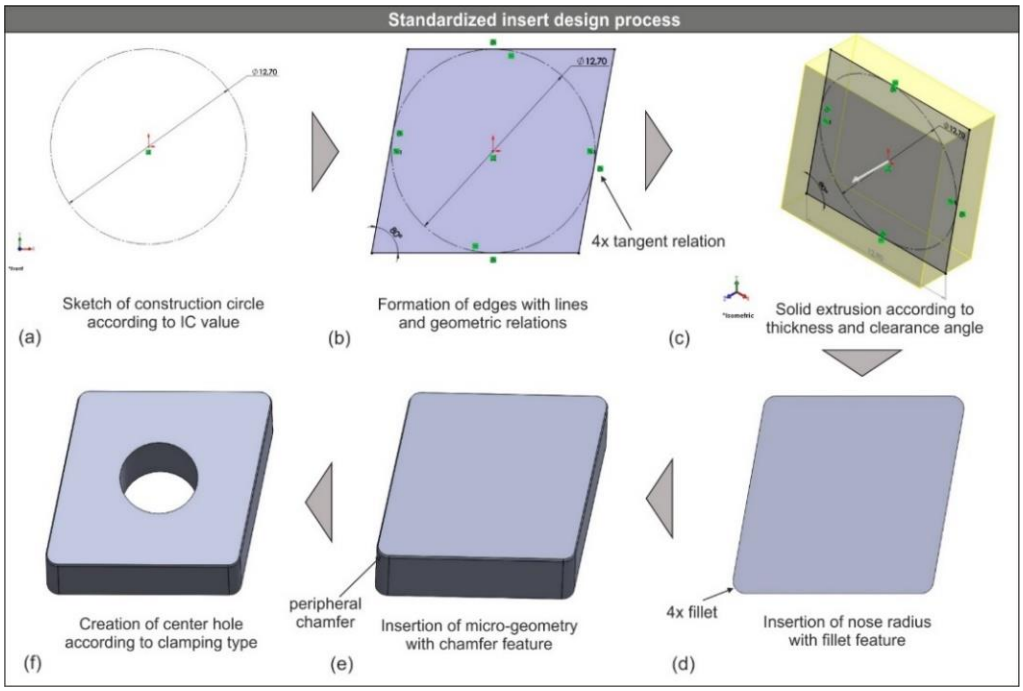

Figure 5. The design workflow for the CNGA-family inserts: (**a**) the construction circle, (**b**) the contour, (**c**) the extrusion, (**d**) the corner radius, (**e**) the micro-geometry and (**f**) the clamping hole.

Figure 5b depicts the next step during the design process which is the insertion of an appropriate number of line sketches (four for this case) that form the selected shape of the tool. Then, the equivalent number of tangent geometric relations is applied between the sketched lines and the construction circle. Moreover, the corner angle is applied based on the corresponding variable value (80° for the diamond-shaped inserts). Because of the used design method and due to the fact that the sketched lines form a closed contour, it is ensured that the upcoming solid model will be consistent. In fact, the formed contour is always a tangential quadrilateral, except for the cases of square and triangle, with varying edge length determined by Equation (1).

$$x = \frac{2r}{\sin \alpha} \tag{1}$$

where x is the length of the edge, r denotes the inradius and α is the corner angle. With the closed contour, the solid model is created based on the selected thickness and cutting edge (Figure 5c). In this case, thickness is equal to 4.76 mm and cutting edge equal to zero. Consequently, the corner radius is applied (Figure 5d) to all cutting points of the insert according to the selected value. The full cutting geometry of the insert is completed with the design of the cutting edge (Figure 5e). The cutting edge is formed according to the selected cutting edge type, chamfer width and chamfer edge (see Figure 3). The final step in the design process is the creation of the center hole (Figure 5f) that is used for the clamping of the insert to the tool-holder. This feature, however, does not affect the FE model setup.

Just before the initiation of the sketch design process, a simple algorithm (Figure 6) performs a check on the shape so that the angles and geometric relations can be applied accordingly. In the case of a square insert, the algorithm skips the tangential quadrilateral shape and uses a center rectangle instead, whereas in the case of a triangular insert, it uses a polygon sketch with three edges so that the triangle can be formed. For the first case, the diagonal q must be determined, while for the latter just the inradius.

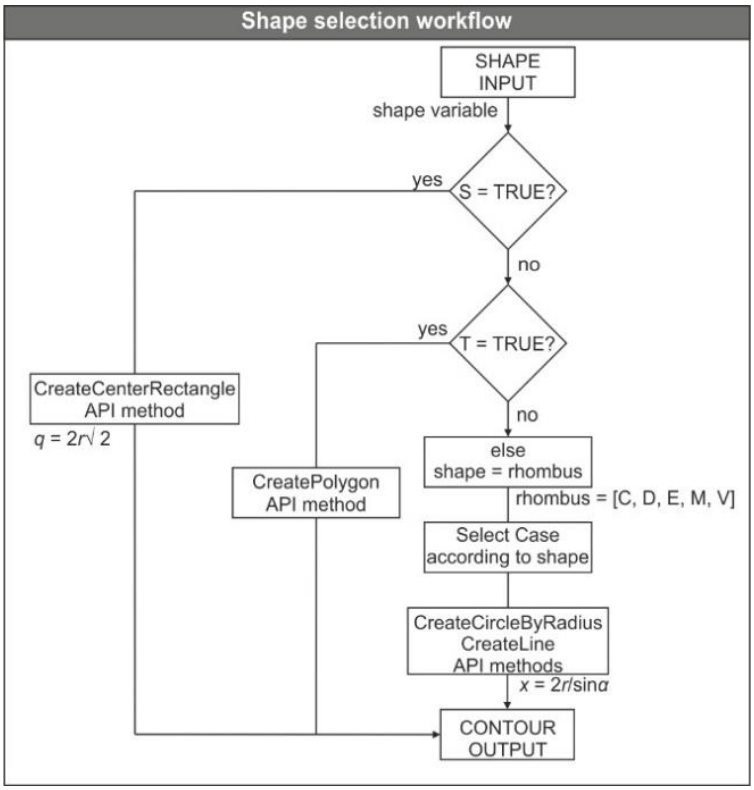

Figure 6. The shape selector algorithm flowchart.

3. Results and Discussion

3.1. Testing of the Generated Cutting Tool Models

In order to validate the functionality of the generated models, an FE model was set and nine 3D turning simulations were carried out. Because the verification of the generated models is a time-consuming process, the test setup was prepared according to widely-used parameters and settings. The selected cutting tool, material and cutting conditions, have already been successfully studied [30–32] and thus, were chosen for this study. The test framework is shown in Figure 7. A sample generated cutting tool with its full geometry (Figure 7a) was saved in STL file format and then imported to DEFORM™-3D ver. 12 for the development of the FE model. It was modelled as rigid and meshed with approximately 50,000 tetrahedral elements. On the other hand, the mesh size of the workpiece varied according to the value of feed. The size of the minimum element was fixed to 25% of the feed for all tests [33]. Additionally, the selected workpiece material is AISI-4140 steel. During the validation tests, the tool used is the CNGA120408 (corner radius of 0.8 mm) and the cutting conditions applied are the produced combinations of the three levels of cutting speed V_c (80, 115 and 150 m/min) and feed f (0.08, 0.11 and 0.14 mm/rev) at depth of cut ap = 0.30 mm. Regarding the cutting angles used, the lead angle is 75° and both the rake and inclination angles are negative with a value of −6°. The simulation tests yielded relatively accurate results both for the cutting forces and the chip formation since the level of convergence for all simulation tests was adequate, considering that most of the FE model parameters such as the material properties, the flow stress constants and the friction coefficients were kept to their default values. Figure 7b illustrates three sample force versus time diagrams at the specified conditions (V_c = 150 m/min, f = 0.14 mm/rev) proving that cutting forces reached the steady state as expected. Furthermore, Figure 7c presents the results for the resultant machining force of the aforementioned test compared to the equivalent experimental one demonstrating an increased level of correlation. The simulated results were compared to experimental values for the same cutting conditions, in order to further examine the validity of the generated CAD models.

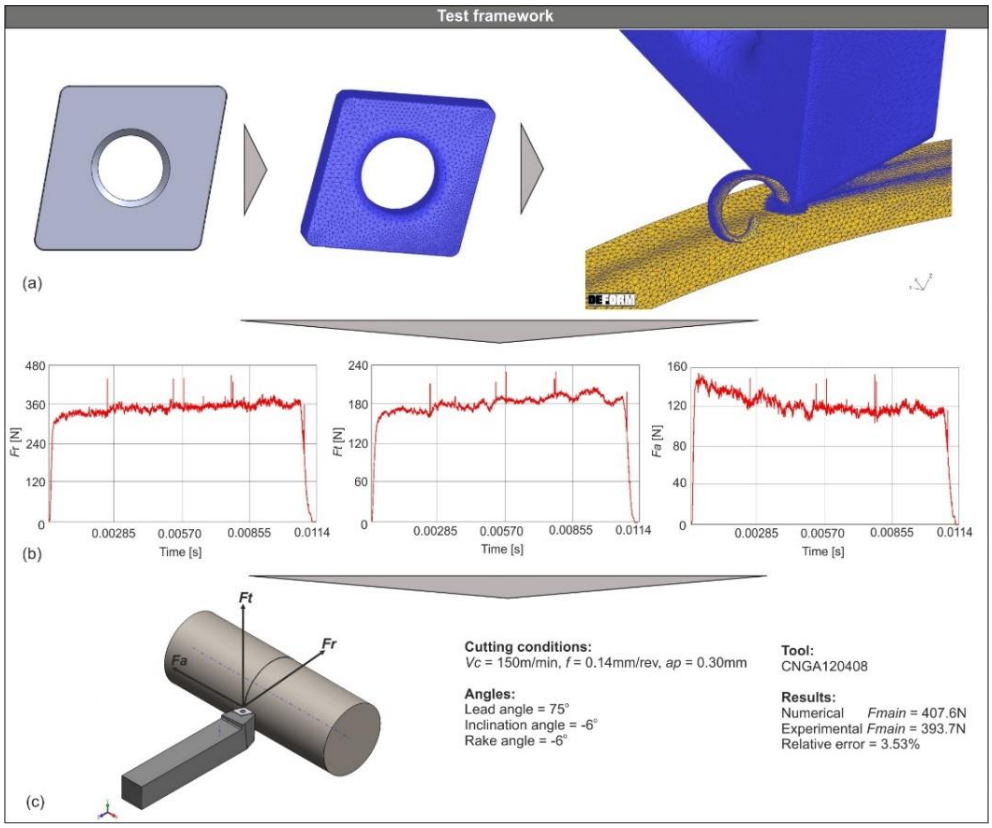

Figure 7. The test framework including: (**a**) the Finite Element (FE) model setup, (**b**) the force diagrams and (**c**) the results.

The complete model setup is shown in Figure 8a. The workpiece was designed in such a way that it resembles a fraction of the cylindrical bar. A more dense mesh with a size ratio of 7:1 was applied to the section of the workpiece where the cutting process takes place. Figure 8b illustrates the analysis domain. An effort was made to keep it as simplified as possible. Additionally, to better approximate the contact interface between the tool and the workpiece, the mesh on the tool was refined locally at the cutting tip by applying a ratio of 4:1 [33], as illustrated in Figure 8c.

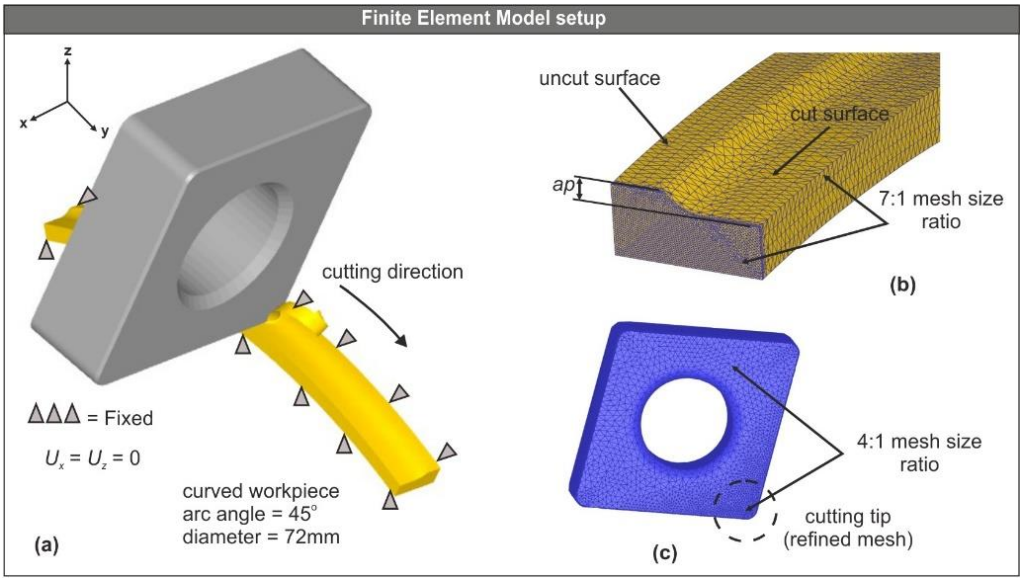

Figure 8. The model setup (**a**), the analysis domain (**b**) and the meshed tool (**c**).

The velocity of the nodes in X and Z axis was set to zero by fixing the workpiece, as shown in Figure 8a. In contrast, the displacement of the tool was allowed by following the trajectory dictated by the cutting direction. Additionally, the boundary conditions for the heat exchange with the environment were applied to all surfaces of the workpiece. The default values of heat transfer coefficient for both convection and conduction were used, as provided by DEFORM™-3D. Hence, the heat transfer coefficient via convection was set to 0.02 N/(s × mm × °C) for dry cutting and via conduction was set to 45 N/(s × mm × °C).

To simulate the friction situation at the tool–workpiece interface, Coulomb's law [33] was used. During machining, the interaction between the bodies of both the tool and the workpiece is a complex problem due to the very high contact pressures that develop. In this case, Coulomb's friction model was selected for its simplicity and because it provides a good approximation of the generated friction forces induced at the sliding zone, which constitutes the main area of interest in machining simulations.

3.2. Comparison of the Obtained Results

Table 3 contains the results of the nine numerical tests compared to the equivalent experimental ones. The experimental values were obtained from the literature [32]. The turning experiments were carried out with the aid of a universal lathe type SN 40C and the tool-holder with ISO designation number PCBNR2525M12. The chemical composition of the AISI-4140 steel in wt% is as follows: C 0.43, Mn 0.79, Si 0.24, S 0.024, Cu 0.025, Al 0.029, Ti 0.004, Nb 0.001, Ni 0.022, Cr 1.10, Mo 0.19, Va 0.005, Sn 0.002 and Fe in balance. Additionally, the chemical composition of the used tool with ISO designation number CNGA120408 (ceramic) is 70% Al_2O_3 and 30% TiC. According to Table 2, all nine tests yielded good results when compared to the experimental ones. However, it is reasonable that in an FE model some discrepancies might occur. In the present study, this is notable mostly in the tangential component where the Mean Absolute Percentage Error (MAPE) is close to 20% in some cases. Despite this fact, the comparison between the numerical and the experimental results of the calculated resultant turning force is in high accordance in most tests. This is proved by an MAPE below 10% for eight out of nine tests and an average MAPE of approximately 5.6%. The high level of agreement in the case of the resultant force is due to the fact that the radial force component is the main contributor to the calculated resultant machining force and at the same time displays a good level of agreement between the numerical and the experimental results.

Table 3. Comparison between experimental and numerical values for the machining components.

	Cutting Conditions			F_r [N]		F_t [N]		F_a [N]	
Std Order	V_c [m/min]	f [mm/rev]	ap [mm]	Exp.	FE Model	Exp.	FE Model	Exp.	FE Model
1	80	0.08	0.30	251.0	284.2	125.1	156.8	114.1	115.7
2	80	0.11	0.30	281.6	302.1	152.1	185.9	126.6	123.4
3	80	0.14	0.30	319.0	339.6	200.2	205.7	144.0	125.6
4	115	0.08	0.30	244.3	269.4	125.3	145.5	118.4	112.1
5	115	0.11	0.30	287.9	295.3	150.5	176.8	134.0	120.5
6	115	0.14	0.30	297.6	324.2	179.9	202.9	133.6	120.8
7	150	0.08	0.30	258.4	251.7	116.1	132.7	116.6	105.9
8	150	0.11	0.30	281.4	291.5	152.5	169.9	125.5	114.5
9	150	0.14	0.30	323.0	337.0	176.1	199.3	140.2	113.2

The below charts (Figure 9) were plotted to visualize all three machining force components and the resultant force. In addition, it is possible to compare the mean values of the produced cutting force components graphically. In particular, Figure 9a depicts the results for the radial force, Figure 9b for the tangential force, Figure 9c for the feed force and lastly Figure 9d for the calculated resultant force. By observing the below charts, it is concluded that the generated CAD model played a major role in the convergence of the results, despite the fact that a few discrepancies exist (mostly in the tangential and the feed force).

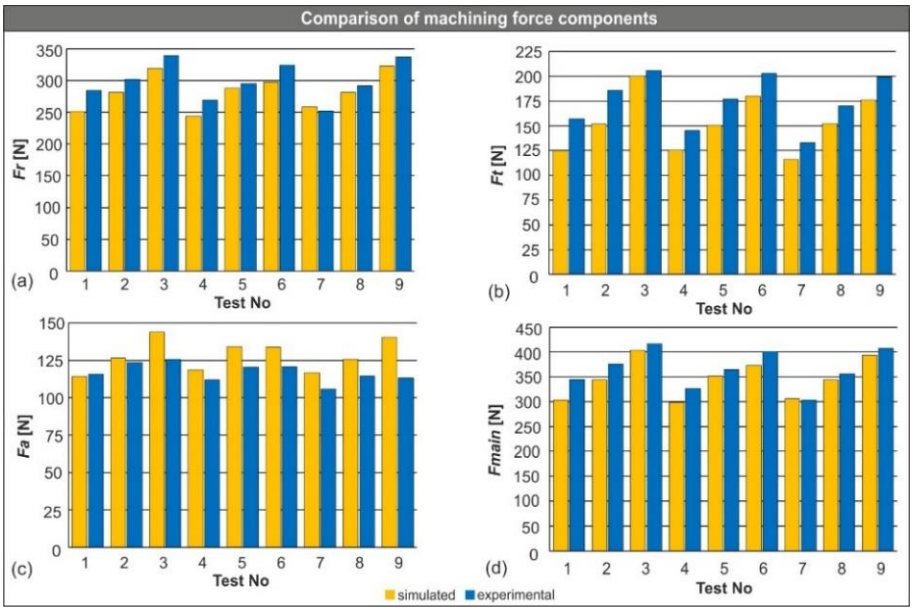

Figure 9. Simulated versus experimental machining force components: (**a**) the radial force, (**b**) the tangential force, (**c**) the feed force and (**d**) the resultant machining force.

4. Conclusions

In the present paper, the development of a designer application with the implementation of the SolidWorks™ API under VBA coding has been presented. The purpose of the developed application is to automatically generate CAD models of cutting tools that can be used with FEA software. Upon finalizing the application, a number of simulation tests have been successfully performed to verify the functionality of the generated models.

In general, the CAD-based programming can be used to automate almost all typical design tasks, hence enhancing the design process of products and systems. Moreover, by implementing the programming tools of modern CAD systems, it is possible to develop simple applets, macros and complete applications.

As the complexity of the under study product or system increases so does the value of the developed tools, further increasing the productivity of the engineers. The presented application can become the basis for developing downstream applications by integrating FEA-based capabilities related to estimation of cutting forces and tool wear, which in general can lead to cutting condition optimization. Finally, it is safe to state the following conclusions with respect to the acquired results:

- The generated cutting tool was successfully imported to DEFORM™-3D and meshed with the maximum available number of elements.
- All the performed simulations were successfully completed within a reasonable amount of time.
- The performance of the under study cutting tool model was high, since the yielded results for the machining forces were on par with the experimental ones.
- Finally, the simulated resultant of the machining forces was in high agreement with the experimental one exceeding 90% in most cases.

Author Contributions: Conceptualization, A.T. and P.K.; methodology, A.T., C.G.-H., J.-L.H.-T. and P.K.; software, A.T.; validation, A.T.; formal analysis, A.T.; investigation, A.T.; resources, P.K.; data curation, C.G.-H., J.-L.H.-T. and P.K.; writing—original draft preparation, A.T.; writing—review and editing, A.T., C.G.-H., J.-L.H.-T. and P.K.; visualization, A.T.; supervision, C.G.-H., J.-L.H.-T. and P.K.; project administration, P.K.; funding acquisition, P.K. All authors have read and agreed to the published version of the manuscript.

Funding: This research received no external funding.

Conflicts of Interest: The authors declare no conflict of interest.

References

1. Wu, Y.; Zhou, Y.; Zhou, Z.; Tang, J.; Ouyang, H. An advanced CAD/CAE integration method for the generative design of face gears. *Adv. Eng. Softw.* **2018**, *126*, 90–99. [CrossRef]
2. Wang, L.; Chen, Z.C. A new CAD/CAM/CAE integration approach to predicting tool deflection of end mills. *Int. J. Adv. Manuf. Technol.* **2014**, *72*, 1677–1686. [CrossRef]
3. Bartłomiej, S. Method of spiral bevel gear tooth contact analysis performed in CAD environment. *Aircr. Eng. Aerosp. Technol.* **2013**, *85*, 467–474. [CrossRef]
4. Garcia-Hernandez, C.; Marín, R.; Talón, J.; Efkolidis, N.; Kyratsis, P. WEDM manufacturing method for noncircular gears using CAD/CAM software. *Strojniški Vestn.-J. Mech. Eng.* **2016**, *62*, 137–144. [CrossRef]
5. Tzivelekis, C.; Yiotis, L.; Fountas, N.A.; Krimpenis, A. Parametrically automated 3D design and manufacturing for spiral-type free-form models in an interactive CAD/CAM environment. *Int. J. Interact. Des. Manuf.* **2015**, *11*, 223–232. [CrossRef]
6. Oancea, G.; Haba, S.-A. Software Tool Used in CAPP/CAM Systems for Rotational Parts. *Sci. Bull. Ser. C Fascicle Mech. Tribol. Mach. Manuf. Technol.* **2016**, *30*, 75–78.
7. Dimitriou, V.; Vidakis, N.; Antoniadis, A. Advanced computer aided design simulation of gear hobbing by means of three-dimensional kinematics modeling. *J. Manuf. Sci. Eng. Trans. ASME* **2007**, *129*, 911–918. [CrossRef]
8. Kyratsis, P.; Bilalis, N.; Antoniadis, A. CAD-based simulations and design of experiments for determining thrust force in drilling operations. *Comput. Des.* **2011**, *43*, 1879–1890. [CrossRef]
9. Ong, S.K.; Nec, A.Y.C. Automating set-up planning in machining operations. *J. Mater. Process. Technol.* **1997**, *63*, 151–156. [CrossRef]
10. Harik, R.F.; Derigent, W.J.E.; Ris, G. Computer aided process planning in aircraft manufacturing. *Comput. Aided. Des. Appl.* **2008**, *5*, 953–962. [CrossRef]
11. Deb, S.; Parra-castillo, J.R.; Ghosh, K. An Integrated and Intelligent Computer-Aided Process Planning Methodology for Machined Rotationally Symmetrical Parts. *Int. J. Adv. Manuf. Syst.* **2011**, *13*, 1–26.
12. Kyratsis, P.; Tzotzis, A.; Tzetzis, D.; Sapidis, N. Pneumatic cylinder design using cad-based programming. *Acad. J. Manuf. Eng.* **2018**, *16*, 107–113.
13. Kyratsis, P.; Tapoglou, N.; Bilalis, N.; Antoniadis, A. Thrust force prediction of twist drill tools using a 3D CAD system application programming interface. *Int. J. Mach. Mach. Mater.* **2011**, *10*, 18–33. [CrossRef]
14. Tzotzis, A.; Garcia-Hernandez, C.; Huertas-Talon, J.-L.; Tzetzis, D.; Kyratsis, P. Engineering applications using CAD based application programming interface. *MATEC Web Conf.* **2017**, *94*, 1–7. [CrossRef]
15. Sapidis, N.; Chatziparasidis, I. Framework to automate mechanical-system design using multiple product-models and assembly feature technology. *Int. J. Prod. Lifecycle Manag.* **2017**, *10*, 124–150. [CrossRef]
16. Du, B.; Wang, X.; Feng, Y.; Yu, D.; Xu, G. Intelligent Assembly Technology Based on Standard Parts Feature of CATIA. *Mod. Appl. Sci.* **2014**, *8*, 49–55. [CrossRef]
17. Roberto, V.; Osorio-Gómez, G. Assembly planning with automated retrieval of assembly sequences from CAD model information. *Assem. Autom.* **2012**, *32*, 347–360. [CrossRef]
18. Vijayaraghavan, A.; Dornfeld, D.A. Automated Drill Modeling for Drilling Process Simulation. *J. Comput. Inf. Sci. Eng.* **2007**, *7*, 276–282. [CrossRef]
19. Li, A.; Zhao, J.; Pei, Z.; Zhu, N. Simulation-based solid carbide end mill design and geometry optimization. *Int. J. Adv. Manuf. Technol.* **2014**, *71*, 1889–1900. [CrossRef]
20. Meyer, R.; Köhler, J.; Denkena, B. Influence of the tool corner radius on the tool wear and process forces during hard turning. *Int. J. Adv. Manuf. Technol.* **2012**, *58*, 933–940. [CrossRef]
21. Karpat, Y.; Ozel, T. Process simulations for 3D turning using uniform and variable microgeometry PCBN tools. *Int. J. Mach. Mach. Mater.* **2008**, *4*, 26–38. [CrossRef]
22. Tzotzis, A.; Garcia-Hernandez, C.; Talón, J.L.H.; Kyratsis, P. Influence of the Nose Radius on the Machining Forces Induced during AISI-4140 Hard Turning: A CAD-Based and 3D FEM Approach. *Micromachines* **2020**, *11*, 798. [CrossRef]
23. Denkena, B.; Lucas, A.; Bassett, E. Effects of the cutting edge microgeometry on tool wear and its thermomechanical load. *CIRP Ann.-Manuf. Technol.* **2011**, *60*, 73–76. [CrossRef]
24. Denkena, B.; Koehler, J.; Rehe, M. Influence of the honed cutting edge on tool wear and surface integrity in slot milling of 42CrMo4 steel. *CIRP Ann.-Manuf. Technol.* **2012**, *1*, 190–195. [CrossRef]

25. Vel, L.; Demazeau, G.; Etourneau, J. Cubic boron nitride: Synthesis, physicochemical properties and applications. *Mater. Sci. Eng. B* **1991**, *10*, 149–164. [CrossRef]
26. Kyratsis, P. Computational design and digital manufacturing. *Int. J. Mod. Manuf. Technol.* **2020**, *12*, 82–91.
27. González-Lluch, C.; Company, P.; Contero, M.; Camba, J.D.; Plumed, R. A survey on 3D CAD model quality assurance and testing tools. *CAD Comput. Aided Des.* **2017**, *83*, 64–79. [CrossRef]
28. Tessier, S.; Wang, Y. Ontology-based feature mapping and verification between CAD systems. *Adv. Eng. Inform.* **2013**, *27*, 76–92. [CrossRef]
29. Dassault Systemes; SOLIDWORKS API Help. Available online: https://help.solidworks.com/2020/English/api/sldworksapiprogguide/Welcome.htm (accessed on 17 July 2020).
30. Gaitonde, V.; Karnik, S.; Figueira, L.; Davim, P. Performance comparison of conventional and wiper ceramic inserts in hard turning through artificial neural network modeling. *Int. J. Adv. Manuf. Technol.* **2011**, *52*, 101–114. [CrossRef]
31. Figueira, L.; Davim, P. Machinability evaluation in hard turning of cold work tool steel (D2) with ceramic tools using statistical techniques. *Mater. Des.* **2007**, *28*, 1186–1191. [CrossRef]
32. Aouici, H.; Elbah, M.; Yallese, M.A.; Fnides, B.; Meddour, I.; Benlahmidi, S. Performance comparison of wiper and conventional ceramic inserts in hard turning of AISI 4140 steel: Analysis of machining forces and flank wear. *Int. J. Adv. Manuf. Technol.* **2016**, *87*, 2221–2244. [CrossRef]
33. Tzotzis, A.; Garcia-Hernandez, C.; Talón, J.L.H.; Kyratsis, P. 3D FE Modelling of Machining Forces during AISI 4140 Hard Turning. *Strojniški Vestn.-J. Mech. Eng.* **2020**, *66*, 467–478. [CrossRef]

Mechanics & Industry **21**, 415 (2020)
© AFM, EDP Sciences 2020
https://doi.org/10.1051/meca/2020046

Mechanics & Industry

Available online at:
www.mechanics-industry.org

Regular Article

FEM based mathematical modelling of thrust force during drilling of Al7075-T6

Anastasios Tzotzis[1,*], César García-Hernández[1], José-Luis Huertas-Talón[1], and Panagiotis Kyratsis[2]

[1] Department of Design and Manufacturing Engineering, University of Zaragoza, 50018, Zaragoza, Spain
[2] Department of Industrial Design Engineering, University of Western Macedonia, 50100, Kila Kozani, Greece

Received: 12 March 2020 / Accepted: 28 May 2020

Abstract. Like most machining processes, drilling is affected by many parameters such as the tool diameter, the cutting speed and feed. The current research investigates the possibility of developing a finite element modelling based prediction model for the generated thrust force during drilling of Al7075-T6 with solid carbide tools. A total of 27 drilling experiments were carried out in order to examine the interaction between three key parameters and their effect on thrust force. In addition, simulations of the experiments were realized with the use of DEFORM3D™ software in order to obtain the necessary numerical data. Finally, a comparison was made between the experimental and the numerical results to verify that reliable modelling is feasible. The mathematical model was acquired with the use of response surface methodology and the verification of the adequacy of the model was performed through an analysis of variance. The majority of the simulations yielded results in agreement with the experimental results at around 95% and the derived model offered an accuracy of 5.9%.

Keywords: al7075 drilling / finite element method / deform3d / response surface methodology / thrust force

1 Introduction

As technology advances, manufacturing industries tend to design products with parts that require machining with the highest standards available and at the lowest possible cost. Such optimization during the manufacturing stage of a product, require a lot of early planning and thorough research, which lead to increase development time and cost. In order to reduce these factors during the development stage, the implementation of finite element method (FEM) and similar techniques are widely applied.

An early example of FEM in machining is the work completed by Klamecki [1] that was published in 1973. Since then, as the computational resources advance, more and more researchers took advantage of FEM in machining. Drilling is one of the most used metal cutting operations, which can benefit from the use of FEM. Due to the fact that drilling is an intricate process, with complex tool and chip geometries, it was included to commercial FEM software in the last few years. Guo and Dornfeld [2] developed a nonlinear 3D finite element model which considers thermal, elastic and plastic parameters to study burr formation in drilling of 304L stainless steel. Similarly, 3D FEM of chip formation during drilling is another topic that is widely studied [3–6]. Chip formation progress, chip thickness, burr height and surface roughness are some of the parameters that are discussed. FEM is used for prediction purposes as well. 3D models and computational methods are used for measuring and predicting important parameters such as thrust force and torque [4,7,8]. In addition to the aforementioned parameters, temperature of the tool-workpiece interface is another important property that can be measured with the aid of finite element (FE) models, in order to develop methods for tool wear prediction and cutting parameters optimization [9,10].

Since metal materials are very common in manufacturing industries, such as aerospatial, automotive and machinery, most studies related in these areas focus on materials like titanium alloys, aluminium alloys and carbon steels. Davim and Maranhão [11] utilized a finite element analysis for examination purposes. Plastic strain and plastic strain rate during the process of machining AISI 1020 steel were the main assessed parameters during their study. Additionally, authors validated the process using experimental values from literature and verified that simulated results were close to the ones found in literature. Belis et al. [12] used the finite element method for the determination of the developed stresses along the cutting edges of a twist drill, while the cutting forces have been

* e-mail: atzotzis@unizar.es

already calculated using a CAD based approach. Lotfi et al. [13] investigated the drilling process of AISI1045 and developed a 3D FE model for prediction purposes of the produced heat and flank wear on the drill by using a modified Usui model.

Parida [14] investigated the evaluation of several properties like torque, thrust force, strain and temperature on drills, with the aid of 3D FE modelling for Ti-6Al-4V alloy. In addition, he experimentally validated the results. Similarly, Nagaraj et al. [15] used DEFORM3D™ to develop a FE based model to simulate the thrust force, stress, strain and temperature at the tool's cutting edge when drilling Nimonic C-263 alloy. Dou et al. [16] worked on a new constitutive model, to improve a prediction model for thrust force and torque. Moreover, authors tested the efficiency of their constitutive model by using finite element modelling for simulating the drilling process of SiCp/Al6063.

Especially for drilling of aluminum alloys of the 7000 series, even though many studies exist in the literature that present experimental analysis of Al7075 drilling [17–19], the number of studies that implement FE models is still low. A study on the thermal and mechanical behavior of aluminum alloys (Al 7075-0) during machining with PCD (polycrystalline diamond) and cemented carbide tools was made by Davim et al. [20]. Additionally, they compared the performances of both tools. Similarly, Ucun [21] emphasized with his study the advantages that arise when 3D modelling the metal cutting processes and examined the performances of the twist and 3-flute drills. The performance of the drills was assessed focusing on the generated thrust force, torque and stress. Sahu and Andhare [22] presented in their work a prediction model using response surface methodology (RSM) for determining the residual stress that occurs when turning Ti-6Al-4V, assisted by 3D FEM and experiments.

With these in mind, the present paper contributes towards both an experimental and a 3D numerical study on drilling of Al7075-T6, with three solid carbide drills of the same geometry, but with different diameters. Investigation of cutting force parameters is a topic with constant research interest [23,24]. The aim of this study is to develop a mathematical model, with the employment of RSM and 3D FEM, for prediction purposes of the thrust force induced during Al7075-T6 drilling under commonly used conditions. This way, time and resources-consuming experimental work can be minimized, as well as the computationally intensive simulation runs. In order to do so, an investigation of the generated thrust forces and chip formation evolution was realized. Additionally, a comparison between the numerical and the experimental results was performed for validation. The proposed methodology ensures that the prediction model can be verified in a cost and time effective way, so that it can be used within the limits of this study.

2 Material and methods

2.1 Experimental setup

During the experimental stage of this research, three drills of the same grade (Kennametal KC7325) were used with

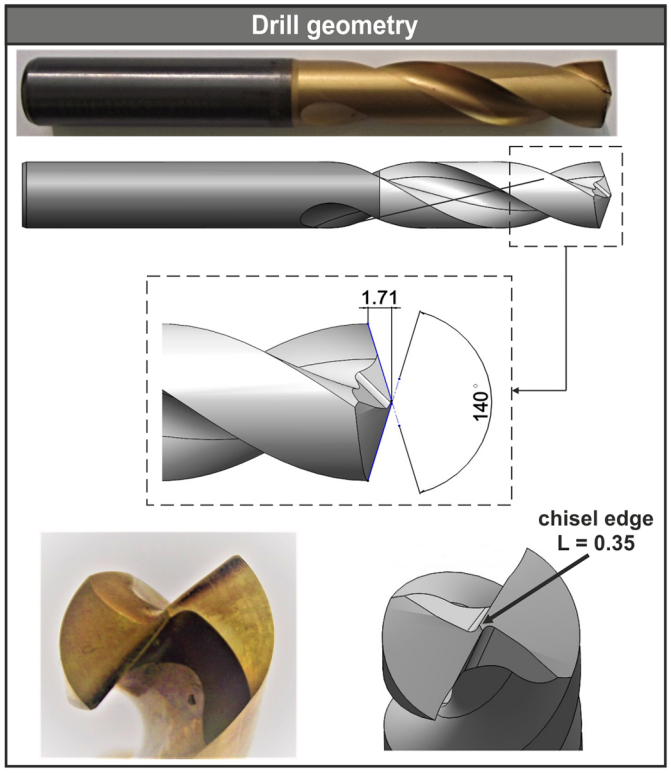

Fig. 1. Geometry parameters for the B041A10000CPG drill.

8 mm, 10 mm and 12 mm diameter respectively. These drills (B041A series) are solid carbide that consist of 10% cobalt and have double coating; a multilayer of TiN/TiAlN with 3.5 micron thickness and an outer layer of TiN with 15 micron thickness. Figure 1 illustrates the CAD model of the Ø10 drill compared to the physical model. The catalogue numbers for reference of the used drills are: B041A08000CPG (8 mm), B041A10000CPG (10 mm) and B041A12000CPG (12 mm).

A plate of Al7075-T6 with dimensions 150 mm × 130 mm × 15 mm served as the workpiece for the experiments that were carried out at three different cutting speeds (50 m/min, 100 m/min, 150 m/min) and three different feeds (0.15 mm/rev, 0.2 mm/rev, 0.25 mm/rev). The cutting conditions were chosen according to the manufacturer's recommended limits for Al7075-T6 alloy with respect to the drill diameters. Thus, the combination of the aforementioned parameters and the three drills used, led to a setup of 27 experiments (each tool was used to drill nine holes on the plate). In order to accurately perform the drilling tests, a HAAS (California, USA) VF1 CNC machining center and a BT40 cone were used. Additionally, a Kistler (Winterthur, Switzerland) type 9257B 3-component dynamometer was used for measuring the developed thrust forces. A typical measuring chain with data acquisition system (Kistler type 5697A1 with 16-bit resolution) was used in order to capture the measurements and store them, with the aid of a three-channel charge amplifier and DynoWare type 2825A software, to a desktop computer for analysis. The sampling rate was set to approximately 10 kHz, based on the specifications of the

Table 1. Basic mechanical and thermal properties of Al7075-T6 [25,26].

Mechanical properties					
Young's modulus	Density	Poisson's ratio	Hardness (HV)	Yield strength	Tensile strength
71.7 GPa	2810 kg/m^3	0.33	175	503 MPa	572 MPa
Thermal properties					
Heat capacity		Thermal expansion		Thermal conductivity	
0.960 J/g°C		22 μm/m°C		41.7 W/mK	

data acquisition system and the mean value of the measured thrust forces was used as the acquired data for easier comparison with the simulated values (see Sect. 3.1). Semi-synthetic oil-based coolant (KOOLrite 2270) was delivered to the tool throughout the whole experimental process. Table 1 contains the most important mechanical and thermal properties of the workpiece material and Figure 2 illustrates the workflow of this project. First stage includes the experimental setup (CNC and dynamometer setup), the execution of the designed experiments and the acquisition of the thrust force. Second stage includes the setup of the numerical model and the implementation of the simulations. Finally, third stage involves the analysis and validation of the results.

2.2 3D finite element model setup

2.2.1 Workpiece model setup

The 3D cutting simulations of the drilling processes were performed in the same order than the experiments with DEFORM3D^{TM} ver. 11.3 simulation software, on a desktop computer with dual-core CPU, 16GB RAM and SSD technology hard drive. In some of the simulations, the drill bit was allowed to fully penetrate the workpiece so that the full thrust force diagram can be acquired. However, most of the simulations were stopped when the thrust forces achieved steady state to save time. Depending on the time step applied, steady state occurred at a different point for each simulation. The time step was calculated based on the drill diameter and cutting speed used in each simulation. For example, the 10 mm tool at 100 m/min cutting speed rotates with 3183 min^{-1} or 53.05 s^{-1} according to equation (1), hence the tool completes one full rotation in 0.0189 s. Finally, the time step can be determined by dividing the previously calculated time value with the number of steps of the tool per revolution (360 steps), thus the time step for this case is 5.24×10^{-5} s. As a rule of thumb, the number of steps during drilling simulation should be close to 360 so that the tool can rotate one degree per step [27]. This way, it is ensured that the simulation will complete in a reasonable time period and, at the same time, yield acceptable results. It is possible though, to use an increased number of steps for an improved accuracy at the cost of very long simulation times

$$V_c = \frac{\pi D N}{1000}, \quad (1)$$

Where V_c is the cutting speed in m/min, D is the tool diameter in mm and N is the spindle speed in min^{-1}.

The workpiece was modelled to be circular and thin, with a thickness of about the radius of the drill for simplification purposes, but not thinner as it would be difficult for the workpiece to support the force of the drill and separation of the nodes would occur in a non-chip forming process according to Gardner and Dornfeld [28]. In addition, a center drill spot with regard to the drill point angle was made on the workpiece (Fig. 3a).

The purpose of this design is to significantly improve the simulation time, firstly because the removal of the material on the spot by the tool can be skipped and secondly because one revolution of the drill can take many time steps [28]. Three similar workpieces were used, but with different sizes, according to each drill geometry (see Tab. 1). All three workpieces were modelled as plastic with a mesh of tetrahedral elements that have four nodes. Depending on the dimensions of each workpiece, the mesh size varied. However, the minimum element size of the mesh was always 50% of the feed, based on the suggestion of DEFORM3D^{TM} [27]. A finer mesh was localized at the center of the workpiece in order to improve the fidelity at the contact interface. A ratio of 10:1 was used with this mesh, so that the total number of elements could be optimized. Even though a finer mesh usually yields more accurate results, the simulation time increases dramatically. Figure 3b depicts the tool-workpiece setup for the Ø10 mm drill.

2.2.2 Drill model setup

To model the drills, only their tips were used for simplification purposes. The drill tips were modelled as rigid with a mesh of approximately 20,000 to 30,000 tetrahedral elements. Since the area of the drill that is in contact with the workpiece is at the tip, a finer mesh with a 4:1 ratio was used at the tip (Fig. 3d). An adaptive remeshing technique was implemented so that more elements were generated in areas where there were large strains and strain rates, high temperatures and large deformations. The default strain and strain rate gradient were used. This technique further improves the simulation time and the produced chip geometry.

2.2.3 Boundary conditions and movement controls

The side of the workpiece was fixed in all positions (X, Y and Z), so that the velocity of all nodes is zero (Fig. 3c).

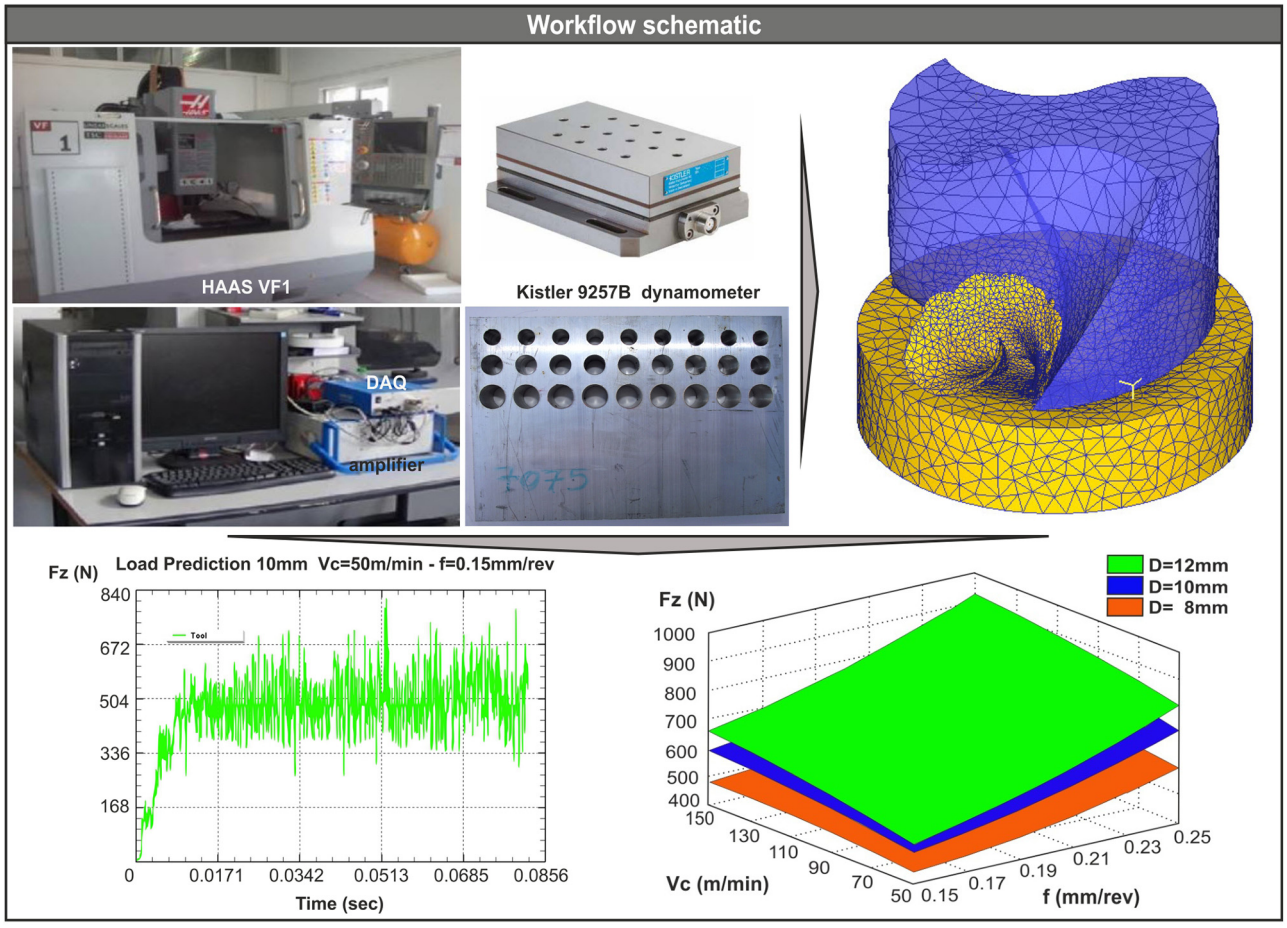

Fig. 2. The workflow of the drilling experiments and simulations.

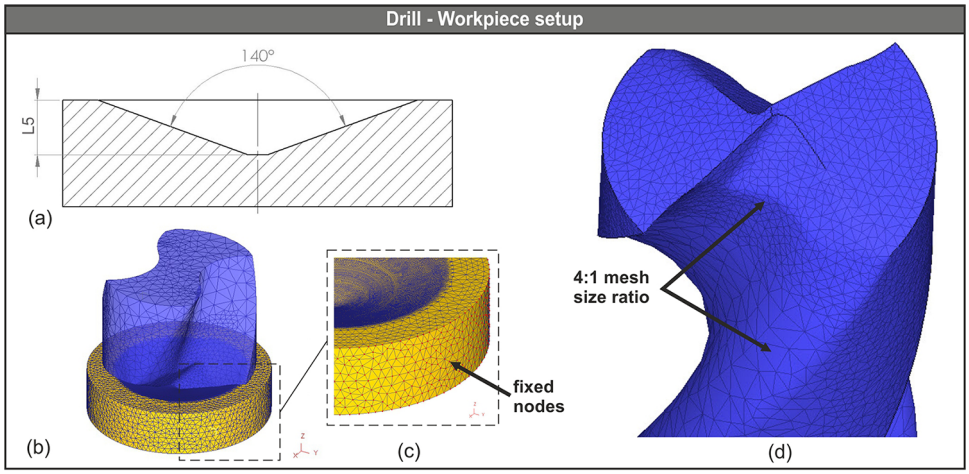

Fig. 3. Workpiece section (a), tool-workpiece setup (b), workpiece nodes (c) and drill model mesh (d).

In addition, heat exchange (with the environment) boundary conditions were assigned to all surfaces of the workpiece. To better approximate heat transfer through convection between the workpiece and the drill surface, a convection coefficient for oil based coolant with value of $2\,\mathrm{N/(s \times mm \times °C)}$ was used [27], whereas for heat transfer through conduction in the tool-workpiece interface, a coefficient with the default value of $45\,\mathrm{N/(s \times mm \times °C)}$ was used. Finally, a master-slave contact relationship was set for the workpiece and the generated chips, because it is most likely that the chips touch the workpiece. To define the rotational and translational movement of the drill, it was set to rotate around Z axis and move along Z axis (feed towards −Z) accordingly.

Table 2. Johnson − Cook constitutive model constants for Al7075-T6 [29].

A (MPa)	B (MPa)	C	n	m	T_0 (°C)	T_m (°C)
546	678	0.024	0.71	1.56	20	635

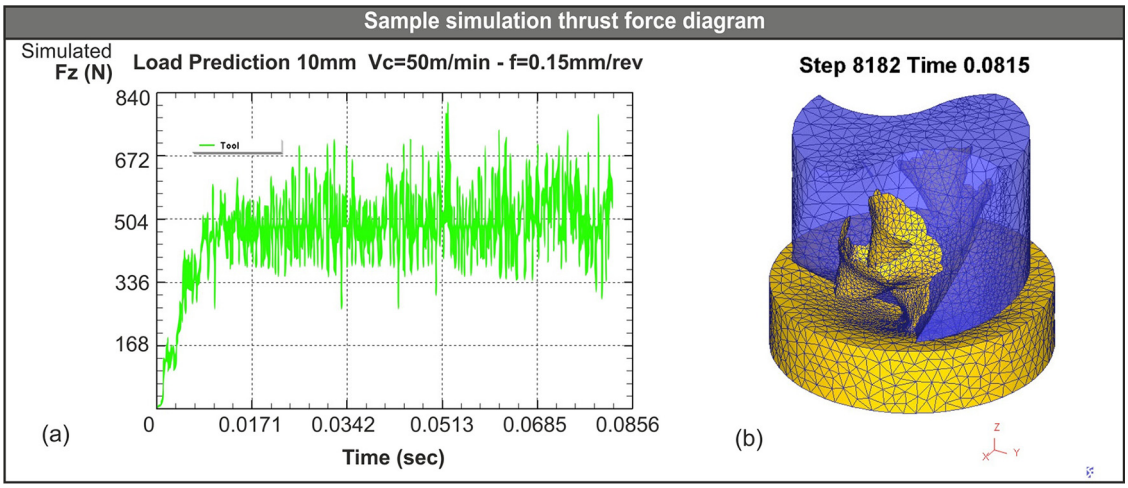

Fig. 4. The simulated thrust forces versus time diagram for the 10 mm tool (a) and the formed chip (b).

2.2.4 Material model setup

In order to simulate the flow stress of the Al7075-T6 alloy during the drilling operation, the generalized Johnson-Cook model was used. This model is widely used for stress analysis in deformations involving high strain, strain rate and temperature, and can be described by equation (2).

$$\sigma = (A + B\varepsilon^n)\left(1 + C\ln\frac{\dot{\varepsilon}}{\dot{\varepsilon}_0}\right)\left[1 - \left(\frac{T - T_0}{T_m - T_0}\right)^m\right], \quad (2)$$

where A is the initial yield stress, B is the strain hardening modulus, C is the strain rate dependence coefficient, ε is the plastic strain, n is the strain hardening exponent, m is the thermal softening coefficient, $\dot{\varepsilon}$ is the plastic strain rate, $\dot{\varepsilon}_0$ is the reference plastic strain rate, T is the reference temperature, T_0 is the bulk temperature and T_m is the melting temperature of the workpiece material. Since this constitutive model is commonly used for numerical studies of metal machining, the material constants of this model have been determined for a wide variety of workpiece materials. The material constants for Al7075-T6 alloy are presented in Table 2. In this study, a reference strain rate of 1/s was used.

The damage model used during this study was the normalized Cockcroft and Latham model in order to simulate the occurrence of material separation, when certain criteria are met. This model is defined as a function of the maximum principal stress σ' normalized with the effective stress $\overline{\sigma}$ [30].

As for the interaction between tool − chip interface, a hybrid model [21] was used for friction. To approximate the frictional stresses around the tool tip, where a more sticking behavior occurs, the shear friction model was used which can be determined by equation (3). This relationship is based on the assumption that the frictional stress is proportional to the shear strength of the weaker of the two materials that are in contact [31].

$$\tau_f = k_\tau \frac{\sigma_y}{\sqrt{3}} \quad (3)$$

where τ_f is the frictional stress, k_τ is a constant and σ_y is the uniaxial yield stress for the material.

In order to describe friction across the sliding zone, the Coulomb's friction model was used. This model is a good estimation for the sliding friction region and uses a constant μ, such that the frictional stress is determined by equation (4).

$$\tau_f = \mu\sigma_n \quad (4)$$

where τ_f is the frictional stress, μ is the friction coefficient and σ_n is the normal stress along the tool − chip interface.

For this study, the constant shear friction coefficient is $m = 0.7$ and the constant Coulomb friction coefficient is $\mu = 0.6$.

3 Results and discussion

3.1 Thrust force evaluation

Figure 4a illustrates a sample thrust force diagram obtained from the simulated drilling process of Al7075-T6 with a solid carbide 10 mm tool at cutting speed of $V_c = 50$ m/min and feed rate of $f = 0.15$ mm/rev. This diagram indicates that the produced thrust force increases

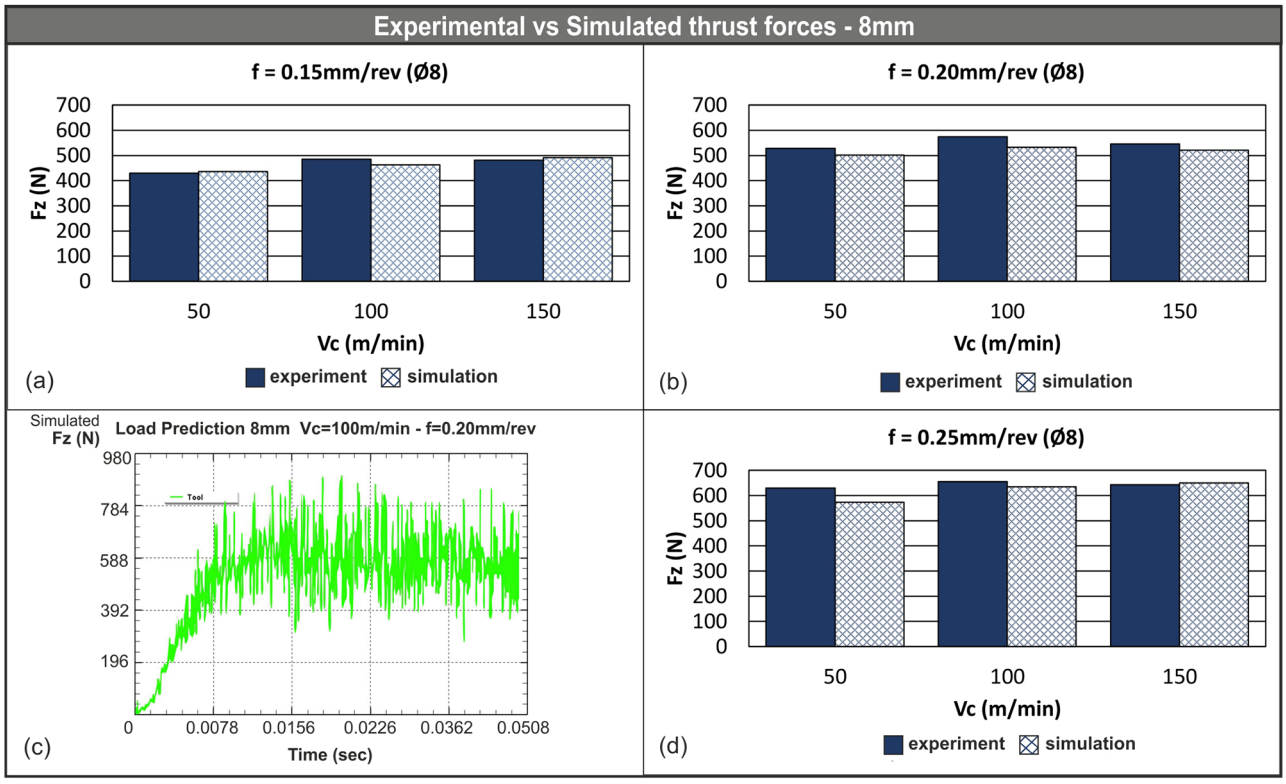

Fig. 5. Experimental versus numerical values of thrust force for the 8 mm drill with varied feed (a), (b), (d) and a sample force-time diagram (c).

rapidly, as soon as chisel's edge starts to press down the surface of the workpiece. Then quickly reaches a steady state, just before 0.0171 s thrust force stops to increase any further and maintains a steady state until the simulation was halted. The produced values of the simulated thrust force for each time step, after the steady state occurred, were used to plot the force-time graphs (Figs. 4a, 5c, 6c and 7c). As shown in Figure 4a, thrust forces fluctuated between 370 and 605 N for the majority of the simulation steps, with a mean value of about 500 N. Figure 4b depicts the produced chip after 8182 steps or 0.0815 s. The aforementioned tendency was observed in all the numerical tests that were performed. In order to eliminate any excessive or non-realistic values of thrust forces that were generated during the remeshing process on the workpiece, the default exponential smoothing (first order) of DEFORM3D™ was implemented.

The processing of the results shows in general a good agreement between the experimental and the numerical results. Figure 5 depicts the comparison between the experimental and the simulated mean values of the produced thrust forces for all nine possible combinations of cutting speed and feed for the 8 mm tool, in addition, a sample thrust force diagram from this set of simulations is depicted (Fig. 5c); it is shown that thrust force increases quickly until approximately 0.0078 s and then stabilizes at a mean value of around 530 N. Relative error between −5% and +2% is found in most of the experiments of this set. In the next cases, between the one with cutting speed of $V_c = 50$ m/min and feed of $f = 0.15$ mm/rev (Fig. 5a) and the one with $V_c = 150$ m/min and feed of $f = 0.25$ mm/rev (Fig. 5d) the relative error is approximately +1%, which is the lowest in the set. On the other hand, the maximum deviation between the experimental and the numerical results occurred in the simulation with cutting speed of $V_c = 100$ m/min and feed of $f = 0.20$ mm/rev (Fig. 5b), as well as with $V_c = 50$ m/min and $f = 0.25$ mm/rev (Fig. 5d). The relative error for these cases is −11% and −9% respectively.

In this set of simulations (8 mm tool), the standard deviation for the thrust force values was found to be between 15 and 142 N. Few cases in this set exhibited similar values of standard deviation and the average standard deviation for the set is close to 62 N. Moreover, the standard deviation for the simulation with cutting speed of $V_c = 50$ m/min and feed of $f = 0.15$ mm/rev (Fig. 5a) was found to be around 15 N, which is the lowest for all sets. In addition, the maximum standard deviation, of about 142 N, was calculated for the simulation with $V_c = 150$ m/min and $f = 0.25$ mm/rev (Fig. 5d).

Results of thrust forces for the 10 mm drill are also in good accordance with the equivalent experimental results. Figure 6 contains the three comparison graphs for the experimental and the simulated mean values of the produced thrust forces for the 10 mm tool and a sample thrust force diagram (Fig. 6c) that indicates the fast increase of thrust force to the point of 0.0089 s followed by a steady state. Mean value of thrust force for the given conditions is around 650 N. Moreover, the percentages of agreement between the experimental and the numerical

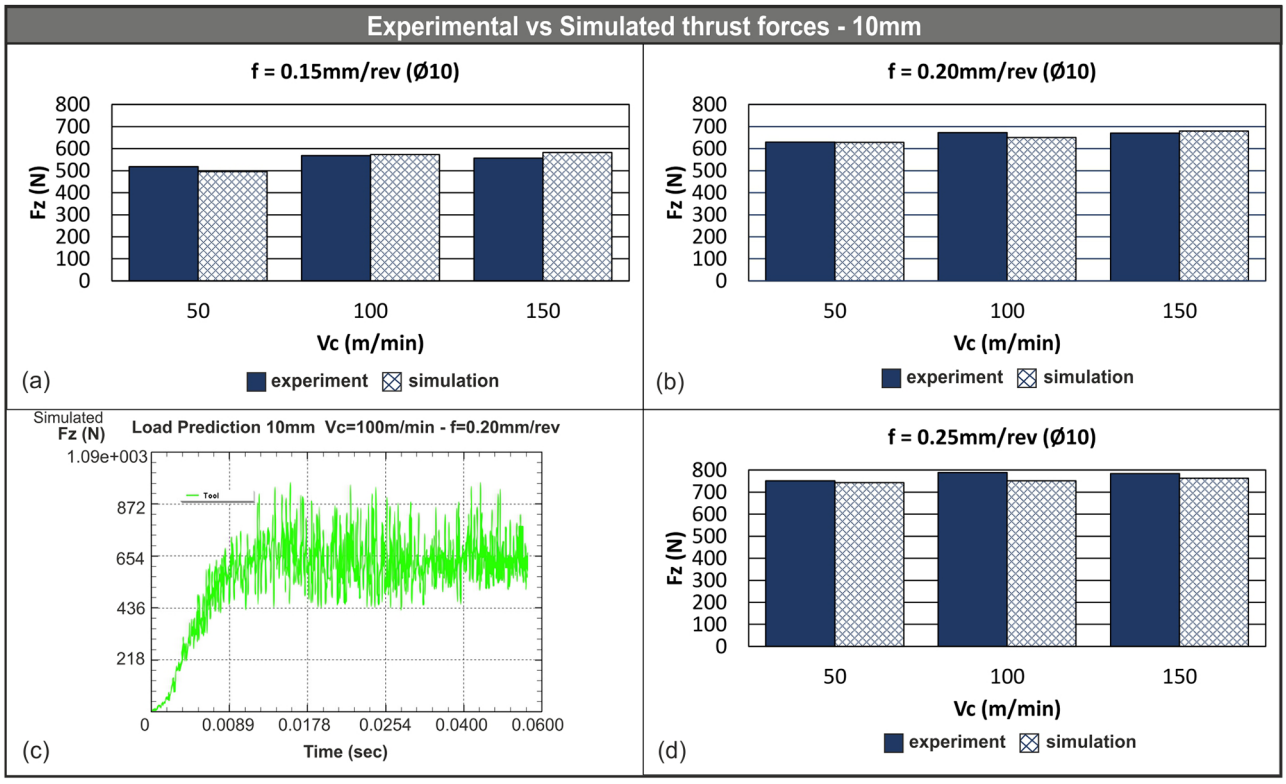

Fig. 6. Experimental versus numerical values of thrust force for the 10 mm drill with varied feed (a), (b), (d) and a sample force-time diagram (c).

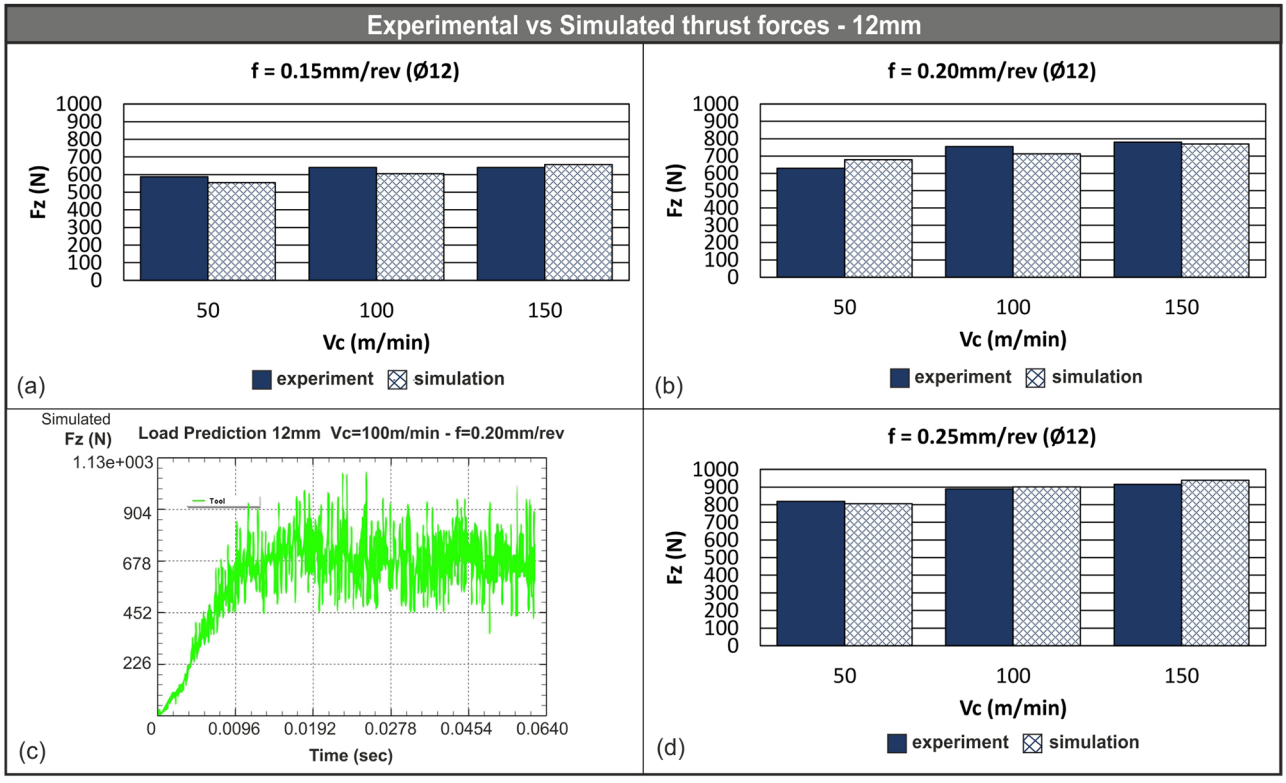

Fig. 7. Experimental versus numerical values of thrust force for the 12 mm drill with varied feed (a), (b), (d) and a sample force-time diagram (c).

results for each combination of cutting conditions tend to fluctuate less, compared to the set of results for the 8 mm drill. Relative error between −4% and +2% constitutes the majority for this set, and in some cases the correlation was close to 99% (cases with cutting speed of $V_c = 50$ m/min and feed of $f = 0.20$ and 0.25 mm/rev − Fig. 6b, d). The maximum deviation between the experimental and the numerical results in this set was found in the simulation with a cutting speed of $V_c = 100$ m/min and a feed of $f = 0.25$ mm/rev (Fig. 6d).

The standard deviation for the thrust force values of each of the simulations for the 10 mm tool, after the first order exponential smoothing, fluctuated between 20 and 75 N with an average value of 52 N. Simulation run with cutting speed of $V_c = 50$ m/min and feed of $f = 0.15$ m/min (Fig. 6a) displayed the lowest value for the set, whereas the simulation with cutting speed of $V_c = 50$ m/min and feed of $f = 0.25$ mm/rev displayed the highest standard deviation (Fig. 6d).

The relative error between the experimental and the numerical values of thrust forces for the results of the last set of simulations (12 mm drill), fluctuated between −6% and +8%. The comparison between the experimental and the numerical results for the thrust forces of all nine simulations in this set is illustrated in Figure 7. The sample thrust force diagram of Figure 7c points out the rapid increase of thrust force until 0.0096 s and the following steady state. Mean value of thrust force for the given conditions is approximately 710 N. Two simulations in this set, the one with $V_c = 150$ m/min and $f = 0.20$ mm/rev (Fig. 7b) and the other with $V_c = 50$ m/min and $f = 0.25$ mm/rev (Fig. 7d) yielded the highest agreement percentage for the set at approximately 99%, which is the highest value of correlation that observed through the whole process of 27 simulations. Additionally, under cutting conditions with $V_c = 100$ m/min and $f = 0.25$ mm/rev (Fig. 7d) the relative error slightly exceeds +1% (simulated value is marginally higher than experimental). Despite this fact, the maximum deviation was found to be in the case with a cutting speed of $V_c = 50$ m/min and a feed of $f = 0.20$ mm/rev (Fig. 7b), which is one of the highest for all the 27 simulations.

The standard deviation for the thrust forces in this set of simulations (12 mm tool) showed values between 50 and 119 N, with most cases yielding values close to 85 N. The lowest standard deviation was found to be approximately 50 N for cutting conditions with cutting speed of $V_c = 150$ m/min and feed of $f = 0.15$ mm/rev (Fig. 7a). On the other hand, the highest value of standard deviation was calculated to be around 119 N for the simulation with $V_c = 50$ m/min and $f = 0.25$ mm/rev (Fig. 7d).

It is worth mentioning that in three cases with cutting speed of $V_c = 150$ m/min, the experimental values of thrust forces were found to be slightly lower compared to the values for $V_c = 100$ m/min. Two of the three cases refer to drilling with the 8 mm tool at a feed of $f = 0.20$ and 0.25 mm/rev respectively, and one case to the drilling with the 10 mm tool at $f = 0.15$ mm/rev as observed in Figures 5b, 5d and 6a. In addition, four cases with $V_c = 150$ m/min display no fluctuation in generated thrust forces compared to the values found with $V_c = 100$ m/min. These cases are: 8 mm tool with $f = 0.15$ mm/rev, 10 mm tool with $f = 0.20$ and 0.25 mm/rev respectively and 12 mm tool with $f = 0.15$ mm/rev.

Figures 8a, 8c and 8e illustrate the variation of the experimental thrust forces with feed for varying tool diameter at certain cutting speed. Similarly, Figures 8b, 8d and 8f depict the variation of simulated values. It is obvious that both feed and cutting speed play an important role to the produced thrust forces, regardless of the tool diameter, especially the feed. There is a small but steady increase in thrust forces as cutting speed increases for each feed value and all tool diameters. Similarly, a noticeable and constant increase in thrust forces is present as feed increases for each cutting speed. For instance, according to figure 8b for the 12 mm tool, simulated thrust forces increase from approximately 550 N to 680 N and finally to 810 N at cutting speed of $V_c = 50$ m/min for each value of feed (0.15, 0.20 and 0.25 mm/rev respectively). The same linear trend applies for the other two tools. However, it is noted that thrust forces for the 8 mm tool increase at a different proportion.

As cutting speed increases, it is clear that simulated thrust forces increase for each value of feed in a similar manner. This pattern is different to the linearity that exists at cutting speed $V_c = 50$ m/min and is displayed mostly at $V_c = 100$ and 150 m/min (Fig. 8d and f). For example, with the 8 mm tool at $V_c = 100$ m/min (Fig. 8d) thrust forces increase from approximately 460 N to 510 N and finally to 630 N for each value of feed (0.15, 0.20 and 0.25 mm/rev). Additionally, for the same tool at $V_c = 150$ m/min (Fig. 8f) the increase pattern is similar, from 490 N to 520 N and then to 650 N.

3.2 Evolution of chip formation

Both the experimental and the simulated results indicate that the produced chip retains the same conical shape on each simulation regardless of the combination of the feed and cutting speed. However, the size of the chip (diameter of the conical shape chip) depends on the drill diameter. This is anticipated due to the fact that a larger flute can remove more material and thus produce wider chips. In general, the size of the flutes is related to the size of the drill.

Figure 9a depicts the evolution of the generated simulated chip during drilling of Al7075-T6 with a 10 mm, two flute twist drill, at 50 m/min cutting speed and 0.15 mm/rev feed rate, whereas Figure 9b illustrates the produced experimental chip for the same cutting conditions.

3.3 Mathematical modelling of thrust force

Since the correlation between the experimental and the numerical results was found to be very high on all three tools, a mathematical model is possible so that future experiments for different drill diameters and similar cutting conditions can be skipped. The proposed mathematical model for thrust force was developed with the aid of RSM, which is a proven statistical methodology that provides excellent experiment design and result presentation. There are cases in literature where researchers in the field of machining have successfully implemented RSM in

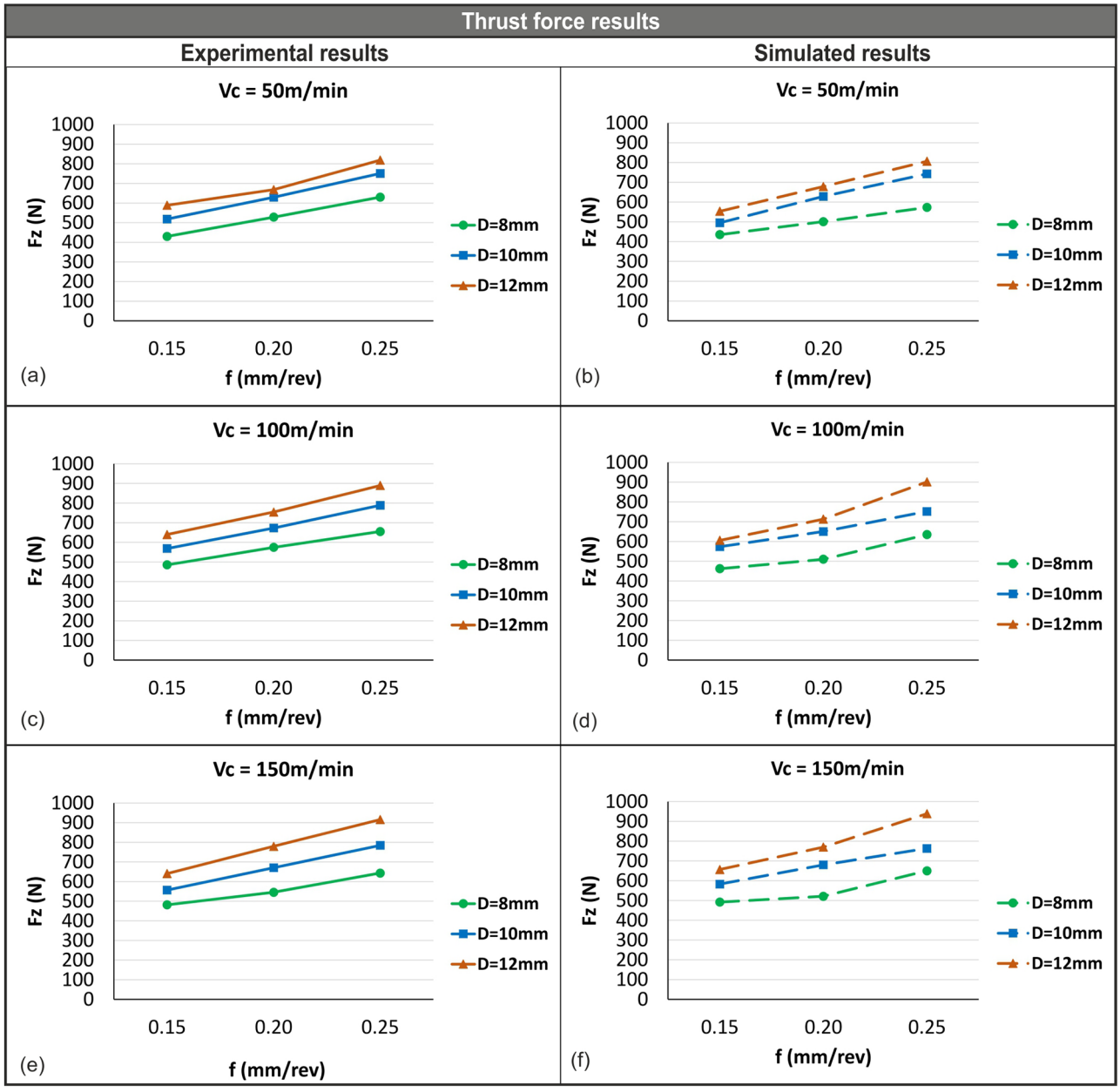

Fig. 8. Variation of the experimental (a), (c), (e) and the numerical (b), (d), (f) values of thrust force with feed for varying tool diameter.

their research [22,32–35] with excellent results, thus the use of RSM was selected for this study. Because this research includes 27 drilling experiments and simulations, the mathematical modelling was performed with a full factorial design in mind, based on the numerical results. Table 3 illustrates the design of experiments and the corresponding output for the numerical study.

The first step that was made during modelling was to fit the regression model. Based on the number of factors (drill diameter, cutting speed and feed) that were involved in the numerical study, the fitted model that occurred is a second order polynomial with linear, quadratic and interactive terms. Equation (5) represents the second order polynomial for this study.

$$Y = b_0 + b_1X_1 + b_2X_2 + b_3X_3 + b_4X_1^2 + b_5X_2^2 + b_6X_3^2 + b_7X_1X_2 + b_8X_1X_3 + b_9X_2X_3 \quad (5)$$

where Y is the response of the model, thus the thrust force in this case, X_i are the coded values of the model (drill diameter, cutting speed and feed) and b_i are the regression coefficients that depend on the number of factors of the model (three in this case).

Using the aforementioned polynomial and the data that are presented in Figures 5–7, the complete mathematical model based on the verified simulated results that was

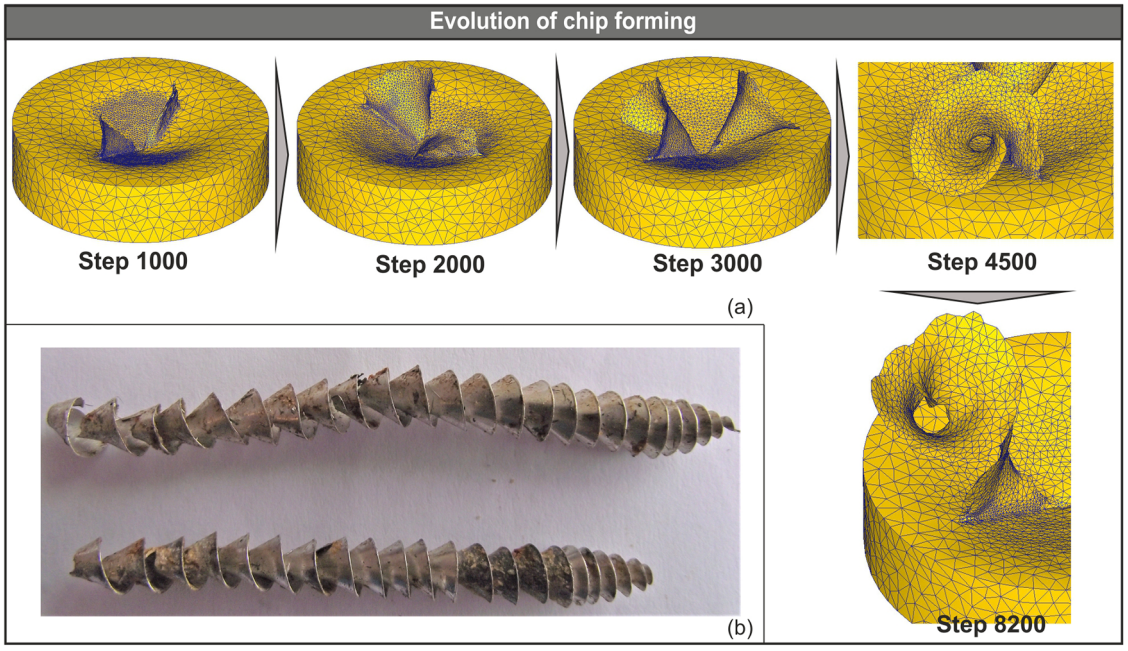

Fig. 9. The evolution of the simulated chip (a) and the experimental one (b) for the 10 mm drill.

Table 3. Design of experiments.

Std order	D (mm)	V_c (m/min)	f (mm/rev)	$F_{z\ \text{simulated}}$ (N)
1	8	50	0.15	435.6
2	8	50	0.20	501.4
3	8	50	0.25	573.5
4	8	100	0.15	462.5
5	8	100	0.20	510.3
6	8	100	0.25	634.9
7	8	150	0.15	491.5
8	8	150	0.20	520.8
9	8	150	0.25	649.8
10	10	50	0.15	495.9
11	10	50	0.20	628.8
12	10	50	0.25	742.9
13	10	100	0.15	573.5
14	10	100	0.20	650.4
15	10	100	0.25	751.6
16	10	150	0.15	582.4
17	10	150	0.20	679.9
18	10	150	0.25	763.0
19	12	50	0.15	553.8
20	12	50	0.20	612.9
21	12	50	0.25	806.7
22	12	100	0.15	605.8
23	12	100	0.20	713.2
24	12	100	0.25	901.3
25	12	150	0.15	656.5
26	12	150	0.20	770.0
27	12	150	0.25	938.7

Table 4. ANOVA results for thrust force.

Source	Degree of freedom	Sum of squares	Mean square	f-value	p-value
Regression	9	427676	47519.5	103.01	0.000
Residual error	17	7842	461.3		
Total	26	435518			
R-sq (adj) = 97.25%					
Term	PE coefficient	SE coefficient	t-value	p-value	
Constant	238	295	0.81	0.432	
D	79.5	46.1	1.73	0.102	
V_c	−0.21	1.06	−0.19	0.848	
f	−4797	1557	−3.08	0.007	
D^2	−5.52	2.19	−2.52	0.022	
V_c^2	−0.00451	0.00351	−1.29	0.215	
f^2	9883	3507	2.82	0.012	
$D \times V_c$	0.20	0.062	3.23	0.005	
$D \times f$	301.6	62.0	4.86	0.000	
$V_c \times f$	−0.56	2.48	−0.22	0.825	

developed, is represented by equation (6).

$$F_z = 238 + 79.5D - 0.21V_c - 4797f - 5.52D^2 - 0.00451V_c^2 + 9883f^2 + 0.2DV_c + 301.6Df - 0.56V_cf \quad (6)$$

where F_z is the thrust force in N, D is the drill diameter in mm, V_c is the cutting speed in m/min and f is the feed in mm/rev.

3.4 Analysis and validation of model

After fitting the model, analysis of variance (ANOVA) has been performed for validation purposes. During this step, a confidence level of 95% was used for all intervals. The adjusted R-squared for this model found to be as high as 97.25% proving the validity of the fit. In addition, the high correlation can be proved by the p-values that are 0.05 and lower. Due to the fact that the significance level is 0.05, the contribution to the validity of the thrust force model according to Table 4 is done by these factors: f with a p-value of 0.007, D^2 with $p = 0.022$, f^2 with $p = 0.012$, $D \times V_c$ with $p = 0.005$ and $D \times f$ with $p = 0.000$.

Table 4 contains the sum of squares and degrees of freedom of the analysis. Sum of squares includes the sum of squared deviations due to each of the nine factors and the sum of squares due to error. Mean square is the ratio of sum of squares to the degree of freedom and the f-value is the ratio of mean square of regression model to the mean square of residual error. Lastly, the p-value of the analysis is 0.000 which means that the correlation is very high as the probability of getting an extreme result is very low.

The significance of the tool diameter D, cutting speed V_c and feed rate f is highlighted with the main effects plot (Fig. 10). As already pointed out with the aid of Figure 8, the key parameters that effect thrust forces are the tool diameter and the feed rate. More importantly, it is obvious that as diameter and feed increase, thrust forces also increases.

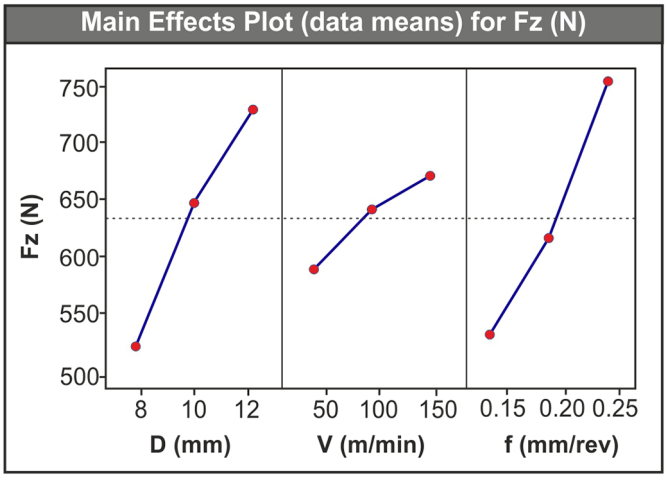

Fig. 10. Main effects plot for thrust force.

Following the validation of goodness of fit, the next step was the residual analysis to check the accuracy of the model. Figure 11 contains four graphs: the normal probability plot of the residuals (Fig. 11a), the residuals versus the fitted values (Fig. 11b), the distribution of error histogram (Fig. 11c) and the residuals versus the order of the data (Fig. 11d). The normality of distribution in all graphs suggests the validity of the regression analysis. Specifically, from the normal probability plot it is understandable that the errors follow an almost linear pattern which means that the errors follow a normal distribution pattern. The residuals versus the fitted values graph shows that the residuals are evenly scattered on both sides of the reference line of the graph, thus the variance is

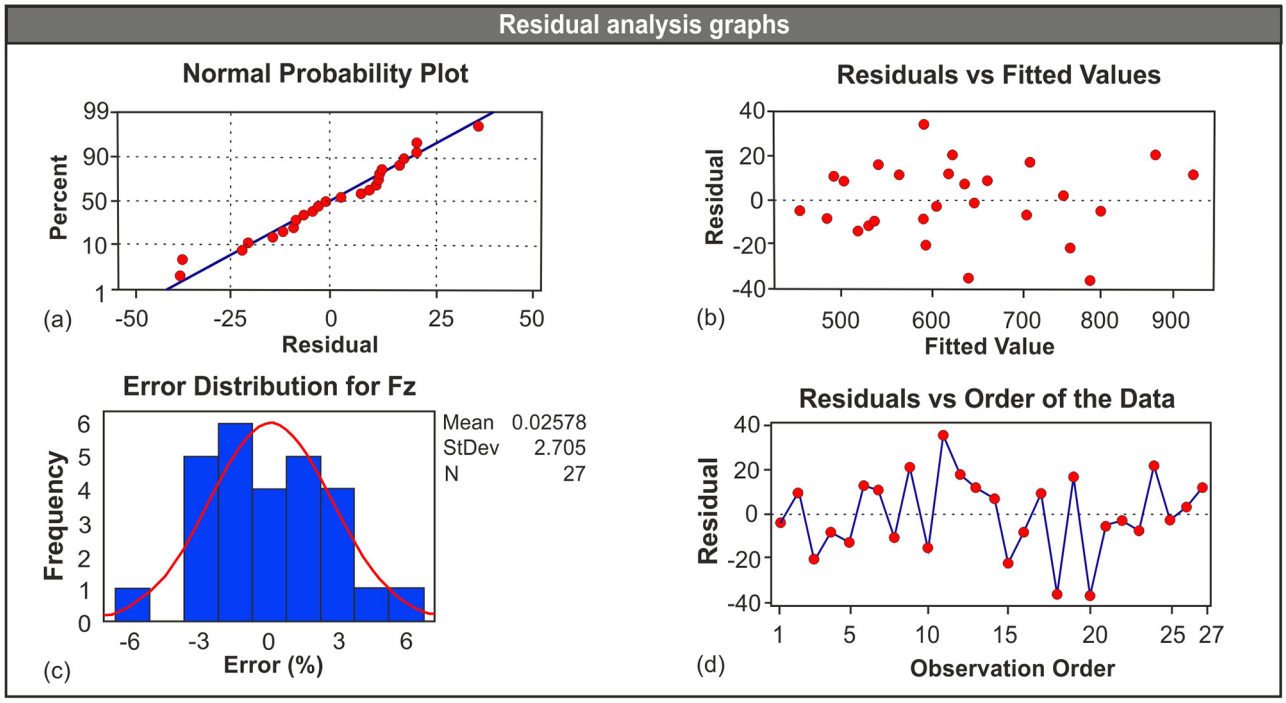

Fig. 11. Residual analysis graphs: probability plot (a), residuals versus fitted values (b), error histogram (c) and residuals versus order (d).

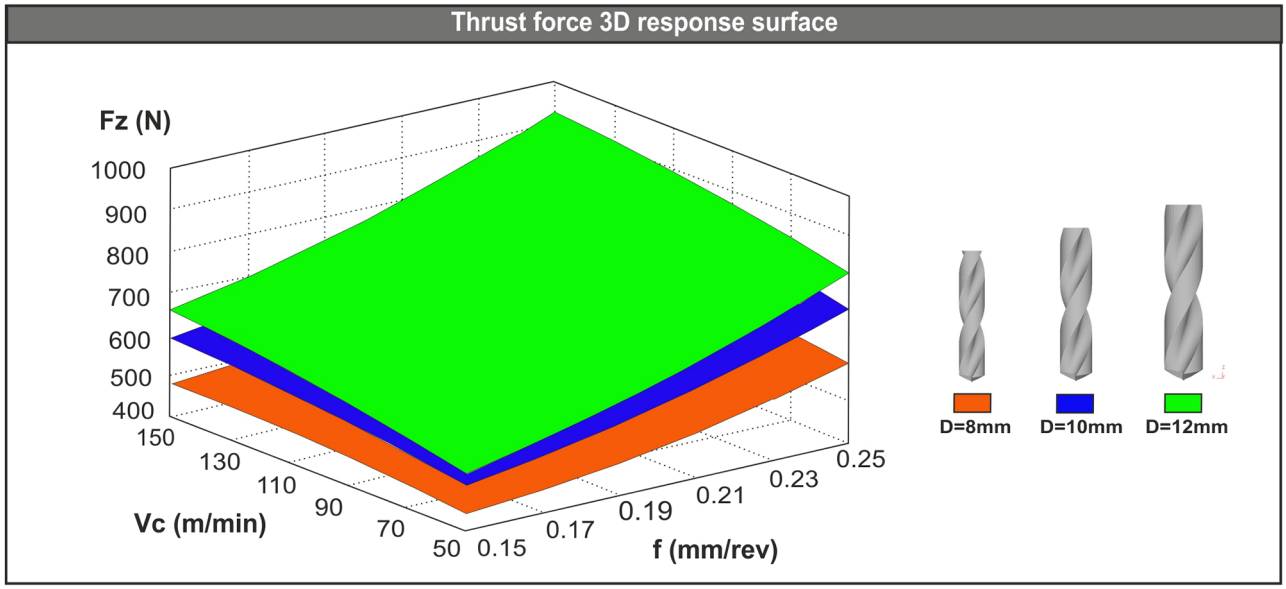

Fig. 12. 3D plots of the thrust force for each drill.

constant. In addition, the histogram depicts a normality in distribution between the error percentages. Finally, the residuals versus order graph indicates that there are no obvious systematic effects in the data due to time.

Final step of the mathematical modelling was the analysis of the developed prediction model. With the aid of 3D response surface plots, the combined effect of the tool diameter and cutting conditions on thrust forces were analyzed. Figure 12 illustrates the generated 3D surfaces for each drill diameter based on the polynomial solutions. The inputs of the polynomial are within the investigated range for cutting speed and feed, thus from 50 to 150 m/min for cutting speed and 0.15 to 0.25 mm/rev for feed. According to Figures 10 and 12 it is observed that:

– As a larger drill diameter is selected, the produced thrust force increases notably (the larger the diameter, the higher values of thrust force).

Table 5. Confirmation of mathematical model for F_z.

Set	Simulated F_z (N)	Predicted F_z (N)	Relative error (%)
I (8 mm)	487.6	483.1	−0.92
II (10 mm)	602.9	582.0	−3.47
III (12 mm)	611.5	636.6	4.11

– Similarly, at higher values of feed, the produced thrust force is significantly increased.
– On the other hand, any increase in cutting speed has limited effect (increase) on thrust force.

Eventually, to further validate the mathematical model, a set of three extra simulations (one for each drill) was performed for the prediction of F_z. The cutting conditions were selected arbitrarily from within the range of the experimental data. The selected conditions are: $V_c = 75$ m/min and $f = 0.18$ mm/rev. Table 5 includes the produced results which are deemed sufficient since the relative error for all three cases is below 5%.

4 Conclusions

The development of a prediction model for the generated thrust forces during drilling of Al7075-T6, with the aid of RSM and the implementation of 3D FEA, is presented in this study. A complete series of 27 3D simulations was carried out under different cutting conditions (speed and feed rate) in addition to the three different tool diameters that were used. The simulated results were validated via experiments and the correlation between the simulated and the experimental results exceeded 95% in most cases. After thoroughly analyzing the model for its accuracy (5.9%) and goodness of fit, it is concluded that the developed model can safely predict the thrust forces under certain limits that are discussed in this research. Moreover, the morphology of the produced chips during drilling of Al7075-T6 was introduced. Finally, through this analysis the following conclusions are drawn:

– Increase in tool diameter and feed rate leads to significant boost of thrust force. Specifically, an increase of close to 20% in thrust force is observed when changing to the 10 mm drill from the 8 mm one or when increasing the feed to 0.20 mm/rev from 0.15 mm/rev. The equivalent shift from 10 mm to 12 mm or from 0.20 mm/rev to 0.25 mm/rev amplifies F_z by more than 40% for both cases.
– On the other hand, any increase in cutting speed increases thrust force at a small but not negligible amount; a step-up from 50 m/min to 100 m/min was estimated to rise F_z approximately by 8.5%, whereas from 100 m/min to 150 m/min by 4%.
– The factors that affect the most the statistical model are: f, D^2, f^2, $D \times V_c$ and $D \times f$ since their p-values is lower than the significance level.
– The produced chips tend to maintain a conical shape, regardless of the cutting conditions, whereas the diameter of the curling of chip increases as larger tool diameter was selected.

Nomenclature

T_0	Bulk temperature of the workpice material (K)
V_c	Cutting speed (m/min)
D	Drill diameter (mm)
$\overline{\sigma}$	Effective stress (N/m^2)
f	Feed (mm/rev)
τ_f	Frictional stress at the tool − chip interface (N/m^2)
A	Initial yield stress (N/m^2)
σ'	Maximum principal stress (N/m^2)
T_m	Melting temperature (K)
σ_n	Normal stress (N/m^2)
ε	Plastic strain
$\dot{\varepsilon}$	Plastic strain rate (s^{-1})
$\dot{\varepsilon}_0$	Reference plastic strain rate (s^{-1})
T	Reference temperature (K)
m	Shear friction coefficient
μ	Sliding friction coefficient
N	Spindle speed (min^{-1})
B	Strain hardening modulus (N/m^2)
n	Strain hardening exponent
C	Strain rate dependence coefficient
m	Thermal softening coefficient for JC model
F_z	Thrust force (N)
σ_y	Uniaxial yield stress (N/m^2)

References

[1] B. Klamecki, Incipient Chip Formation in Metal Cutting – A Three Dimensional Element Analysis, Urbana-Champaign: University of Illinois, 1973
[2] Y.B. Guo, D.A. Dornfeld, Finite element modeling of burr formation process in drilling 304 stainless steel, J. Manuf. Sci. Eng. **122**, 4 (2000)
[3] M. Abouridouane, F. Klocke, D. Lung, Microstructure-based 3D finite element model for micro drilling carbon steels, Proc. CIRP **8** (2013)
[4] X. Nan, L. Xie, W. Zhao, On the application of 3D finite element modeling for small-diameter hole drilling of AISI 1045 steel, Int. J. Adv. Manuf. Technol. **84** (2016)

[5] P.J. Arrazola, T. Matsumura, A. Kortabarria, A. Garay, D. Soler, Finite element modelling of chip formation process applied to drilling of Ti64 alloy in: Proceedings of the 6th International Conference on Leading Edge Manufacturing in 21st Century: LEM 2011, J-Stage, 2011, pp. 1–6
[6] M. Asad, T. Mabrouki, H. Ijaz, M. Aurangzeb Khan, W. Saleem, On the turning modeling and simulation: 2D and 3D FEM approaches, Mech. Ind. **15**, 5 (2014)
[7] O. Isbilir, E. Ghassemieh, Finite element analysis of drilling of titanium alloy, Proc. Eng. **10** (2011)
[8] X. Gao, H. Li, Q. Liu, P. Zou, F. Liu, Simulation of stainless steel drilling mechanism based on Deform-3D, Adv. Mater. Res. **160–162**, (2011)
[9] A. Majeed, A. Iqbal, J.J. Lv, Enhancement of tool life in drilling of hardened AISI 4340 steel using 3D FEM modeling, Int. J. Adv. Manuf. Technol. **95** (2018)
[10] S.F. Miller, A.J. Shih, Thermo-mechanical finite element modeling of the friction drilling process, J. Manuf. Sci. Eng. **129**, (2007)
[11] J.P. Davim, C. Maranhão, Study on plastic strain and plastic strain rate in machining of steel AISI 1020 using FEM analysis, Mater. Des. **30**, 1 (2009)
[12] T. Belis, P. Kyratsis, A. Antoniadis, Stress Analysis on Twist Drill Tools Combining CAD based Methodology and Finite Element Analysis, NOVA Science Publishers, chapter **2**, pp. 31–42, 2013
[13] M. Lotfi, S. Amini, I.Y. Al-Awady, 3D numerical analysis of drilling process: heat, wear, and built-up edge, Adv. Manuf. **6** (2018)
[14] A.K. Parida, Simulation and experimental investigation of drilling of Ti-6Al-4V alloy, Int. J. Light Mater. Manuf. **1**, 3 (2018)
[15] M. Nagaraj, A.J.P. Kumar, C. Ezilarasan, R. Betala, Finite element modeling in drilling of Nimonic C-263 alloy using deform-3D, C − Comput. Model. Eng. Sci. **118**, 3 (2019)
[16] T. Dou, H. Fu, Z. Li, X. Ji, S.S. Bi, Prediction model, simulation, and experimental validation on thrust force and torque in drilling SiCp/Al6063, Int. J. Adv. Manuf. Technol. **103** (2019)
[17] J.R. Flachs, M. Salahshoor, S.N. Melkote, Mechanistic models of thrust force and torque in step-drilling of Al7075-T651, Prod. Eng. **8** (2014)
[18] E. Bahçe, B. Özdemir, Investigation of the burr formation during the drilling of free-form surfaces in al 7075 alloy, J. Mater. Res. Technol. **8**, 5 (2019)
[19] J.Y. Kao, C.Y. Hsu, C.C. Tsao, Experimental study of inverted drilling Al-7075 alloy, Int. J. Adv. Manuf. Technol. **102** (2019)
[20] J.P. Davim, C. Maranhão, M.J. Jackson, G. Cabral, J. Grácio, FEM analysis in high speed machining of aluminium alloy (Al7075-0) using polycrystalline diamond (PCD) and cemented carbide (K10) cutting tools, Int. J. Adv. Manuf. Technol. **39** (2008)
[21] İ. Ucun, 3D finite element modelling of drilling process of Al7075-T6 alloy and experimental validation, J. Mech. Sci. Technol. **30** (2016)
[22] N.K. Sahu, A.B. Andhare, Prediction of residual stress using RSM during turning of Ti-6Al-4V with the 3D FEM assist and experiments, SN Appl. Sci. **1** (2019)
[23] S.N. Grigoriev, M.A. Volosova, V.D. Gurin, A.Y. Seleznyov, Investigation of force parameters acting on a single cutting insert made of ceramics in face milling of hardened steel, Mech. Ind. **16**, 702 (2015)
[24] H. Aouici, M. Elbah, A. Benkhelladi, B. Fnides, L. Boulanouar, Comparison on various machinability aspects between mixed and reinforced ceramics when machining hardened steels, Mech. Ind. **20**, 109 (2019)
[25] MatWeb Material Property Data, https://www.matweb.com, Accessed: 29/11/2019
[26] E. Jafarzadeh, M.R. Movahhedy, S. Khodaygan, Prediction of machining chatter in milling based on dynamic FEM simulations of chip formation, Adv. Manuf. **6** (2018)
[27] Scientific Forming Technologies Corporation, DEFORM V11.3 (PC) Documentation, 2016
[28] J.D. Gardner, D. Dornfeld, Finite Element Modeling of Drilling Using DEFORM, Simulation (2006)
[29] N.S. Brar, V.S. Joshi, B.W. Harris, Constitutive model constants for Al7075-T651 and Al7075-T6, AIP Conf. Proc. **1195**, 945 (2009)
[30] M.G. Cockcroft, D.J. Latham, Ductility and the Workability of Metals, J. Inst. Met. **96** (1968)
[31] M. Agmell, Applied FEM of metal removal and forming − first edition, Studentlitteratur, Lund, 2018
[32] S. Kosaraju, V.G. Anne, Optimal machining conditions for turning Ti-6Al-4V using response surface methodology, Adv. Manuf. **1** (2013)
[33] P. Kyratsis, C. Garcia-Hernandez, D. Vakondios, A. Antoniadis, Thrust Force and Torque Mathematical Models in Drilling of Al7075 Using the Response Surface Methodology in: J.P. Davim (ed.), Design of Experiments in Production Engineering, Springer International Publishing, Cham 2016, pp. 151–164
[34] P. Kyratsis, A. Markopoulos, N. Efkolidis, V. Maliagkas, K. Kakoulis, Prediction of thrust force and cutting torque in drilling based on the response surface methodology, Machines **6**, 2 (2018)
[35] W. Frifita, S. Ben Salem, A. Haddad, M. Athmane Yallese, Optimization of machining parameters in turning of Inconel 718 Nickel-base super alloy, Mech. Ind. **21**, 2 (2020)

Cite this article as: A. Tzotzis, C. García-Hernández, J.-L. Huertas-Talón, P. Kyratsis, FEM based mathematical modelling of thrust force during drilling of Al7075-T6, Mechanics & Industry **21**, 415 (2020)

Strojniški vestnik - Journal of Mechanical Engineering 66(2020)7-8, 467-478

DOI:10.5545/sv-jme.2020.6784 Original Scientific Paper
Received for review: 2020-05-25
Received revised form: 2020-07-01
Accepted for publication: 2020-07-14

3D FE Modelling of Machining Forces during AISI 4140 Hard Turning

Anastasios Tzotzis[1,*] – César García-Hernández[1] – José-Luis Huertas-Talón[1] – Panagiotis Kyratsis[2]
[1]University of Zaragoza, Department of Design and Manufacturing Engineering, Spain
[2]University of Western Macedonia, Department of Product and Systems Design Engineering, Greece

Hard turning is one of the most used machining processes in industrial applications. This paper researches critical aspects that influence the machining process of AISI 4140 to develop a prediction model for the resultant machining force-induced during AISI 4140 hard turning, based on finite element (FE) modelling. A total of 27 turning simulation runs were carried out in order to investigate the relationship between three key parameters (cutting speed, feed rate, and depth of cut) and their effect on machining force components. The acquired numerical results were compared to experimental ones for verification purposes. Additionally, a mathematical model was established according to statistical methodologies such as the response surface methodology (RSM) and the analysis of variance (ANOVA). The plurality of the simulations yielded results in high conformity with the experimental values of the main machining force and its components. Specifically, the resultant cutting force agreement exceeded 90 % in many tests. Moreover, the verification of the adequacy of the statistical model led to an accuracy of 8.8 %.
Keywords: AISI 4140 turning, machining forces, 3-dimensional finite element modelling, response surface methodology

Highlights
- *A 3D FE model has been established for the hard turning of AISI 4140.*
- *In addition, a statistically based prediction model for the resultant machining force has been developed.*
- *Through RSM and ANOVA, the effect of the cutting parameters on the machining force components and their relationship were investigated.*
- *The numerical results were in complete accordance with the experimental ones; the relative error was estimated within the range of -10 % to 12 % for most of the cases.*
- *The prediction model offered an accuracy of 8.8 %.*

0 INTRODUCTION

Hard turning is a cost-effective machining operation since it can reduce finish grinding of parts and, in some cases, eliminate it. The term "hard turning" refers to the turning operation of hardened steel with hardness between 58 and 62 HRC [1]. Additionally, hardened steel is an essential work material in industrial applications. Therefore, many researchers developed an increased interest in the investigation of hard turning and similar machining processes [2] to [6]. One of the latest advances in machining studies is the implementation of the finite element method (FEM) with the aid of specialized software.

In recent years, the 2D orthogonal cutting finite element (FE) model have proved to be a valuable tool for many researchers. Klocke et al. [7] simulated the high-speed orthogonal turning of AISI 1045 steel using commercial software. Yen et al. [8] developed a methodology to predict the tool wear evolution and tool life in orthogonal cutting using FEM simulations. Arrazola et al. [9] employed a 2D FE model with the use of arbitrary Langrangian Eulerian (ALE) formulation for prediction purposes of the serrated chip during AISI 4140 machining. Similar studies have been conducted to examine the generated chip morphology and cutting forces via 2D modelling for homologous materials [10] to [12], but this model has several restrictions that limit its field of application. In contrast, the constant advancement of computational resources resulted in the emergence of 3D modelling, which does not have the limitations of 2D models. Therefore, FE modelling in three dimensions can help researchers to study several aspects of machining at a greater extent. Tool wear analysis and temperature distribution on the cutting tip of tools has been studied extensively [13] to [15], as well as the prediction of the cutting forces and residual stresses, and the optimization of the machining conditions [16] to [18]. Three-dimensional modelling is also used for investigation purposes on the turning of hardened steels; in most cases, the results are experimentally validated. Guo and Liu [19] established a geometric model and a general practical, explicit 3D FE model to analyse the hard turning of AISI 52100; the model predictions provide reasonable accuracy for several cutting results. Later, Özel et al. [20] utilized 3D FE modelling to predict chip formation, forces, temperatures, and tool wear during hard turning of AISI 4130 with polycrystalline

*Corr. Author's Address: University of Zaragoza, Campus Rio Ebro, C/ Maria de Luna 3, 50018, Zaragoza, Spain, atzotzis@unizar.es

cubic boron nitride (PcBN) tools. Lian et al. [21] proposed a structural model for soft/hard composite-coated textured (SHCCT) tools and confirmed it with a three-dimensional numerical simulation. The proposed model was applied to AISI 1045 hard turning and was analysed via orthogonal experiments for different coating thickness, material, and ratios of the soft/hard coatings. Magalhães et al. [22] aimed to provide a better understanding of the mechanical and thermal loads involved in cutting, with respect to the variation of the tool's edge discretization. To do so, they prepared numerical simulations of AISI 5115 steel hard turning using finite element analysis (FEA).

The advent of more advanced inserts, such as PcBN, polycrystalline diamond (PCD), chemical vapour deposition (CVD) and ceramics, lead to more efficient machining and overall to better quality finished parts. In particular, ceramic tools are preferred when machining hardened steels; therefore, the analysis of hard turning with ceramics and the effects of various conditions is a research area that can benefit from the implementation of FEM. Hu and Huang [1] and [14] researched the influence of tool shape and cutting angles on the contact stresses, sliding speed, and temperature with the aid of 3D FEM and experimental testing; they also established a new type of tool life model for nano-ceramic tools, which includes several parameters. Moreover, they studied the effects of cutting speed on the high-speed turning of AISI 1013 with ceramics by using similar methodologies.

An adequate number of solely experimental research studies can be found in the literature, related to the hard turning of steel; however, the implementation of FEM in such studies remains limited, especially during the investigation of the modern standardized turning inserts. In the present paper, the components of the turning force-induced during the hard turning of AISI 4140 is examined with respect to several combinations of cutting speed, feed, and depth of cut. The study has been carried out with the aid of a commercially available finite model analysis (FEA) software (DEFORM3D™). In addition to the established FE model, a prediction model for the main machining force based on statistical methods has been developed. Furthermore, both the FE model and the statistical prediction model were validated via comparison with equivalent experimental results that are available in the literature [23].

1 METHODOLOGIES

1.1 Experimental Layout

The experimental values [23] used in this study were acquired with the aid of a three-component dynamometer, (Kistler 9257B) and a standard data acquisition system which includes a charge amplifier, a data acquisition card (A/D2855A3), and the appropriate software (DynoWare 2825A1-1). The turning experiments were performed with the aid of a universal lathe type SN 40C and the tool-holder PCBNR2525M12. The chemical composition of the material being studied (AISI 4140) in wt%, is as follows: C 0.43, Mn 0.79, Si 0.24, S 0.024, Cu 0.025, Al 0.029, Ti 0.004, Nb 0.001, Ni 0.022, Cr 1.10, Mo 0.19, Va 0.005, Sn 0.002, and Fe in balance. In addition, the chemical composition of the used ceramic tool (CNGA120408) is 70 % Al_2O_3 and 30 % TiC.

1.2 CAD-Based Layout

A CAD-based setup of the turning experiments was realized in SolidWorks™ 2018 in order to acquire an overview of the process and extract the necessary information that was used to build a simplified 3D FE model. The tool of this study is comprised of a tool-holder and a conventional turning insert with ISO designation numbers PCBNR2525M12 and CNGA120408, respectively. A cylindrical bar with a diameter of 72 mm served as the workpiece. In addition, the selected material for the workpiece is AISI 4140 steel, whereas the insert is an uncoated ceramic. The angles related to the cutting process are from the tool-holder and insert geometry. Hence, the lead angle is 75°, and both the rake and inclination angle are negative with a value of −6°.

Fig. 1a depicts a schematic of the tool-workpiece setup along the machining forces: F_t stands for the tangential force, F_r is the radial force, and finally F_a is the developed feed force. In contrast, Fig. 1b shows the most important dimensions of the insert. The CNGA-ceramic family are 80° rhombic inserts used for machining hardened steel.

The cutting conditions applied in the present research include three levels of cutting speed (80 m/min, 115 m/min, 150 m/min), feed (0.08 mm/rev, 0.11 mm/rev, 0.14 mm/rev) and depth of cut (0.10 mm, 0.20 mm, 0.30 mm). Thus, the total number of simulation tests that were carried out, based on the unique factor level combinations, is twenty-seven.

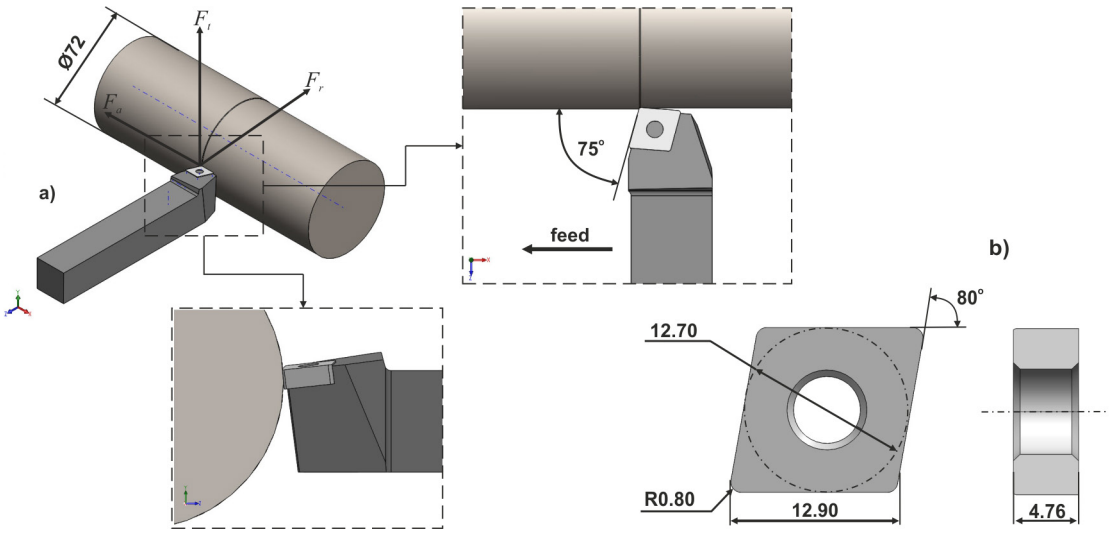

Fig. 1. *CAD models of a) the cylindrical workpiece, and b) the CNGA120408 insert*

Table 1 summarizes the factors, and their levels that are found in the present study.

Table 1. *Process conditions of the turning FE model*

Level	V_c [m/min]	f [mm/rev]	ap [mm]
I	80	0.08	0.10
II	115	0.11	0.20
III	150	0.14	0.30

1.3 3D FE Model Setup

Commercially available FEA software was used (DEFORM3D™ ver. 12) to perform the simulation tests of the 3D turning process without making any assumptions that are associated with the orthogonal cutting conditions [24]. The tests were performed on a desktop PC with six-core CPU 3.60 GHz, 16 GB RAM and SSD technology hard drive. With the given specifications, the completion time for the simulations with a feed value of 0.14 mm/rev, 0.11 mm/rev and 0.08 mm/rev was about 6 hours, 10 hours and 18 hours accordingly. This difference in time is due to the fact that the mesh size of the workpiece varied from test to test.

In order to achieve the aforementioned reasonable simulation times, an effort to simplify the problem was made. For example, only a small area of the workpiece was used, instead of the entire cylindrical model. Specifically, the workpiece was converted to a circular arc with a diameter of 72 mm and an angle of 45° (Fig. 2a). In addition, the workpiece was generated with an already cut surface based on the depth of cut (Fig. 2c). The specified geometry constitutes the analysis domain of the problem.

1.3.1 Tool – Workpiece Interface Definition

Both the model of the insert and the model of the simplified workpiece were designed in SolidWorks™. The first was designed according to the ISO 13399 (see Fig. 1b), whereas the latter was designed with respect to the depth of cut, the corner radius of the tool and the diameter of the cylindrical steel bar. Both models were saved in STL file format and then imported to the analysis software for the development of the FE model. The tool was modelled as rigid and meshed with approximately 50,000 tetrahedral elements. Moreover, the mesh was refined locally by applying a size ratio of 4:1 close to the cutting tip, as shown in Fig. 2b, because this area of the insert is in contact with the uncut surface of the workpiece. the workpiece was modelled to have plastic behaviour, and its mesh size varied between roughly 90,000 and 140,000 elements. This variance occurred due to the size of the minimum triangular element which depends on the value of feed; the size of the minimum element was fixed to 25 % of the feed for all cases [24]. Additionally, a more dense mesh with a size ratio of 7:1 was applied to the section of the workpiece where contact with the tool is present. Fig. 2c illustrates the section of the workpiece and the formation of the mesh.

Since chip formation in turning is a process in which large deformations, strains and high temperatures develop, an adaptive remeshing method was implemented. The used method involves local

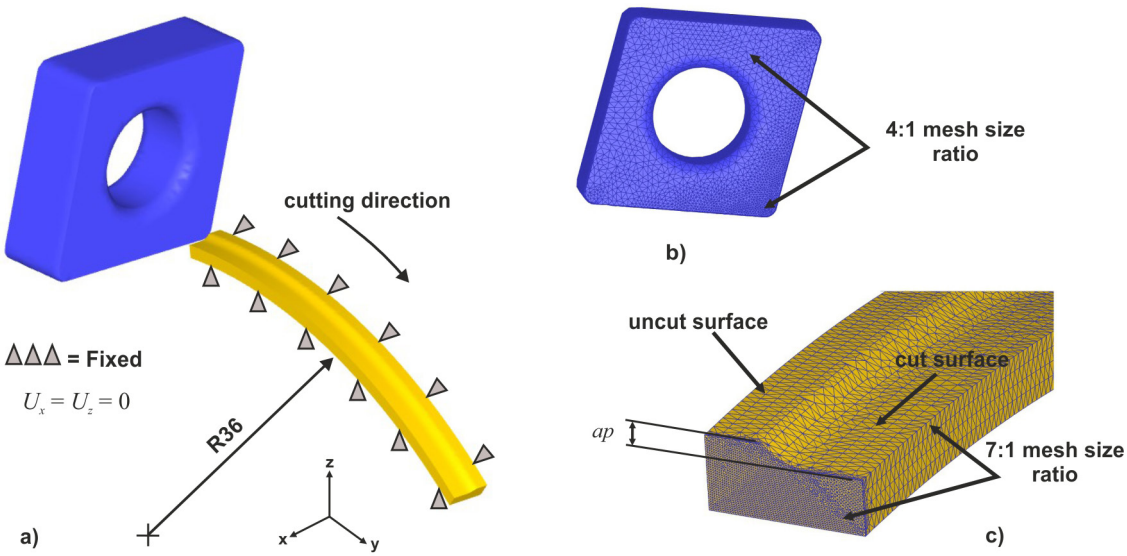

Fig. 2. *a) The FE model setup, b) the meshed insert, and c) the analysis domain*

remeshing with the default interference depth, strain and strain rate distribution so that more elements can be generated in the area of interest. The goal of the implementation of this method is to improve the simulation time and the geometry of the formed chip.

Next, the necessary boundary conditions were defined. The workpiece was fixed so that the velocity of the nodes in X and Z axis was equal to zero, as shown in Fig. 2a. The tool was also allowed to follow the trajectory as dictated by the cutting direction (Fig. 2a). Furthermore, the boundary conditions for the heat exchange with the environment were attributed to all surfaces of the workpiece. The default values of heat transfer coefficient for both convection and conduction were used. According to DEFORM3D™ manual **[24]**, the default value for the heat transfer coefficient via convection is 0.02 N/(s×mm×°C) for dry cutting and via conduction is 45 N/(s×mm×°C).

1.3.2 Tool–Workpiece Material Modelling

In this study, the material modelling for the hard-turning of AISI 4140 was realized with the Johnson-Cook plasticity model, which is widely used to approximate machining processes that are followed by large deformations and high temperatures. The relationship between the constitutive parameters is described by Eq. (1) **[18]**.

$$\sigma = \left(A + B\varepsilon^{n}\right)\left(1 + C\ln\frac{\dot{\varepsilon}}{\dot{\varepsilon}_0}\right)\left[1 - \left(\frac{T - T_0}{T_m - T_0}\right)^{m}\right]. \quad (1)$$

In the given equation, σ denotes the equivalent stress, A is the initial yield stress, B is the strain hardening modulus, C is the strain rate dependence coefficient, ε is the plastic strain, n is the strain hardening exponent, m is the thermal softening coefficient, is the plastic strain rate, whereas is the reference plastic strain rate, T is the reference temperature, T_0 is the ambient temperature, and finally T_m is the melting temperature of the workpiece material. The most important thermo-mechanical properties of AISI 4140 and ceramic tool material are presented in Table 2. The elastic modulus, the thermal expansion, the thermal conductivity and the heat capacity of the workpiece material are all temperature dependent, thus their values were expressed as a function of temperature $f(Temp)$. Additionally, the Johnson-Cook model constants are included in Table 3. The properties and the model constants for the steel are available in the software's library. For the simulation tests that are discussed in this paper, a reference strain rate of 1/s was employed.

The phenomenon of the material separation that takes place during turning was approximated with the employment of the normalized Cockroft-Latham damage model, which can be expressed by Eq. (2) **[25]**. In this expression, the maximum principal stress is normalized by the effective stress.

$$D_c = \int_0^{\varepsilon_f} \frac{\sigma_{\max}}{\bar{\sigma}} d\varepsilon_{pl}, \quad (2)$$

where D_c represents the material constant in the fracture criterion, σ_{max} is the maximum tensile

Table 2. *Thermo-mechanical properties for tool* **[1]** *– workpiece* **[24]**

	Material	Young's Modulus [GPa]	Density [kg/m^3]	Poisson's ratio	Hardness [HRC]
Mechanical properties	AISI4140	212 @ 20 °C 192 @ 300 °C 164 @ 600 °C	7850	0.30	60
	Ceramic	415	3500	0.22	–

	Material	Heat capacity [J/(kgK)]	Thermal expansion [μm/(mK)]	Thermal conductivity [W/(mK)]
Thermal properties	AISI4140	362 @ 20 °C	11.9 @ 20 °C	41.7 @ 20 °C
		446 @ 300 °C	13.6 @ 300 °C	41.4 @ 300 °C
		610 @ 600 °C	14.9 @ 600 °C	34.1 @ 600 °C
	Ceramic	334	8.4	7.5

Table 3. *Johnson–Cook constitutive model constants for AISI4140* **[24]**

A [MPa]	B [MPa]	C	n	m	T_0 [°C]	T_m [°C]
106	1167	0.0352	0.1424	0.763	20	1547

principal stress, is the effective stress, ε_f is the limit fracture strain and ε_{pl} is the plastic strain.

Next, Coulomb's law was utilized to model the friction situation at the tool-workpiece interface. The interaction between two bodies that are under very high contact pressure is a complex problem in machining processes; although more advanced models are available in the literature, Coulomb's friction model provides a good approximation of the friction forces that develop during sliding zone, which is important when studying machining processes. Eq. (3) **[26]** can be used to estimate the frictional stresses defined by Coulomb's law.

$$\tau_f = \mu\sigma_n, \tag{3}$$

where τ_f is the frictional shear stress, μ is the shear friction coefficient and σ_n is the tool–chip interface stress. In the present investigation, the value of the shear friction coefficient was taken equal to 0.577 according to Astakhov **[26]**.

2 RESULTS AND DISCUSSION

2.1 FE Evaluation of the Machining Force Components

Figs. 3a, 3b, and 3c illustrate the force versus time diagrams of the three components (F_r, F_t and F_a) of the main machining force that were generated during AISI 4140 hard turning with the next cutting parameters: V_c = 150 m/min, f = 0.14 mm/rev and ap = 0.30 mm. It is pointed out that all three forces increase rapidly until steady state is achieved; then at about 0.011 s, force values plummet, which means that the insert reached the other end of the workpiece and material separation halted. Even though a sudden increase in force occurred at some time steps, the overall fluctuation of the curve is small. Any fluctuation is due to the remeshing process that takes place between time steps. In order to soften this effect, the default first-order exponential smoothing of DEFORM3D™ was applied. According to Aouici et al. **[23]**, the experimental values for the force components during the aforementioned conditions are F_r = 246 N, F_t = 167.6 N and F_a = 108.8 N, respectively. The force values found after running the equivalent simulation test are F_r = 259.2 N, F_t = 154.8 N and F_a = 108.3 N which indicates a high level of agreement; specifically, the relative error was estimated -5.1 %, 8.3 % and 0.5 % accordingly. In addition to the forces, Fig. 3d depicts the chip formation procedure for the same conditions. A typical curling of the chip based on the cutting speed, feed, and depth of cut is present. Finally, a similar trend for the curve was noticed in all of the rest simulation tests with the exception of the occurrence of the spikes that varied in amount and magnitude.

With the processing of the results, the next graphs were plotted for comparison purposes, as illustrated in Fig. 4. These graphs present the mean values of the radial force (Fig. 4a), the tangential force (Fig. 4b), the feed force (Fig. 4c) and the resultant of the three components (Fig. 4d) for both the simulations and the experiments. The overall agreement between the simulated and the experimental values is good with relative error between -5.3 % and 12.7 % for the F_r, -9.4 % and 11.6 % for the F_t, -14.8 % and 13 % for the F_a. Moreover, the simulated resultant cutting force

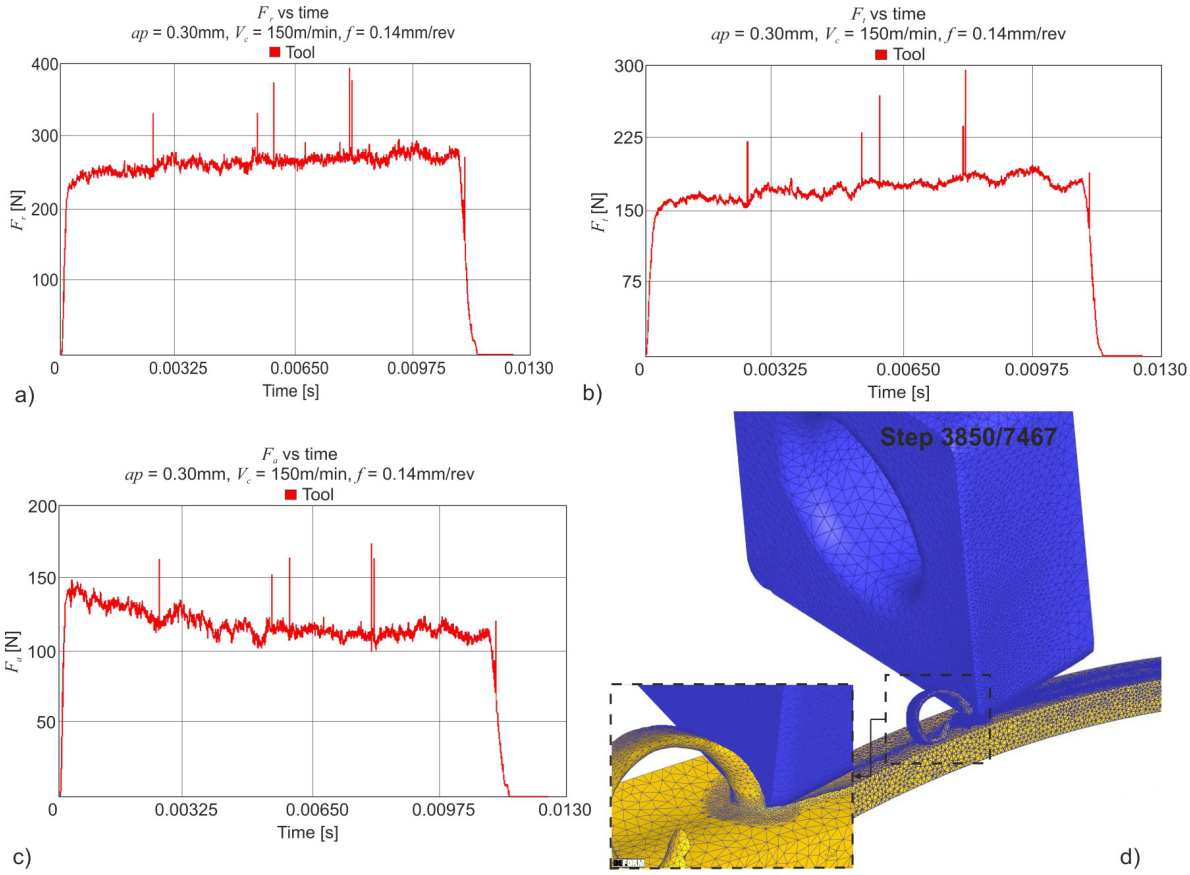

Fig. 3. *a), b) and c) FE model sample results for turning forces, and d) chip formation*

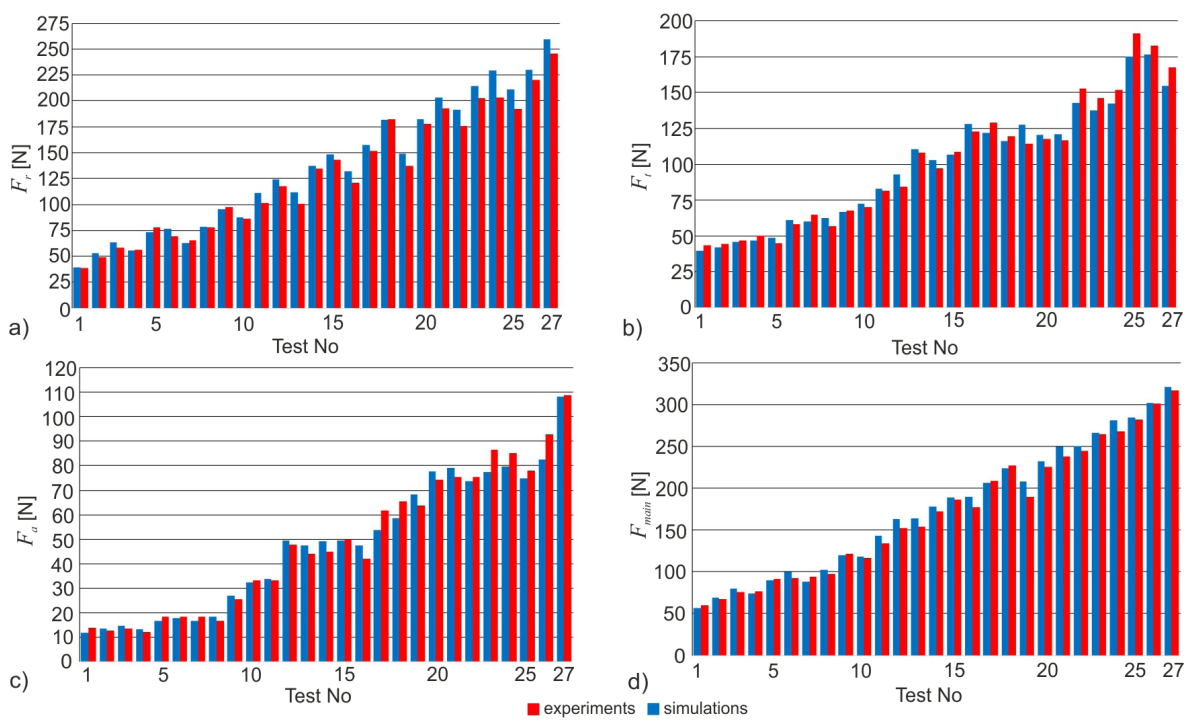

Fig. 4. *Comparison between simulated and experimental turning forces*

is in accordance with the estimated experimental one with a relative error of about -9.1 % to 9.4 %

It can also be observed that the dominant of the three components is the radial force which eventually affects the resultant cutting force the most (Fig. 4d), in contrast to the effect of the feed force, which is subtle. Furthermore, the resultant cutting forces are of the same magnitude with those found in the work of Gaitonde et al. [27] during the turning of AISI D2 at the same cutting conditions and similar ceramic tools (CC650WG). Additionally, it was found that any increase in the feed rate boosts the cutting forces considerably. Aouici et al. [23] and [28] presented results close to those available in this investigation, for turning of AISI 4140 and AISI D3 steel respectively, with similar cutting tools (CC6050) and identical cutting conditions. In contrast, it is noted that increasing the cutting speed usually leads to a decrease in all three force components (F_r, F_t and F_a). Finally, the depth of cut has the greatest influence on cutting forces, which is reported as well in the literature [23], [28] and [29]. Specifically, the cutting forces increase significantly as the cutting insert goes deeper into the material. The findings of this study are discussed in detail in Section 2.2.

2.2 Modelling of the Resultant Cutting Force Based on Statistical Methods

After the completion of the 27 simulation runs, it is concluded that the increased percentage of agreement between the experimental and the numerical values is preserved throughout the testing (see Table 4). Thus, a statistical model is feasible so that future experiments for different depths of cut and similar machining conditions can be minimized. The RSM was employed in this study to develop the proposed statistical model for prediction purposes of the main cutting force during AISI 4140 hard turning. RSM is a well-established methodology that is often used to optimize process conditions or determine the interaction between multiple factors. Additionally, it provides concise presentation of results. This methodology was successfully utilized in many studies related to machining processes such as turning and drilling [4], [15] and [30] to [32]; therefore, it was selected for the current work. Based on the parameters involved (see Table 1) and the number of simulation runs, a full factorial design with three factors was realized. Because the relationship between the variables and the output in this study is anticipated to be non-linear, the regression model can be described with a second-order polynomial, as seen in Eq. (4). This polynomial includes linear, quadratic, and interactive terms: Y is the output of the model, thus the main machining force, in this case, X_i are the coded values (cutting speed, feed and depth of cut) and b_i are the vectors that contain the regression coefficients.

$$Y = b_0 + b_1X_1 + b_2X_2 + b_3X_3 + b_4X_1^2 + b_5X_2^2 + b_6X_3^2 + b_7X_1X_2 + b_8X_1X_3 + b_9X_2X_3. \quad (4)$$

Eq. (5) presents the complete statistical model for the resultant machining force based on the aforementioned formula and the data of the verified FE model (see Table 4).

$$F_{main} = -112.2 + 0.566V + 820f + 422.1ap - 0.00074V^2 - 1860f^2 + 125ap^2 - 0.67Vf + 0.708Vap + 3124fap, \quad (5)$$

where F_{main} is the resultant machining force in N, V is the cutting speed in m/min, f is the feed in mm/rev and ap is the depth of cut in mm.

The design of experiments (see Table 4) contains the estimation of the resultant cutting force for all 27 combinations of machining parameters, derived from the experiments [23], the simulations and the statistical model. The comparison of these results shows an increased correlation. Specifically, the highest level of agreement between the numerical values and the experimental ones is observed in the test number 26 (relative error 0.2 %), whereas the lowest in test number 19 (relative error 12.4 %). Between the values obtained from the regression model and the numerical values, test number 19 yielded an agreement of almost 100 %. In contrast, the lowest level of accordance (91.2 %) was found to be in the first test. Eventually, for the comparison case between the statistical values and the experimental ones, a high correlation is highlighted with a mean absolute percentage error of approximately 4.6 %. Furthermore, the best level of agreement (99.6 %) was achieved in the second test, whereas the worst (86.6 %) in the first one. By observing Table 4 and the charts of Fig. 4, the following statements can be made for the FE model:

- The radial force is the dominant of the three components.
- Higher values of feed rate affect all forces, but the tangential force is affected the most due to the increase of the sheared chip region.
- The depth of cut has a strong impact on all machining forces as anticipated; as the tool cuts deeper in the material, the tool-workpiece contact length increases. For instance, the main cutting force increases approximately 43.6 % (from

Table 4. *Main machining force comparison between experimental, simulated and statistical values*

Std Order	Cutting parameters			F_{main} [N]		
	V_c [m/min]	f [mm/rev]	ap [mm]	Experiments	FE model	Regression model
1	80	0.08	0.10	59.9	56.9	51.9
2	115	0.08	0.10	67.5	69.0	73.6
3	150	0.08	0.10	76.0	79.5	92.0
4	80	0.11	0.10	76.3	73.9	67.2
5	115	0.11	0.10	91.5	89.7	88.3
6	150	0.11	0.10	92.4	99.6	106.0
7	80	0.14	0.10	94.2	88.4	80.8
8	115	0.14	0.10	97.5	102.2	101.1
9	150	0.14	0.10	121.3	119.5	118.1
10	80	0.08	0.20	116.1	118.2	128.5
11	115	0.08	0.20	134.3	142.8	159.6
12	150	0.08	0.20	152.2	163.1	187.4
13	80	0.11	0.20	154.2	164.1	146.3
14	115	0.11	0.20	172.2	178.4	176.8
15	150	0.11	0.20	186.5	189.2	203.8
16	80	0.14	0.20	177.3	189.7	162.4
17	115	0.14	0.20	208.6	206.1	192.1
18	150	0.14	0.20	227.3	223.4	218.5
19	80	0.08	0.30	189.8	207.7	207.6
20	115	0.08	0.30	225.7	232.1	248.1
21	150	0.08	0.30	238.0	249.6	285.3
22	80	0.11	0.30	244.6	250.2	227.9
23	115	0.11	0.30	264.1	266.2	267.7
24	150	0.11	0.30	267.7	281.2	304.2
25	80	0.14	0.30	282.3	284.5	246.4
26	115	0.14	0.30	300.9	301.5	285.5
27	150	0.14	0.30	316.9	320.7	321.3

223.4 N to 320.7 N) for the same conditions (V_c = 150 m/min, f = 0.14 mm/rev) and an increase in depth of cut from 0.20 mm to 0.30 mm.

- Lastly, as cutting speed rises, the turning forces decrease in most cases, so does the main cutting force. For example, at ap = 0.30 mm, f = 0.14 mm/rev and V_c = 150 m/min, 115 m/min and 80 m/min the resultant force is equal to 320.7 N, 301.5 N and 284.5 N respectively. The primary reason for this tendency is that an increase in temperature at the shear plane region, resulting in the plastic softening of the deformation zone which ultimately lowers the shear strength of the material.

Fig. 5 illustrates the relative error percentage between the values of resultant machining force derived from the regression model and the experiments, as well as between the regression model and the simulations. The graph indicates that both lines follow a similar trend with the exception of two points (tests number 6 and 19) where more abrupt increase in experimental values occurred.

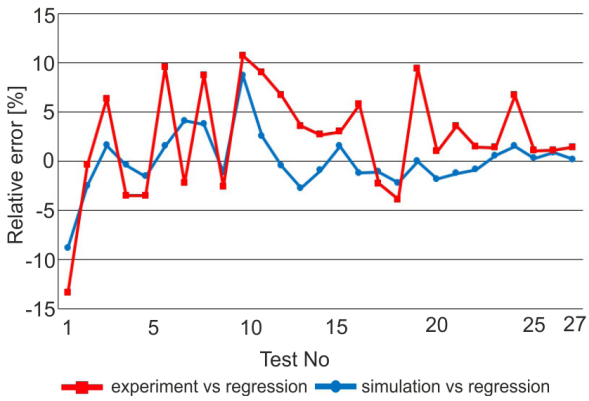

Fig. 5. *Relative error comparison between simulations and experiments*

Moreover, the maximum error was found to be -13.4 % and -8.8 % for the regression versus

experiments and the regression versus simulations, respectively (test number 1 for both cases). In contrast, the lowest value of error was determined to be -0.4 % (test 2) for the regression versus experiments and close to zero (test 19) for the regression versus simulations. Finally, the mean absolute percentage error was estimated 2 % for the regression versus simulations case and 4.6 % for the regression versus experiments case.

2.3 Validation of the Statistical Model

Due to the number of independent variables taken into account in current research, the validity of the fit was analysed with ANOVA. A standard confidence level of 95 % was used for all intervals throughout the analysis, which revealed a successful fit of the model with an adjusted R-squared of 99.72 %. Furthermore, according to the significance level of 0.05 and to Table 4 the terms that contribute the most to the model are the *ap* and the $f \times ap$ with a *p*-value equal to 0.000, as well as the constant with p = 0.005. Last but not least, $V \times ap$ and *f* have great impact on the model with *p*-values of 0.060 and 0.089 respectively, even though are higher than 0.05. The sum of squares and the degrees of freedom for the analysis are included in Table 5. With the total sum of squares which is the sum of squared deviations due to each of the nine factors and the sum of squares attributed to the error, it is possible to determine the dispersion of data points. In addition, the mean square is the ratio of the sum of squares to the degree of freedom and the *f*-value is the ratio of the mean square of the regression model to the mean square of residual error. Lastly, the fact that the *p*-value of the regression was estimated 0.000 indicates the very high correlation of the model and eliminates the probability of yielding unusual results.

With the validation of goodness of fit, a residual analysis was performed to check the accuracy of the model. The graphs that are illustrated in Fig. 6 proves that the model has very good accuracy. In particular, the normal probability plot (Fig. 6a) shows a normality in the distribution of the residuals with no serious departures from the straight line. Additionally, the residuals versus the fitted values (Fig. 6b) indicate a constant variance of the residuals since they are almost evenly scattered on both sides of the reference line. The overall normality is present in the residuals versus the order graph also (Fig. 6d). It is observed that there are no systematic faults, and the residuals are independent of one another. Eventually, the normality in the distribution of the error percentages can be displayed in the error histogram (Fig. 6c) and proved by the fit line.

The analysis of the developed prediction model was carried out with the aid of 3D response surface plots for visualizing the data gathered from Fig. 4 and Table 4. That is, the combined effect of the machining conditions and the depth of cut on the generated radial, tangential and feed forces were investigated. Fig. 7 illustrates the plotted 3D surfaces for each depth of cut value based on the polynomial solutions. The cutting speed and the feed are the input parameters of the polynomial with values within the investigated range,

Table 5. *ANOVA results for the main machining force*

Source	Degree of freedom	Sum of squares	Mean square	*f*-value	*p*-value
Regression	9	165668	18407.6	1012.4	0.000
Residual error	17	309	18.2		
Total	26	165977			
R-sq (adj) = 99.72 %					

Term	PE Coefficient	SE Coefficient	*f*-value	*p*-value
Constant	−112.8	35.1	−3.19	0.005
V	0.566	0.359	1.58	0.134
f	820	455	1.80	0.089
ap	422.1	92.9	4.55	0.000
V^2	−0.00074	0.00142	−0.52	0.609
f^2	−1860	1934	−0.96	0.350
ap^2	125	174	0.72	0.482
$V \times f$	−0.67	1.17	−0.57	0.574
$V \times ap$	0.708	0.352	2.01	0.060
$f \times ap$	3124	410	7.61	0.000

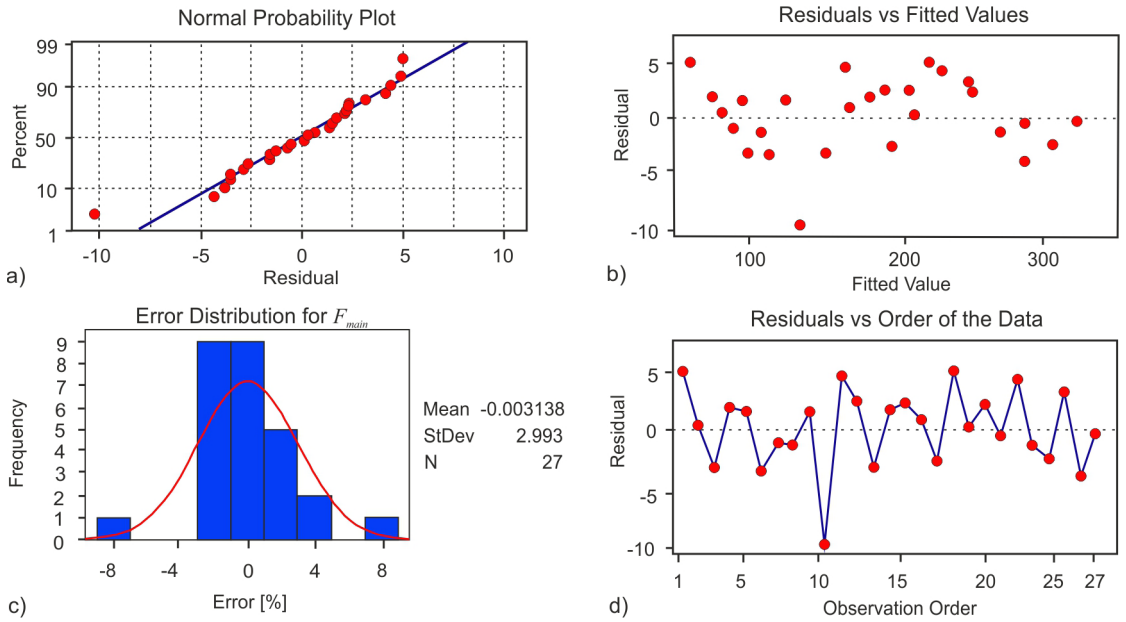

Fig. 6. *Residual analysis graphs: a) probability plot, b) residuals versus fitted values, c) error histogram, and d) residuals versus order*

hence 80 m/min to 150 m/min for cutting speed (step of 10 m/min) and 0.08 mm/rev to 0.14 mm/rev for feed (step of 0.01 mm/rev). According to Fig. 7 it is concluded that:

- The depth of cut affects the resultant machining force significantly; as the depth of cut increases, so does the force.
- Similarly, higher values of feed have a great impact on the main machining force.
- Eventually, even though higher cutting speeds result in lowering the machining force, the effect is limited.

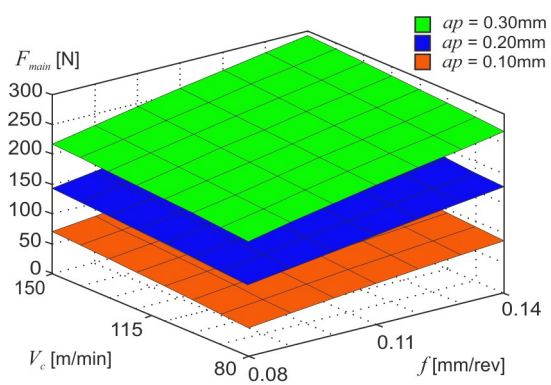

Fig. 7. *3D plots of the F_{main} for each depth of cut*

Conclusively, six extra simulation runs were accomplished to further validate the prediction model of F_{main} by utilizing randomly selected conditions from within the range of the data employed in this study, forming the following sets: I, II and III with V_c = 100 m/min, f = 0.12 mm/rev and ap = 0.15 mm, 0.25 mm and 0.30 mm respectively. IV, V and VI with V_c = 130 m/min, f = 0.10 mm/rev and ap = 0.15 mm, 0.25 mm and 0.30 mm respectively. The results are presented in Table 6, in which it is highlighted that the relative error is low for all cases.

Table 6. *Confirmation of prediction model for F_{main}*

Set	Simulated F_{main} [N]	Predicted F_{main} [N]	Relative error [%]
I	147.8	133.6	−9.61
II	239.3	225.3	−5.85
III	260.4	272.2	4.53
IV	140.5	130.4	−7.19
V	233.8	218.0	−6.76
VI	248.9	262.8	5.58

3 CONCLUSIONS

In this study, the development of a 3D FE model, as well as a prediction model for the main machining force induced during hard turning of AISI 4140, were presented. A series of 27 3D simulations were conducted under different conditions of cutting speed and feed in addition to the three different depths of cut. The obtained numerical results were validated via experimental values that are available in the literature,

and it was observed that are in high agreement that surpasses 90 % in most of the runs. The accuracy (8.8 %) and goodness of fit of the statistical model, dictate that both the developed models (FE and statistical) can securely predict the resultant machining forces when applied within the scope of this study. In conclusion, the following remarks are pointed out:

- Higher values of depth of cut and feed rate significantly increase machining forces, especially the depth of cut is the factor that effects F_{main} the most. Specifically, according to the simulated values of F_{main} (see Table 3), an average increase of about 104 % in the resultant cutting force is observed when the depth of cut changes from 0.10 mm to 0.20 mm. The equivalent shift from 0.20 mm to 0.30 mm amplifies F_{main} by approximately 50 %.
- Similarly, when feed changes from 0.08 mm/rev to 0.11 mm/rev and from 0.11 mm/rev to 0.14 mm/rev, the resultant cutting force gains an increase of about 24 % and 16 % respectively.
- In contrast, the generated forces decrease as cutting speed increases; however, the changes induced by cutting speed are trivial compared to the ones caused by the depth of cut and feed. The average percentage of decrease observed in F_{main}, is estimated at approximately 10 % when cutting speed shifts from 150 m/min to 115 m/min. Additionally, as the value of V_c lowers from 115 m/min to 80 m/min, the F_{main} decreases ny about 13 % on average.
- The factors that have great impact on the statistical model based on the significance level are: ap, $f \times ap$, constant, $V \times ap$ and f.

4 REFERENCES

[1] Hu, H.-J., Huang, W.-J. (2014). Tool life models of nano ceramic tool for turning hard steel based on FEM simulation and experiments. *Ceramics International*, vol. 40, no. 7, Part A, p. 8987-8996, **DOI:10.1016/j.ceramint.2014.01.095**.

[2] Davim, J.P., Figueira, L. (2007). Machinability evaluation in hard turning of cold work tool steel (D2) with ceramic tools using statistical techniques. *Materials & Design*, vol. 28, no. 4, p. 1186-1191, **DOI:10.1016/j.matdes.2006.01.011**.

[3] Asiltürk, I., Akkuş, H. (2011). Determining the effect of cutting parameters on surface roughness in hard turning using the Taguchi method. *Measurement*, vol. 44, no. 9, p. 1697-1704, **DOI:10.1016/j.measurement.2011.07.003**.

[4] Mia, M., Dhar, N.R. (2016). Response surface and neural network based predictive models of cutting temperature in hard turning. *Journal of Advanced Research*, vol. 7, no. 6, p. 1035-1044, **DOI:10.1016/j.jare.2016.05.004**.

[5] Quiza, R., Figueira, L., Davim, J.P. (2008). Comparing statistical models and artificial neural networks on predicting the tool wear in hard machining D2 AISI steel. *International Journal of Advanced Manufacturing Technology*, vol. 37, no. 7-8, p. 641-648, **DOI:10.1007/s00170-007-0999-7**.

[6] Gaitonde, V.N., Karnik, S.R., Figueira, L., Davim, J.P. (2011). Performance comparison of conventional and wiper ceramic inserts in hard turning through artificial neural network modeling. *International Journal of Advanced Manufacturing Technology*, vol. 52, no. 1-4, p. 101-114, **DOI:10.1007/s00170-010-2714-3**.

[7] Klocke, F., Raedt, H.-W., Hoppe, S. (2001). 2D-FEM simulation of the orthogonal high speed cutting process. *Machining Science and Technology*, vol. 5, no. 3, p. 323-340, **DOI:10.1081/MST-100108618**.

[8] Yen, Y.-C., Söhner, J., Weule, H., Schmidt, J., Altan, T. (2002). Estimation of tool wear of carbide tool in orthogonal cutting using FEM simulation. *Machining Science and Technology*, vol. 6, no.3, p. 467-486, **DOI:10.1081/MST-120016256**.

[9] Arrazola, P.J., Villar, A., Ugarte, D., Marya, S. (2007). Serrated chip prediction in finite element modeling of the chip formation process. *Machining Science and Technology*, vol. 11, no. 3, p. 367-390, **DOI:10.1080/10910340701539882**.

[10] Agmell, M., Ahadi, A., Ståhl, J.-E. (2013). The link between plasticity parameters and process parameters in orthogonal cutting. *Procedia CIRP*, vol. 8, p. 224-229, **DOI:10.1016/j.procir.2013.06.093**.

[11] Yameogo, D., Haddag, B., Makich, H., Nouari, M. (2017). Prediction of the cutting forces and chip morphology when machining the Ti6Al4V alloy using a microstructural coupled model. *Procedia CIRP*, vol. 58, p. 335-340, **DOI:10.1016/j.procir.2017.03.233**.

[12] Wan, L., Wang, D., Gao, Y. (2015). Investigations on the effects of different tool edge geometries in the finite element simulation of machining. *Strojniški vestnik - Journal of Mechanical Engineering*, vol. 61, no. 3, p. 157-166, **DOI:10.5545/sv-jme.2014.2051**.

[13] Attanasio, A., Ceretti, E., Rizzuti, S., Umbrello, D., Micari, F. (2008). 3D finite element analysis of tool wear in machining. *CIRP Annals*, vol. 57, no. 1, p. 61-64, **DOI:10.1016/j.cirp.2008.03.123**.

[14] Hu, H.-J., Huang, W.-J. (2013). Effects of turning speed on high-speed turning by ultrafine-grained ceramic tool based on 3D finite element method and experiments. *International Journal of Advanced Manufacturing Technology*, vol. 67, no. 1-4, p. 907–915, **DOI:10.1007/s00170-012-4535-z**.

[15] Malakizadi, A., Gruber, H., Sadik, I., Nyborg, L. (2016). An FEM-based approach for tool wear estimation in machining. *Wear*, vol. 368-369, p. 10-24, **DOI:10.1016/j.wear.2016.08.007**.

[16] Arisoy, Y., Özel, T. (2015). Prediction of machining induced microstructure in Ti-6Al-4V alloy using 3-D FE-based simulations: Effects of tool micro-geometry, coating and cutting conditions. *Journal of Materials Processing Technology*, vol. 220, p. 1-26, **DOI:10.1016/j.jmatprotec.2014.11.002**.

[17] Vijayaraghavan, V., Garg, A., Gao, L., Vijayaraghavan, R., Lu, G. (2016). A finite element based data analytics approach for modeling turning process of Inconel 718 alloys. *Journal of*

Cleaner Production, vol. 137, p. 1619-1627, **DOI:10.1016/j.jclepro.2016.04.010**.

[18] Rami, A., Kallel, A., Sghaier, S., Youssef, S., Hamdi, H. (2017). Residual stresses computation induced by turning of AISI 4140 steel using 3D simulation based on a mixed approach. *International Journal of Advanced Manufacturing Technology*, vol. 91, no. 9-12, p. 3833-3850, **DOI:10.1007/s00170-017-0047-1**.

[19] Guo, Y. B. and Liu, C. R. (2002). 3D FEA modeling of hard turning. *Journal of Manufacturing Science and Engineering*, vol. 124, no. 2, p. 189-199, **DOI:10.1115/1.1430678**.

[20] Özel, T., Karpat, Y., Srivastava, A. (2008). Hard turning with variable micro-geometry PcBN tools. *CIRP Annals*, vol. 57, no. 1, p. 73-76, **DOI:10.1016/j.cirp.2008.03.063**.

[21] Lian, Y.-S., Mu, C.-L., Liu, M., Chen, H.-F., Yao, B. (2019). Three-dimensional numerical simulation of soft/hard composite-coated textured tools in dry turning of AISI 1045 steel. *Advances in Manufacturing*, vol. 7, no. 2, p. 133-141, **DOI:10.1007/s40436-019-00249-2**.

[22] Magalhães, F.C., Ventura, C.E.H., Abrão, A.M., Denkena, B. (2020). Experimental and numerical analysis of hard turning with multi-chamfered cutting edges. *Journal of Manufacturing Processes*, vol. 49, p. 126-134, **DOI:10.1016/j.jmapro.2019.11.025**.

[23] Aouici, H., Elbah, M., Yallese, M.A., Fnides, B., Meddour, I., Benlahmidi, S. (2016). Performance comparison of wiper and conventional ceramic inserts in hard turning of AISI 4140 steel: analysis of machining forces and flank wear. International *Journal of Advanced Manufacturing Technology*, vol. 87, no. 5-8, p. 2221-2244, **DOI:10.1007/s00170-016-8567-7**.

[24] Scientific Forming Technologies Corporation. DEFORM V11.3 (PC) (2016). Documentation. SFTC, Columbus.

[25] Mirghasemi, S.M., Eivani, A.R., Seyedein, S H., Jafarian, H.R. (2018). A comparison between routine vs. normalized Cockroft-Latham fracture criteria for prediction of fracture during equal channel angular pressing. *Engineering Fracture Mechanics*, vol. 199, p. 721-729, **DOI:10.1016/j.engfracmech.2018.07.016**.

[26] Astakhov, V.P. (2006). *Tribology of Metal Cutting*, Elsevier, Amsterdam.

[27] Gaitonde, V.N., Karnik, S.R., Figueira, L., Davim, J.P. (2009). Analysis of machinability during hard turning of cold work tool steel (type: AISI D2). *Materials and Manufacturing Processes*, vol. 24, no. 12, p. 1373-1382, **DOI:10.1080/10426910902997415**.

[28] Aouici, H., Bouchelaghem, H., Yallese, M.A., Elbah, M., Fnides, B. (2014). Machinability investigation in hard turning of AISI D3 cold work steel with ceramic tool using response surface methodology. *International Journal of Advanced Manufacturing Technology*, vol. 73, p. 1775-1788, **DOI:10.1007/s00170-014-5950-0**.

[29] Lalwani, D.I., Mehta, N.K., Jain, P.K. (2008). Experimental investigations of cutting parameters influence on cutting forces and surface roughness in finish hard turning of MDN250 steel. *Journal of Materials Processing Technology*, vol. 206, no. 1-3, p. 167-179, **DOI:10.1016/j.jmatprotec.2007.12.018**.

[30] Çiçek, A., Kıvak, A., Samtaş, T., Çay, G. (2012). Modelling of thrust forces in drilling of AISI 316 stainless steel using artificial neural network and multiple regression analysis. *Strojniški vestnik - Journal of Mechanical Engineering*, vol. 58, no. 7-8, p. 492-498, **DOI:10.5545/sv-jme.2011.297**.

[31] Efkolidis, N. García-Hernández, C., Huertas-Talón, J.L., Kyratsis, P. (2018). Modelling and prediction of thrust force and torque in drilling operations of Al7075 using ANN and RSM methodologies. *Strojniški vestnik - Journal of Mechanical Engineering*, vol. 64, no. 6, p. 351-361, **DOI:10.5545/sv-jme.2017.5188**.

[32] Tzotzis, A., García-Hernández, C. Huertas-Talón, J.L., Kyratsis, P. (2020). FEM based mathematical modelling of thrust force during drilling of Al7075-T6. *Mechanics & Industry*, vol. 21, no. 4, p. 1-14, **DOI:10.1051/meca/2020046**.

micromachines

MDPI

Article

Influence of the Nose Radius on the Machining Forces Induced during AISI-4140 Hard Turning: A CAD-Based and 3D FEM Approach

Anastasios Tzotzis [1,*], César García-Hernández [1], José-Luis Huertas-Talón [1] and Panagiotis Kyratsis [2]

[1] Department of Design and Manufacturing Engineering, University of Zaragoza, 50018 Zaragoza, Spain; cesarg@unizar.es (C.G.-H.); jhuertas@unizar.es (J.-L.H.-T.)

[2] Department of Product and Systems Design Engineering, University of Western Macedonia, 50100 Kila Kozani, Greece; pkyratsis@uowm.gr

* Correspondence: atzotzis@unizar.es

Received: 4 August 2020; Accepted: 21 August 2020; Published: 23 August 2020

Abstract: The present study investigated the performance of three ceramic inserts in terms of the micro-geometry (nose radius and cutting edge type) with the aid of a 3D finite element (FE) model. A set of nine simulation runs was performed according to three levels of cutting speed and feed rate with respect to a predefined depth of cut and tool nose radius. The yielded results were compared to the experimental values that were acquired at identical cutting conditions as the simulated ones for verification purposes. Consequently, two more sets of nine simulations each were carried out so that a total of 27 turning simulation runs would adduce. The two extra sets corresponded to the same cutting conditions, but to different cutting tools (with varied nose radius). Moreover, a prediction model was established based on statistical methodologies such as the response surface methodology (RSM) and the analysis of variance (ANOVA), further investigating the relationship between the critical parameters (cutting speed, feed rate, and nose radius) and their influence on the generated turning force components. The comparison between the experimental values of the cutting force components and the simulated ones demonstrated an increased correlation that exceeded 89%. Similarly, the values derived from the statistical model were in compliance with the equivalent FE model values due to the verified adequacy.

Keywords: AISI4140 turning; machining forces; tool micro-geometry; nose radius; 3D FEM; DEFORM3D; RSM

1. Introduction

Turning is one of the most widely used machining operations in industry. In particular, turning of hardened steel is an indispensable part in a modern manufacturing framework. Moreover, AISI-4140 is preferred for the production of many typical mechanical parts such as gears, shafts, and bearings [1]. For these reasons, a number of studies exist in the literature that investigate various aspects that occur during the machining of hardened steel [2–6]. The methods that are usually implemented in such research usually involve experimental work, statistical, and numerical analyses. However, the number of cases that use the finite element method (FEM) during numerical analysis is not high. Furthermore, the majority of FEM-based numerical studies tend to develop 2D models.

Saez-de-Buruaga et al. [7] proposed a methodology that determined the influence of cutting conditions on the developed cutting temperatures that was compared to the 2D simulated results of the tool/chip contact temperatures. Ye et al. [8] studied high speed cuttings of various metallic materials over wide ranges of cutting speeds. The authors used the model for prediction purposes of

the critical cutting speed at which the serrated chip flow occurs. Similarly, Shuang et al. [9] performed 2D cutting simulations to better understand the chip formation and material behavior during high speed machining of the Ti6Al4V alloy. Orthogonal cutting simulations provide researchers with important insights into numerous machining aspects such as the estimation of tool wear, machining forces, temperatures, residual stresses, etc. at reasonable computational cost [4,10–12]. Despite the fact that 3D simulations require a hefty amount of computational resources compared to 2D, they do not share the restrictions that two-dimensional simulations have [13]. In addition, three-dimensional FEM enabled by high-end computers provide better visualization and understanding of practical cutting operations [14].

With the aid of 3D FEM, complex operations such as drilling and milling can be studied in order to obtain more information on important parameters such as the developed forces, tool wear, and microstructure [15–17]. The three-dimensional FEM has also been used during investigations of turning with the same success. An early example is the work of Guo and Liu [18], who developed a general practical explicit 3D finite element analysis (FEA) model for the analytical purposes of AISI-52100 hard turning with the use of polycrystalline cubic boron nitride (PCBN) inserts. Later, Karpat and Ozel [19] developed a 3D FEM-based model to predict forces and temperatures on various uniform and variable edge micro-geometry PCBN turning inserts. Malakizadi et al. [20] presented a FEM-based approach to predict the flank wear for uncoated cemented carbide tools during conventional turning. Similarly, Lotfi et al. [21] worked on the estimation of the tool wear during turning of Inconel 625 with the aid of FEA. The authors used PVD-TiAlN coated carbide and ceramic inserts in order to study the effect of cutting parameters on the tool wear, temperatures and stress distribution. Hu and Huang [22] examined the effects of cutting speed on the turning force, the temperature distribution, and the tool wear during turning of AISI-4130 with ceramic tools based on 3D FEM. Magalhães et al. [23] presented a finite element (FE) model for hard turning with PCBN inserts prepared with multi-chamfered edges and examined the effects on tool wear and residual stresses.

The present paper investigates the effects of the cutting tool's micro-geometry, specifically the nose radius, chamfer width, and angle on the generated machining force components during AISI-4140 hard turning. The tools under study were ceramic inserts of the CNGA family and the research was carried out according to three levels of cutting parameters (cutting speed, feed rate, and nose radius) at a certain depth of cut. The numerical simulations were performed with the aid of DEFORM™-3D FEA software so that a FE model could be established. Moreover, a comparison between the experimental results found in the literature [24] and the numerical ones was conducted for validation purposes. Finally, after validating the FE model, a statistical model based on the response surface methodology (RSM) was developed.

2. Materials and Methods

2.1. CAD-Based Application for Designing Turning Inserts

Nowadays, most tool manufacturers provide CAD models of their products that can be used in 3D simulation runs. However, in most cases, these models are simplified versions and usually miss critical geometric aspects that have important effects on the yielded simulated results. One such geometric parameter is the type of cutting edge. The same conditions also apply to other cutting tools (e.g., drills). In order to overcome this obstacle, a simple yet effective CAD-based application was developed with the aid of the SolidWorks™ application programming interface (API) that accelerated the design process of the insert models used in this study and can be implemented in future projects. Similar work has been done in the past by Vijayaraghavan [25] for drilling tools. The code for this application was developed in Visual Basic for Applications (VBA™) with similar methodologies found in the work of Oancea and Haba [26], and Kyratsis et al. [27]. The graphical interface of the application is illustrated in Figure 1a, whereas Figure 1b contains the workflow. A graphical interface provides users with a simple way to operate the application; in the present case, it was used to select the

design parameters according to ISO-13399 standards. Some design parameters are the shape of the insert, the internal circle's diameter, the cutting edge length, the angle of the corners, the nose radius, the insert's thickness, and the type of the cutting edge along with the chamfer width and chamfer angle. With the selection of the required parameters, the user can click on the "Design Insert" command button so that the automated design process may begin. According to Figure 1b, the design procedure begins with the declaration of the variables that correspond to each of the geometric characteristics of the insert. Consequently, these parameters are linked with the appropriate variables and a new part of the document is created. Later, a fresh sketch is inserted on the preselected plane and the design of the insert contour takes place based on the parameters seen in Figure 1a (inscribed circle, nose radius, cutting edge length, thickness, corner angle, chamfer width, and chamfer angle). The plane was selected in this way, so that the coordinate system of the model matched the coordinate system of the FEA software. Finally, a solid model of the insert is created with the aid of the "FeatureExtrusion2" method, which can then be saved in both native and "STL" file format. Prior to finalizing the model, the micro-geometry is applied according to the type of cutting edge, the chamfer width, and angle that are selected. In order to apply the aforementioned features to the model, the topology selection routine of the program was executed. With this routine, it is possible to automatically find and select the outer edges of the insert, which can be achieved by traversing all the available edges of the solid model that are then stored to a matrix. Each one of the edges receives a unique name so that they can be called and used at any time. Additionally, the traversal of the edges is achieved with the implementation of a "For" loop. Moreover, the API methods that are responsible for the extraction of the edges and the insertion of the chamfer feature are the "GetEdges" and "InsertFeatureChamfer" accordingly.

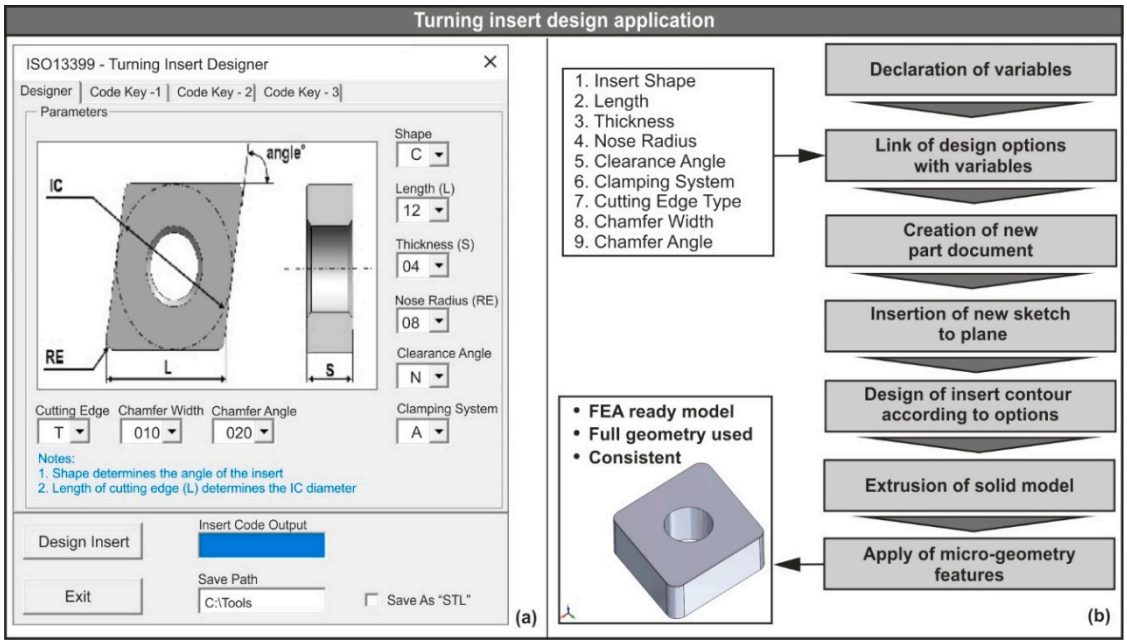

Figure 1. (**a**) The graphical interface of the designer application and (**b**) its workflow.

The generated solid model is a fully defined, consistent model with the full geometry of the equivalent physical model that can be used in FEA. Even though the tool during machining simulations is defined as rigid and thus its properties are not as critical as the workpiece's properties [28], the full geometry of the tool, on the other hand, is crucial. Therefore, such models provide increased accuracy during the analysis and the chance of acquiring non-realistic results is minimal.

2.2. CAD-Based Layout of the Turning Process

In order to build a simplified analysis domain of the turning process, a CAD-based setup was prepared with the aid of Dassault Systemes (Vélizy-Villacoublay, France) SolidWorks™ 2018.

All conditions and geometric characteristics that may affect the cutting process were taken into account. The tool assembly used in this study consisted of a tool-holder and three versions of a conventional rhombic-shaped turning insert. The ISO designation number of the tool-holder was PCBNR2525M12 and the equivalent number for the three inserts was CNGA120404, CNGA120408, and CNGA120412, respectively. The workpiece model was designed as a cylindrical bar with a diameter of 72 mm. Additionally, the applied material for the workpiece was AISI-4140 steel, whereas the insert was ceramic.

The physical model of the tool-holder is depicted in Figure 2a, whereas the CAD-based turning process setup is presented in Figure 2b, along with the generated machining forces: F_t is the tangential force, F_r is the radial force, and F_a represents the feed force. Moreover, Figure 2b includes two schematics that focus on the angles related to the cutting process and the feed direction. These angles are inherited from the tool-holder and the turning insert geometry. Thus, the lead angle was 75° and both the rake and inclination angle were negative with a value of −6°.

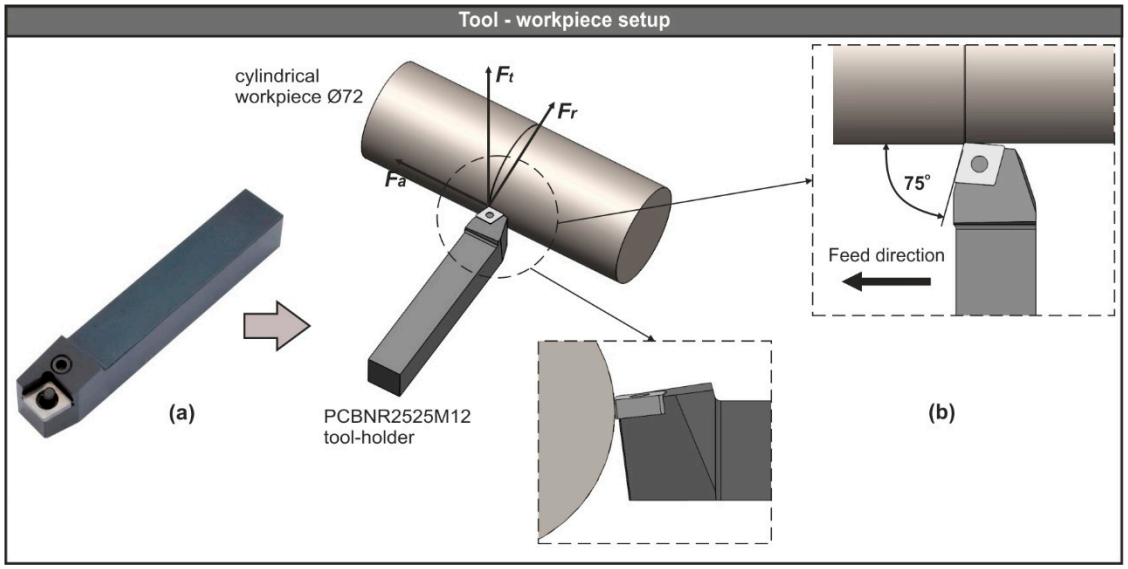

Figure 2. (**a**) The physical model of the PCBNR2525M12 tool-holder and (**b**) the CAD-based tool-workpiece setup.

Figure 3a illustrates the physical model of the CNGA120408T01020 (nose radius *re* = 0.80) uncoated ceramic insert, whereas Figure 3b depicts all critical geometric characteristics of the CNGA1204xx turning inserts. The CNGA-ceramic family were negative, 80° rhombic inserts used for machining cast iron and hardened steel.

In the present study, twenty-seven simulation runs were carried out based on the unique combinations of the three levels of cutting conditions: cutting speed (80 m/min, 115 m/min, 150 m/min), feed rate (0.08 mm/rev, 0.11 mm/rev, 0.14 mm/rev), and nose radius (0.40 mm, 0.80 mm, 1.20 mm). The levels of the aforementioned cutting parameters and their values are summarized in Table 1. In addition, the depth of cut was maintained at 0.30 mm for all tests.

Table 1. Process conditions of the turning finite element (FE) model.

Level	V_c (m/min)	f (mm/rev)	*re* (mm)
I	80	0.08	0.40
II	115	0.11	0.80
III	150	0.14	1.20

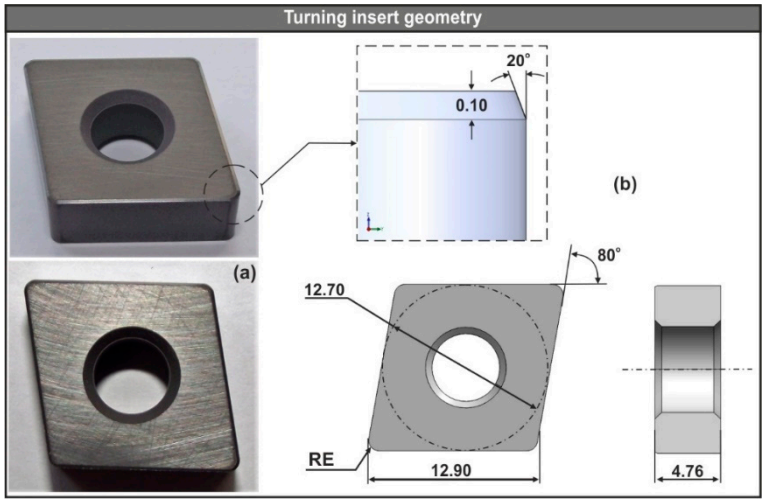

Figure 3. (**a**) The physical model of the CNGA120408T01020 ceramic and (**b**) the analogous CAD model with detailed geometry.

2.3. Pre-Processing of the 3D FE Turning Model

For the 3D simulation tests, a commercially available FEA software was used, namely SFTC (Columbus, Ohio USA) DEFORM™-3D ver. 12. A desktop PC with six-core CPU 3.60 GHz, 16 GB RAM, and SSD technology hard drive was utilized to carry out the simulations. The completion time for the simulation tests with a feed value of 0.14 mm/rev, 0.11 mm/rev, and 0.08 mm/rev was approximately 6, 10, and 22 h, respectively. The reason for the varied completion time is that the mesh size of the workpiece depends on the selected feed value.

After establishing the CAD-based setup of the turning operation, the next step was the preparation of a simplified analysis domain that led to reasonable completion times for the simulation tests. The key points of the simplified setup were the use of the insert model instead of the whole tool assembly and the conversion of the full cylindrical workpiece model to a smaller part, according to the cutting path (circular arc with a diameter of 72 mm and an angle of 45°—see Figure 4a). To further improve the simulation times, the workpiece was designed partially cut based on the depth of cut (Figure 4b).

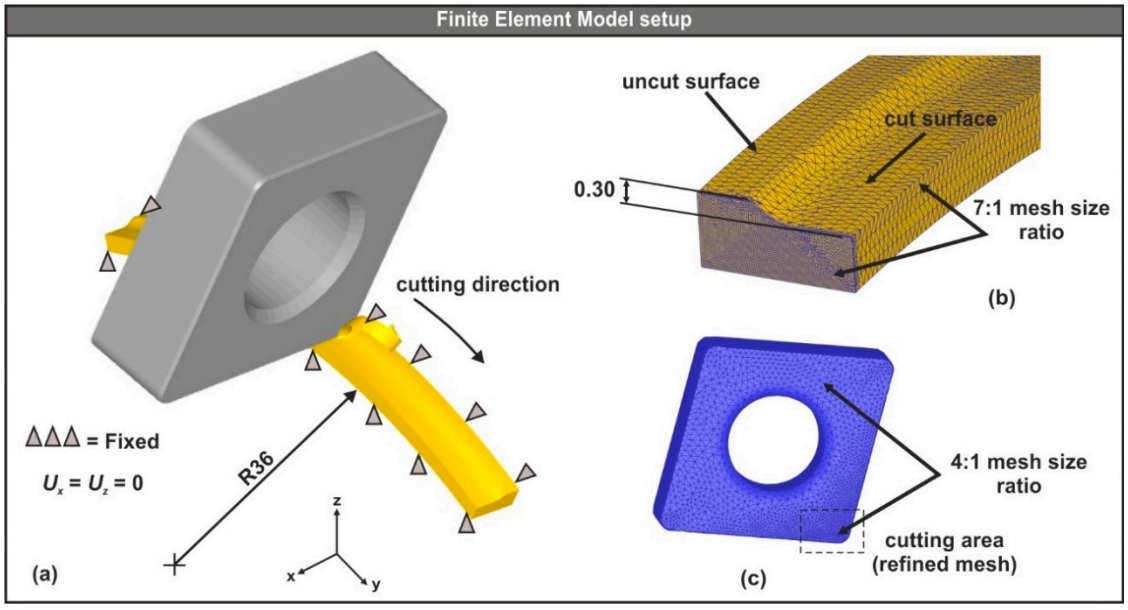

Figure 4. (**a**) The FE model setup, (**b**) the analysis domain, and (**c**) the meshed tool.

2.3.1. Configuration of the Insert-Workpiece Interface

The models of the three turning inserts were designed according to the ISO-13399 norms (see Figure 3b), whereas the simplified version of the workpiece was designed with respect to the depth of cut, the nose radius of the tool and the diameter of the steel bar. Moreover, the workpiece was modeled as deformable (plastic) with a mesh that varied between 100,000 and 150,000 elements depending on the size of the minimum element, which was fixed to 25% of the feed value for all tests [29]. Since the area of interest is at the uncut surface of the workpiece, where contact between the insert and the workpiece exists, a finer mesh was applied with a 7:1 ratio (see Figure 4b). In contrast, the insert was modeled as rigid and meshed with the maximum allowed number of tetrahedral elements, which was approximately 50,000 for this case. Furthermore, in order to increase the fidelity of the area near the cutting edge that is in contact with the uncut surface of the workpiece, the related mesh was locally refined with a size ratio of 4:1 (see Figure 4c).

Mesh definition is the parameter that most affects the simulation performance. In order to maintain both the geometry of the chip during forming and the required state variables in the target areas, an adaptive remeshing technique was implemented. The goal of this method is to adoptively refine the mesh of the workpiece so that after a specified number of time steps, the minimum required number of mesh elements is preserved. Hence, the quality of the simulation results were kept to a satisfactory level and at the same time, the simulation runs required a reasonable amount of time to complete.

Finally, the deformation and thermal boundary conditions were set. Specifically, the workpiece was fixed according to Figure 4a, so that the velocity of the nodes in both the X and Z axes was set to zero. In contrast, the insert model was allowed to follow the cutting path, as shown in Figure 4a. The heat exchange between the surface elements of the workpiece and the tool for both convection and conduction were also defined. The value for the heat transfer coefficient via convection that was used in this study was 0.02 N/(s × mm × °C) for dry cutting and via conduction, it was 45 N/(s × mm × °C). These values are the ones provided by default in the DEFORM™-3D software [13].

2.3.2. Modeling of the Insert-Workpiece Materials

The Johnson–Cook material model was used in this study to represent the mechanical behavior of the workpiece. This model is widely accepted by researchers, especially when high strain, strain rate, and temperatures are present during the process. According to Melkote et al. [30], this model has a simple form and is easy to implement and calibrate. The following analytical expression (Equation (1)) constitutes the strain hardening properties of the material, the strain rate sensitivity, and the thermal softening properties accordingly.

$$\sigma = (A + B\varepsilon^n)\left(1 + C\ln\frac{\dot{\varepsilon}}{\dot{\varepsilon}_0}\right)\left[1 - \left(\frac{T - T_0}{T_m - T_0}\right)^m\right] \quad (1)$$

In the previous formula, σ is the equivalent stress; A is the initial yield stress; B is the strain hardening modulus; C denotes the strain rate dependence coefficient; ε represents the plastic strain; n is the strain hardening exponent; m is the thermal softening coefficient; and $\dot{\varepsilon}$ is the plastic strain rate, whereas $\dot{\varepsilon}_0$ is the reference plastic strain rate; finally T, T_0, and T_m stand for the reference temperature, the ambient temperature, and the melting temperature of the workpiece material, respectively. To adapt the model for the present case, the constants that are available in Table 2 for the AISI-4140 flow stress were used. All the important properties as well as the model constants of the steel material are available in the software's library.

Table 2. The Johnson–Cook model constants for AISI-4140 steel [13].

A (MPa)	B (MPa)	C	n	m	T_0 (°C)	T_m (°C)
106	1167	0.0352	0.1424	0.763	20	1547

Table 3 contains both the mechanical and the thermal properties that were used in the present numerical study. In particular, the elastic modulus, the thermal expansion, the thermal conductivity, and the heat capacity of AISI-4140 were expressed as a function of temperature f (Temp) due to the fact that they are temperature dependent. In addition, a reference strain rate of 1/s was used.

Table 3. Thermo-mechanical properties for the ceramic insert [31] and steel workpiece [13].

Mechanical Properties	**AISI-4140**	**Ceramic**
Young's Modulus (GPa)	212 @ 20 °C 192 @ 300 °C 164 @ 600 °C	415
Density (kg/m^3)	7850	3500
Poisson's ratio	0.30	0.22
Hardness (HRC)	60	–
Thermal Properties	**AISI-4140**	**Ceramic**
Heat capacity (J/kgK)	362 @ 20 °C 446 @ 300 °C 610 @ 600 °C	334
Thermal expansion (μm/mK)	11.9 @ 20 °C 13.6 @ 300 °C 14.9 @ 600 °C	8.4
Thermal conductivity (W/mK)	41.7 @ 20 °C 41.4 @ 300 °C 34.1 @ 600 °C	7.5

In order to approximate the fracture of the material that occurs due to the material separation under the action of stress, the normalized Cockroft–Latham damage model was employed.

Equation (2) represents the modified criterion developed by Cockroft and Latham [32]. In this formula, the maximum principal stress is normalized by the effective stress.

$$D_c = \int_0^{\varepsilon_f} \frac{\sigma_{\max}}{\overline{\sigma}} d\varepsilon_{pl} \tag{2}$$

In the integral, Dc is the material constant in the fracture criterion; σ_{max} is the maximum tensile principal stress; $\overline{\sigma}$ denotes the effective stress; ε_f represents the limit fracture strain; and finally, ε_{pl} stands for the plastic strain. This criterion is widely accepted and was implemented in early FE studies such as in the formability of solid cylindrical and ring test specimens by Kobayashi and Lee [33] as well as in the determination of workability in bar extrusion and drawing by Oh et al. [34]. Later, Oyane et al. [35] attempted to predict the fracture strain in actual metal working processes using the basic criterion.

Modeling of the friction situation between two bodies is a very complicated problem, especially when extreme contact pressures develop such as in the case of machining. In order to approximate the phenomena that occur during the contact between the insert and the workpiece, Coulomb's law was utilized. In the work of Zorev [36], the contact area between the cutting tool and the machined workpiece was divided into sticking and sliding zones. With this in mind, Equation (3) [37] can be used to estimate the developed frictional stresses according to Coulomb's law.

$$\tau_f = \mu \sigma_n \tag{3}$$

where τ_f is the frictional shear stress; μ denotes the shear friction coefficient; and σ_n represents the tool-chip interface stress. Previous studies [38,39] suggest a value of friction coefficient between 0.5 and 0.6 when studying the machining of AISI-4140 steel at cutting speeds and feed rates similar to the

ones used in the present work. Considering the conditions utilized in this research, the shear friction coefficient for the numerical model was set to 0.577 [40].

3. Results and Discussion

3.1. Assessment of the Cutting Force Components Using FEM

A sample of the generated cutting force components versus time diagrams based on the 3D numerical model are depicted in Figure 5. In particular, Figure 5a–c illustrate the aforementioned diagrams for the radial force (F_r), the tangential force (F_t), and the feed force (F_a) that were generated during AISI-4140 hard turning with the CNGA120404 (re = 0.40 mm) insert. Similarly, Figure 5d–f corresponded to the CNGA120408 (re = 0.80 mm) insert and consequently Figure 5g–i relate to the CNGA120412 (re = 1.20 mm) insert. The following cutting conditions apply for all the previously mentioned sets: V_c = 150 m/min, f = 0.14 mm/rev, and ap = 0.30 mm. All force versus time diagrams are divided into two phases: the entry phase where force increases quickly as soon as the tool touches the uncut surface of the material and the following steady state phase where force maintains a steady mean value. Finally, when the tool finishes its pass on the workpiece and material removal ends, the force value rapidly decreases until it reaches zero.

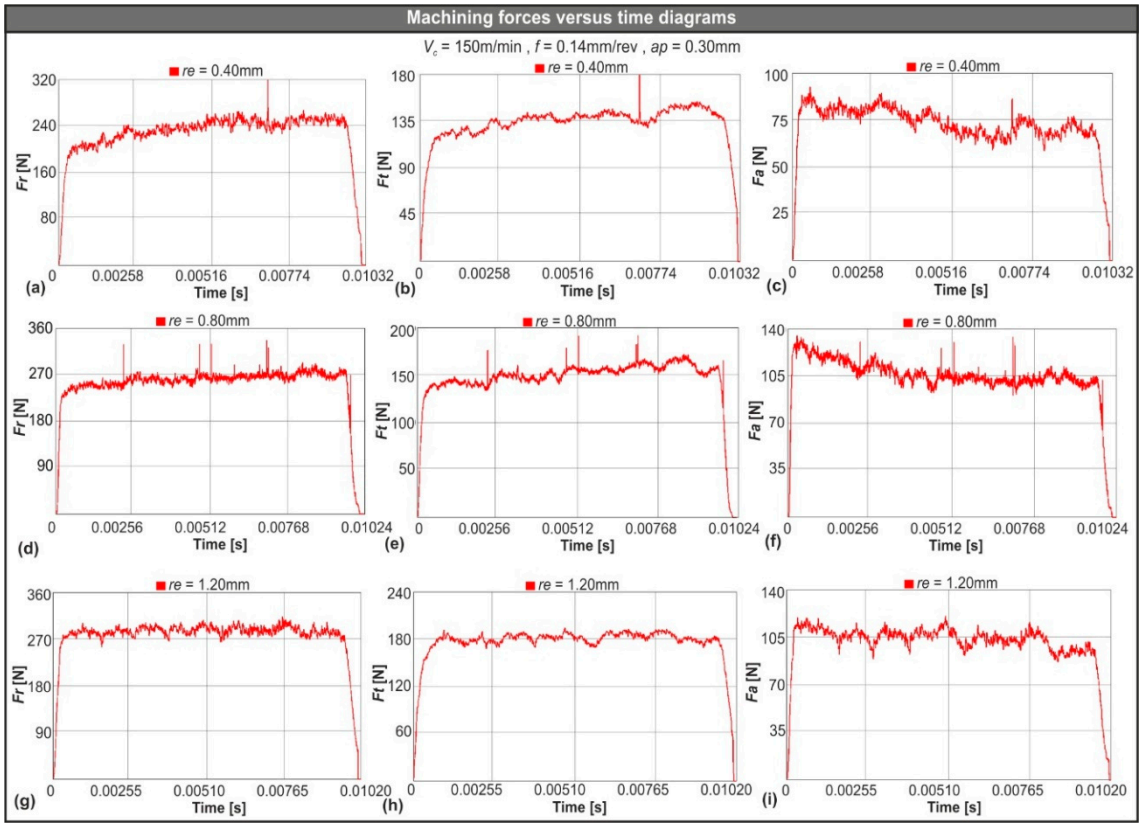

Figure 5. (**a**–**c**) Sample machining forces versus time diagrams for 0.40 mm nose radius, (**d**–**f**) 0.80 mm, and (**g**–**i**) 1.20 mm.

Every few time steps, a remeshing procedure occurs in order to keep the necessary minimum amount of elements. Due to this phenomenon, force spikes might appear during the simulation process. Even though the effect of these spikes to the mean value of force is minimal, the default first order exponential smoothing of DEFORM™-3D was enabled to eliminate any unrealistic values.

For the numerical model calibration, a set of experimental values (see Table 4) were used for the exact machining conditions and tools. According to Table 4, the level of agreement between the experimental and the numerical results for F_{main} is high. Furthermore, based on the findings

of Aouici et al. [24] the experimental analysis of the machining components for the next indicative conditions: V_c = 115 m/min, f = 0.11 mm/rev, and ap = 0.30 mm showed an increased correlation with the equivalent simulated results that were derived from the present study. That is, F_r = 202.3 N, F_t = 146.0 N, and F_a = 86.6 N for the experiments and F_r = 214.4 N, F_t = 137.5 N, and F_a = 77.4 N for the simulations, leading to an estimated relative error of 6.0%, −5.8%, and −10.6%, respectively.

Table 4. Main machining force comparison between the experimental and numerical values.

	Cutting Parameters				F_{main} (N)		
Std Order	V_c **(m/min)**	f **(mm/rev)**	ap **(mm)**	re **(mm)**	**Experiments**	**FE Model**	**Relative Error (%)**
1	80	0.08	0.30	0.80	189.8	207.7	9.4
2	80	0.11	0.30	0.80	244.6	250.2	2.3
3	80	0.14	0.30	0.80	282.3	264.5	−6.3
4	115	0.08	0.30	0.80	225.7	232.1	2.8
5	115	0.11	0.30	0.80	264.1	266.2	0.8
6	115	0.14	0.30	0.80	300.9	281.5	−6.4
7	150	0.08	0.30	0.80	238.0	249.6	4.9
8	150	0.11	0.30	0.80	267.7	281.2	5.1
9	150	0.14	0.30	0.80	316.9	320.7	1.2

With the calibration of the model, two new sets of 3D simulations were performed. Each set consisted of nine simulation tests that were carried out under identical conditions and in the same order as the calibration set. In addition, different tools were used with a nose radius of 0.40 mm and 1.20 mm, respectively (see Table 1). The yielded results were used to plot the charts that are presented in Figure 6. With the plotted results, it is possible to compare the mean values of the generated machining force components for each tool graphically. In particular, Figure 6 contains the results for the radial force (Figure 6a), the tangential force (Figure 6b), the feed force (Figure 6c), and the resultant of the three individual forces (Figure 6d).

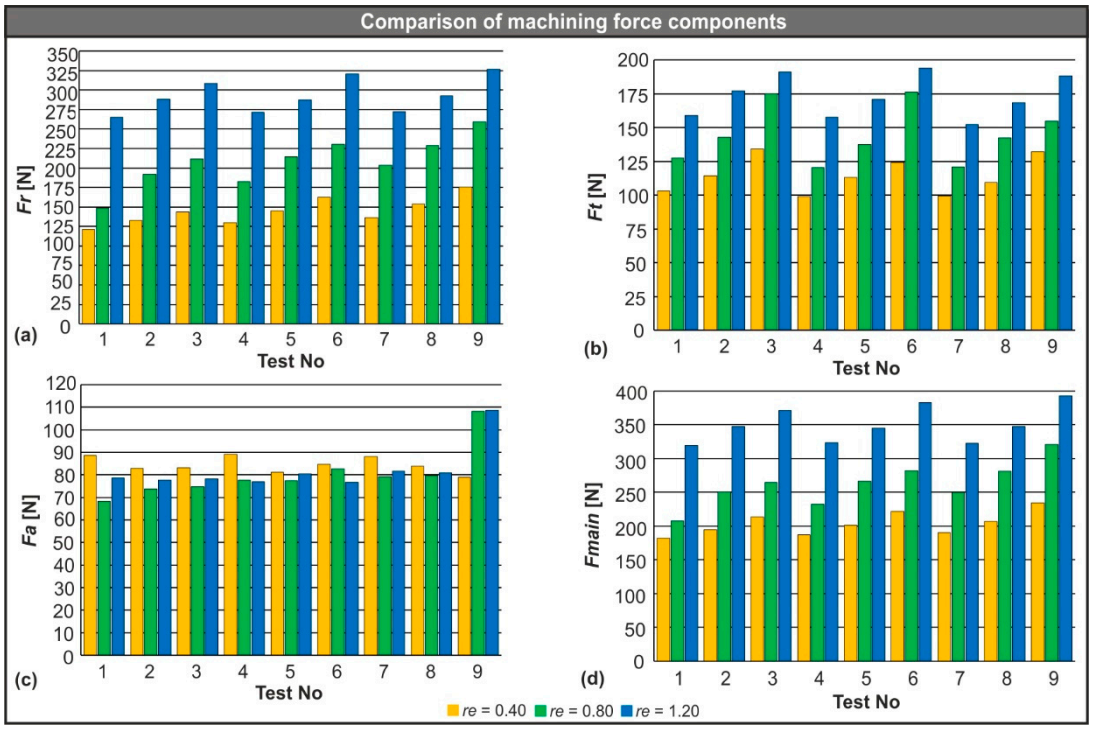

Figure 6. (**a**) Comparison of the radial force, (**b**) the tangential force, (**c**) the feed force, and (**d**) the resultant machining force based on the different nose radii.

Observations of the results from Table 4 and Figure 6 led to the following conclusions:

- The radial force is the component that contributes to the resultant machining force the most. In test number nine, for example, this contribution was approximately 56.6%, 65.3%, and 69.2% for each value of nose radius of 0.40 mm, 0.80 mm, and 1.20 mm, respectively. The same trend was observed in the rest of the tests.
- Any increase in feed rate affects all forces except the feed force. Even though the amount of change is not significant, it cannot be considered negligible either. Specifically, an increase in the feed rate from 0.08 mm/rev to 0.11 mm/rev increased the resultant machining force by about 7.6%, 16.0%, and 7.7% for each nose radius (0.40 mm, 0.80 mm, and 1.20 mm, respectively). Similarly, when the feed rate changed from 0.11 mm/rev to 0.14 mm/rev, the feed rate rose by approximately 10.9%, 13.7%, and 10.4% for the same nose radii, respectively.
- In contrast, the nose radius of the inserts had a notable impact on the generated cutting forces. The main machining force increased by 28% on average when the nose radius of the tool changed from 0.40 mm to 0.80 mm. Furthermore, the tool with the 1.20 mm nose radius produced even higher forces. The change from the 0.80 mm nose radius to the 1.20 mm increased F_{main} by 35% on average.
- Finally, any change in cutting speed had a limited effect on the turning forces. A slight decrease in cutting forces was noted as lower cutting speeds were applied. In particular, by lowering cutting speed from 150 m/min to 115 m/min, the decrease was estimated as approximately 4.5% and for the equivalent shift from 115 m/min to 80 m/min, the reduction was found to be close to 3.4%.

The conditions that were applied in the present research were successfully implemented in previous experimental studies [2,6,41–43] for hard turning of similar materials. Davim and Figueira [6] and Quiza et al. [43] used ceramic inserts with designation numbers CNMA120408T01020 and CNGA120408T0120 correspondingly during turning of AISI-D2 at a 0.2 mm depth of cut. Aouici et al. [41,42] reported results of similar magnitude as the present work during turning of both AISI-D3 and AISI-H11 steel with the ceramic SNGA120408T01020 and cubic boron nitride (CBN) SNGA120408S01020 inserts at depths of cut between 0.15 and 0.45 mm, respectively. Furthermore, the authors stated that the radial force was the governing component. In addition, the effects of feed rate and cutting speed were also discussed in the work of Aouici et al. for AISI-4140 [24], clearly verifying the aforementioned observations of the present research.

3.2. Modelling of the Resultant Cutting Force Using RSM

In addition to the 3D FE model, a statistically based model was developed with the aid of the response surface methodology (RSM). The purpose of this model was to reduce the number of simulation tests required to predict the cutting forces induced during machining of AISI-4140 under different conditions. The RSM is a well-established statistical tool that formulates a defined relation between two groups of data; one contains dependent variables and the other independent variables. This methodology was embraced by many researchers for prediction and optimization purposes during studies related to typical machining processes [2,3,15,44–46] due to the fact that it is versatile and can generate both linear and quadratic models. The three levels of the cutting parameters used (see Table 1) and the number of the numerical tests led to a full factorial design with three factors and a total of twenty-seven experiments. The generated regression model is a second order polynomial that is described by Equation (4). This polynomial includes linear, quadratic, and cross-product terms because the relationship between the input variables and the response is non-linear. In Equation (4), Y is the response of the model (resultant machining force), a_0 denotes the fixed term, X_i are the input variables (cutting speed, feed rate and nose radius), and b_i, b_{ij}, b_{ii} refer to the vectors that contain the regression coefficients (linear, quadratic, and cross-product, respectively).

$$Y = a_0 + \sum_{i=1}^{n} b_i X_i + \sum_{i,j}^{n} b_{ij} X_i X_j + \sum_{i=1}^{n} b_{ii} X_i^2 \quad (4)$$

Equation (5) presents the complete statistical model for the resultant machining force based on the aforementioned formula and the data of the verified FE model (see Table 4).

$$F_{main} = 158.1 - 0.109V - 822f + 48.8re + 0.00046V^2 + 4504f^2 + 56.6re^2 + 3.03Vf - 0.093Vre + 498fre \quad (5)$$

In Equation (5), F_{main} is the resultant machining force in N; V is the cutting speed in m/min; f is the feed rate in mm/rev; and re represents the insert's nose radius in mm.

Table 5 presents the complete design of experiments that includes all the possible combinations of cutting conditions along with the predicted values of the resultant machining force. The predicted values were derived from both the numerical and the statistical model. Additionally, the comparison between the aforementioned values indicated a strong correlation. The lowest absolute percent error was found to be approximately 6.5% for test number 10, whereas the mean absolute percentage error (MAPE) was close to 2%, which proved the increased agreement between the two models.

Table 5. Main machining force comparison between the simulated and statistical values.

	Cutting Parameters			F_{main} (N)	
Std Order	**V_c (m/min)**	**F (mm/rev)**	**re (mm)**	**FE Model**	**RegressionModel**
1	80	0.08	0.40	182.3	176.3
2	80	0.11	0.40	194.1	190.6
3	80	0.14	0.40	213.6	212.9
4	115	0.08	0.40	186.5	182.8
5	115	0.11	0.40	201.0	200.3
6	115	0.14	0.40	221.3	225.8
7	150	0.08	0.40	190.2	190.5
8	150	0.11	0.40	206.5	211.1
9	150	0.14	0.40	233.7	239.8
10	80	0.08	0.80	207.7	236.0
11	80	0.11	0.80	250.2	256.2
12	80	0.14	0.80	284.5	284.5
13	115	0.08	0.80	232.1	241.2
14	115	0.11	0.80	266.2	264.6
15	115	0.14	0.80	301.5	296.1
16	150	0.08	0.80	249.6	247.5
17	150	0.11	0.80	281.2	274.1
18	150	0.14	0.80	320.7	308.8
19	80	0.08	1.20	319.1	313.7
20	80	0.11	1.20	346.9	339.9
21	80	0.14	1.20	371.3	374.3
22	115	0.08	1.20	323.3	317.6
23	115	0.11	1.20	344.4	347.0
24	115	0.14	1.20	382.6	384.5
25	150	0.08	1.20	322.4	322.7
26	150	0.11	1.20	347.4	355.2
27	150	0.14	1.20	392.3	395.9

3.3. Validation of the RSM Based Model

The analysis of variance (ANOVA) was employed to validate the model with a standard significance level equal to 0.05. The power of the test was sufficient since the analysis yielded a successful fit of the model with an adjusted R-squared of 98.80% and the obtained ANOVA results are presented in Table 6. The contribution of the factors to the model was highlighted with the aid of the p-value. Hence, the constant, the re^2 term and the $f \times re$ term contributed the most, indicating the strong influence of the corner radius to the generated forces. In addition, the total sum of squares was used to express the total variation of the response, which can be visualized with the aid of the data points dispersion graph

(see Figure 7a). Last but not least, the *p*-value of the regression model suggests that the probability of acquiring extreme results is thin.

Table 6. Analysis of variance (ANOVA) results for the resultant machining force.

Source	Degree of Freedom	Sum of Squares	Mean Square	*f*-Value	*p*-Value
Regression	9	113,045	12,560.6	238.87	0.000
Residual Error	17	894	52.6		
Total	26	113,939			
		R-sq (adj) = 98.80%			
Term	**PE Coefficient**	**SE Coefficient**	***t*-Value**	***p*-Value**	
Constant	158.1	59.8	2.64	0.017	
V	−0.109	0.611	−0.18	0.861	
f	−822	774	−1.06	0.303	
re	48.8	39.5	1.24	0.233	
V^2	0.00046	0.00242	0.19	0.853	
f^2	4504	3289	1.37	0.189	
re^2	56.6	18.5	3.06	0.007	
$V \times f$	3.03	1.99	1.52	0.147	
$V \times re$	−0.093	0.150	−0.62	0.540	
$f \times re$	498	174	2.86	0.011	

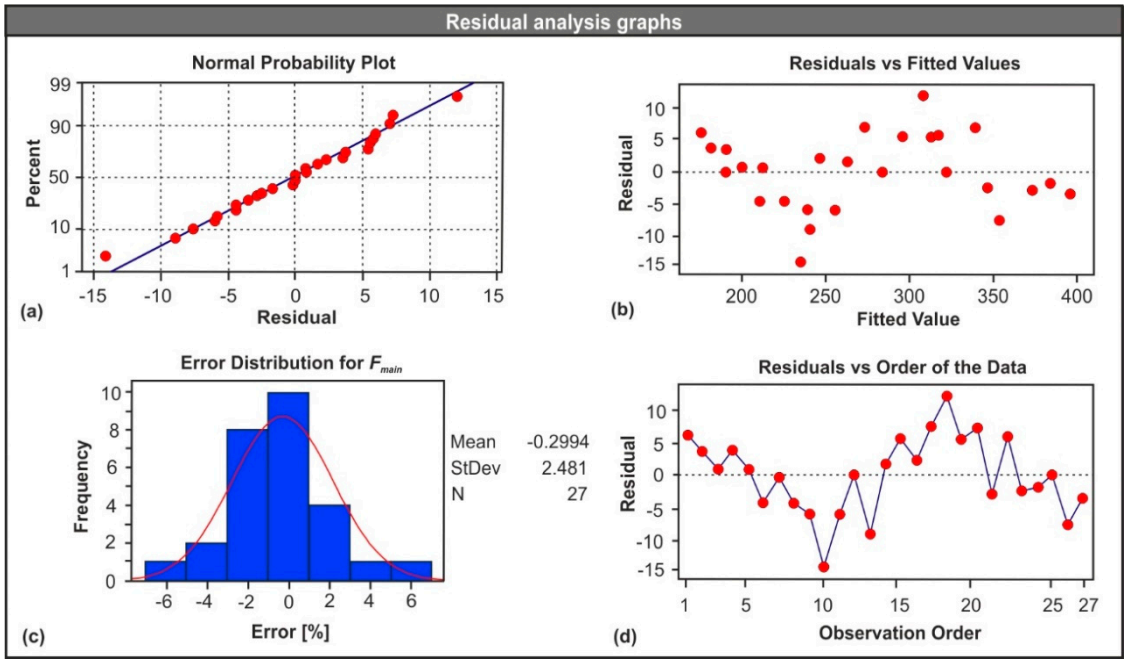

Figure 7. Residual analysis graphs: (**a**) probability plot, (**b**) residuals versus fitted values, (**c**) error histogram, and (**d**) residuals versus order.

Figure 7 contains the graphical results of the ANOVA that are crucial when checking the validity of the regression model. Specifically, Figure 7a illustrates the normal probability plot, which indicates any departures of the data points from the fit line. In this case, there were no such points. Figure 7b depicts the residuals versus the fitted values plot, which highlights the way the data points are scattered across the reference line. In the present case, it is clear that they were almost evenly scattered on both sides of the line. Figure 7c shows the error percentage histogram along with the fit line in order to check the normality in the error distribution. It is clear that error uniformity was present in the model. Furthermore, the overall normality can be checked by Figure 7d, which illustrates the residuals versus

the order of the data. By observing the points in Figure 7d, it can be concluded that no systematic faults were present in the model, since no specific trends or patterns were formed.

Finally, the 3D response surface plots were prepared in order to visualize the performance of the developed regression model according to the data that are available in Figure 6 and Table 5. The performance with respect to the cutting speed, the feed rate, and the tool nose radius are illustrated in Figure 8. Moreover, the 3D plots graphically represent the polynomial solutions of the model according to the range of the cutting conditions found in the present paper. Finally, via the 3D plots it could be observed that:

- The nose radius had a strong impact on the resultant turning force. In fact, an increase from 0.40 mm to 1.20 mm almost doubled the resultant force regardless of the conditions.
- Any increase in feed rate acts as increasing the main cutting force, but at a much lower grade compared to the effect of the nose radius.
- Finally, any change in the cutting speed did not seem to have a significant influence on the main cutting force.

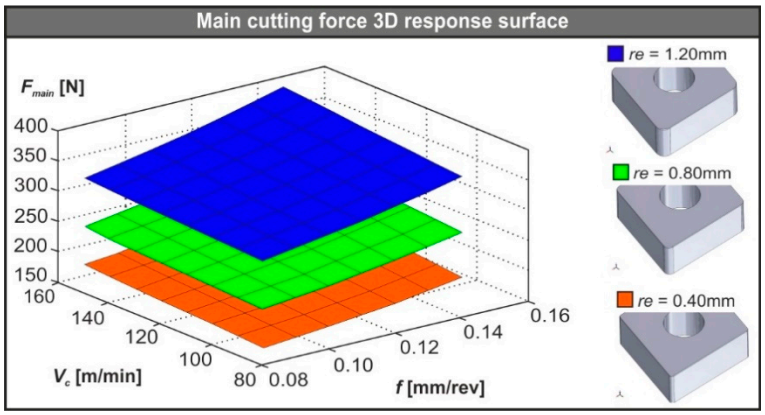

Figure 8. 3D plots of the F_{main} for each nose radius.

To further examine the validity of the statistical model, six extra simulation tests were carried out with different cutting conditions than the ones used for the establishment of the FE model. However, the parameters were chosen from within the range of the already employed data. Table 7 contains the results for the following conditions at a depth of cut equal to 0.30 mm: I (V_c = 100 m/min, f = 0.10 mm/rev, and re = 0.40 mm), II (V_c = 120 m/min, f = 0.10 mm/rev, and re = 0.80 mm), III (V_c = 140 m/min, f = 0.10 mm/rev, and re = 1.20 mm), IV (V_c = 100 m/min, f = 0.12 mm/rev, and re = 0.40 mm), V (V_c = 120 m/min, f = 0.12 mm/rev, and re = 0.80 mm), and VI (V_c = 140 m/min, f = 0.12 mm/rev, and re = 1.20 mm). The lowest level of agreement (relative error of 10.8%) between the predicted value of F_{main} and the simulated one was found in test number 5, a fact that indicates that the model provides safe predictions.

Table 7. Confirmation of the prediction model for F_{main}.

Test No.	Simulated F_{main} (N)	Predicted F_{main} (N)	Relative Error (%)
I	197.4	189.7	−3.9
II	242.1	257.0	6.2
III	316.4	341.3	7.9
IV	217.6	203.1	−6.6
V	248.8	275.6	10.8
VI	385.7	365.1	−5.3

4. Conclusions

The present paper presented a 3D FE model for the hard turning of AISI-4140 as well as a prediction model for the resultant machining force, based on statistical methods. A set of experimental results that were available in the literature was used to verify the FE model, and consequently, a complete design of experiments was prepared according to three levels of cutting speed, feed rate, and tool nose radius. Further validation of the statistical model was made to ensure that the model could safely predict the resultant cutting force within the range of conditions found in the present study. Additionally, the influence of the nose radius on the produced cutting forces was investigated and graphically presented. Finally, the following conclusions can be drawn:

- F_r is the governing force during hard turning of AISI-4140, which in most cases represents two-thirds of the produced resultant machining force.
- When feed rate changed from 0.08 mm/rev to 0.11 mm/rev F_{main} gained an average increase of about 10.4%. Similarly, a shift from 0.11 mm/rev to 0.14 mm/rev increased F_{main} by approximately 11.7%, regardless of the nose radius value.
- The nose radius of the cutting edge affects the generated cutting forces substantially. It was highlighted that a higher value of nose radius leads to higher values of cutting forces, and depending on the applied cutting conditions, the increase percentage exceeded 30% in most cases.
- Finally, changing the cutting speed did not seem to influence the main cutting force notably.

Author Contributions: Conceptualization, P.K.; methodology, A.T. and J.-L.H.-T.; software, A.T.; validation, A.T.; formal analysis, A.T.; investigation, A.T.; resources, P.K.; data curation, J.-L.H.-T.; writing—original draft preparation, A.T.; writing—review and editing, P.K.; visualization, A.T.; supervision, C.G.-H., J.-L.H.-T. and P.K.; project administration, C.G.-H.; funding acquisition, P.K. All authors have read and agreed to the published version of the manuscript.

Funding: This research received no external funding.

Conflicts of Interest: The authors declare no conflict of interest.

References

1. Sayuti, M.; Sarhan, A.A.D.; Salem, F. Novel uses of SiO_2 nano-lubrication system in hard turning process of hardened steel AISI4140 for less tool wear, surface roughness and oil consumption. *J. Clean. Prod.* **2014**, *67*, 265–276. [CrossRef]
2. Gaitonde, V.N.; Karnik, S.R.; Figueira, L.; Davim, J.P. Analysis of machinability during hard turning of cold work tool steel (type: AISI D2). *Mater. Manuf. Process.* **2009**, *24*, 1373–1382. [CrossRef]
3. Meddour, I.; Yallese, M.A.; Bensouilah, H.; Khellaf, A.; Elbah, M. Prediction of surface roughness and cutting forces using RSM, ANN, and NSGA-II in finish turning of AISI 4140 hardened steel with mixed ceramic tool. *Int. J. Adv. Manuf. Technol.* **2018**, *97*, 1931–1949. [CrossRef]
4. Elkaseer, A.; Abdelaziz, A.; Saber, M.; Nassef, A. FEM-based study of precision hard turning of stainless steel 316L. *Materials* **2019**, *12*, 2522. [CrossRef] [PubMed]
5. Meddour, I.; Yallese, M.A.; Khattabi, R.; Elbah, M.; Boulanouar, L. Investigation and modeling of cutting forces and surface roughness when hard turning of AISI 52100 steel with mixed ceramic tool: Cutting conditions optimization. *Int. J. Adv. Manuf. Technol.* **2015**, *77*, 1387–1399. [CrossRef]
6. Davim, J.P.; Figueira, L. Machinability evaluation in hard turning of cold work tool steel (D2) with ceramic tools using statistical techniques. *Mater. Des.* **2007**, *28*, 1186–1191. [CrossRef]
7. Saez-de-Buruaga, M.; Soler, D.; Aristimuño, P.X.; Esnaola, J.A.; Arrazola, P.J. Determining tool/chip temperatures from thermography measurements in metal cutting. *Appl. Therm. Eng.* **2018**, *145*, 305–314. [CrossRef]
8. Ye, G.G.; Chen, Y.; Xue, S.F.; Dai, L.H. Critical cutting speed for onset of serrated chip flow in high speed machining. *Int. J. Mach. Tools Manuf.* **2014**, *86*, 18–33. [CrossRef]

9. Shuang, F.; Chen, X.; Ma, W. Numerical analysis of chip formation mechanisms in orthogonal cutting of Ti6Al4V alloy based on a CEL model. *Int. J. Mater. Form.* **2018**, *11*, 185–198. [CrossRef]
10. Arrazola, P.J.; Villar, A.; Ugarte, D.; Marya, S. Serrated chip prediction in finite element modeling of the chip formation process. *Mach. Sci. Technol.* **2007**, *11*, 367–390. [CrossRef]
11. Klocke, F.; Raedt, H.-W.; Hoppe, S. 2D-FEM Simulation of the Orthogonal High Speed Cutting Process. *Mach. Sci. Technol.* **2001**, *5*, 323–340. [CrossRef]
12. Calamaz, M.; Coupard, D.; Girot, F. A new material model for 2D numerical simulation of serrated chip formation when machining titanium alloy Ti-6Al-4V. *Int. J. Mach. Tools Manuf.* **2008**, *48*, 275–288. [CrossRef]
13. *DEFORM*, version 11.3 (PC); Documentation; Scientific Forming Technologies Corporation: Columbus, OH, USA, 2016.
14. Arrazola, P.J.; Özel, T.; Umbrello, D.; Davies, M.; Jawahir, I.S. Recent advances in modelling of metal machining processes. *CIRP Ann. Manuf. Technol.* **2013**, *62*, 695–718. [CrossRef]
15. Tzotzis, A.; García-hernández, C.; Kyratsis, P. FEM based mathematical modelling of thrust force during drilling of Al7075-T6. *Mech. Ind.* **2020**, *415*, 1–14. [CrossRef]
16. Arisoy, Y.M.; Özel, T. Prediction of machining induced microstructure in Ti-6Al-4V alloy using 3-D FE-based simulations: Effects of tool micro-geometry, coating and cutting conditions. *J. Mater. Process. Technol.* **2015**, *220*, 1–26. [CrossRef]
17. Davoudinejad, A.; Tosello, G.; Parenti, P.; Annoni, M. 3D finite element simulation of micro end-milling by considering the effect of tool run-out. *Micromachines* **2017**, *8*, 187. [CrossRef]
18. Guo, Y.B.; Liu, C.R. 3D FEA modeling of hard turning. *J. Manuf. Sci. Eng. Trans. ASME* **2002**, *124*, 189–199. [CrossRef]
19. Karpat, Y.; Ozel, T. Process simulations for 3D turning using uniform and variable microgeometry PCBN tools. *Int. J. Mach. Mach. Mater.* **2008**, *4*, 26–38. [CrossRef]
20. Malakizadi, A.; Gruber, H.; Sadik, I.; Nyborg, L. An FEM-based approach for tool wear estimation in machining. *Wear* **2016**, *368–369*, 10–24. [CrossRef]
21. Lotfi, M.; Jahanbakhsh, M.; Farid, A.A. Wear estimation of ceramic and coated carbide tools in turning of Inconel 625: 3D FE analysis. *Tribol. Int.* **2016**, *99*, 107–116. [CrossRef]
22. Hu, H.J.; Huang, W.J. Effects of turning speed on high-speed turning by ultrafine-grained ceramic tool based on 3D finite element method and experiments. *Int. J. Adv. Manuf. Technol.* **2013**, *67*, 907–915. [CrossRef]
23. Magalhães, F.C.; Ventura, C.E.H.; Abrão, A.M.; Denkena, B. Experimental and numerical analysis of hard turning with multi-chamfered cutting edges. *J. Manuf. Process.* **2020**, *49*, 126–134. [CrossRef]
24. Aouici, H.; Elbah, M.; Yallese, M.A.; Fnides, B.; Meddour, I.; Benlahmidi, S. Performance comparison of wiper and conventional ceramic inserts in hard turning of AISI 4140 steel: Analysis of machining forces and flank wear. *Int. J. Adv. Manuf. Technol.* **2016**, *87*, 2221–2244. [CrossRef]
25. Vijayaraghavan, A. *Automated Drill Design Software*; Consortium on Deburring and Edge Finishing. Berkeley University: Berkeley, CA, USA, 2006.
26. Oancea, G.; Haba, S.-A. Software Tool Used in CAPP/CAM Systems for Rotational Parts. *Sci. Bull. Ser. C Fascicle Mech. Tribol. Mach. Manuf. Technol.* **2016**, *30*, 75.
27. Kyratsis, P.; Tzotzis, A.; Tzetzis, D.; Sapidis, N. Pneumatic cylinder design using cad-based programming. *Acad. J. Manuf. Eng.* **2018**, *16*, 107–113.
28. Gardner, J.D.; Dornfeld, D. *Finite Element Modeling of Drilling Using DEFORM*; Consortium on Deburring and Edge Finishing. Berkeley University: Berkeley, CA, USA, 2006.
29. Tzotzis, A.; Garcia-Hernandez, C.; Talón, J.L.H.; Kyratsis, P. 3D FE Modelling of Machining Forces during AISI 4140 Hard Turning. *Strojniški Vestn. J. Mech. Eng.* **2020**, *66*, 467–478. [CrossRef]
30. Melkote, S.N.; Grzesik, W.; Outeiro, J.; Rech, J.; Schulze, V.; Attia, H.; Arrazola, P.J.; M'Saoubi, R.; Saldana, C. Advances in material and friction data for modelling of metal machining. *CIRP Ann. Manuf. Technol.* **2017**, *66*, 731–754. [CrossRef]
31. Hu, H.J.; Huang, W.J. Tool life models of nano ceramic tool for turning hard steel based on FEM simulation and experiments. *Ceram. Int.* **2014**, *40*, 8987–8996. [CrossRef]
32. Cockcroft, M.G.; Latham, D.J. Ductility and the Workability of Metals. *J. Institue Met.* **1968**, *96*, 33–39.
33. Kobayashi, S.; Lee, C. Deformation mechanics and workability in upsetting solid circular cylinders. *Proc. North. Am. Metalwork. Res. Conf.* **1973**, *1*, 185–204.

34. Oh, S.; Chen, C.; Kobayashi, S. Ductile fracture in axisymmetric extrusion and drawing—Part 2: Workability in extrusion and drawing. *J. Manuf. Sci. Eng. ASME* **1979**, *101*, 36–44. [CrossRef]
35. Oyane, M.; Sato, T.; Okimoto, K.; Shima, S. Criteria for ductile fracture and their applications. *J. Mech. Work. Technol.* **1980**, *4*, 65–81. [CrossRef]
36. Zorev, N.N. Inter-relationship between shear processes occurring along tool face and shear plane in metal cutting. *Int. Res. Prod. Eng.* **1963**, *49*, 143–152.
37. Agmell, M. *Applied FEM of Metal Removal and Forming*, 1st ed.; Studentlitteratur: Lund, Sweden, 2018; ISBN 978-91-44-12507-7.
38. Arrazola, P.J.; Meslin, F.; Marya, S. A technique for the identification of friction at tool/chip interface during machining. In Proceedings of the 6th CIRP International Workshop on Modeling of Machining Operations, Hamilton, ON, Canada, 20 May 2003; pp. 1–6.
39. Haglund, A.J.; Kishawy, H.A.; Rogers, R.J. An exploration of friction models for the chip-tool interface using an Arbitrary Lagrangian—Eulerian finite element model. *Wear.* **2008**, *265*, 452–460. [CrossRef]
40. Astakhov, V.P. *Tribology of Metal Cutting*, 1st ed.; Elsevier Ltd.: Amsterdam, The Netherlands, 2006; ISBN 0080451497.
41. Aouici, H.; Bouchelaghem, H.; Yallese, M.A.; Elbah, M. Machinability investigation in hard turning of AISI D3 cold work steel with ceramic tool using response surface methodology. *Int. J. Adv. Manuf. Technol.* **2014**, *73*, 1775–1788. [CrossRef]
42. Aouici, H.; Yallese, M.A.; Chaoui, K.; Mabrouki, T.; Rigal, J.F. Analysis of surface roughness and cutting force components in hard turning with CBN tool: Prediction model and cutting conditions optimization. *Meas. J. Int. Meas. Confed.* **2012**, *45*, 344–353. [CrossRef]
43. Quiza, R.; Figueira, L.; Davim, J.P. Comparing statistical models and artificial neural networks on predicting the tool wear in hard machining D2 AISI steel. *Int. J. Adv. Manuf. Technol.* **2008**, *37*, 641–648. [CrossRef]
44. Sahu, N.K.; Andhare, A.B. Prediction of residual stress using RSM during turning of Ti–6Al–4V with the 3D FEM assist and experiments. *SN Appl. Sci.* **2019**, *1*, 1–14. [CrossRef]
45. Efkolidis, N.; Hernández, C.G.; Talón, J.L.H.; Kyratsis, P. Modelling and prediction of thrust force and torque in drilling operations of Al7075 using ANN and RSM methodologies. *Strojniški Vestn. J. Mech. Eng.* **2018**, *64*, 351–361. [CrossRef]
46. Chmielewski, T.; Swiercz, D.O. Multi-Response Optimization of Electrical Discharge Machining Using the Desirability Function. *Micromachines* **2019**, *10*, 72. [CrossRef]